

The Quest for Stability of Perovskite Solar Cells: Understanding Degradation, Improving Lifetimes and Towards Experimental Standards

THÈSE N° 8106 (2018)

PRÉSENTÉE LE 9 FÉVRIER 2018
À LA FACULTÉ DES SCIENCES DE BASE
LABORATOIRE DE PHOTONIQUE ET INTERFACES
PROGRAMME DOCTORAL EN SCIENCE ET GÉNIE DES MATÉRIAUX

ÉCOLE POLYTECHNIQUE FÉDÉRALE DE LAUSANNE

POUR L'OBTENTION DU GRADE DE DOCTEUR ÈS SCIENCES

PAR

Konrad DOMANSKI

acceptée sur proposition du jury:

Prof. F. Nüesch, président du jury
Prof. M. Graetzel, Dr W. R. Tress, directeurs de thèse
Prof. U. Bach, rapporteur
Dr T. Moehl, rapporteur
Prof. C. Ballif, rapporteur



ÉCOLE POLYTECHNIQUE
FÉDÉRALE DE LAUSANNE

Suisse
2018

Acknowledgements

First of all, I would like to thank my PhD supervisor, Prof. Michael Grätzel. He has not only selected me to undertake doctoral studies in his group but also, from the beginning, put a lot of trust in me by encouraging me to pursue my research interests freely. At the same time, Michael was always there to answer my questions, give me advice and support me in my many extra-curricular activities. I believe this freedom was one of the main reasons, why my doctoral studies have been such an enjoyable experience.

I also would like to thank Dr. Wolfgang Tress, a great friend, mentor and my co-supervisor. From the very beginning of my studies, Wolfgang offered me his unconditional support. We had countless discussions on countless topics – both scientific and those less scientific. He has also been a great companion in hiking, climbing, skiing and enjoying time after work in general. Finally, together we built the stability setup, which has been one of the main achievements of my PhD. I also would like to thank Prof. Anders Hagfeldt, who entrusted me developing the stability setup and generously backed the project financially. Anders has also been very involved in my research and I am very grateful to him for his contribution and his recommendations.

I want to thank Dr. Juan-Pablo Correa-Baena for being a great friend personally and a mentor professionally. I learned a lot about both science and inter-personal relations from Juan-Pablo. That is not to mention that he is the impersonation of optimism, having good time and simply such a cheerful personality. I also thank Prof. Antonio Abate for his friendship, collaborations and teaching me to be professional. I thank Dr. Thomas Moehl for introducing me to LPI, supervising my first project when I joined the lab and finally, for being one of the examiners at my PhD exam. I also thank Prof. Mohammad Khaja Nazeeruddin for his role in my admission and his supervision in the first year of my PhD.

I also would like to thank the remaining members of my Thesis Jury Committee: Prof. Frank Nüesch, Prof. Udo Bach and Prof. Christophe Ballif, for their time to review my work, their criticism and time to attend my private defence.

I owe special thanks to Benjamin Le Geyt and Supardi Sujito, electronic engineers who designed and assembled most of the electronics for the stability setup and wrote software to operate it. Similarly, I would like to thank Christophe Clement and Andre Fattet, mechanical engineers who supported the development of the mechanical components of the setup and who taught me how to use SolidWorks. Finally, I owe thanks to Antonio Oliveira, who helped me interfaces all the pieces of the equipment together.

Further, I would like to thank Heidi Francelet and Carmen Biagini for their excellent administrative support, as well as all past and present members of LPI-LSPM: master students, fellow PhD students, postdocs, scientists and the administrative staff, who have been great colleagues creating dynamic and vibrant environment. I would like to specifically thank Amita Ummadisingu, Marko Stojanovic and Nathalie Flores-Diaz for keeping up the group spirit. I also would like to thank many great collaborators I had a pleasure to work with during my PhD. While the list would be too long mention them all, I would like to especially thank Dr. Nicolas Mine, Dr. Kerttu Aitola, Taisuke Matsui, Dr. Cristina Roldán Carmona, Alwin Daus and Essa Alharbi. I believe having reliable and honest collaborators is the key to scientific success.

I would like to thank all member of Innovation Forum Lausanne for their trust, patience and teaching me professionalism and entrepreneurship. I have special thanks for Beatrice Volpe, Caterina Bigoni, Niccolo dal Santo and Jakub Vohryzek.

Coming to Lausanne in 2014, I could not wish to make so many great friends outside of work. Again too many to mention them all. I would like to thank Onur Yuruten for his friendship, company in the mountains and teaching me his stoic attitude to life. I would like to thank Manos Kokustos for his friendship and political discussions. I thank Martin Friedl and Irene Bardi for their kindness, friendship, time in the mountains and buying exactly the same set of mountaineering gear :) I also thank Carlos Becker for his friendship, organizing cooking reunions, feeding me a huge amount of carrot cake and discussing interesting and often intriguing approaches to life. I thank Anli Tang for his friendship, wine tastings and the many initiatives he always has. I thank Róger Bermúdez-Chacón and Eirini Arvaniti for their great humour, friendship and kindness.

I also would like to thank all my friends, who live in various parts of the world and who, despite being far away, keep in touch. Very special thanks to Agata Kujda and Marysia Sujkowska – the two absolutely positively crazy ladies. Also thanks to Vsevolod Kachanov, Anastasia Rajevskaia, Szymon Rozwadowski, Alan and Ola Klikuszowian, Gosia and Karol Fornalscy, Mateusz Hyła, Damian Pabiś, Monika and Szymon Foltyn, Magda Sawicka, Przemek Głowacki, Łukasz Wroczyński, Monika Królak, Marcin Iwanow, Mateusz Lisewski, Yasemin Bashir and Rysiek Kaleta. Your friendship means a lot to me and I am always looking forward to our reunions.

Na koniec chcę podziękować mojej wspaniałej rodzinie: moim rodzicom, którzy zawsze wspierali mnie w moich dążeniach do celu, zapewnili mi edukację i ciepło rodzinnego domu. Mojemu bratu, Pawłowi za jego poczucie humoru, odwiedziny i nasze dyskusje. Moim dziadkom za ich bezwarunkową miłość i wsparcie oraz całej rodzinie, która zawsze dopingowała mnie. Finally, I would like to thank my wonderful wife, Agata, for all the love and care she has given me. She has always been there for me, helped me develop as a person and accompanied me through many crazy moments and ideas – one being moving to Switzerland in the first place. I love you more than anything in this world!

Lausanne, 30 November 2017

Abstract

Perovskite solar cells (PSCs) have attracted a substantial interest owing to a very fast achievement of efficiencies >20 % within only several years of development. However, for any solar cell to become technologically viable, two additional milestones have to be achieved alongside high efficiency: means of industrial production and good operational stability. The former being mostly the focus of the private sector and industrially-oriented research institutes, understanding degradation and improving the stability of PSCs has become one of the major research topics in the field of emerging photovoltaics. This is also the focus of this thesis, where I investigate different degradation mechanisms in PSCs with the aim of extending their long-term stability. This dissertation can be divided into four parts: in the first one, I show how, through a series of prototypes, I designed and built a dedicated setup to investigate stability of PSCs. I also show how I developed its variation to improve by 700 % the efficiency of measuring current-voltage characteristics of our solar cells.

Subsequently, I describe the intrinsic instability of, at the time, state-of-the-art PSCs. I show how, along with my colleagues, we managed to achieve breakthrough room temperature stability coupled with record efficiency through incorporation of Cs into perovskite. Next, I describe how and why these solar cells suffer from irreversible degradation if left at elevated temperatures however. This is due to a vulnerability to Au diffusion from the electrode, through Spiro-MeOTAD hole transporting layer into the perovskite. I show how, by incorporation of Cr diffusion barrier I managed to circumvent this problem (albeit at considerable efficiency loss). Subsequently, I describe an alternative solution to the problem by substituting Spiro-MeOTAD with PTAA – a polymeric hole transporting layer. This approach effectively stops Au diffusion without compromising device efficiency, which was at the same time improved by incorporating Rb into the perovskite. Finally, a third approach is presented: replacing the Au electrode with one based on carbon nanotubes. This gives away with using Au and PTAA – both prohibitively expensive materials – and hence paves the way towards facile and inexpensive fabrication of stable PSCs.

In the third part, I describe the effects of mobile ions in the perovskite on the behaviour of PSCs. First, I show how they lead to a partial reversibility of losses in aged devices. This has potentially far-reaching consequences for the way stability measurements of PSCs are conducted and how their lifetime is reported. Next, I show how the ionic movement in the perovskite can lead to PSCs with certain architecture to work as high-gain photodetectors. This is enabled by piling up of ions at the interfaces within the devices, which modifies the energy levels within.

Finally, in the last chapter I describe systematically, how different factors such as temperature, illumination, atmosphere, load on the device and cycling of the environmental conditions affect the stability of PSCs. Based on this, I discuss the important parameters to control when ageing PSCs, as the first attempt to bring the community to a consensus on how to measure stability of PSCs. This is urgently needed to streamline the efforts to create stable PSCs and to commercialize the technology.

Keywords

Perovskite Solar Cells, Photovoltaics, Stability, Ageing, Ionic Movement

Résumé

Les cellules solaires Pérovskites (CSPs) ont attiré l'attention de la communauté scientifique, grâce aux hautes efficacités qui ont été atteintes en un laps de temps très court. Cependant, l'efficacité n'est qu'une étape parmi d'autres importantes sur la route de la commercialisation cette technologie photovoltaïque. Les autres étant, la possibilité d'une production à grande échelle mais aussi la durabilité des performances de ces modules solaires. Le premier étant purement un problème concernant les industries, la durabilité mais plus particulièrement la compréhension des mécanismes de dégradation des CSPs, est devenu un sujet de recherche majeur dans le domaine des CSPs.

Cette thèse, s'attaque donc aux problèmes de détérioration des CSPs. J'y étudie plusieurs mécanismes d'altération possible dans le but d'améliorer la stabilité à long terme de ces modules solaires. Cette dissertation est divisée en 4 parties. Dans la première, j'y présente le développement d'un instrument servant à étudier la stabilité des CSPs et à améliorer les méthodes de mesures des paramètres de nos cellules solaires.

Ensuite, je décris l'instabilité intrinsèque d'une CSP. Je montre aussi comment, avec mes collègues, nous avons réussi à atteindre une stabilité record à température ambiante, grâce à l'incorporation de cations de césium dans le cœur des Pérovskites. Puis, je présente et explique pourquoi ces cellules souffrent d'une dégradation irréversible lorsqu'elles sont exposées à des températures élevées. J'éluclides ce mystère en exposant leur vulnérabilité à la diffusion d'or depuis la contre électrode, à travers la couche conductrice de trou : le spiro-MeOTAD. Je présente ensuite deux alternatives à ce problème : la première étant l'incorporation d'une barrière de diffusion à base de chrome, mais au prix d'une perte d'efficacité, et la deuxième étant la substitution du spiro-MeOTAD par un polymère le PTAA. Cette dernière permettant de stopper la diffusion d'or tout en laissant les efficacités inchangées. De plus, l'incorporation de cation de rubidium dans la Pérovskite a permis de booster l'efficacité de ces cellules polymériques. Puis, Je démontre le potentiel des nanotubes de carbone comme remplaçant à l'or. Ceci permet ainsi de réduire les coûts et faciliter la fabrication des CSPs.

Dans la troisième partie de ma thèse, je corrèle les effets des ions mobiles au comportement des CSPs. Je démontre comment ils sont responsables des pertes partiellement réversibles dans des cellules âgées. Ce phénomène a des conséquences importantes sur la façon dont la stabilité des cellules Pérovskites est mesurée. Ensuite, je présente de quelle façon le mouvement ionique peut permettre aux CSPs, ayant une configuration spécifique, d'être utilisées comme photo détecteurs à gain élevé. Ceci est dû à l'empilement des ions aux interfaces à l'intérieur des modules qui change les niveaux énergétiques, du matériau.

Finalement, je présente dans le dernier chapitre la façon dont les facteurs tels que l'illumination, l'atmosphère ou encore la charge électrique, affectent la stabilité des CSPs. Sur la base de ces résultats, je discute d'importance et de paramètres à contrôler lors de la mesure de la stabilité afin d'homogénéiser la procédure utilisée par la communauté des CSP. Ce dernier élément étant essentiel au développement de modules stables afin de pouvoir, plus tard, commercialiser cette technologie.

Mots-clés

Cellules Solaires Pérovskites, Photovoltaïque, Stabilité, Détérioration, Mouvement ionique

Contents

Acknowledgements	iii
Abstract	v
Keywords	v
Résumé	vii
Mots-clés	vii
Preface	11
List of Abbreviations and Symbols	13
Chapter 1 Introduction	15
1.1 Motivation	16
1.1.1 Global Warming Challenge	16
1.1.2 Renewable Energy Potential	17
1.1.3 Economics of Photovoltaic Energy Conversion	18
1.2 Perovskite Solar Cells	20
1.2.1 Perovskite Properties	20
1.2.2 Device Architectures.....	20
1.2.3 Working Principles of Perovskite Solar Cells	22
1.2.4 Measuring Performance and J-V hysteresis in Perovskite Solar Cells	23
1.2.5 Ionic Motion in Perovskite Solar Cells	25
1.3 Stability of Perovskite Solar Cells.....	26
1.3.1 Intrinsic Stability of the Perovskite Layer	27
1.3.2 Intrinsic Stability of the Device Architecture.....	28
1.3.3 Extrinsic Factors.....	28
1.3.4 State-of-the-Art Stability of Perovskite Solar Cells.....	29
1.4 Thesis Synopsis	29
1.4.1 Aim of the Thesis	29
1.4.2 Outline of the Thesis.....	29

Chapter 2 Design and Building Solar Cell Stability and J-V Measurement Setups.....	31
2.1 Stability Measurement Setup	32
2.1.1 First Prototype – Temperature Control.....	32
2.1.2 Second Prototype – Atmospheric Chamber	33
2.1.3 Final Design.....	34
2.2 J-V Measurement Setup	37
2.3 Software.....	37
2.3.1 Device Control Software.....	37
2.3.2 Environment Control Software.....	39
2.3.3 Central Control	40
2.4 Future Developments of the Stability Measurement Setup.....	41
Chapter 3 Improving the Stability of Perovskite Solar Cells	43
Chapter 3.....	44
3.1 Background	44
3.2 My preliminary work.....	44
3.3 High-Temperature Stability	45
3.4 Reversible vs Irreversible Degradation	47
3.5 Protocols for Ageing Perovskite Solar Cells	49
Chapter 4 Not All That Glitters Is Gold: Metal-Migration-Induced Degradation in Perovskite Solar Cells.....	53
Chapter 5 Incorporation of Rubidium Cations and PTAA Hole Transport Layer into Perovskite Solar Cells Improves High-Temperature Stability and Efficiency.....	77
Chapter 6 High Temperature-Stable Perovskite Solar Cells Based on Low-Cost Carbon Nanotube Hole Contact.....	115
Chapter 7 Migration of Cations Induces Reversible Performance Losses over Day/Night Cycling in Perovskite Solar Cells.....	121
Chapter 8 Mobile Ions Explain Workings of Perovskite Photodetectors: Analyzing the Interplay between Photoconductivity and Voltage-Driven Energy-Level Alignment	153
Chapter 9 Towards Consensus on How to Age Perovskite Solar Cells	179
Conclusions	203
Achieved Results	203
Future Work	205
Quo Vadis? – The Outlook for Stability of Perovskite Solar Cells	206
References	207
Curriculum Vitae	215

Preface

This thesis is written in a “compiled” format as outlined by EPFL regulations CDoct 109 (November 2015) and CDoct 110 (January 2016). Its advantages include the fact that the work presented has been already subjected to a formal peer-review process and has been exposed to broader criticism by scientific community.

The thesis begins with **Introduction** chapter to outline the motivation, scientific background and to put the work described here in context. The second chapter presents how I designed and built a state-of-the-art solar cell stability measurement setup, which has been the enabling tool for most of work presented here. The third chapter describes how my research direction evolved and it is an essential link between the papers presented further. Following, each chapter (4-9) constitutes a peer-reviewed paper published in a scientific journal. Each chapter starts with a short narrative paragraph to put the work into context and to support the storyline. At the beginning of each chapter, in a red box, relevant information is given about the publication and my individual contribution to the work described. The papers presented in this thesis are reproduced with permission of the respective publishers and they include:

1. **Domanski K**, Correa-Baena J-P, Mine N, Nazeeruddin MK, Abate A, Saliba M, et al. Not All That Glitters Is Gold: Metal-Migration-Induced Degradation in Perovskite Solar Cells. *ACS Nano*. 2016.
2. Saliba M, Matsui T, **Domanski K**, Seo J-Y, Ummadisingu A, Zakeeruddin SM, et al. Incorporation of Rubidium Cations into Perovskite Solar Cells Improves Photovoltaic Performance. *Science*. 2016.
3. Aitola K, **Domanski K**, Correa-Baena J-P, Sveinbjornsson K, Saliba M, Abate A, et al. High Temperature-Stable Perovskite Solar Cells Based on Low-Cost Carbon Nanotube Hole Contact. *Adv Mater*. 2017.
4. **Domanski K**, Roose B, Matsui T, Saliba M, Turren-Cruz S-H, Correa-Baena J-P, et al. Migration of Cations Induces Reversible Performance Losses over Day/Night Cycling in Perovskite Solar Cells. *Energy Environ Sci*. 2017.
5. **Domanski K**, Tress W, Moehl T, Saliba M, Nazeeruddin MK, Grätzel M. Working Principles of Perovskite Photodetectors: Analyzing the Interplay between Photoconductivity and Voltage-Driven Energy-Level Alignment. *Adv Funct Mater*. 2015.
6. **Domanski K**, Alharbi E, Hagfeldt A, Grätzel M, Tress W. Systematic Investigation of the Impact of Operation Conditions on the Degradation Behaviour of Perovskite Solar Cells. *Nature Energy*. Accepted.

The ordering of the chapters loosely correspond to the chronological order the work has been performed. The thesis ends with a **Conclusions** paragraph summarizing the findings described here and outlining the possible directions of future research. It also contains my subjective outline on the future of research into stability of perovskite solar cells. All papers presented in this thesis as *Chapters* are either first or co-first authored by me.

The **References** at the end of this thesis are common for **Chapters 1-3** as well as the short paragraphs linking the chapters. Each article presented in **Chapters 4-9** is self-containing, meaning that the reference section is integrated within.

During my doctoral studies, I also contributed to the following papers, some of which are mentioned in **Chapter 3**:

1. Moehl T, Im JH, Lee YH, **Domanski K**, Giordano F, Zakeeruddin SM, et al. Strong Photocurrent Amplification in Perovskite Solar Cells with a Porous TiO₂ Blocking Layer under Reverse Bias. *J Phys Chem Lett*. 2014.
2. Saliba M, Matsui T, Seo J-Y, **Domanski K**, Correa-Baena J-P, Nazeeruddin MK, et al. Cesium-Containing Triple Cation Perovskite Solar Cells: Improved Stability, Reproducibility and High Efficiency. *Energy Environ Sci*. 2016.
3. Anaraki EH, Kermanpur A, Steier L, **Domanski K**, Matsui T, Tress W, et al. Highly Efficient and Stable Planar Perovskite Solar Cells by Solution-Processed Tin Oxide. *Energy Environ Sci*. 2016.
4. Correa-Baena J-P, Anaya M, Lozano G, Tress W, **Domanski K**, Saliba M, et al. Unbroken Perovskite: Interplay of Morphology, Electro-Optical Properties, and Ionic Movement. *Adv Mater*. 2016.
5. Matsui T, Petrikyte I, Malinauskas T, **Domanski K**, Daskeviciene M, Steponaitis M, et al. Additive-Free Transparent Triarylamine-Based Polymeric Hole Transport Materials for Stable Perovskite Solar Cells. *ChemSusChem*. 2016.
6. Gholipour S, Correa-Baena J-P, **Domanski K**, Matsui T, Steier L, Giordano F, et al. Highly Efficient and Stable Perovskite Solar Cells based on a Low-Cost Carbon Cloth. *Adv Energy Mater*. 2016.
7. Seo J-Y, Matsui T, Luo J, Correa-Baena J-P, Giordano F, Saliba M, [...] **Domanski K** et al. Ionic Liquid Control Crystal Growth to Enhance Planar Perovskite Solar Cells Efficiency. *Adv Energy Mater*. 2016.
8. Correa-Baena J-P, Tress W, **Domanski K**, Anaraki EH, Turren Cruz SH, Roose B. et al. Identifying and Suppressing Interfacial Recombination to Achieve High Open-Circuit Voltage in Perovskite Solar Cells. *Energy Environ Sci*. 2017.
9. Tress W, Yavari M, **Domanski K**, Yadav P, Niesen B, Correa-Baena J-P, et al. Interpretation and Evolution of Open-Circuit Voltage, Recombination, Ideality Factor and Subgap Defect States during Reversible Light-Soaking and Irreversible Degradation of Perovskite Solar Cells. *Energy Environ Sci*. 2017
10. Yavari M, Mazloum-Ardakani M, Gholipour S, Turren-Cruz SH, **Domanski K**, Taghavinia N. et al. Carbon Nano Particles in Efficient Perovskite Solar Cells. *Adv Energy Mater*. Accepted.
11. Collavini S, Saliba M, Tress W, Holzhey PJ, Völker SF, **Domanski K**, et al. Ethylene Glycol-[60]fullerene Polymers for Perovskite Solar Cells with Improved Moisture Resistance and Reduced Hysteresis. *Submitted*.
12. Daus A, Roldán-Carmona C, **Domanski K**, Knobelspies S, Cantarella G, Vogt C, et al. Metal-halide perovskite based field-effect transistor gate dielectrics and photodetectors enabled by PMMA lift-off process. *Submitted*.

List of Abbreviations and Symbols*

**These abbreviation and symbols are used throughout Chapters 1-3, Abstract, Conclusions and the paragraphs linking the chapters. Abbreviations in Chapters 4-9 are defined separately in each article.*

COP	Conference of the Parties to the United Nations Framework Convention on Climate Change
AFOLU	Agriculture, Forestry and Other Land Uses
PV	Photovoltaic
LCOE	Levelized Cost of Electricity
BOS	Balance of Systems
PSC	Perovskite Solar Cell
PCE	Power Conversion Efficiency
DSSC	Dye-Sensitised Solar Cell
HTL/M	Hole Transport Layer/Material
ETL	Electron Transport Layer
FTO	Fluorine-Doped Tin Oxide
ITO	Indium-Doped Tin Oxide
HOMO	Highest Occupied Molecular Orbital
LUMO	Lowest Unoccupied Molecular Orbital
MPP(T)	Maximum Power Point (Tracking)
V_{oc}	Open-Circuit Voltage
J_{sc}	Short-Circuit Current Density
FF	Fill Factor
J-V	Current-Voltage
LED	Light Emitting Diode
UV	Ultraviolet
RH	Relative Humidity
OPV	Organic Photovoltaic
PC	Personal Computer
CPU	Central Processing Unit
RAM	Random Access Memory
ASCII	American Standard Code for Information Interchange
PTAA	Poly[bis(4-phenyl)(2,4,6-trimethylphenyl)amine
Spiro-MeOTAD	$N^2,N^2',N^{2''},N^{2'''},N^7,N^7',N^{7''},N^{7''}'$ -octakis(4-methoxyphenyl)-9,9'-spirobi[9H-fluorene]-2,2',7,7'-tetramine

Chapter 1 Introduction

This chapter describes the broad motivation for research and investment into renewable energy, photovoltaics and new photovoltaic technologies. Specifically, it provides background information on perovskite solar cells, its architectures and operating principles. Special attention is given to the topics of hysteresis, ionic motion and stability of perovskite solar cells. Additionally, this chapter describes the motivation for the specific work presented here and puts it in context.



(Picture from <http://www.business-standard.com>)

1.1 Motivation

1.1.1 Global Warming Challenge

One of the major challenges humanity is facing in XXI century is to reign in global warming, which can otherwise have far-reaching and potentially catastrophic consequences. As demonstrated by the historic success of the COP21 summit in Paris in 2015, there is a global will to tackle the issue (even if some notable politicians, not accidentally climate change deniers, speak against it) and the international community is pledging to unite in efforts against climate change.

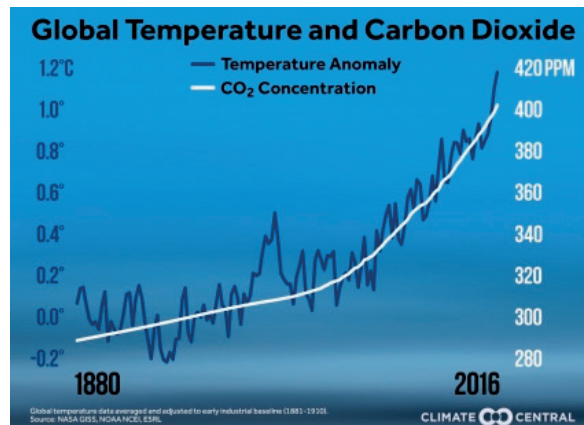


Figure 1:1 Historic correlation between global temperatures and atmospheric CO₂ levels. (Figure from <http://www.climate-central.org>)

Global warming is caused by accumulation of greenhouse gasses (mainly CO₂, CH₄ and N₂O) in the atmosphere, which trap Sun's heat reflected by the Earth's surface.^{1,2} While these gasses occur in the atmosphere naturally, since the industrial revolution in XIX century human activities have been adding large quantities - thus perturbing the natural equilibrium. CO₂ is the greenhouse gas, which is responsible for most of global warming.³ It is mostly emitted as a waste product of burning fossil fuels. The humans are also impeding the natural process of CO₂ capture by deforestation. Strong correlation exists between global temperatures and atmospheric CO₂ levels (**Figure 1:1**).

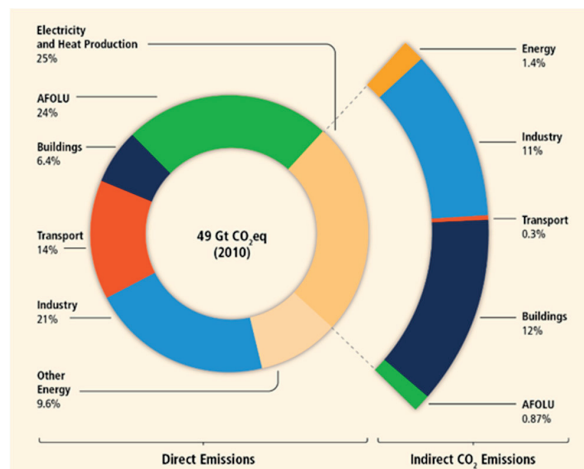


Figure 1:2 Share of human activities towards emissions of CO₂. AFOLU: Agriculture, Forestry and Other Land Uses. (Figure from Ref. ³)

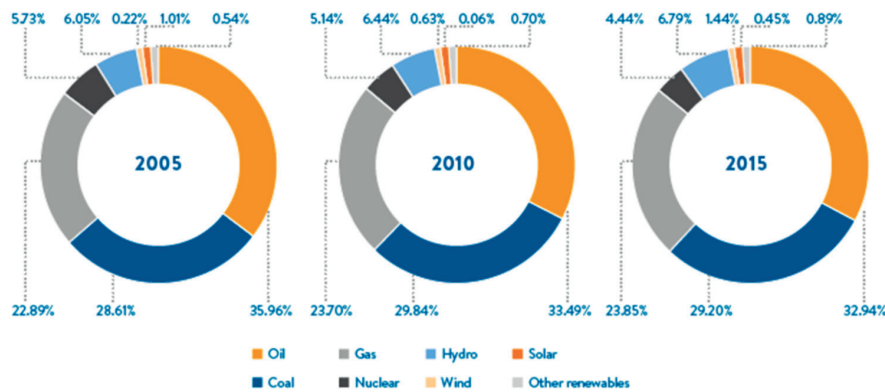


Figure 1:3 Global primary energy mix evolution. (Figure from Ref.⁴)

As the Earth's temperature increases, feedback loops accelerate the process (e.g. as polar ice melts, the Earth's surface becomes on average less reflective thus absorbing more heat). The two other main greenhouse gases, (CH₄ and N₂O), while produced by humans in much lower quantities, are far more effective in trapping heat than CO₂. The former is a by-product of livestock farming, while the latter is emitted as result of various agricultural and industrial activities including proliferation of nitrogen-based fertilizers and burning of fossil fuels.

The strategies to fight global warming are mostly based on eliminating its root cause – greenhouse gasses (apart from stopping deforestation and so-called geoengineering solutions, which remain unproven and very risky; in the future the use of so-called carbon sinks may also become more widespread). Three main areas of human activities are responsible for most of the emissions (**Figure 1:2**). These are electricity and heat production, transportation, industrial production, and agriculture. Of these, generation of electricity, transportation, residential and commercial heating as well as generation of electricity and heat needed for industrial processes are responsible for lion's share of the emissions. Despite the continuous drive to make these processes more sustainable, over 80% of the energy globally is still supplied by burning fossil fuels such as coal, oil and natural gas (**Figure 1:3**).⁴ Hence, the strategies to tackle global warming, very often focus on substituting fossil fuel-generated energy with one derived from carbon-neutral sources such as nuclear, hydro, wind, geothermal, biomass and solar.

1.1.2 Renewable Energy Potential

Environmental issues aside, fossil fuels are limited commodities and they will not be able to power the growing energy appetite of the world economy for much longer. The world reserves of oil and gas are expected to be depleted within several decades, while these of coal will most likely not last beyond the turn of the century if the growing energy demand is not met with alternative energy sources. Nuclear energy has been exploited for years making it an obvious substitute. However, the reserves of fissile material are also limited. Furthermore, the growing security concerns coupled with a very high upfront capital cost of nuclear energy resulted in retreat of nuclear power in the West.

In principle, the amount of renewable energy available for harvesting is many orders of magnitude larger than the energy consumed by the humanity. An old *cliché* is that the amount of sunlight reaching the Earth in just one hour is enough to power the world economy for a full year (however, the technical potential is only a fraction of that). In practice, for renewable energy to be embraced, it has to be price-competitive against the energy derived from conventional sources. Each of the renewable energy

sources has its limitations; for example, the availability of hydroelectricity is limited geographically and it is often concentrated in remote areas, from where it is costly to transport it to consumers. It also has a significant environmental footprint as large areas have to be flooded, and it is highly dependent on rainfall. On the other hand, the amount of geothermal, wave and biomass energy potentially available for harvesting is too little to realistically contribute a significant share into a global energy mix.^{5,6} This leaves wind and solar energy as the main contenders to substitute the fossil-fuel energy production and to satisfy the rising energy demand. They have their own disadvantages though; the relatively high price aside, they are intermittent by nature as wind and sunlight are not available on demand. Hence, a power grid, which integrates a substantial amount of wind and solar power, will inevitably have to contain storage capacity, large overcapacity backed up with conventional power plants, or a very efficient way of energy re-distribution between remote areas. Despite this, very likely wind and solar power will jointly supply most of the energy in the future. In this thesis, I will focus on one particular type of solar energy conversion systems: solar photovoltaics (PVs) that convert sunlight directly into electricity.

1.1.3 Economics of Photovoltaic Energy Conversion

The main parameter determining a commercial attractiveness of a PV installation is Levelized Cost of Electricity (LCOE), which describes the cost of kWh of electricity produced. It takes into account the discounted total life cycle cost of a system including installation, maintenance, decommissioning and financing, and divides it by the lifetime energy produced. LCOE depends strongly on the local conditions of the site, as the energy produced is a function of the amount of sunlight and temperature (as well as the nominal efficiency of the solar module). It also strongly depends on the lifetime of the system given the high initial capital investment into installing a PV system compared with the marginal costs of producing an additional kWh of electricity. LCOE for a PV power plant in Germany was 8 ct€/kWh at the end of 2016 (it is several times higher for small-scale, rooftop systems).⁷ This is still considerably higher than for conventional power plants (which have often been already paid off).⁸ However, LCOE for a PV installation has sustained a long downwards trend caused in large by the falling price of solar panels as the production rates increase (**Figure 1:4**). It is estimated that over the past four decades the price of solar modules decreased by a quarter each time the cumulative production doubled.⁷

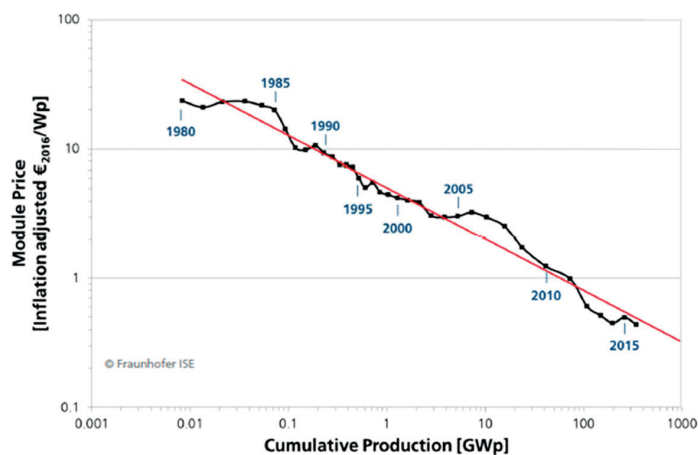


Figure 1:4 Price learning curve for solar panels (modules). From Ref.⁷

The cost of a PV system is composed of multiple elements such as the cost of solar cells, the cost of making a solar panel, the price of an inverter, electrical connections and installation materials (all components, other than photovoltaic panels are called “Balance of System” or BOS). One has to also take into account the cost of installation, land acquisition and its preparation (in case of utility systems), legal costs including permissions and, in some cases, a tracker to follow the Sun. Of these, the cost of solar cells is the single largest cost component, even if it only constitutes a minority share of the total price. The exact share depends on the type of system and the type of solar cells used: it is lower (<25 %) in case of residential systems, where installation costs are higher and profit margins larger for the retailers.⁹ For utility scale systems it can be as high as 40%.⁹ Furthermore, it tends to be higher for crystalline silicon solar cells than for CdTe ones, which in turn have higher installation costs.⁹

Today, almost 95% of the installed PV capacity is supplied by silicon (mono- and polycrystalline; c-Si) with the remaining catered by thin film technologies such as CdTe, Cl(G)S and amorphous silicon (a-Si) (**Figure 1:5**).^{7,10} Despite the rapidly falling prices of these established technologies, grid parity (parity between the electricity price on a wholesale energy market and that produced by the system in question) is achieved only in few places. This fact motivates research into new photovoltaic technologies that have potential to be fabricated at lower cost. This may be by employing inexpensive starting materials, facile manufacturing techniques, by reducing the cost of assembling these new solar cells into modules and by increasing the efficiency and/or lifetime over these of the established PV technologies. Researchers also seek to overcome the limitations of the establish PV technologies such as their rigidity and brittleness, lack of colour tunability, semi-transparency and patternability. Amongst the emerging technologies stand out perovskite solar cells (PSCs) – a relatively recent discovery, which promises to lower the cost of photovoltaic energy while introducing useful additional features such as flexibility and a possibility to make them in different colours. PSCs are exceptional in a way that they can achieve high power conversion efficiencies, while utilising a potentially inexpensive fabrication process, which does not require expensive high purity materials and high temperature processing. They can also be potentially printed on large-area substrates to lower the cost of module production.

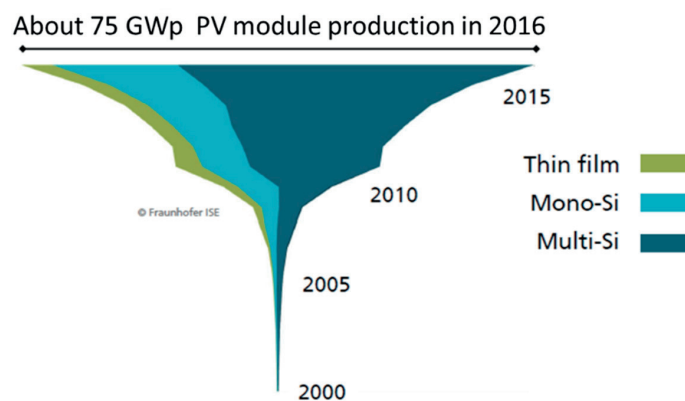


Figure 1:5 Global PV module production by technology. Figure from Ref. ⁷

1.2 Perovskite Solar Cells

1.2.1 Perovskite Properties

PSCs are a new type of solar cells based on (typically) organic-inorganic semiconductor compounds adopting an ABX_3 perovskite-type structure (**Figure 1:6**). Although the class of materials has been known since late XIX century, their photovoltaic potential has only been realized in the past decade. The “photovoltaic” perovskites are based on a limited number of ions to make up the ABX_3 structure. The A-cation can be occupied by $CH_3NH_3^+$, $CH(NH_2)_2^+$, or inorganic Cs^+ or Rb^+ cations. The B-cation is in most cases Pb^{2+} , although Sn^{2+} is also used. The X-site can be occupied by I^- , Br^- or Cl^- . While most of the perovskite compositions used these days employ a mixture of ions on both A and B-sites, the compound that first excited the PV research field was $CH_3NH_3PbI_3$. This is due to its favourable optoelectronic properties, which are rarely seen in materials that are fabricated by “dirty” solution-based methods. $CH_3NH_3PbI_3$ is characterized by 1.55 eV bandgap¹¹, which correspond to absorption onset at the edge of the visible light spectrum (800 nm). This lies close to the optimum bandgap for efficient solar cells (1.1-1.4 eV) allowing PSCs to theoretically reach 31% power conversion efficiency (PCE).¹² Additionally, $CH_3NH_3PbI_3$ is characterized by low exciton binding energy (30 mV), which means that photo-generated charges can separate readily at room temperature.¹³ Finally, the material displays high and balanced diffusion lengths for both electrons and holes ($0.1-1 \mu m$)¹⁴⁻¹⁶ and sufficiently high charge mobilities.^{13,17} This means that the charges can efficiently diffuse to the electrodes before recombining. The favourable combination of optoelectronic properties makes perovskites very attractive materials for photoactive layers in solar cells.

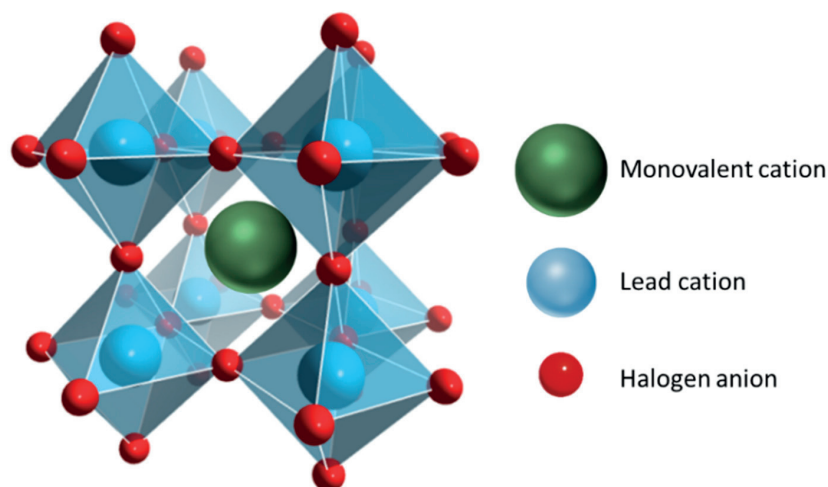


Figure 1:6 The structure of the perovskite compounds used for solar cells. (Picture adapted from <https://chemicalstructure.net>)

1.2.2 Device Architectures

The first embodiments of perovskite solar cells were based on dye-sensitized solar cell (DSSC) architecture and $CH_3NH_3PbI_3$ (perovskite) was used as a sensitizer on thick mesoporous scaffolds.¹⁸ It was coupled with liquid electrolyte, which resulted in a very limited stability of such devices. This architecture yielded power conversion efficiency (PCE) of 3.8 %. The breakthrough came when an all solid-state architecture was realized with 9 % PCE.¹⁹ From then on, PSCs experienced rapid development. The thickness of the mesoporous scaffold decreased by an order of magnitude²⁰⁻²³ and it was realized

that perovskite can efficiently conduct holes and electrons alike making it a much more conventional semiconductor material than thought initially.^{14,15,24} Since then, the PCEs experienced rapid improvement and within several years of development the values improved beyond 22 %, rivalling more established PV technologies.²⁵

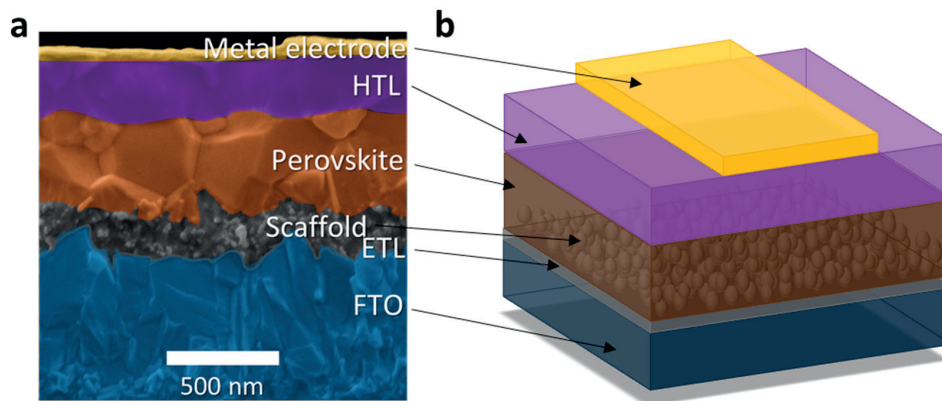


Figure 1:7 a) SEM picture and b) schematics of state-of-the-art perovskite solar cells based on a “normal” architecture and a mesoporous scaffold. Figure re-drawn based on Ref.²⁶

Today, state-of-the-art perovskite solar cells are typically less than 1 μm thick and contain perovskite sandwiched between hole and electron charge transport layers (HTL and ETL respectively). These are typically placed between a metal electrode (Au, Ag and Al are used most often) and another transparent one such as FTO or ITO (fluorine or indium-doped tin oxide). Often, a mesoporous scaffold is employed on top of the ETL in order to improve perovskite film quality and charge transport. However, this is optional and “planar” devices have been demonstrated with performance close to that of their scaffold-based counterparts.^{27,28} When electrons are collected at the transparent electrode, and holes – at the metal one, the device is said to have a “normal” architecture. If the opposite is true, the architecture is called “inverted”. So far, the best performing devices employ a “normal” architecture. However, the different choice of charge transporting materials available with “inverted” architectures (notably inorganic ones) means that both architecture enjoy sustained interest of the researchers.^{22,29,30}

Figure 1:7 shows a mesoporous scaffold-based device with a “normal” architecture. ETL is made of a continuous, thin layer of TiO_2 , which is most often deposited on FTO via spray pyrolysis of TiO_2 precursor solution. The scaffold is fabricated by spin coating and sintering TiO_2 nanoparticles to form an interconnected mesoporous network. HTL is Spiro-MeOTAD in this case, which is deposited via spin coating. The electrode is thermally evaporated and is made of Au. The perovskite is in this case composed of a mixture of different anions and cations. The monovalent cation sites are shared by methylammonium (CH_3NH_3^+), formamidium ($\text{CH}(\text{NH}_2)_2^+$) and Cs^+ cations. The metal sites are occupied by Pb^{2+} cations. The halogen anion sites are shared by I^- and Br^- anions. PSCs based on this composition and architecture are currently amongst the best-performing ones. The early successful methods for depositing perovskite involved a two-step formation process in which PbI_2 was first deposited by spin coating and then converted to $\text{CH}_3\text{NH}_3\text{PbI}_3$ by dipping in $\text{CH}_3\text{NH}_3\text{I}$ solution.²⁰ However, this deposition method did not allow for precise composition control and soon a single-step method was devised.³¹ That method involves spin coating perovskite solution in one step. Before the drying of the film is complete,

it is washed with an antisolvent to induce fast and homogenous crystallization. Alternatively quick drying under vacuum can be employed.³² To this date, most PSCs are fabricated via one-step, antisolvent method. However, perovskite can also be thermally evaporated^{33,34}, which can be useful for certain experiments where solvents could dissolve the underlying layers, as I show in **Chapter 8**.

1.2.3 Working Principles of Perovskite Solar Cells

Perovskites behave much like traditional semiconductors. Light is absorbed by the material, which leads to excitation of an electron from valence to conduction band of perovskite and the creation of an electron-hole pair (**Figure 1:8 a**). The charges dissociate readily thanks to the low exciton binding energy and they are free to move across the device. Being characterised by balanced, relatively high charge mobilities (compared to organic or other hybrid materials) and long charge diffusion lengths, perovskites are efficient at transporting both holes and electrons. Electrons can either diffuse through perovskite to the continuous ETL, or do so via the mesoporous scaffold (if present and made out of suitable electron transport material such as TiO_2). Subsequently, the electrons are collected at the electrode (**Figure 1:8 b**). Photogenerated holes diffuse through perovskite to reach HTL, from where they are collected at the metal electrode.

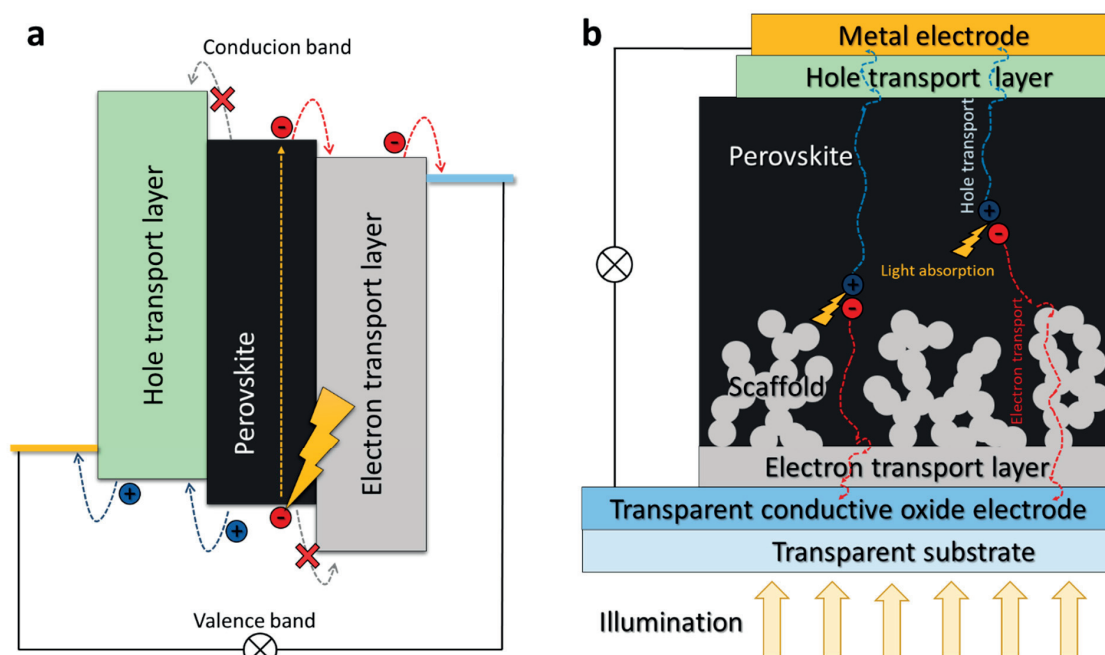


Figure 1:8 Working principles of PSCs with a) the schematic energy diagram of a PSC. b) schematics of the “normal”-architecture PSC with mesoporous scaffold. Charge generation and transport processes are presented schematically.

Electron and hole transport layers (also referred to as “blocking” or “charge selective” layers) are vital parts of PSCs. Their main role is to prevent the “wrong” charges being collected at the electrodes, while allowing the “right” ones to pass. This is achieved by the selection of materials with appropriate energy levels with respect to those of perovskite. A good HTL material should have its conduction band or lowest unoccupied molecular orbital (LUMO) far above that of perovskite. At the same time, its valence band or highest occupied molecular orbital (HOMO) should be just slightly above perovskite’s valence band. The opposite is required for ESL material as depicted in **Figure 1:8 a**. Lack of this charge selectivity is very detrimental to the device. If, for example, an electron reaches the metal contact, it recombines

non-radiatively with one of many holes present at the contact.^{35,36} This process leads to loss of photo-generated charges and hence it is highly unwanted.

Charge recombination can additionally occur at defects in the perovskite. This can be at interfaces, grain boundaries or an impurities in the perovskite.^{37–39} Again, this results in non-radiative loss, where the photogenerated carriers are converted into heat. This process is unwanted and should be impeded. On the other hand, photogenerated carriers can recombine leading to a re-emission of a photon. This so-called radiative recombination cannot be avoided and one would generally wish for all recombination in the device to happen radiatively.⁴⁰ Radiative recombination leads to phenomenon called luminescence, where the device emits light. When the source of electron excitation is primary light absorption by the material, this process is called photoluminescence. When instead the electrons are excited by external bias, one talks about electroluminescence. The latter is the basics of operation of LEDs, which can be seen as a device opposite of a solar cell. A solar cell, where the recombination occurs mostly radiatively usually has high luminescence yields. Hence a good solar cell is usually a decent LED and vice-versa.^{41,42}

1.2.4 Measuring Performance and J-V hysteresis in Perovskite Solar Cells

Soon after the emergence of PSCs, researchers realized that their PCE measurement is not always straightforward. Conventionally, PCE of a PV cell is determined by performing a current-voltage (J-V) sweep under standard 1-sun intensity (1000 W m^{-2} illumination with AM1.5G spectrum). The result is a curve, which crosses the voltage, x-axis at the point called open-circuit voltage (V_{oc}) and the current, y-axis at the point called short-circuit current density (J_{sc} ; **Figure 1:9 a**). However, the diode behaviour of solar cells means that the curve is not square and that the power extracted from the device is less than the product of V_{oc} and J_{sc} . Instead, one has to find so-called maximum power point (MPP) – the point, at which voltage and current result in maximum power (P_{max}) extracted from the device (**Figure 1:9 b**). To arrive at PCE, one has to divide this by the incident light power density (P_{in} ; **Equation 1:1**).

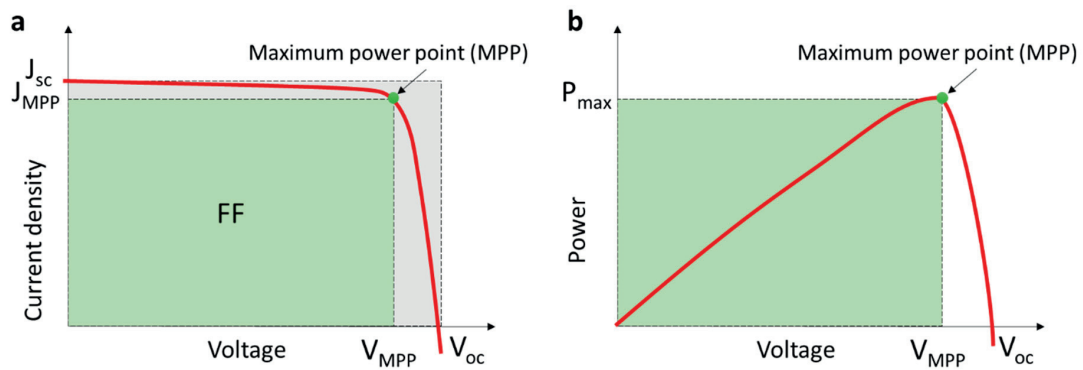


Figure 1:9 a) Typical J-V curve of a solar cell characterized under illumination and b) power output as a function of voltage

V_{MPP} and J_{MPP} are not very practical parameters to characterize solar cells. Instead, one can introduce a geometrical factor (fill factor, or FF) to relate those to V_{oc} and J_{sc} . Altogether FF, V_{oc} , J_{sc} and PCE are the most commonly used performance metrics to characterize solar cells.

$$PCE = \frac{P_{max}}{P_{in}} = \frac{V_{MPP} J_{MPP}}{P_{in}} = FF \frac{V_{oc} J_{sc}}{P_{in}} \quad (1:1)$$

This way of extracting PCE from a solar cell is normally independent of J-V scan direction and it works accurately as long as the measured solar cell is always under quasi steady-state conditions. This requires the device to be in equilibrium under each potential as it is being measured. The condition is readily satisfied for most types of solar cells provided that the J-V scan is not performed with an excessively fast rate ($>100 \text{ V s}^{-1}$). However, this is not always the case for PSCs. Dualeh *et al.* and Snaith *et al.* were the first to show that depending on J-V scan direction (open- to short-circuit, or the opposite), the result of the measurement is different.^{43,44} This phenomenon is called J-V hysteresis. A more in depth study followed by Unger *et al.*⁴⁵, where the authors have shown that PCE depends additionally on scan rate. Additionally, they investigated current transient behaviour when a potential on a devices was changed from V_{oc} to J_{sc} . The transient phenomena were shown to occur on a timescale of seconds, which was correlated to scan rate-dependent hysteresis. Additionally, pre-conditioning under forward bias prior to a J-V scan was shown to improve the apparent efficiency of the devices, while the opposite effect was found when the devices were pre-conditioned under reverse bias. Finally, the authors have shown that hysteresis-free curves can be obtained when scan is performed either very fast or very slowly, but only in the latter case steady-state conditions are achieved for measurement of a valid PCE.

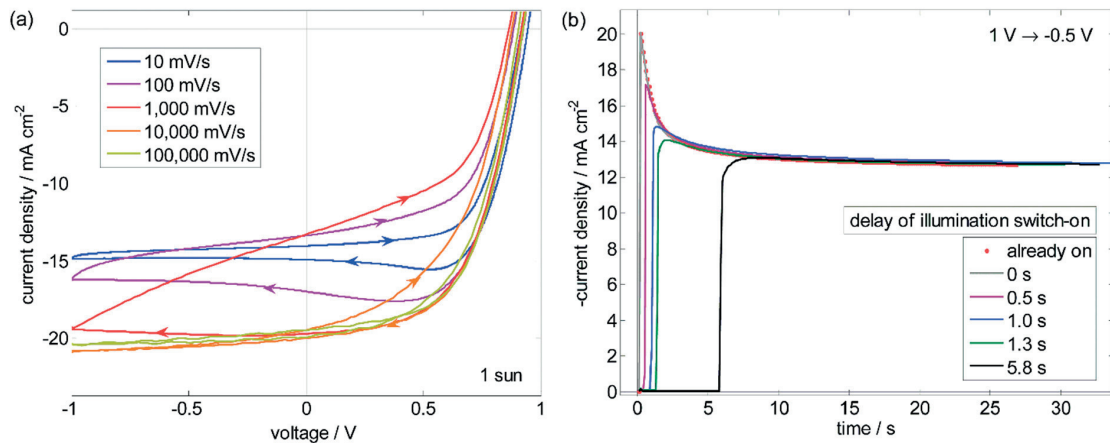


Figure 1:10 a) Rate-dependent J-V hysteresis in PSCs as shown by Tress *et al.*⁴⁶ The arrows denote scan direction. **b)** Slow transient photocurrent response after the voltage is switched from 1 V to -0.5 V at $t=0$. The illumination is on during the whole time (red dots) or switched on later (solid lines). The light acts as a probe for the slow process which shows a response time in the range of 10 s independent of illumination. Reproduced with permission from Ref.⁴⁶

A more thorough study still was undertaken by Tress *et al.*⁴⁶ Having studied rate-dependent hysteresis, the effect of pre-conditioning on J-V characteristics, and transient current response to step-change in potential (**Figure 1:10**), the authors concluded that a slow field-induced process is active in the perovskite cancelling the electric field in the device at any applied potential. This was attributed to an illumination-independent build-up of space charge close to the electric contacts.

Soon after the discovery of J-V hysteresis, an intense discussion started on the origins of the phenomenon and several explanations for the J-V hysteresis in PSCs were suggested: slow electronic trapping⁴⁷, ferroelectric behaviour^{48–51}, light-induced structural changes⁵², and ion migration^{46,53–55}. Interestingly, it has been shown previously that J-V hysteresis can arise due to capacitive effects in Si and CdTe solar cells.^{56,57} However, capacitive effects have been excluded as a possible source of hysteresis in PSCs due to the unrealistically high amount of charge, which would have to be stored internally to account for the very large differences between forward and backward scans.⁴⁶ The potential ferroelectric behaviour in PSCs would be expected on much shorter timescales than the observed J-V hysteresis (which is

observed in the timescale of seconds) and transient behaviour.⁵³ It is now widely believed that even if perovskites show ferroelectric behaviour, it is not the main origin of J-V hysteresis. Also light-induced structural changes have been excluded as the reason for hysteretic behaviour of PSCs, since the phenomena has been observed independently of illumination.^{46,58}

1.2.5 Ionic Motion in Perovskite Solar Cells

Today, a broad consensus has been reached that the motion of ions (and their vacancies) in the perovskite is to blame for the J-V hysteresis.^{59–63} It is believed that halide defects (with their low formation energy in perovskites) can migrate and cause the J-V hysteresis observed on the timescale of seconds-minutes.^{53,64,65} The additional arguments for ionic origins of J-V-hysteresis include strong dependence on scan rate, pre-conditioning, temperature⁵³, and the sensitivity to device fabrication and ageing⁴⁶. Moreover, perovskite-type halides have long been known as ionic conductors.^{66,67} Xiao *et al.* have also provided visual evidence that ion migration occurs within perovskites when they are placed between two electrodes, across which voltage is applied.⁶⁸ Finally, it has been shown that the activation energy for the slow process in PSCs coincides with the expected activation energy for movement of halide defects in these materials.^{53,62}

Yuan *et al.* deposited perovskite between two horizontal electrodes and mapped local potential in these devices.⁶⁹ The authors showed that, when such device is biased, the movement of ionic species creates a p-i-n structure in the direction transverse to the electrodes. They also demonstrated that such a structure can display diode behaviour (despite a fully symmetric architecture and the lack of charge-selective contacts) and that by pre-conditioning the device, the diode behaviour can be completely reversed. Furthermore, the mobilities of migrating ions were estimated as $\sim 10^{-9} \text{ cm}^2 \text{ V}^{-1} \text{ s}^{-1}$ and the activation energy for the process was found at $\sim 360 \text{ meV}$, which again is close to the expected value for halide defect migration in $\text{CH}_3\text{NH}_3\text{PbI}_3$.⁵³ Finally, the authors suggested that there exists an additional contribution from "even slower" ions, which may suggest that several different types of ions are mobile in $\text{CH}_3\text{NH}_3\text{PbI}_3$. The demonstration of the later was the subject of my work presented in **Chapter 7**. O'Regan *et al.* undertook an extensive study on the origins of J-V hysteresis in PSCs. They have found two types of charges present in PSCs: a capacitive electronic charge ($\sim 0.2 \mu\text{C cm}^{-2}$) and another, larger charge ($\sim 40 \mu\text{C cm}^{-2}$), which was assigned to the mobile ions. Correspondingly, transient photovoltage decays were found to be strongly double-exponential with two distinct time constants. The fast decay ($\sim 1 \mu\text{s}$) was assigned to the predominant recombination mechanism in PSC, while the slow decay ($\sim 1 \text{ s}$) was hypothesised to origin from the mobile ionic species.

Despite the strong evidence of relation between ionic motion and J-V hysteresis in PSCs, devices with certain architectures (inverted; with organic charge transport layers) display no, or very little hysteresis.^{33,70} So called "inverted" hysteresis has also been observed, where the PCE derived from the forward J-V scan is greater than that from the backward scan (in most cases the opposite is observed).^{70,71} If the bulk diffusion of ions was the only cause of hysteresis, all devices employing perovskite should be similarly affected. The fact that this is not necessarily always the case, suggests that J-V hysteresis is a more complex process. Jena *et al.* have suggested that the unusual J-V behaviour in PSCs may originate from the interface between FTO and ETL (TiO_2).⁷² The authors investigated devices with active layers made of either $\text{CH}_3\text{NH}_3\text{PbI}_3$ or PbI_2 . Interestingly, substantial J-V hysteresis was observed in both types of devices. Since PbI_2 is not a ferroelectric material, this result is an additional argument in favour of non-ferroelectric origins of J-V hysteresis in PSCs. At the same time, it has been long known that halide

defect diffusion can take place in ionic crystals such as PbI_2 .⁷³ Subsequently, the authors investigated the role of FTO/ TiO_2 interface on the hysteresis. Double-layered structures, FTO/ TiO_2 , were prepared and their J-V characteristics were measured. These structures were shown to also display hysteretic behaviour, which prompted the authors to conclude that this interface plays a major role in the observed hysteresis in PSCs. However, J-V hysteresis has also been observed in devices without a TiO_2 ETL, where perovskite was in direct contact with FTO.⁷⁴ This suggests that the actual origins of hysteresis are more intricate than solely ionic motion effects or solely electronic effects at interfaces. In fact, it is a complex interplay of both.⁶² Ion mobility in perovskite will be used to explain working principles of perovskite photodetector in **Chapter 8** and to explain reversible losses incurred by PSC under illumination in **Chapter 7**.

1.3 Stability of Perovskite Solar Cells

The efficiencies of PSCs have now achieved values that are commercially attractive and (on a laboratory scale) rival these of established photovoltaic technologies. However, for any solar cell technology to be commercialized, operational stability and inexpensive manufacturing methods have to be demonstrated alongside high PCE (**Figure 1:11**). The use of abundant starting materials and inexpensive manufacturing techniques makes perovskite solar cells potentially very price competitive. Promising progress is also being reported on upscaling the production of PSCs.^{32,75–77} However, questions remain whether PSCs can ever achieve the stabilities, which would make them suitable for commercial products – especially for solar panels, where a lifetime of at least a decade is required to make even a very inexpensive solar module worth the labour cost of installation and replacement.

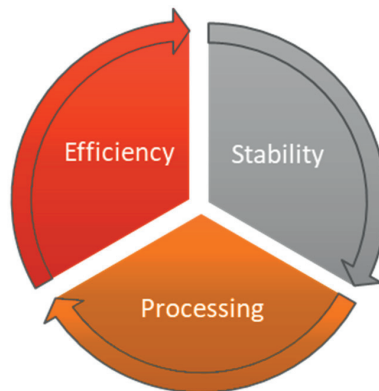


Figure 1:11 The “Holy Grail” of photovoltaics: technology that is efficient, stable and inexpensive to manufacture.

Having been initially in the shadow of the research into improving PCE, dedicated studies on stability of PSCs have now started appearing. Nevertheless, the question of whether PSCs are stable had been asked since the early days of the field.^{78–80} In general, the issues regarding the stability of PSCs can be categorized broadly into three groups as summarized in **Figure 1:12**:

- intrinsic stability of the perovskite layer
- intrinsic stability of the device architecture
- extrinsic effects on stability

Additionally, the question on how to measure the stability of PSCs has to be tackled. Here the ionic motion and J-V hysteresis create an additional obstacle.

1.3.1 Intrinsic Stability of the Perovskite Layer

The two main intrinsic factors influencing the stability of perovskites are temperature and illumination as any solar cell inherently operates under light and at elevated temperatures. The extreme temperatures of solar cells can fluctuate between $-40\text{ }^{\circ}\text{C}$ and $85\text{ }^{\circ}\text{C}$.⁸¹ Moreover, during fabrication of PSCs, perovskite has to usually undergo thermal annealing at temperatures beyond $100\text{ }^{\circ}\text{C}$.⁸² Hence, thermal robustness of the perovskite layer is a prerequisite for the material to be employed in any useful photovoltaic devices. Fortunately, studies on thermal stability of $\text{CH}_3\text{NH}_3\text{PbI}_3$ have shown that the material is stable at temperatures up to $200\text{ }^{\circ}\text{C}$.⁸³ However, this is not necessarily the case for all perovskite compositions and the once state-of-the-art composition using a mixture of iodine and bromine halides as well as MA and FA, has proven to be prone to intrinsic phase instability and decomposition already at room temperature.^{84,85} An incorporation of Cs into the mix as a third cation, helped stabilise the photoactive phase and overcome this problem.^{82,86} This was also a basis of our own achievement of a breakthrough stability mentioned in **Chapter 3**.

Another essential requirement for a solar cell material is to be stable under illumination. While perovskite films are generally stable in the dark given an absence of humidity,⁸⁷ they appear to degrade under illumination at a presence of oxygen.⁸⁸ However, they are stable in inert atmosphere, which makes perovskite-based solar cells potentially possible to stabilize.^{42,82,88}

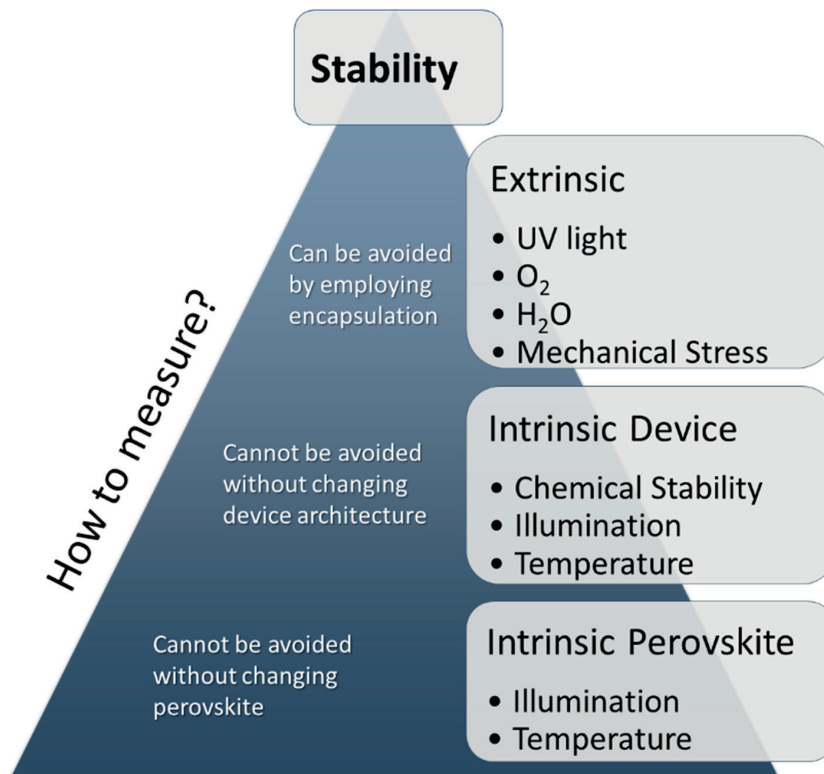


Figure 1:12 Stability considerations of PSCs can be divided into three groups: intrinsic stability of perovskite layer, intrinsic stability of the device architecture and extrinsic stability.

1.3.2 Intrinsic Stability of the Device Architecture

The architecture of a device can have a significant effect on stability. For example, it has been demonstrated that placing Ag electrodes on perovskite results in formation of AgI and severe device degradation.⁸⁹ Hence, an architecture in which iodine from perovskite can reach Ag electrode is inherently instable. Similarly, as I demonstrate in **Chapter 4**, using Spiro-MeOTAD as HTL sandwiched between perovskite and Au electrode is intrinsically instable under elevated temperatures.^{26,90} This problem can be overcome by employing alternative HTL layers as I show in **Chapter 5**. Alternatively one can use carbon-based electrodes^{91,92} as I show in **Chapter 6** or ones based on metal oxides.⁹³ It has been also suggested that additives in HTL can react with perovskite.⁹⁴ Many such combinations potentially exist meaning that each new PSC architecture has to be tested for stability and the possibilities of extrapolation are limited.

1.3.3 Extrinsic Factors

Niu *et al.* have reviewed the main environmental factors influencing the stability of perovskite: moisture, oxygen and ultraviolet (UV) light.⁹⁵ The extrinsic factors can be in principle eliminated by employing suitable solar cell encapsulation. However, in practice the extrinsic factors limit the lifetime of the solar panels as no encapsulation is perfect. The quality of encapsulation (permeability) along with the sensitivity of a device to the extrinsic factors ultimately determines the lifetime of the product.

The concerns about the intrinsic stability of PSCs were from early days motivated by the fact that perovskites themselves are soluble in water and moisture sensitivity has been a worry ever since.^{78,96–99} Upon exposure to moisture $\text{CH}_3\text{NH}_3\text{PbI}_3$ dissolves to PbI_2 , which itself is soluble in water.¹⁰⁰ This aggravates the problem of perovskite stability as it poses a risk of PbI_2 leakage and ecological hazards. The process of perovskite dissolution can be extremely fast (several hours) if the films are exposed to near 100% relative humidity (RH) environment. However, its dynamics can be much slower at low RH levels, at least in the absence of illumination.¹⁰⁰ The role of oxygen appears to be limited compared to that of water. In the absence of illumination, it does not degrade perovskite any more than keeping the devices in N_2 atmosphere.^{100,101} However, coupled with illumination, it can result in severe degradation.⁸⁸ A mechanism for this light induced and oxygen mediated degradation has been postulated. The light-excited electrons can be transferred to adsorbed oxygen forming superoxide anion. This superoxide can react with both MA cation and iodine thus leading to decomposition of $\text{CH}_3\text{NH}_3\text{PbI}_3$.⁸⁸

UV light is considered an extrinsic degradation factor as it can be in practice blocked at low cost and without a significant detrimental effect on the PCE of the solar cell. Most commonly used ESL and mesoporous scaffolds are based on TiO_2 . TiO_2 is a wide bandgap semiconductor that absorbs principally UV light. It is widely-used as a photo catalyst for oxidizing water to create hydroxyl radicals and to oxidize organic materials.¹⁰² It has been reported that after even short exposure to UV under ambient atmospheric conditions, perovskite irreversibly degrades to PbI_2 .^{102,103} Rapid loss of photocurrent was also reported for encapsulated devices exposed to UV light. However, the performance loss was not permanent and it was recoverable following exposure to oxygen.¹⁰⁴ It has been also suggested that avoiding the use of TiO_2 altogether can increase UV stability of PSCs.⁷⁹ As I show in **Chapter 9**, the UV instability is not as large of a problem as though initially back in 2013-14, when the above-cited publications appeared. Since then, perovskite compositions have evolved significantly and new fabrication methods resulted in less defective device layers. Having said that UV light does seem to accelerate degradation of TiO_2 -based devices.

In principle, one should also consider factors such as thermal cycling, mechanical stress etc. These can damage the encapsulation and lead to failure of a solar cell. In **Chapter 9**, I show preliminary results on thermal cycling of unencapsulated PSCs. However, for a technology at a research stage such as PSCs, these factors do not necessarily have to be of concern yet and more fundamental degradation pathways should be investigated and understood first.

1.3.4 State-of-the-Art Stability of Perovskite Solar Cells

Over the past several years, the stabilities of PSCs have experienced a very rapid advancement from lifetimes measured in days to years.¹⁰⁷ Promising device stabilities were achieved with various device architectures. For example, Grancini *et al.* have reported HTL-free PSCs with carbon contacts and virtually no degradation over a 1-year long light soaking test at 55 °C. Arora *et al.* have shown comparatively high stabilities over a period of 1000 h when devices with CuSCN HTL and a thin layer of reduced graphene oxide were aged under illumination, at MPP and 60 °C.¹⁰⁸ Furthermore, Bush *et al.* have recently reported perovskite-silicon tandem solar cells with promising stability over a period of 1000 h under illumination and close to room temperature.¹⁰⁹ Finally, I present in **Chapter 5** a stability of PSCs with PTAA HTL that retain 95 % of PCE after being aged for 500 h at 85 °C, under 1 sun illumination and MPP.⁴²

However, the lack of dedicated protocols for ageing and data reporting practices, makes quantifying stability challenging and comparison of stability reported by various groups is very hard. This is especially true as tests are conducted at different temperatures, different loads, atmospheres and using different illumination sources. Moreover, promising stability of both encapsulated and unencapsulated devices has been achieved, albeit at different conditions.

1.4 Thesis Synopsis

1.4.1 Aim of the Thesis

At the time I started working on this thesis, PSCs were generally characterized by very poor stability. Additionally, little was known about degradation pathways in PSCs – a prerequisite for developing strategies for stability enhancement. The aim of the work described in this thesis was to understand and improve the stability of PSCs. The questions of how and why PSCs degrade were at the core of each chapter presented here. This was in the context of specific device architectures, perovskite compositions and different stress factors that PSCs can be exposed to. As subsequent degradation pathways were identified, the aim was to find a way to improve the stability of PSCs by employing new perovskite compositions and device architectures. As such, a substantial part of this thesis deals with how to avoid high-temperature instability in PSCs. Finally, having acquired experience in measuring stability of PSCs, the aim of this thesis is to help reach the PSC community a consensus on how to investigate the stability of PSCs in a meaningful and reproducible way.

1.4.2 Outline of the Thesis

This thesis is a report on over 3 years of my work on the topic of PSC stability and several closely related subjects. The next chapter describes how I designed and built state-of-the-art solar cell stability and J-V measurement setups, which was the enabling tool for all work described here subsequently. The third chapter describes how my research direction evolved and with inclusion of additional, unpublished data, it is an essential link between the subsequent chapters. The fourth chapter is a report

on the discovery of an intrinsic high-temperature instability of (at the time) state-of-the-art PSCs. The fifth chapter describes how incorporation of a polymeric HTL coupled with incorporation of Rb into perovskite overcame this challenge. Chapter 6 presents an alternative approach using a potentially inexpensive carbon-based back contact material. The seventh chapter describes how migration of ions inside the perovskite influences stability measurements of PSCs. In the eighth chapter, the analogous phenomenon is shown to enable PSCs with a specific architecture to work as photodetectors with high gain. Finally, the ninth chapter is a detailed investigation of how different factors influence ageing of PSCs. It also advocates the adoption of standard procedures of ageing PSCs and it demonstrates how I implement stability measurements in our laboratory. This last chapter is in fact a synopsis of all the other chapters and it was the result of my accumulated experience in research on stability of PSC.

Chapter 2 Design and Building Solar Cell Stability and J-V Measurement Setups

THE CONTEXT

Having completed a master thesis on understanding degradation pathways in organic solar cells, I wanted to use my experience to focus on investigating the stability of perovskite solar cells. The case was very compelling as the field was achieving ever-higher power conversion efficiencies and the questions of stability began to surface. Our laboratory had at the time limited stability measurement capabilities, which were not sufficient for the projects I envisaged. Most importantly, we lacked the means to control temperature of samples, while they were measured. I decided to build a simple setup to do just this. As encouraging results started to accumulate thanks to the temperature-controlled setup, I managed to convince my superiors to invest in building first a prototype and then a full-scale version of the ageing setup. Having obtained experience in parallel measurement of multiple samples at a time, I also built a setup to measure J-V characteristics of perovskite solar cells, which improved the efficiency of the measurement by 700%.

This chapter describes the 2.5 year-long ongoing process of developing solar cell ageing capabilities in our laboratory, which involved building several prototypes of both software and hardware, and which was guided by the stability results I was obtaining continuously using the subsequent embodiments of the setup. The work presented here was from the early stages a close collaboration with Dr. Wolfgang Tress, who wrote the software to operate the subsequent version of the ageing setup. It also would not be possible without help of Benjamin Le Geyt, Supardi Sujito, Christophe Clement and Andre Fattet, engineers from electrical and mechanical workshops who helped us manufacture the components needed. Finally, the financial and moral support of Prof. Anders Hagfeldt was crucial. This chapter also describes a variation of the stability measurement setup, which I built for J-V measurements.

My contribution:

I conceptually designed the setups and led their development, coordinating with different people involved in the project. I also designed all mechanical and some electronic components and assembled the pieces. I contributed conceptually to the design of the software used to operate the setups.



2.1 Stability Measurement Setup

2.1.1 First Prototype – Temperature Control

The first prototype of the stability measurement setup was a simple adaptation of a standard sample holder used in our laboratory for measuring J-V characteristics of solar cells. The modification was the introduction of a Peltier element in contact with the back of a sample, which could control its temperature (either heat or cool) **Figure 2:1** shows how the temperature control worked conceptually. Feedback was provided from a thermocouple inserted between the Peltier element and the sample. A soft thermal padding was employed to protect the delicate backside of the sample. The Peltier element was placed on a copper heat exchanger (a pipe) through which cold gas could be blown (heat conductive paste was used to increase heat transfer efficiency). The temperature was read from a multimeter and the user could adjust current flowing through Peltier element to achieve the desired temperature of the sample. This setup allowed for temperature-dependent measurements of electronic characteristics and *in situ* ageing measurements. One sample could be measured at a time.

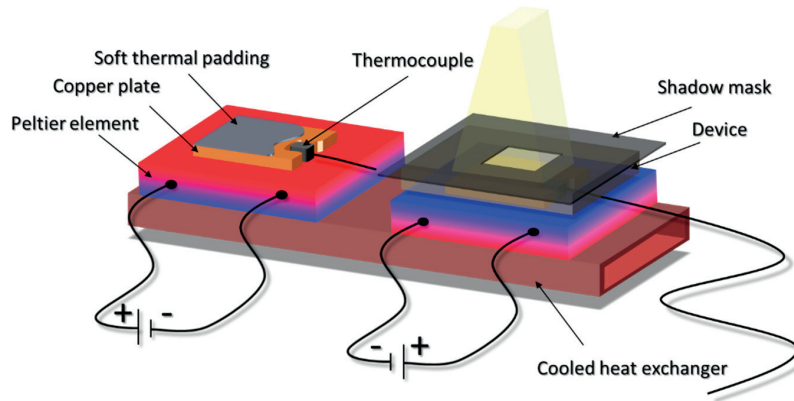


Figure 2:1 The schematic of the temperature control in the first prototype of the ageing setup.

Figure 2:2 shows a picture of the holder. The sample rested on pin legs and it was fixed in the holder by screwing a shadow mask on top of it. The setup was completed with a potentiostat to measure the device loaded. The illumination was supplied externally – in most cases by driving an array of white LED diodes or by placing the holder under a solar simulator.

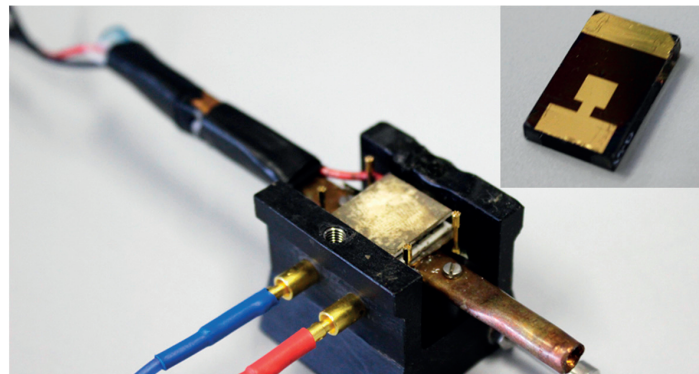


Figure 2:2 Picture of the first prototype of the ageing setup. Note the thermocouple plate is missing in this picture to uncover the Peltier element.

2.1.2 Second Prototype – Atmospheric Chamber

While the first prototype enabled us new types of measurements, it was clear from the beginning that its usability was limited due to the fact it did not allow for atmosphere control for long-term measurements. Additionally, the small, gas-cooled heat exchanger did not allow for exploring negative temperatures. The setup also required a manual temperature adjustment.

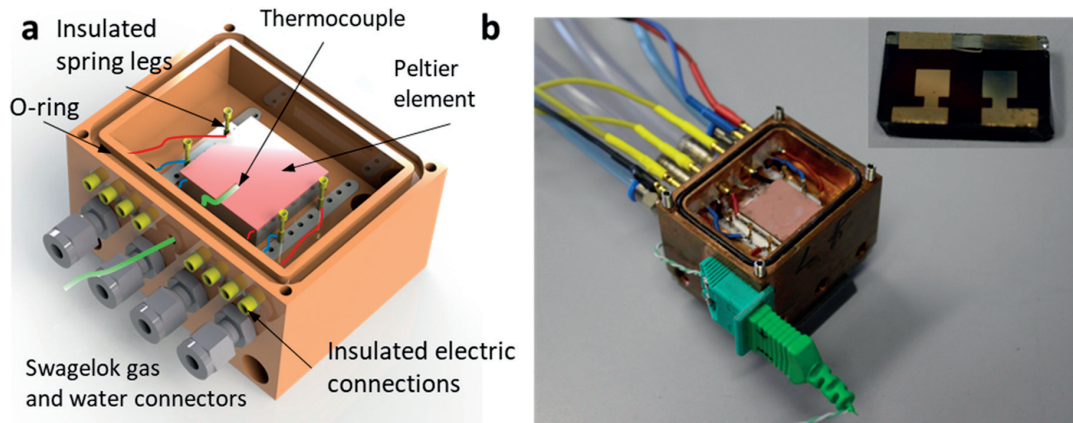


Figure 2:3 a) design and b) picture of the holder constituting the second prototype of the ageing setup. The inset shows the two-pixel architecture of the solar cell the holder could support.

A new holder was designed and built to enable atmospheric control and it was made in a form of a copper, airtight atmospheric chamber that would be closed with a glass lid (**Figure 2:3**). It was also designed to accommodate a new solar cell architecture we started using in our laboratory at the time – with two solar cells (devices/pixels) on one substrate (inset in **Figure 2:3**). The working principle of this second holder was the same as that of the previous one: the sample rested on pin legs (insulated with plastic from the body of the holder) and Peltier element coupled with a thermocouple was used to control temperature of the sample. However, the bottom of the holder was cooled with water in order to significantly extend the working temperature range to from $-30\text{ }^{\circ}\text{C}$ to $+180\text{ }^{\circ}\text{C}$. Temperatures below $-100\text{ }^{\circ}\text{C}$ could also be reached when the coolant was liquid nitrogen instead of water.

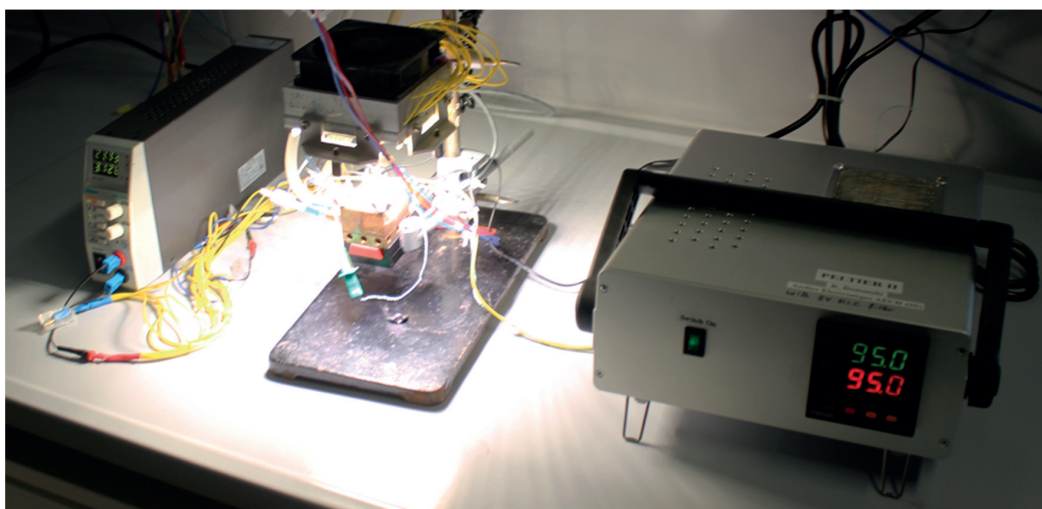


Figure 2:4 The second prototype of the ageing setup. In the center sits the water-cooled copper holder under a white LED lamp. On the righthandise is the PID controller to control the temperature of the sample in the holder.

Another upgrade was in form of a dedicated temperature controller (on the right in **Figure 2:4**). It was based on a PID module, which would read the temperature from a thermocouple and (through a feedback loop) supply the right current to the Peltier element to reach the user-defined setpoint. The controller could be connected to a PC to control it remotely and to set useful parameters such as temperature ramp or safety temperature limits. The illumination was achieved by placing the holder either under a solar simulator or under a white LED array (centre) driven by a laboratory power supply (left in **Figure 2:4**). The devices were connected to a two-channel potentiostat (not pictured here) to be measured. I built two such complete setups allowing for a measurement of four devices simultaneously (2 samples, 2 pixels each).

2.1.3 Final Design

The second prototype, although very successful in producing data, which would later become the centerpiece of several publications, lacked automation and a capacity needed to collect statistics and running several experiments simultaneously. Hence, I decided to build a full-scale stability setup, which would enable a very precise control of environmental conditions at a large testing capacity. My goal was to develop a state-of-the-art tool, which would be very flexible and useful far beyond stability measurements. With a generous financial support of Prof. Anders Hagfeldt, I aimed at maximum experimental conditions control and versatility combined with user friendliness and reliability.

The design of the sample holder is based on the second prototype. While, four of those prototype holders are joined together into a single structure (**Figure 2:5**), each sample remains independent and its temperature can be varied independently of the others'. However, the thermocouple is replaced with a Pt100 thermometer, which is easier to interface with. Another important change is that the holder is equipped with a radiator coupled with a fan, thus eliminating the need for water cooling. The setup provides temperature control in the approximate range $-15\text{ }^{\circ}\text{C} - 180\text{ }^{\circ}\text{C}$ (under 1 sun illumination – slightly lower temperatures can be achieved in the dark).

All connectors are airtight. The atmosphere is the same for all samples and the gas is supplied by a central pipe (a system of channels inside the body of the holder is used to redistribute the gas equally to each sample). The gas outlets from each sample are connected together and further connected to a 5 mBar overpressure valve to maintain positive overpressure inside the holder and to prevent oxygen and humidity entering the experimental environment. Finally, in the centre of a holder a Si photodiode is placed in order to measure the illumination upon the holder.

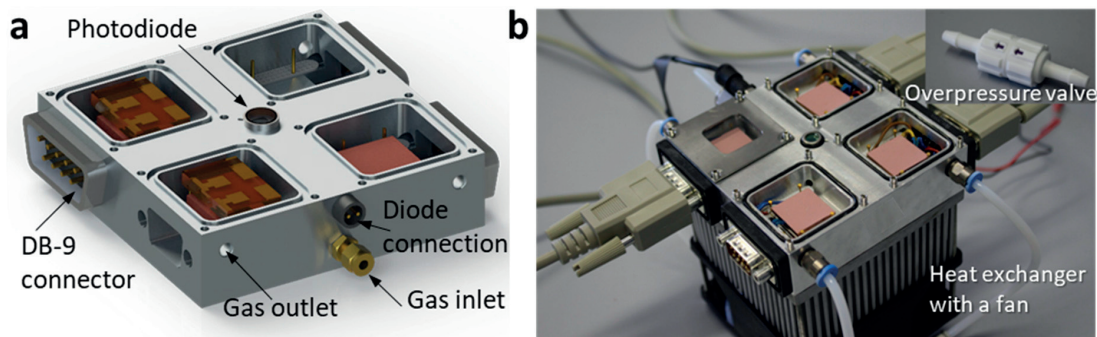


Figure 2:5 a) design and b) picture of the holder for the final embodiment of the ageing setup. The inset shows a 5 mBar overpressure valve connected to the gas outlet and used to maintain a small overpressure inside the holder.

The sample holder is connected with DB-9 cables (9-pin cable) to a custom-built control unit (**Figure 2:6 b, c**). The control unit contains PID temperature controllers for each sample as well as a PID controller for the white LED panel used to illuminate the holder. The feedback loop is created with the use of the photodiode and precise illumination control between 10^{-5} suns to equivalent of 3 suns is possible with this arrangement. The large illumination range is especially practical for investigating the properties of solar cells as a function of light intensity (which often vary logarithmically). Coupled with a large temperature range, this capability is very useful far beyond stability measurements. Each control unit can supply two sample holders and it is connected to a 16 channel potentiostat (**Figure 2:6 b**), which measures all devices in parallel (2 holders, 4 devices each with 2 pixels each). Two control units and two potentiostats form the setup accommodating 32 devices overall (**Figure 2:6 c**).

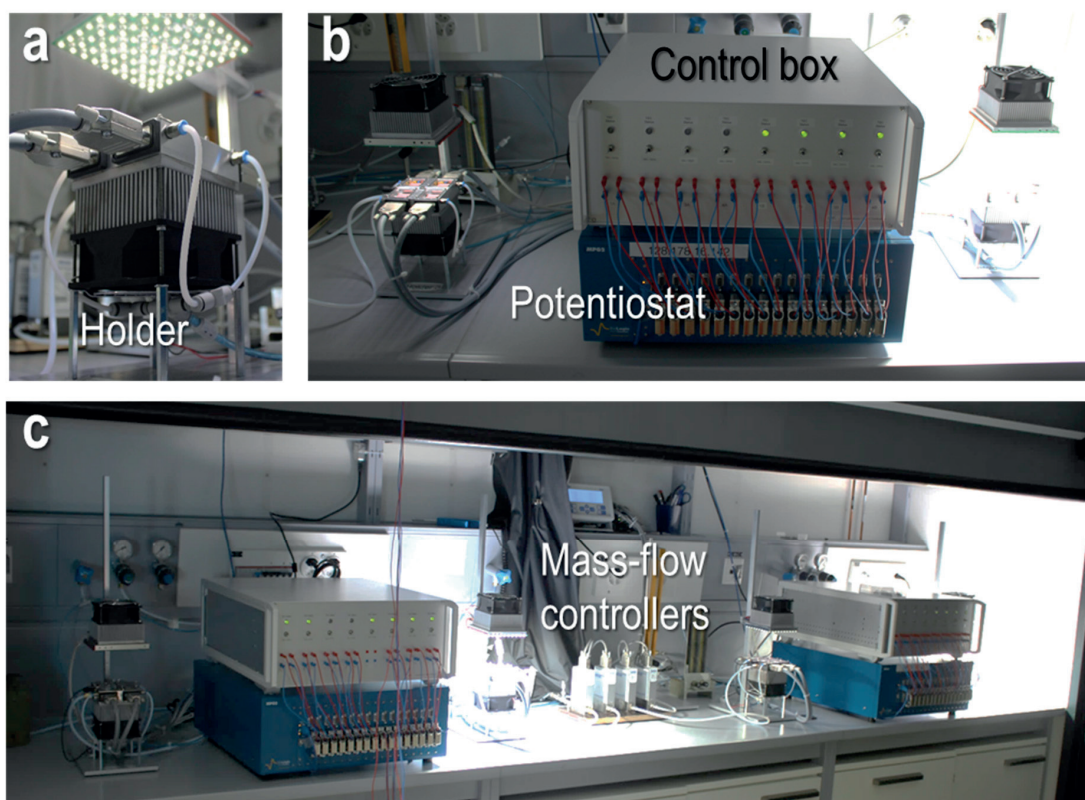


Figure 2:6 Picture of a) sample holder under light and b) the 2 sample holders connected to a control unit (white box) and a potentiostat (blue box). c) The picture of a complete setup including mass flow controllers (centre).

Finally, the setup allows for a precise atmospheric control in each of the holders. The user has at their disposal bottled gas sources as well as nitrogen generator and air dryer. Four mass flow controllers are used for this purpose (**Figure 2:7**). Each of these can be supplied with a different gas and each holder can be supplied by more than one mass flow controller thus mixing different gasses. This allows for a precise atmosphere tuning (e.g. by setting ratios of O_2 and N_2 flows to 1:1 or 1:10). It is also possible to pass any gas through a water bubbler and thus saturating it with it. As this thesis is being prepared, we are working towards installing O_2/H_2O sensors at the outlets of the weathering chamber to create an atmosphere control feedback loop.



Figure 2:7 Mass flow controllers used to control the atmosphere in the sample holders. Each of these can be connected to a different gas and a precise flow rate can be programmed.

Figure 2:8 shows the schematics of the setup and how different components interact with each other. The differently coloured arrows show different sub-systems. The default illumination source is white LED array, which can be controlled precisely through a feedback loop. However, it is also possible to illuminate the sample holders with a solar simulator with an AM 1.5G spectrum, or with any other lamp.

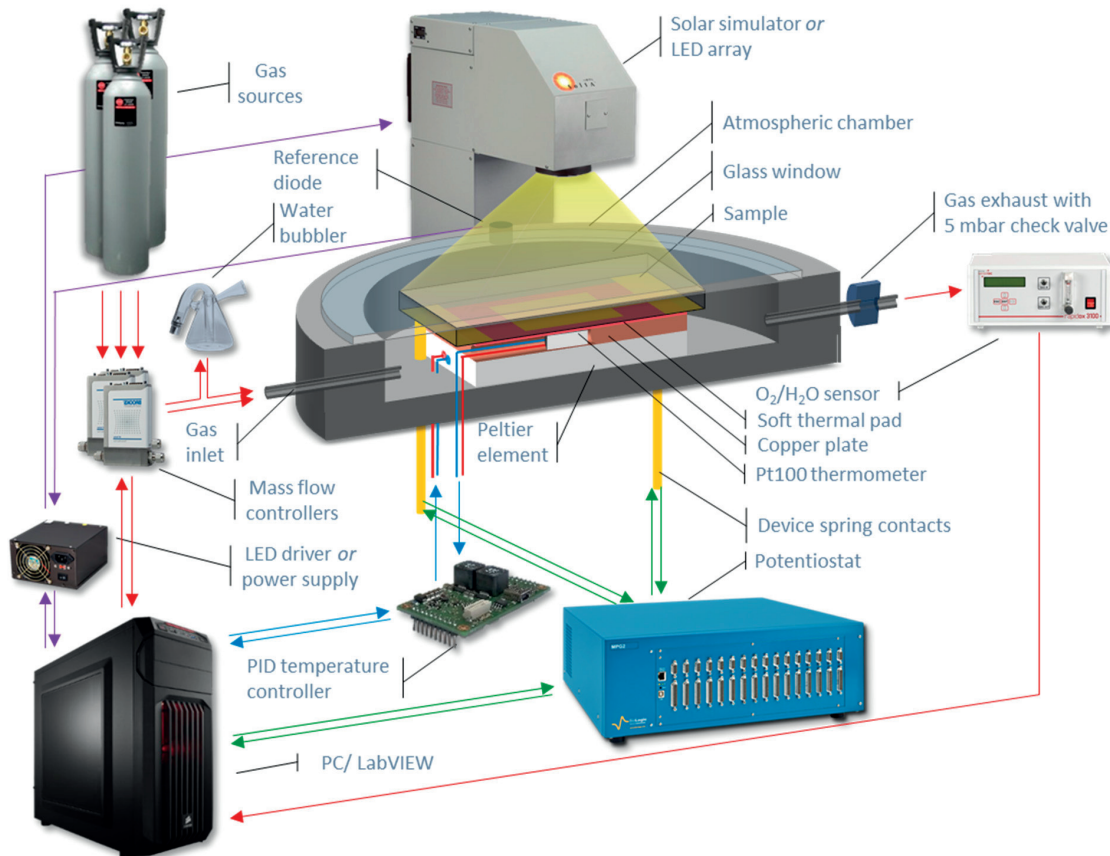


Figure 2:8 The schematics of the ageing setup. The concept of the weathering chamber is shown in cross-section. The differently coloured arrows show how different components of the setup interact with each other.

2.2 J-V Measurement Setup

Motivated by the need to improve the efficiency of J-V measurements in our laboratory (measuring one 2-pixel sample at 10 mV s^{-1} typically takes 8 minutes; a typical batch would contain up to 20 samples), I designed a simplified version of the sample holder described above, which can host 4 samples (8 devices/pixels) (**Figure 2:9**). The samples are placed on spring pin legs and are held in place by a magnetic shadow mask, which is fixed on top with strong neodymium magnets. This provides a very quick way of fixing the samples in place. The alignment of the mask can be done very easily thanks to red LEDs placed behind the samples (red light is absorbed least strongly by perovskite). The holder is connected with a single cable to a multi-channel potentiostat via a small interface box (not shown here). The illumination is from an AAA-rated AM1.5G solar simulator and a silicon photodiode in the holder is used to create a feedback loop to ensure a precise illumination control and power conversion calculation of the device measured. Building of this setup increased the efficiency of J-V measurements by 700% cutting the time needed to measure a batch of 12 samples from over 3 h to only 25 minutes. I built two such systems.

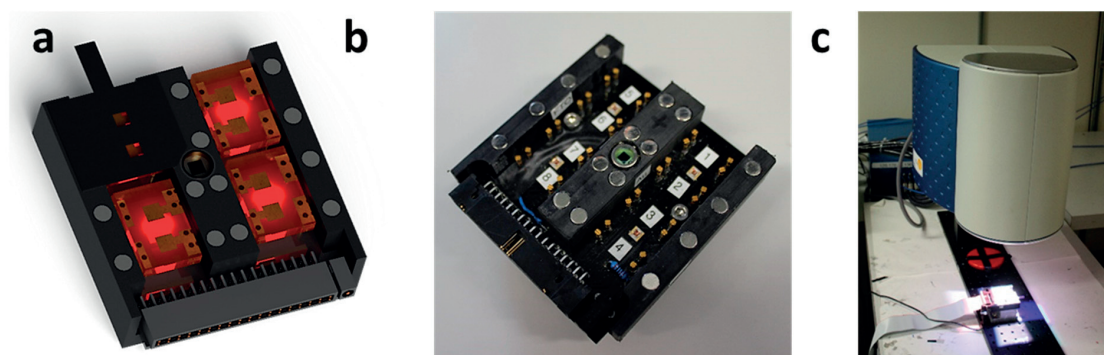


Figure 2:9 a) the model and b) the picture of the J-V sample holder. c) the complete J-V measurement setup with a solar simulator and a multi-channel potentiostat in the back (blue box).

2.3 Software

Both the stability and J-V measurement setups are controlled through a custom-built LabVIEW software that enables parallel measurements, measurement programming as well as data analysis. It is also possible to pre-program a sequence that can be then executed without user's supervision – this being especially useful for long-term stability measurements. The software is divided into 2 programs. The first one controls the potentiostat and it is used for electronic measurement of the samples. It is common for both the J-V and the stability measurement setup. The second part is used to control the temperature of the samples and the illumination in the stability setup. The efficient design, allows the software to run on a standard PC with a 4-core 3.4 GHz CPU and 16 GB of RAM.

2.3.1 Device Control Software

Figure 2:10 shows the main panels in the device control software. The top one is used to program the measurements. The user can set the bounds and speed of J-V scans as well as a preference to measure J-V in both directions. In case the user wants to perform stability measurements, they have an option to keep the device for a specific period at certain load: constant voltage, constant current, or at maximum power point (MPP), which is tracked dynamically by a standard “perturb and observe” method. This last condition is the default choice for stability measurements but can be also used to extract a

stabilised power output from a device as an addition to a J-V scan. The user can also choose to loop the procedure: for example, measuring a J-V curve every 30 minutes and keeping the devices at MPP in between. Auxiliary graphics are integrated in the software to help user monitor the status of their experiment.

The bottom panel in **Figure 2:10** is designed with stability measurements in mind. It displays the evolution of performance metrics of devices as well as environmental conditions such as sample temperature and illumination, over time. The user can compare multiple data traces at a time and display multiple parameters simultaneously. The user can conveniently export the visible data to an Excel spreadsheet. Alongside the performance parameters of the devices, sample temperature and illumination are also logged for each device in ASCII files.

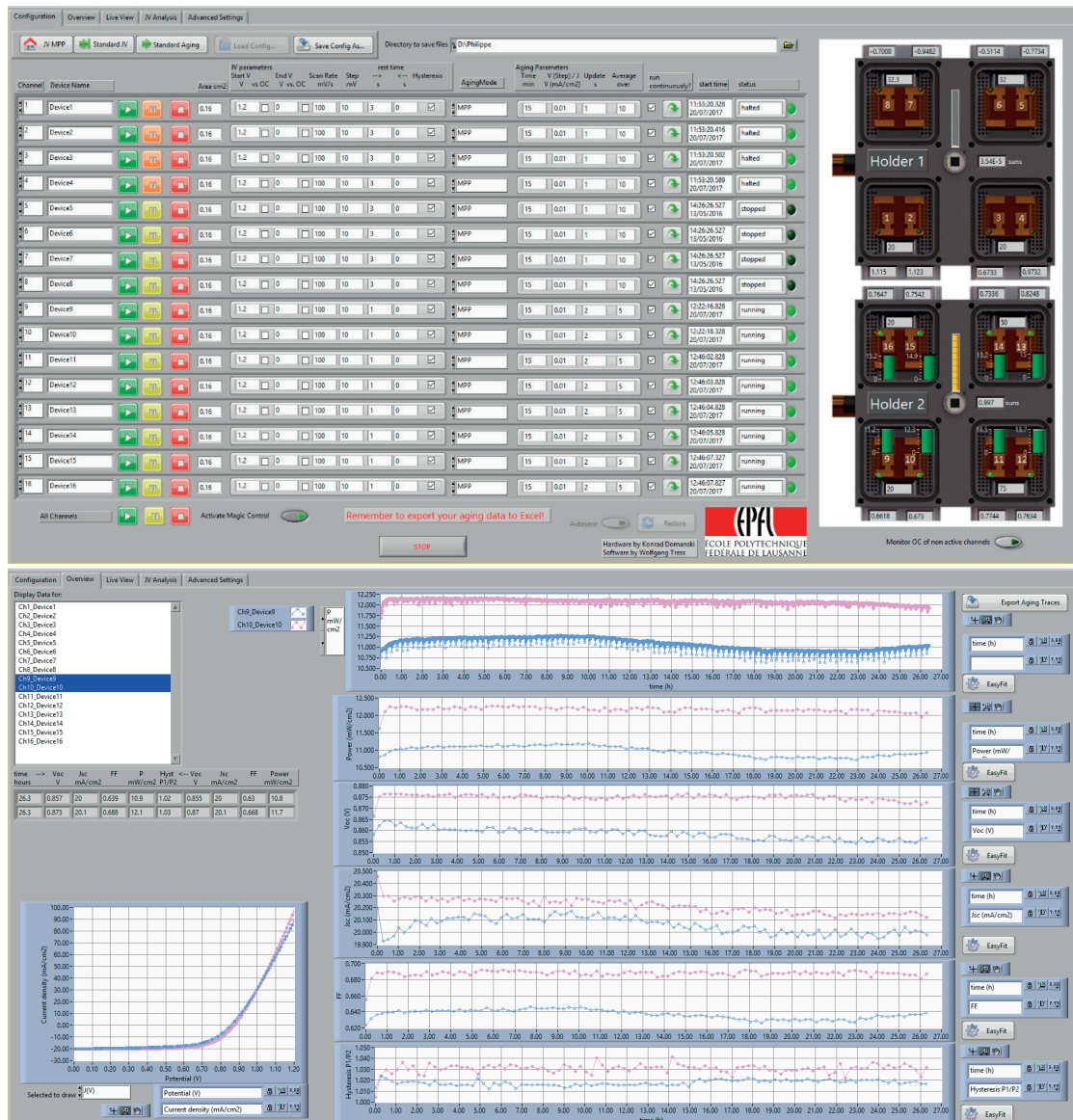


Figure 2:10 The main panels of the software used to control the stability and J-V measurement setups. The top panel is used to program the measurements. The bottom panel displays the evolution of solar cell performance parameters during ageing.

Figure 2:11 displays the part of the software, which is designed for J-V measurements. The top window shows the live view of the measurement. The bottom window allows for analysis of a number of J-V curves measured previously. The user can overlay them and J-V parameters (PCE, V_{OC} , J_{SC} , FF, and hysteresis) are conveniently extracted for each J-V curve. Again, the user can export the data to an Excel spreadsheet or they can generate a report containing graphs.

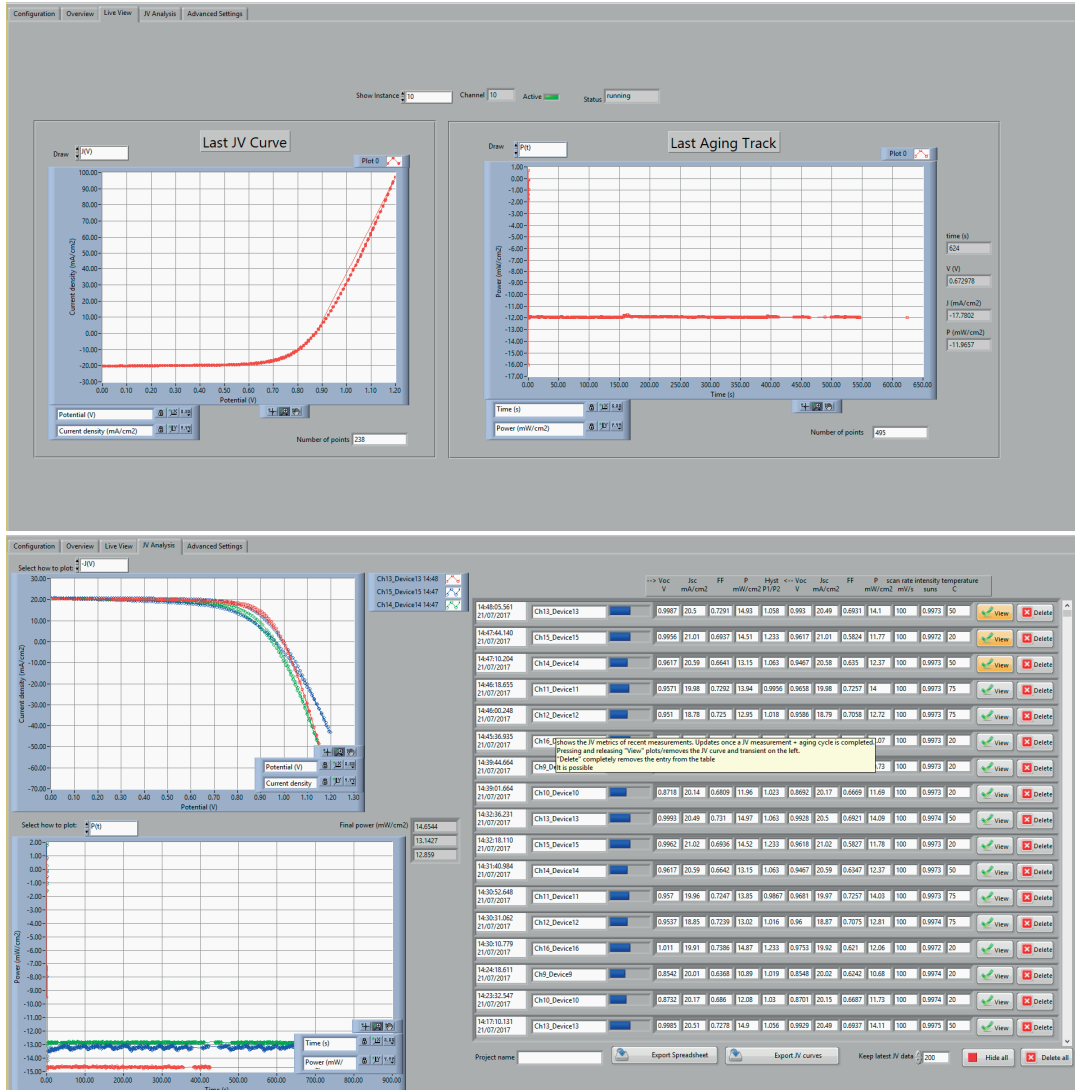


Figure 2:11 J-V measurement specific part of the software. The top panel is used to display the live view of the measurement along with the last J-V curve collected. The bottom panel allows the user to analyze a number of J-V curves measured in the past.

2.3.2 Environment Control Software

The environment control software is used exclusively with the stability measurement setup. It allows the user to control temperature and illumination of the samples. **Figure 2:12** shows the main two windows of the software. The top window allows the user to manually change the temperature and illumination of the samples. The bottom window allows for automation of the control of the environmental conditions. The user can program for example light or temperature cycling. Because the program

can “talk” to the device control program, it is also possible to program J-V or MPP tracking measurements and synchronise them with temperature and illumination variations.

Not shown here are also additional windows to track temperature and illumination over time. There exist also a configuration window to calibrate the setup and a separate measurement status monitoring window.

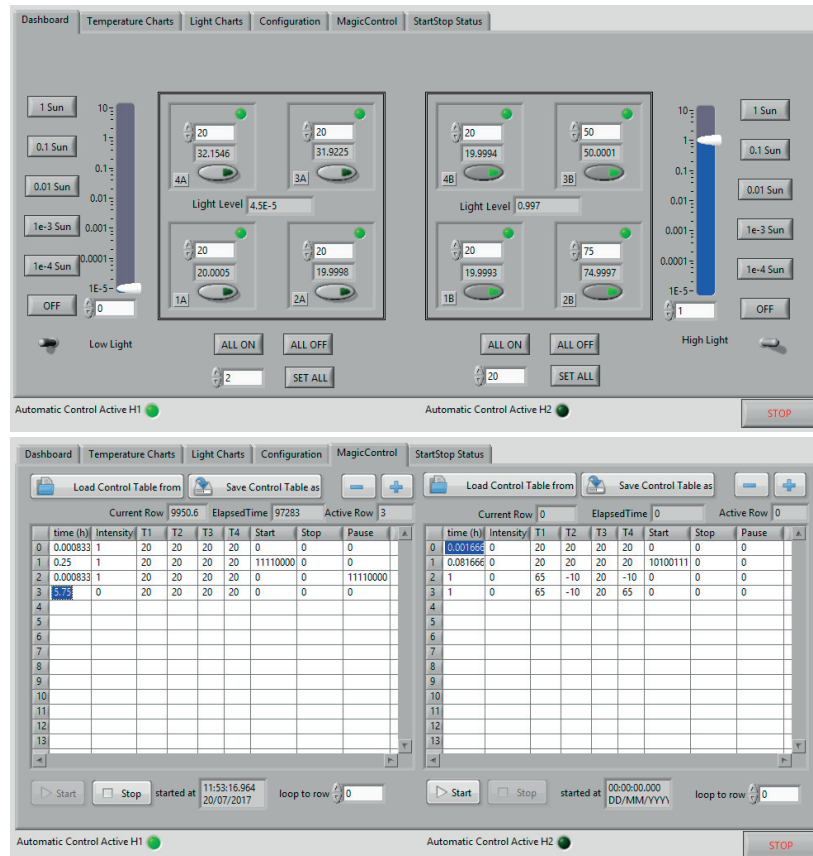


Figure 2:12 The environment control software. The top panel offers the user the possibility to manually control illumination and temperature of the samples. The bottom panel allows pre-programming the experiment.

2.3.3 Central Control

The stability measurement setup is controlled from two PCs (**Figure 2:13**). Each PC is connected to one potentiostat, one control box and two sample holders. This arrangement lowers the risk of a single PC failure, while allowing two users to work simultaneously. The components are connected with each other via sheathed Ethernet cables to minimize the outside disturbances. Finally, each PC is connected to internet and it is equipped with Team Viewer software allowing for a remote control. This way, the user does not have to be physically present in the laboratory to conduct their experiments. It also gives the user a way of conveniently monitoring their experiments. An analogous infrastructure is in place for the J-V measurement setup. The design objective for the stability and J-V measurement software was to make it as user friendly as possible so that the members of the laboratory can quickly become independent users of the equipment.



Figure 2:13 Picture of the “command and control center” of the stability measurement setup. Each PC is connected to two monitors and is used to control half of the setup (2 holders, 1 potentiostat, 1 control box).

2.4 Future Developments of the Stability Measurement Setup

Since its inception, the stability measurement setup has been subject to constant improvements. The ones already planned or being executed at the time this thesis is being prepared include:

- Installing oxygen and humidity sensors at exhausts of the sample holders

So far, we lack means to measure purity of exhaust gasses in the sample holders. While we feed in very pure gases and usually purge the sample holders overnight before starting the measurements, we do not know the precise levels of oxygen and humidity in the experimental environment. For this reason, we are equipping the system with the required sensors. It will also allow us to create a feedback loop with mass flow controllers to fine-tune levels of oxygen and humidity in the environment (so far we rely on gas flow ratios). The software will be modified for automatic control.

- AC measurements board

So far, the setup can only perform DC characterisation. However, very useful information can be extracted with a use of spectroscopic measurements such as electrochemical impedance spectroscopy. The potentiostats used in the stability setup allow for an integration of one AC board in addition to the 16 DC boards already installed. The AC measurements can then be performed sequentially across all channels. Such additional *in situ* measurement capabilities would add much value to the setup and they would help with understanding of the origins of observed degradation.

- Backup power

Stability measurements are by definition long-term. Unfortunately, this comes with a substantial risk experiments are disturbed before completion. One such disturbing occurrences, which happen at EPFL approximately twice a year are power cuts. For this reason, we plan to purchase an uninterrupted power supply (UPS), which is essentially a power supply equipped with a battery pack to keep the setup running throughout a power blackout. The laboratory will be also connected to a diesel generator-backup power line to make sure that even a long power cut (longer than a battery can bridge) will not disturb the experiments (UPS is still needed to cover the time until diesel generator powers up).

Chapter 3 Improving the Stability of Perovskite Solar Cells

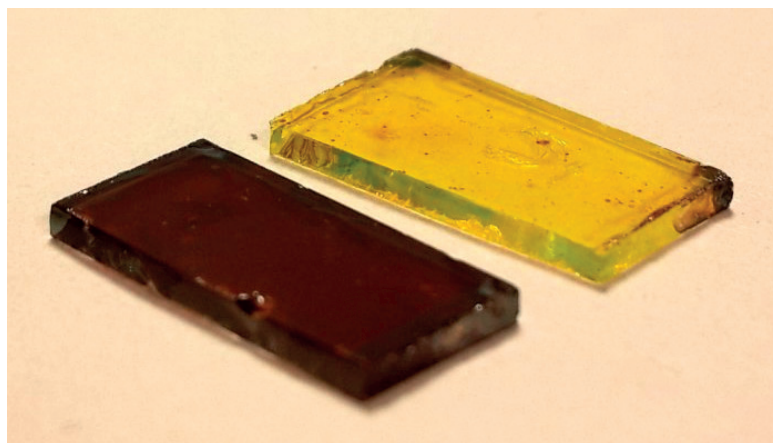
THE CONTEXT

At the time I started my PhD, the new trend and the new state-of-the-art perovskite solar cells were based on perovskite containing a mixture of iodine, bromine, methylammonium and formamidinium. While these devices showed high efficiencies^{31,41}, I soon realized that their stability was very poor. While building a prototype of what later became an ageing setup, I got involved in a project of my colleagues, where they developed “triple cation” perovskite including caesium (alongside methylammonium and formamidinium). I soon discovered that the devices containing caesium showed breakthrough stability.⁸² While unravelling different degradation mechanisms in PSCs, I also started collaborating with my colleagues on improving stability of devices with different architectures: planar ones²⁷, devices with polymeric hole HTLs⁴² and additive-free HTLs⁹⁴

The purpose of this chapter is to present my research into stability of perovskite solar cells as a single story and to put the subsequent chapters into context. Apart from describing my main research achievements, I present additional data that led to those discoveries. I attempt to offer more explanation of my motivations as well as refer to literature that influenced the direction of my research. Finally, I describe several side directions of my research that led to various collaborations. I finish with proposing several protocols for investigation of operational stability of perovskite solar cells. As the result, this chapter is more narrative than the other ones in this thesis.

My contribution:

The original data presented in this chapter was collected by me. When referring to the studies, where I was a contributing author, I was mostly responsible for the stability-related sections of those works.



(Picture from <http://www.electronicweekly.com>)

3.1 Background

At the time when I started working on this thesis perovskite films were mostly based on compounds such as $\text{CH}_3\text{NH}_3\text{PbI}_3$ or $\text{CH}_3\text{NH}_3\text{PbBr}_3$, which are composed of Pb cation and a single cation on A-site and a single halide anion on X-side in the ABX_3 perovskite structure. The most widely-used perovskite deposition method (widely-referred to as *sequential deposition*) involved depositing a film of perovskite precursor and then converting it to perovskite.²⁰ In mid-2014, a new method of perovskite deposition was invented. The films were deposited from in a single step and the crystallization was induced by washing the film with anti-solvent.³¹ This method allowed for mixing different perovskite precursors in a single solution, which in turn gave the researchers a good control over film composition and morphology (which was much more challenging with sequential deposition method). Soon, the perovskite composition of state-of-the-art devices evolved towards “mixed” compounds, where multiple cations were employed on A-site and multiple halides were sharing the X-sites.¹¹⁰ The motivation for this was to realize perovskites with more suitable bandgaps for photovoltaic applications. The fine-tuning of those mixtures resulted with devices employing $\text{MA}_{1-x}\text{FA}_x\text{Pb}(\text{I}_{1-y}\text{Br}_y)_3$ (MA being CH_3NH_3 and FA being $\text{NH}_2\text{CH}_2\text{NH}_3$) perovskite to achieve over 20 % PCE.^{41,111}

3.2 My preliminary work

After 20 % PCE values have been achieved by early 2015¹¹¹, it started to become clear that the very rapid improvement in PCEs could not continue at the same speed for much longer. At the same time, stability started to receive increasing attention and papers, where improving stability (as opposed to only efficiency) was the main goal started to attract wide interest.^{92,112} At that time, our laboratory had just achieved very high PCEs of 20.8 % with the mixed perovskite compounds.⁴¹ However, long-term stability could not be investigated on that occasion due to the lack of suitable experimental equipment. After building the prototype of stability measurement setup, I investigate the stability of those devices. Having measured multiple cells, the most stable ones degraded still rather fast (**Figure 3:1**) with estimated T_{80} lifetime (time it takes solar cell to lose 20% of its efficiency) of around only 500 h (as extrapolated from the linear degradation component). This was surprisingly poor given the very mild ageing conditions in inert atmosphere, room temperature and under UV-free light. Soon, reports emerged that the mixed MA/FA, I/Br perovskites are prone to photo-induced phase separation¹¹³ and trap formation under illumination.⁵²

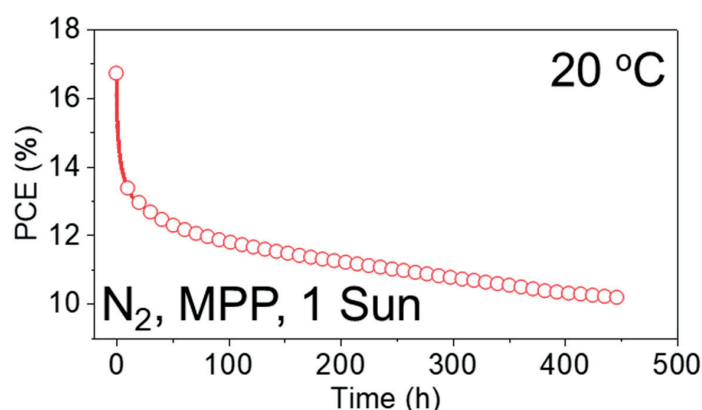


Figure 3:1 Degradation of the most stable device of its kind I measured. The device architecture is TiO_2 compact / TiO_2 mesoporous / $\text{MA}_{0.17}\text{FA}_{0.83}\text{Pb}(\text{I}_{0.83}\text{Br}_{0.17})_3$ / Spiro-MeOTAD / Au. Ageing was done under inert atmosphere, white LED light and at room temperature. The device was kept at MPP.

Against this backdrop, my colleagues were working on improving the perovskite solar cells by incorporation of an additional cation on the perovskite's A-site – Cs.⁸² The motivation for this was to alter the morphology of perovskite film and surpass the formation of the detrimental “yellow” phase. The devices fabricated with addition of Cs showed superior PCE at over 21 % and much improved reproducibility. They also exhibited better thermal stability. I got involved in this work by investigating the operational stability of these devices and soon realized that addition of small amount of Cs critically improves stability of mixed perovskite-based devices under illumination (**Figure 3:2**). We explained this based on the fact that addition of more components into the film results in its entropic stabilisation.^{114,115} Moreover, the addition of Cs suppresses the hexagonal, “yellow” phase, which may otherwise grow as the devices age. This is caused by the small radius of Cs⁺, which results in lowering of the effective Cs/MA/FA cation radius in the perovskite compound. This in turn shifts the Goldschmidt tolerance factor towards cubic, “black”, photoactive phase. Following the discovery of Cs-enhanced PSC stability, I was also involved in a study, where we showed that “planar” devices (without mesoporous TiO₂ scaffold) based on Cs-containing perovskite are equally stable.²⁷

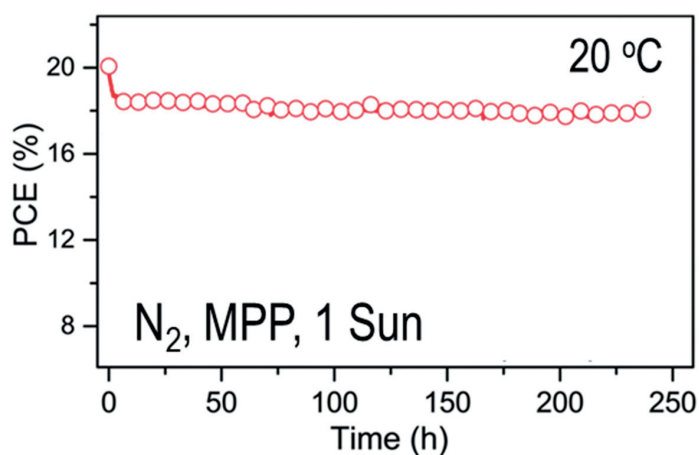


Figure 3:2 Room-temperature degradation of Cs-containing perovskite-based devices. The device architecture is TiO₂ compact/TiO₂ mesoporous / Cs₅(MA_{0.17}/FA_{0.83})₉₅Pb(I_{0.83}Br_{0.17})₃ /Spiro-MeOTAD /Au. Ageing was done under inert atmosphere, white LED light and at 20 °C. The devic was kept at MPP. Reproduced with permission from Ref.⁸²

3.3 High-Temperature Stability

While inclusion of Cs into perovskite constituted a major breakthrough in stability of PSCs, the experiments were all conducted at room temperature. However, when operating in the field, the temperature of solar cell can reach much higher values. For this reason, I started investigating how these devices behave at temperatures 60 °C – 85 °C. I found that at those elevated temperatures the devices degrade very rapidly and to a great extent (**Figure 3:3**) – stopping functioning after only several tens of hours. I verified that this was independent of illumination, mesoporous scaffold or the presence of Cs in the perovskite film. In **Chapter 4** I describe how I discovered that the primary degradation mechanism involves Au diffusion from the electrode, across the Spiro-MeOTAD layer and into perovskite.²⁶ I also show how by employing a thin Cr interlayer below Au electrode Au migration can be effectively stopped – thus critically improving the stability.

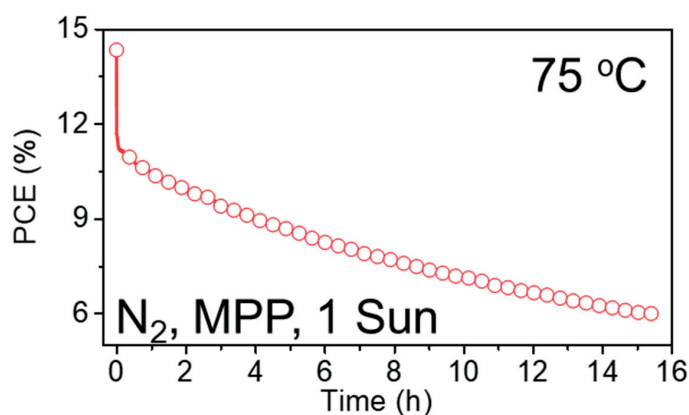


Figure 3:3 High-temperature degradation of Cs-containing perovskite-based devices. The device architecture is TiO_2 compact/ TiO_2 mesoporous/ $\text{Cs}_5(\text{MA}_{0.17}/\text{FA}_{0.83})_{95}\text{Pb}(\text{I}_{0.83}\text{Br}_{0.17})_3$ /Spiro-MeOTAD/Au. Ageing was done under inert atmosphere, white LED light and at 75 °C. The device was kept at MPP. Reproduced with permission from Ref.²⁶

While the Cr interlayer eliminates the problem of Au migration, it is not a panacea. In our case, the efficiency of the devices with Cr layer decreased to 13 % (from 20 % for devices with Au electrode only). This was probably due to higher series resistance or work function mismatch of the Au/Cr/Spiro-MeOTAD stack. At the same time, the alternative strategy to using a metal diffusion barrier was to employ a different HTM. Spiro-MeOTAD, which has been first used for solid-state DSSCs,¹¹⁶ is a small-molecule HTM, which means that the molecules constituting it are not chemically bonded (**Figure 3:4**; only Van der Waals bonds are formed). Additionally, it is prone to crystallization at high temperatures¹¹⁷, which may make it vulnerable to Au migration. Finally, Spiro-MeOTAD has a relatively high glass transition temperature (T_g) of 125 °C,¹¹⁸ which makes it brittle (“glassy”) at all the temperatures experienced by solar cells under operation. The brittle Spiro-MeOTAD may be prone to cracking as I observed in the aged devices in **Chapter 4**. For PTAA, T_g is 46 °C,¹¹⁹ which means that the polymer is in its flexible (“rubbery”) phase during stability measurements under elevated temperatures.

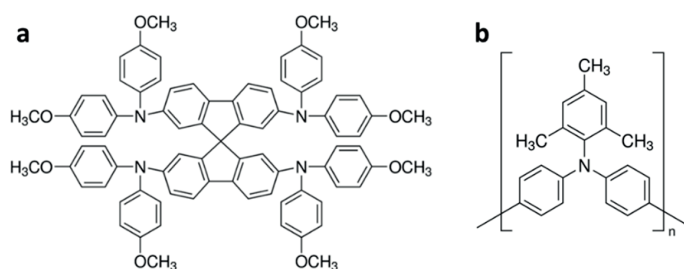


Figure 3:4 Chemical structure of a) Spiro-MeOTAD and b) PTAA.

Motivated by the high performance of PTAA-based devices^{31,110,120–122}, I explored possibilities of using PTAA to substitute Spiro-MeOTAD as HTM to improve stability, while simultaneously retaining high efficiency of the devices. Being thermally stable and polymeric in nature, PTAA had a good potential to achieve this goal. **Figure 3:5** shows the first ageing experiment I conducted using a PTAA-based device. The device shows breakthrough high-temperature stability as compared to its Spiro-MeOTAD based counterpart. While the efficiency of the device decreases upon heating (due to loss of V_{oc}), this particular device had over 19 % initial efficiency. Hence, this turned out to be a very promising way for coupling high efficiency with high-temperature stability

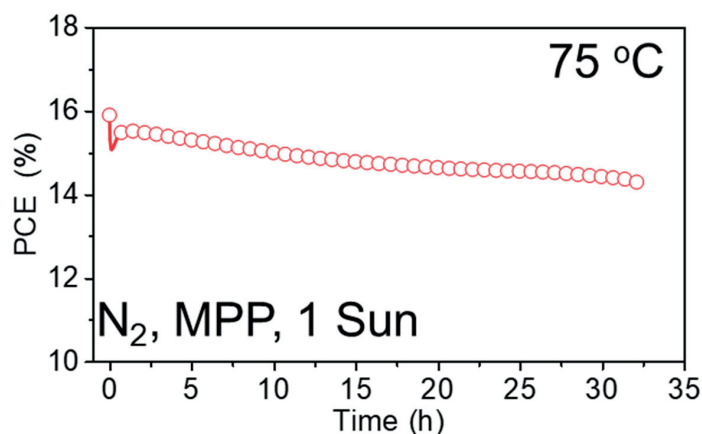


Figure 3:5 High-temperature degradation of Cs-containing perovskite-based devices with PTAA HTL. The device architecture is TiO_2 compact/ TiO_2 mesoporous / $\text{Cs}_5(\text{MA}_{0.17}/\text{FA}_{0.83})_{95}\text{Pb}(\text{I}_{0.83}\text{Br}_{0.17})_3$ /PTAA /Au. Ageing was done under inert atmosphere, white LED light and at 75 °C. The device was kept at MPP.

Having realized excellent high-temperature stability of PTAA-based devices, I started a collaboration with my colleagues, who discovered that adding Rb to perovskite (as the 4th cation) further improves the efficiency of the devices. By combining our two studies, we demonstrated devices with record efficiencies, while at the same time achieving unprecedented high-temperature stability. This work is described in **Chapter 5**.

In the meantime, discussion on the possible role of HTM additives on degradation of PSCs has ensued. For example, 4-tert-butylpyridine and Li salts, which are widely used to dope Spiro-MeOTAD, have been reported to adversely influence the chemical stability of perovskite.^{123,124} Furthermore, acetonitrile which is used as solvent for many widely-used additives can corrode the perovskite.⁹⁵ Collaborating with my colleagues, we showed that indeed HTMs without additives are potentially more stable.⁹⁴ We demonstrated this in polymeric HTMs with structures based on PTAA motif. Firstly, we demonstrated that when undoped, these PTAA derivatives yield PSCs with higher efficiencies than those based on undoped PTAA. However, most importantly we demonstrated that, when employed, those HTMs give superior high-temperature stability when doping is not employed.

While using polymeric HTMs turned out to be an effective way to achieve high-temperature stability of PSCs, the materials employed are prohibitively expensive (both to purchase and, in case of Au, to process) to be employed on a large scale required for PSCs to contribute to global energy production. As Au migration is the major high-temperature degradation factor in PSCs, I substituted Au electrode with carbon-based one. This not only allowed for good high-temperature stability but also the resulting devices could be potentially much less expensive to produce.⁹¹ This work is described in **Chapter 6**.

3.4 Reversible vs Irreversible Degradation

Working on degradation of PSCs, I realized that aging of perovskite solar cells resembles that observed in organic solar cells and often 2 distinct regimes are observed: an initial fast exponential one (termed *burn-in* in OPV), which is followed by a more linear regime.¹²⁵ I observed this for PSCs with several different architectures (mesoporous scaffold-based ones, planar, and inverted) and different perovskite compositions, but almost never for carbon-electrode based ones. Contrary to burn-in behaviour in OPV, I found that if the aged perovskite devices are left in the dark for several hours, they mostly

recover the exponential losses experienced during ageing under illumination. After an in depth analysis, I realized that mobile cations are responsible for this behaviour.¹²⁶ These can migrate on the time-scale of hours causing slow changes in the electric field distribution in the device. This in turn has impact on its photovoltaic performance. I described this discovery in **Chapter 7**. Further, in **Chapter 9** I show that this behaviour is less bias-dependent and more illumination-dependent.

By the time this thesis was submitted, investigations of stability of PSCs have become a widespread practice and many new studies now involve a kind of stability assessment. However, as of 2017, there is no consensus on how to measure the stability of perovskite solar cells and the multitude of different tests employed renders the data reported by different groups effectively incomparable. While some studies involved leaving unencapsulated devices in a drawer and measuring them periodically¹¹² (**Figure 3:6**), others investigated encapsulated devices under illumination and load (**Figure 3:7**).¹⁰⁹ It should be no surprise to the reader that those results are hardly comparable. The situation bares resemblance of the early days of the PSC field, where the (previously-unknown) phenomenon of hysteresis led to erroneous and incomparable reports of PCEs.^{43,46}

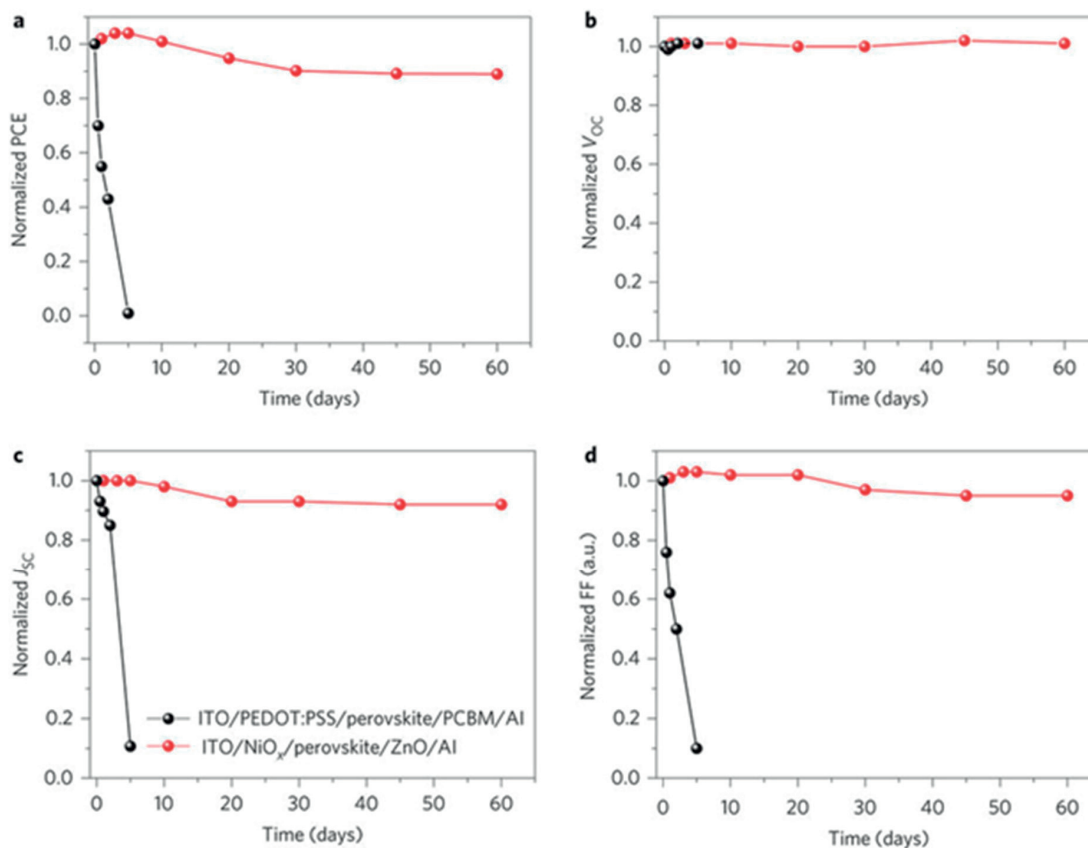


Figure 3:6 Example of stability measurement. Comparison of 2 device architectures. The devices are left in the drawer under poorly-defined conditions and their efficiency is measured periodically. Reproduced with permission from Ref.¹¹²

For the reasons outlined above, I systematically investigated ageing behaviour of PSC to deduce, which factors are critical for ageing. Considering the effect of illumination, temperature, atmosphere and load on the device, I concluded the most reliable way to investigate operational stability of PSCs is under illumination, MPP, inert atmosphere and both room and elevated temperatures. I also recommended that researchers should allow their devices to “recover” in the dark after the experiment is

completed, in order to disentangle potential reversible and irreversible losses. The study is presented in **Chapter 9** and it aims of stirring the discussion on how to age PSCs. I hope that it will inspire similar, systematic investigations of degradation factors in PSCs and hence contribute to future consensus on the most reliable way to assess operational stability of PSCs.

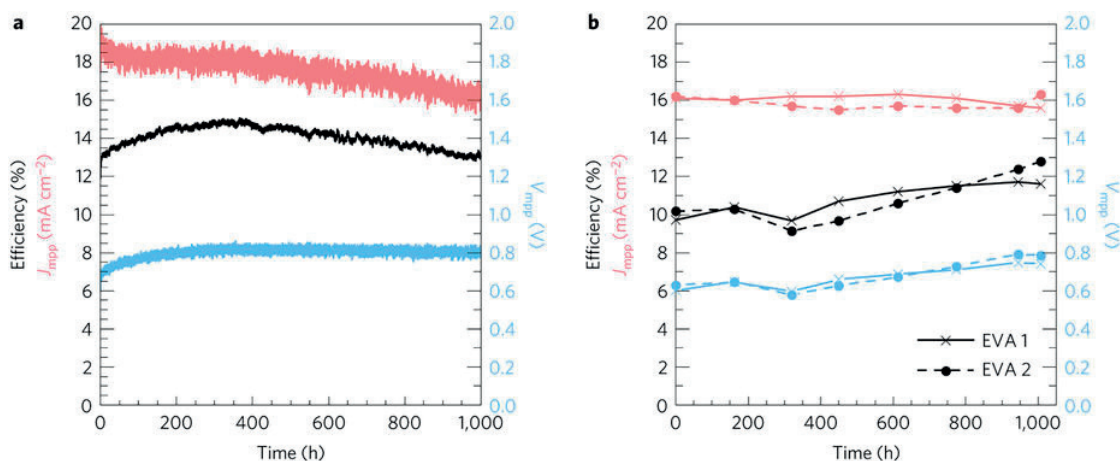


Figure 3:7 Example of stability measurement. Stability measurement of a) unencapsulated device under illumination and under load. b) stability investigation of encapsulated devices under damp atmosphere and high temperature. Reproduced with permission from Ref.¹⁰⁹

3.5 Protocols for Ageing Perovskite Solar Cells

For commercial PV panels rigorous industrial standards such as IEC 61215 exist to describe pass-fail qualification tests, as outdoor testing under real operation conditions is not feasible due to the long times required (>20 years).¹⁰⁵ These standards are the result of many years of experience and analysis of common field failures (corrosion, delamination, broken cells and connecting elements, hot spots etc.) and vary slightly for different technologies. All these protocols are designed for the product “PV panel” which is exposed to accelerated stress tests mainly targeting design and material errors, which would lead to field failures. Thus, such tests (although required for any type of solar panel to be installed outdoors), are not the best choice to assess the stability of a novel material system and identify wear-out and failure mechanisms. On the other hand, to guarantee comparability and relevance of reported stability results, the perovskite research community should follow common protocols or even reach a consensus on how to report stability data similarly to the organic photovoltaics (OPV) community releasing specific testing protocols (ISOS-3).¹⁰⁶ In fact, ISOS-3 protocols are already very useful for investigating stability of PSCs. However, they have to be adapted to given certain specificities of PSCs, such as mobile ions that induce potentially reversible degradation. The question whether flushing unencapsulated PSCs with an inert gas promotes perovskite decomposition should also be answered and the conclusion – reflected in future ageing protocols.

With this in mind, as an extension of the work described in **Chapter 9** (and based on results described in that chapter), below I propose the following implementations for lab-scale ageing experiments satisfying both, the assessment of operation stability and the investigation of degradation mechanisms. Error! Reference source not found.3:1 recommends ageing protocols differing in purpose and sophistication, while

Table 3:13:2 outlines PSCs ageing setup designs to allow for the accomplishment of the outlined standards. The first, *Dark heat stress* test should be seen as a first step towards characterizing PSC stability, which should be then followed with operational stability measurements repeated at 20 °C and 65 - 85 °C. I intend these as a starting point for the discussion on how future consensus PSCs ageing protocols should be defined.

Table 3:1 Recommended ageing protocols for PSCs.

Test type	Dark heat stress		Basic, Operational		Advanced, Operational
Illumination	Dark		1 Sun white LED, or solar simulator		1 Sun white LED, or solar simulator
Temperature	65 - 85 °C		Ambient and 65 - 85 °C*		20 and 65 - 85 °C*
Load	n/a (open-circuit)		Open-/short-circuit/ MPP**		MPP + periodic J-V
Atmosphere	Ambient	N ₂ /Ar glovebox	Ambient	N ₂ /Ar glovebox	Flushed N ₂ /Ar and controlled
Encapsulation	Yes	Optional	Yes	Optional	Optional
Dark recovery	n/a		Recommended		Recommended

*If only one condition is chosen, data obtained at 65 °C is more significant for estimating stability under real operation conditions

**Constant load resistor can be used to reach approximate MPP for relatively stable devices

Table 3:2 Recommended setup requirements for ageing of PSCs.

Setup design	Dark heat stress	Basic, operational	Advanced, operational
Illumination	No	White LED or Solar Sim.	White LED or Solar Sim.
Electrical Char.	Single channel	Single channel	Multi-channel
Temperature control	Hotplate	Hotplate	Active with feedback
Atmosphere control	No	No	Active with feedback
Load options	n/a	Open-/short-circuit, constant load	Open-/short-circuit, MPP
In situ measurements	Not required	Single J-V	J-V, EIS, transients

Given its simplicity (only a hotplate and *ex-situ* J-V measurement setup are required for implementation), the *Dark heat stress* test is a very useful tool to screen a large number of device types with respect to thermal stability. It involves keeping the devices on a hotplate (at 65 - 85 °C) and measuring them periodically. The test can be conducted under ambient conditions on encapsulated devices, or in a glovebox without a need for further encapsulation. *Dark heat stress* can be seen as the first step in stability testing of new device architectures. Poor dark thermal stability may signal that the device stack is inherently instable and there is no need for harder-to-implement operational stability tests. However, once again I would like to stress that dark stability testing should not be seen as an alternative to operational stability investigation. Stability measured this way should be accordingly referred to as “thermal stability”.

The *Basic* operational stability measurement setup should allow for keeping the devices constantly under illumination and measuring them *in situ*. The minimum to attain this is to set up an illumination source (e.g. white LEDs or a solar simulator; spectra should be reported) and a single J-V measurement unit (e.g. a source measure unit or a potentiostat). The devices should be left under 1 Sun illumination

at open- or short-circuit (constant load resistor can be used to reach approximate MPP for relatively stable devices) and their J-V curves measured periodically. It is strongly recommended that this is done *in situ* by multiplexing devices with a measurement unit. Otherwise, the devices can start “recovering” before they are measured *ex situ* one-by-one. The experiment should be done at ambient, room temperature and also at 65 - 85 °C. If the researchers decide to do only one of these experiments, data obtained at 65 - 85 °C is more significant for estimating stability under realistic operational conditions. Finally, the experiment can be either conducted in the ambient atmosphere on encapsulated devices or in a clean N₂/Ar filled glovebox without a need for further encapsulation. Compared to the *Advanced* protocol described below, I believe the *Basic* protocol should provide a conservative estimation of stability.

The *Advanced* operational stability measurement setup aims to introduce a high level of environmental factors control and standardization. The setup requires investing in dedicated infrastructure such as multi-channel measurement units or specifically designed MPP tracking solutions, as well as a weathering chamber. The light source should be an AM 1.5G solar simulator or white LED (spectrum should be supplied). The setup should also employ an active temperature control, which allows for keeping the devices at a precise set point (with an additional possibility for temperature cycling, if required). Again, I recommend that the experiments are repeated at 20 and 65 - 85 °C (at device; not necessarily the same as the temperature inside the weathering chamber), while flushed with inert gas. Ideally, one should also have means for measuring and controlling the levels of O₂ and H₂O in the environment. Encapsulation can be employed on top of that to ensure that no O₂ or H₂O enters the device and that no volatile compounds escape the device. Finally, for the *Advanced* protocol I recommend periodic measurements of J-V curves to extract additional information about the ageing behaviour of the devices such as J_{sc}, V_{oc}, FF and hysteresis evolution. Additionally, electrochemical impedance spectroscopy (EIS) and transient measurements can be implemented *in situ*. This protocol is most suited to investigate the specificities of PSCs.

Common for all protocols, I encourage the researchers to decide the experiment duration based on the behaviour of the aged devices, aiming at arriving at linear degradation regime (if applicable) before extrapolating the data. I also invite the researchers to check, whether their devices recover after being stored in the dark for several hours (I would use at least 10 h for a full recovery). In order to allow for data comparability between different groups, I recommend that these protocols are employed in cases when ageing is performed as a routine measurement aimed at comparing the stability of different devices either within one study or in literature. This would involve assessing the stability of a new device architecture, a new hole transporting material or perovskite composition, where the focus is not on understanding the degradation mechanisms but rather on quantifying the behaviour.

I recommend weathering chambers for atmosphere control for mainly two purposes: to investigate the influence of different gases on degradation and to provide an inert atmosphere to avoid extrinsic degradation factors. At first glance, the latter represents the case of an ideally encapsulated device and therefore encapsulation of the device is not required. However, continuous flushing with gas keeps the partial pressure of volatile decomposition products such as hydrogen iodide and methylamine¹²⁷ low and might promote a decomposition of (particularly CH₃NH₃PbI₃) perovskite, especially at elevated temperatures, which can be avoided for all-inorganic perovskites.¹²⁸ Therefore, it is recommended to characterize encapsulated devices even in case of an inert atmosphere, which also reduces the undesired and uncontrolled effect of trace gases.

Chapter 4 Not All That Glitters Is Gold: Metal-Migration-Induced Degradation in Perovskite Solar Cells

THE CONTEXT

My first project, which aimed to further the understanding degradation of PSCs, explored the effect of elevated temperatures on those devices. Solar cells operating in realistic conditions have to routinely deal with elevated temperatures up to 65 °C and even 85 °C in extreme cases. When I exposed our state-of-the-art devices with Cs-containing perovskite to these conditions, very fast degradation was observed on the timescale of hours. While this was surprising enough given the excellent room-temperature stability of those same devices, the most interesting finding was the discovery of the culprit – Au that diffuses from the metal electrode through hole transporting layer and into the perovskite. Once there, it “does not glitter”. Instead, it irreversibly destroys the solar cells.²⁶

This chapter is based on a peer-review paper published in *ACS Nano* in May 2016 entitled:

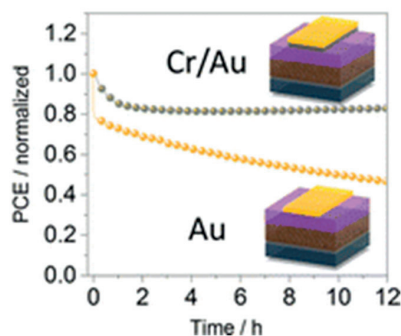
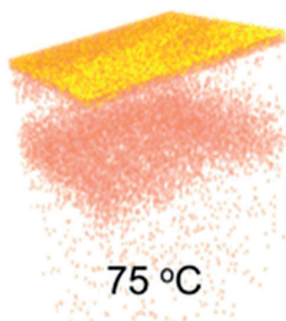
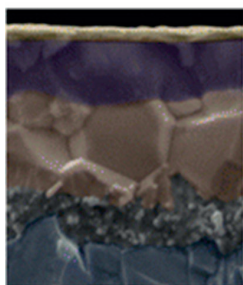
Not All That Glitters Is Gold: Metal-Migration-Induced Degradation in Perovskite Solar Cells

authored by:

Konrad Domanski, Juan-Pablo Correa-Baena, Nicolas Mine, Mohammad Khaja Nazeeruddin, Antonio Abate, Michael Saliba, Wolfgang Tress, Anders Hagfeldt and Michael Grätzel.

My contribution:

I was the main author of this publication. I initiated the project, performed most of the measurements presented in this work and reached out to collaborators to obtain additional measurements. I also analyzed the data, prepared the figures and wrote the first version of the manuscript.



Not All That Glitters Is Gold: Metal-Migration-Induced Degradation in Perovskite Solar Cells

Konrad Domanski,[†] Juan-Pablo Correa-Baena,^{*,‡} Nicolas Mine,[§] Mohammad Khaja Nazeeruddin,^{||} Antonio Abate,^{†,⊥} Michael Saliba,[†] Wolfgang Tress,[†] Anders Hagfeldt,[‡] and Michael Grätzel[†]

[†]Laboratory for Photonics and Interfaces and [‡]Laboratory of Photomolecular Science, Institute of Chemical Sciences and Engineering, École Polytechnique Fédérale de Lausanne, CH-1015 Lausanne, Switzerland

[§]Laboratory for Nanoscale Materials Science, Swiss Federal Laboratories for Materials Science and Technology, CH-8600 Dübendorf, Switzerland

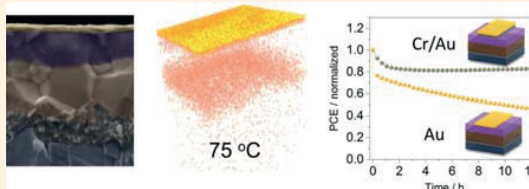
^{||}Group for Molecular Engineering of Functional Materials, Institute of Chemical Science and Engineering, École Polytechnique Fédérale de Lausanne, CH-1950 Sion, Switzerland

[⊥]Adolphe Merkle Institute, University of Fribourg, CH-1700 Fribourg, Switzerland

Supporting Information

ABSTRACT: Perovskite solar cells (PSCs) have now achieved efficiencies in excess of 22%, but very little is known about their long-term stability under thermal stress. So far, stability reports have hinted at the importance of substituting the organic components, but little attention has been given to the metal contact. We investigated the stability of state-of-the-art PSCs with efficiencies exceeding 20%. Remarkably, we found that exposing PSCs to a temperature of 70 °C is enough to induce gold migration through the hole-transporting layer (HTL), spiro-MeOTAD, and into the perovskite material, which in turn severely affects the device performance metrics under working conditions. Importantly, we found that the main cause of irreversible degradation is not due to decomposition of the organic and hybrid perovskite layers. By introducing a Cr metal interlayer between the HTL and gold electrode, high-temperature-induced irreversible long-term losses are avoided. This key finding is essential in the quest for achieving high efficiency, long-term stable PSCs which, in order to be commercially viable, need to withstand hard thermal stress tests.

KEYWORDS: perovskite solar cells, stability, degradation, secondary ion mass spectrometry, gold, metal electrodes, buffer layers



While the power conversion efficiencies (PCEs) of organic–inorganic perovskite solar cells (PSCs) have rapidly achieved remarkable values of 22.1%,¹ this has not been matched by equal developments in long-term stability.^{2,3} At this stage, operational stability is considered one of the main obstacles for the commercialization of PSCs.^{4,5}

The perovskites used in photovoltaics commonly employ an ABX₃ formula, where A is a monovalent cation (methylammonium, MA; formamidinium, FA; Cs, *etc.*), B is a divalent metal, such as Sn or Pb, and X is I, Br, or Cl. In previous studies, perovskite films have been subjected to different environmental conditions such as temperature, humidity, and illumination.^{6–8} It has been found that the stability of this material class varies greatly depending on the mixing of A and X ions.^{9–12} Perovskites are thermally stable at temperatures not exceeding those typically achieved by solar cells in operation (up to 85 °C),^{6,7} with humidity identified as the main degradation trigger.^{6,13} Similarly, stability of complete PSC devices has been investigated with relation to the same environmental factors.^{6,14–18} Interestingly, in addition to the perovskite-related

degradation, the stability of the devices was found to greatly depend on device architecture.^{17,19–24} This was explained partly by interfacial degradation^{19,25} and also by degradation of the charge-transporting layers.^{14,22} Recently, there have been efforts to substitute the widely used organic spiro-MeOTAD hole-transporting layer (HTL) with inorganic materials to improve the stability of PSCs.^{20,21,26} However, it is still unclear what the mechanism increasing the stability is. Furthermore, while most of the published reports focus on dark “shelf stability”,^{20,22,27} only a handful have investigated devices under load and illumination^{17,18,26,28} and even fewer attempted to match the realistic operation conditions of solar cells by subjecting them simultaneously to temperatures in excess of 70 °C,²⁹ which are routinely achieved on a hot, sunny day.³⁰

Received: April 18, 2016

Accepted: May 17, 2016

Published: May 17, 2016



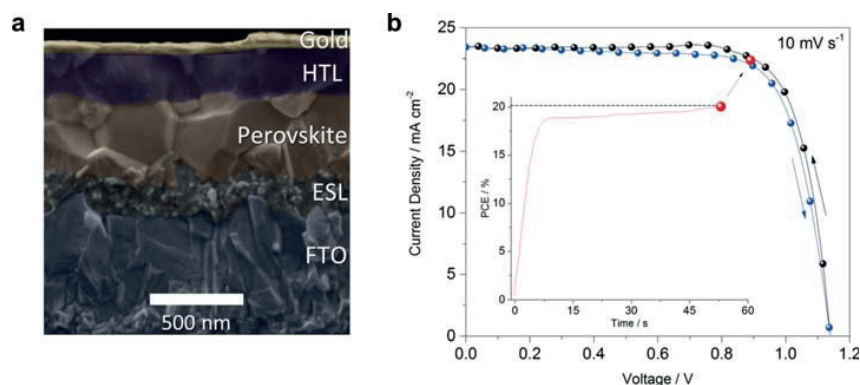


Figure 1. Structure of the PSCs studied in this work. (a) SEM image of the cross section of full devices containing the triple cation perovskite. (b) J - V curve of a high efficiency device used in this study. The J - V curve is recorded at 10 mV s^{-1} . The inset shows stabilized power output by maximum power point (MPP) tracking for 55 s. The MPP tracking begins around V_{oc} and is updated every 150 ms.

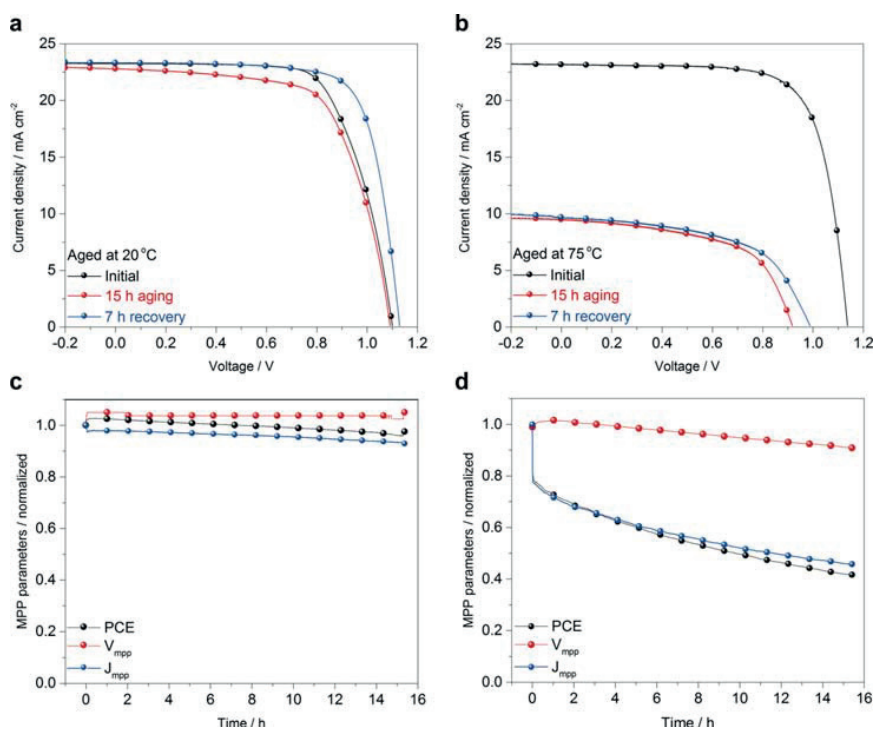


Figure 2. Performance of devices composed of the triple cation perovskite operated at maximum power point at different temperatures. (a,b) J - V characteristics of the devices aged at 20 and 75 °C, respectively: before, at the end of the 15 h aging experiment, and after 7 h of recovery in the dark at 20 °C and under nitrogen flow. J - V curves are recorded at 20 °C and with a 10 mV s^{-1} scan rate. (c,d) Evolution of PCE, V_{MPP} , and J_{MPP} during aging at maximum power point. The values are normalized to the initial ones. See Scheme S1 for the explanation of the experimental procedure.

Here, we investigate the stability of state-of-the-art perovskite devices with PCEs above 20%. We show that operating devices, employing a spiro-MeOTAD HTL and a Au or Ag back contact (the most widely used architectures, currently yielding the highest PCEs), at temperatures exceeding 70 °C causes irreversible changes to the devices, which results in a dramatic performance loss. By means of elemental analysis on aged

devices, we observe that considerable amounts of Au from the electrode diffuse across the HTL into the perovskite layer. We pinpoint the diffused Au to cause the irreversible loss of open-circuit voltage (V_{oc}), fill factor (FF), and short-circuit current density (J_{sc}) in the aged devices. We further show that introduction of a Cr interlayer alleviates the problem of fast device aging at elevated temperatures. This is an encouraging

finding as it shows that neither perovskite nor spiro-MeOTAD is the limiting factor for the high-temperature stability of PSCs.

RESULTS AND DISCUSSION

The PSCs were fabricated on fluorine-doped tin oxide (FTO) glass and composed of a typical stack of compact TiO₂/mesoporous TiO₂/perovskite/spiro-MeOTAD/Au as recently reported by us.³¹ The active layer of the device consists of a perovskite-filled mesoporous TiO₂ scaffold and a solid perovskite layer sitting on top of it. The chemical composition of the perovskite precursor is a Cs-containing FA_{0.83}MA_{0.17}Pb-(I_{0.83}Br_{0.17})₃ formulation, referred to as “triple cation” perovskite in this work.¹² Figure 1a shows the cross-sectional scanning electron microscopy (SEM) image of the device with a thin perovskite-infiltrated mesoporous TiO₂ layer (an electron selective layer, ESL) of ca. 200 nm and a 500 nm perovskite capping layer composed of large crystals. A 200 nm layer of spiro-MeOTAD (as HTL) sits atop the perovskite layer, and finally, a gold top electrode is deposited to contact the device. With this architecture, we achieved very high PCEs of up to 20.6% (stabilized at 20.0%; Figure 1b).

The aging experiments were conducted by keeping the devices at controlled temperature (20 or 75 °C), in nitrogen atmosphere and under 1 sun equivalent white light-emitting diode (LED) illumination at maximum power point (MPP) for over 15 h (see Scheme S1). Figure 2a shows the current–voltage (*J–V*) curves of the device aged at 20 °C: before, at the end of the aging experiments, and after 7 h of recovery (in dark, under nitrogen flow and 20 °C; cf. Figure S1a for the evolution of *J–V* parameters), while Figure 2c shows the evolution of PCE, *V*_{MPP}, and *J*_{MPP} over the course of the experiment. The 20 °C device has shown very high stability overall, with *V*_{oc} being the most stable parameter individually. The limited decrease in PCE was mostly due to a small and temporary loss of *J*_{sc} and the device regained its performance following 7 h of recovery (Table 1).

Table 1. *J–V* Parameters of Aged PSCs^a

	PCE (%)	<i>V</i> _{oc} (mV)	<i>J</i> _{sc} (mA cm ⁻²)	FF
initial	17.7	1105	23.3	0.69
after aging at 20 °C	16.5	1097	22.8	0.66
after 7 h recovery	19.7	1138	23.3	0.74
initial	19.4	1142	23.2	0.73
after aging at 75 °C	4.9	922	9.5	0.57
after 7 h recovery	5.3	991	9.6	0.55

^aThe data were extracted from the backward scan of the devices shown in Figure 2. *J–V* curves were all recorded at 20 °C and 10 mV s⁻¹.

On the other hand, the degradation of the device aged at 75 °C was much more severe (Figure 2b,d and Figure S1b), and no recovery was seen. All *J–V* metrics saw a substantial reduction, with *J*_{sc}/*J*_{MPP} suffering the most and the earliest into the experiment. Additionally, a large, irreversible loss of *V*_{oc} was observed. This pattern of small, reversible PCE loss for devices aged around room temperature and a severe, permanent PCE loss including a substantial reduction in *V*_{oc} after aging at 75 °C is reproducible, and we confirmed this by repeating the experiment several times (Figure S2). A similar pattern was found for samples aged under the identical conditions but by keeping the devices at *V*_{oc} indicating that the degradation was not primarily due to the load on the device (Figure S3).

Moreover, a similar observation was made for devices aged at 75 °C in the dark (Figure 4c), confirming that light was only partially responsible for the degradation. Hence, we concluded that the heating is responsible for most of the degradation.

In order to investigate the effect of aging on perovskite, we performed UV–visible absorption spectroscopy (Figure S4) and X-ray diffraction (XRD) measurements (Figure S5) before and after the aging experiments (Au electrode was removed). No major difference was found in the material’s structural and optical properties with the temperature treatment. The absorption of aged devices was independent of the aging temperature. Similarly, XRD analysis showed no correlation between temperature of aging and perovskite degradation. However, the peak indicating the presence of PbI₂ ($2\theta = \sim 12.8^\circ$; the devices are fabricated with a small PbI₂ excess) has slightly increased in both devices aged at 20 and 75 °C.

Since the structural and optical changes of the perovskite are not the main cause of the dramatic device performance loss, the elemental composition of the aged devices was investigated. Time of flight secondary ion mass spectroscopy (ToF-SIMS) elemental depth profiling is a perfectly suited technique for this, and it has been proven to work well to characterize perovskite-based devices.^{32–34} By rastering an energetic beam of ions across a sample and analyzing the debris of those collisions, spatially resolved elemental maps can be obtained. Figure 3a shows a depth profile of an as-fabricated control device, which has never been exposed to high-intensity light, electric field, or temperature higher than room temperature. The Au⁻ ion trace is indicative of the top electrode; the CN⁻ ion can be ejected from either the spiro-MeOTAD HTL or the perovskite layer. I⁻ comes from the perovskite layer, TiO₂⁻ is from either the mesoporous scaffold or the ESL; and SnO₂⁻ is from the FTO electrode. The relative intensity of CN⁻ and I⁻ from the HTL to the FTO layer is beyond the scope of this publication and will be the subject of future work. Further, these ions are sensitive to diffusion and segregation at the surface because of the primary ion bombardment/implantation, which can explain their long diffusion tails in the FTO and the substrate.³⁵ We clearly see a sharp interface between Au and HTL; however, roughness induced by the primary ion erosion explains the sharpness decrease with the increased fluence. Moreover, passing the TiO₂ mesoporous layer also affects the interface evaluation.

When comparing the control device with the aged ones (see Figure S6 for full SIMS profiles and the Methods section for an explanation of how ToF-SIMS profiles can be compared), one striking observation for the device aged at 70 °C is the occurrence of a Au⁻ signal (in yellow) in the mesoporous TiO₂ perovskite, which peaks close to the TiO₂/SnO₂ interface. This unexpected occurrence of the high Au peak is the first ever reported direct evidence of metal migrating from the electrode to inside the perovskite layer. This phenomenon, however, has been observed previously in inorganic semiconductors for several different metals such as Au, Ag, Ni, Cu, and Fe.^{36–40} Figure 3b presents the 3D distribution of the ions shown in Figure 3a across a 100 μm² region of the samples (see Movie S1 for an animated 3D reconstruction). One can clearly see that the respective ions are distributed uniformly in the *xy* plane of the device. At 70 °C, a considerable amount of Au has diffused inside the perovskite layer and accumulated close to the TiO₂/SnO₂ interface.

Inductively coupled plasma mass spectrometry (ICP-MS) was used to quantify the amount of Au diffused in the

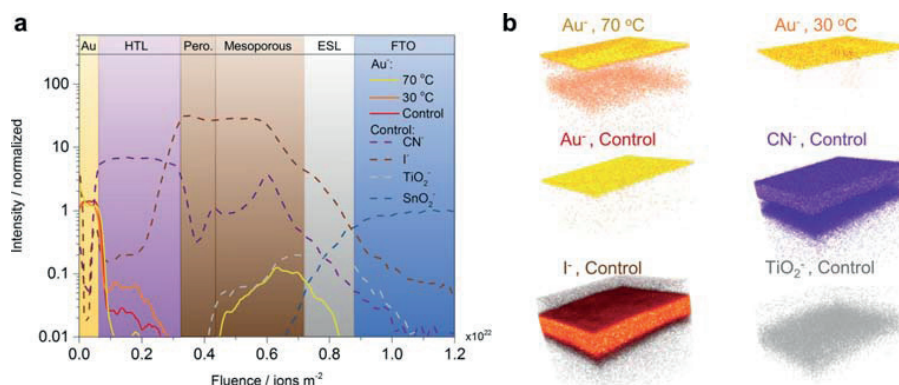


Figure 3. ToF-SIMS depth profiles of the aged PSC devices. (a) Profile showing the concentration of selected species across the control device. The profile of Au⁻ is compared to that of the devices aged at 30 and 70 °C. (b) Reconstructed elemental 3D maps for the ions traced in the depth profile. The *xy* dimensions of the analyzed area are 10 × 10 μm.

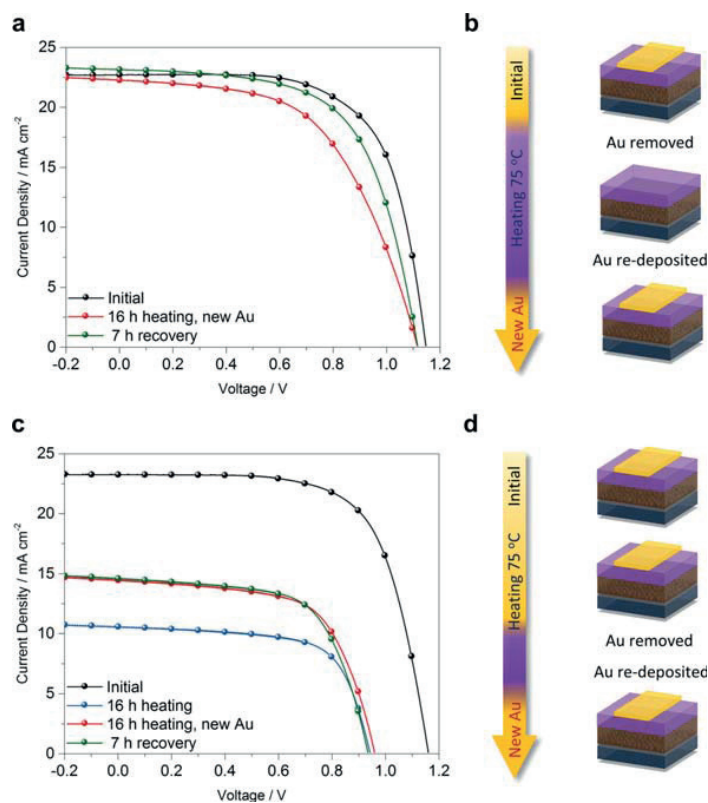


Figure 4. Pinpointing the degradation to Au diffusion. (a,c) *J*–*V* curves of two identically prepared Au-contacted devices (two pixels fabricated on the same substrate) heated in the dark at 75 °C in N₂ atmosphere for 16 h. (b,d) Step-by-step treatment of the respective devices. The device in (a) had the electrode removed before the heating phase. For the device in (c), the original Au electrode remained in place during the aging and was removed directly afterward. Both devices had the electrode re-deposited subsequently. Devices were exposed to light only during *J*–*V* measurements. The recovery of all devices was in the dark at 20 °C and nitrogen flow. *J*–*V* curves were recorded at 20 °C with a 10 mV s⁻¹ scan rate.

perovskite in one control device and one device aged at 70 °C. This was done by removing the Au electrode and dissolving the active layers of the devices (for more information, see Scheme

S2). The measurement found a large amount of Au in the sample aged at 70 °C (72.8 ng), while the level of Au found in the control sample was below the detection limit of the

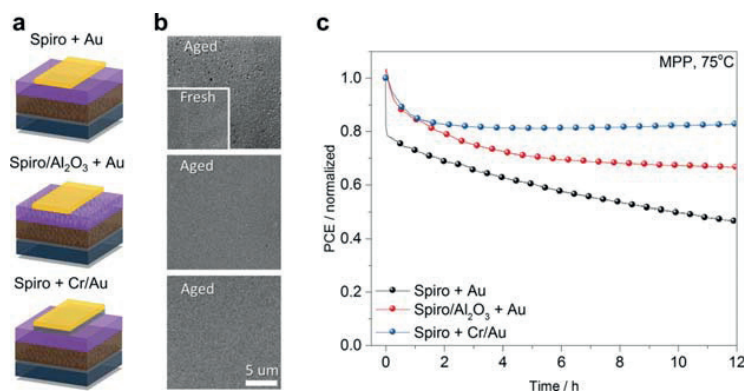


Figure 5. Solving the problem of metal-migration-induced degradation. (a) Schematics of three devices with different HTL/electrode configurations. (b) Top view SEM images of fresh/degraded Au electrodes of the devices. (c) Results of maximum power point tracking aging of the corresponding devices. The aging was done under 1 sun illumination at 75 °C and N₂ flow. The values are normalized to the initial ones.

instrument (~ 1 ng for the amount of solution used). This translated to a concentration of 1.45 nM cm^{-2} of Au (or $8.9 \times 10^{14} \text{ Au atoms cm}^{-2}$; compared to $\sim 10^{17} \text{ Pb atoms cm}^{-2}$) in the perovskite layer of the aged device.

Based on the evidence (ToF-SIMS, ICP-MS), it was concluded that Au from the top electrode can diffuse across the organic spiro-MeOTAD HTL and into the perovskite before it is stopped at the TiO₂/perovskite interface. Since some Au was already found within the HTL of the control device (Figure 3), it shows that spiro-MeOTAD is a very poor barrier for the migration of Au. Therefore, even heat produced during back contact evaporation is sufficient to cause Au diffusion into the HTL. Subsequently, the Au⁻ signal in HTL increases in the device aged at 30 °C. However, this does not seem to have a detrimental effect on the performance of the device. When the aging temperature is increased to 70 °C, Au appears to easily pass through the HTL and accumulate within the perovskite layer. It appears that only when inside the perovskite, Au critically degrades the performance of PSCs.

Au diffusing inside the perovskite can have several detrimental effects. First of all, it can produce shunts across the device, reducing the FF.²⁴ Moreover, Au atoms can create deep trap states within the semiconductor, which enhances nonradiative recombination and consequently degrades V_{oc} as well as J_{sc} . Indeed, we observe a severe, irreversible reduction in V_{oc} , J_{sc} , and FF in the devices aged at high temperature. The phenomenon of Au creating mid-band-gap states for silicon devices has been reported before.^{36,37}

In order to pinpoint the observed degradation to Au diffusion into perovskite and to exclude possible influence of interfacial or HTL degradation, we performed dark heating experiments on two identically fabricated devices, one of which had the Au electrode temporarily removed for the duration of the heating phase (see Methods). We found that the device heated without the Au electrode did not degrade significantly and later recovered almost all of its initial performance (Figure 4a). On the other hand, the device aged with Au on top has seen a severe degradation (Figure 4c) similar to that shown above. While replacing the Au electrode of the degraded devices with a fresh one helped to partially recover J_{sc} , the loss of V_{oc} and FF was permanent. The reason for the recovered J_{sc} is likely due to the partially reversible nature of degradation in

PSCs when they are left in the dark. We note that the process of replacing the electrode takes around 1.5 h. However, it may also indicate degradation of the Au/spiro-MeOTAD interface.

Next, Au was compared to the other most widely used electrode for PSCs, namely, Ag. The average initial efficiency of Ag-contacted devices was 11.8% compared to 18.3% for Au-contacted devices from the same batch. By heating the devices to 75 °C in the dark and in a nitrogen atmosphere, we found that devices with a Ag electrode degrade dramatically, as seen for the Au analogues (Figure S7). While the loss of V_{oc} was relatively lower, the increased degradation may come from the fact that iodine can migrate through the HTL, reacting with Ag and altering the electronic properties of the Ag/HTL interface.^{23,27} A similar phenomenon has been also shown for Al-contacted devices.²⁷ This further confirms that metal electrodes (Au and Ag) are intrinsically incompatible with organic spiro-MeOTAD HTL-based perovskite devices such as solar cells,^{41–43} photodetectors,^{44–46} lasers,⁴⁷ and LEDs.⁴⁸ The problem of metal-induced degradation cannot be simply resolved by sealing the devices, and metal diffusion must be stopped by an alternative HTL or an interfacial layer preventing this phenomenon.

Several strategies were explored to resolve the issue of metal-migration-induced degradation of PSCs. First, the HTL was modified by mixing spiro-MeOTAD with Al₂O₃ nanoparticles. This approach has been proposed by Guarnera *et al.* to stop metal diffusion across the HTL.²⁴ While the stability of as-prepared devices aged under MPP conditions and 75 °C was improved significantly, the extent of degradation proved unacceptable and a linear degradation component was observed (Figure 5b and Figure S8).

Thin interlayers of Cr (10 nm) were deposited as diffusion barriers between the spiro-MeOTAD HTL and Au. The initial performance of these devices was 13.0%, which was lower than that without a Cr layer and likely due to high series resistance or work function mismatch of the Au/Cr/spiro-MeOTAD stack. By subjecting the Cr/Au devices to realistic solar cell operating conditions (75 °C, 1 sun illumination, and MPP tracking), the stability was found to improve critically (Figure 5c), and any degradation was reversible (due to an increase of V_{oc} the device outperformed itself following 9 h of recovery, Figure S9a). After an early period of exponential decay, the

PCE stabilized at 83% of the initial value. Importantly, no degradation of V_{oc} in the aged devices occurred (Figure S9), indicating that Au diffusion across the HTL into perovskite has been hindered by the Cr interlayer. We have confirmed this by performing ICP-MS spectrometry on the aged Cr/Au devices and not finding any trace of Au or Cr inside the perovskite layer. Furthermore, we imaged the fresh and degraded Au electrodes of the three devices with different HTL/electrode configurations (Figure 5b). While the Au electrode of the spiro-MeOTAD + Au device became evidently porous following high-temperature exposure, both devices with spiro-MeOTAD/ Al_2O_3 + Au and spiro-MeOTAD + Cr/Au architectures had no visible evidence of electrode degradation or decomposition. This finding suggests that it is plausible that the spiro-MeOTAD layer cracks when heat-stressed, which in turn creates pores and a point of contact between Au/perovskite. This effect could be hindered by a Cr interlayer, or cracking of spiro-MeOTAD could be considerably reduced by mixing it with Al_2O_3 .

The high-temperature stability of Cr/Au devices is unprecedented, and such behavior has never been observed in devices using Au or Ag as contacts. In addition, deposition of a thin Cr interlayer is industrially feasible as Cr can be evaporated from Cr-plated W wires by sublimation. Finally, this work brings to light the misconception that the perovskite materials and HTLs are the main contributors to the long-term degradation of device performance. Several reports of successful employment of inorganic HTLs, inorganic interfacial layers, or transparent conductive oxide electrodes have shown considerable improvement of PSC stability.^{20,24–26,50} Although not directly acknowledged, the improvement in stability may have come from hindering metal diffusion from the contact across the HTL into the perovskite rather than more efficient protection of perovskite from oxygen or humidity.

CONCLUSIONS

We investigated the stability of state-of-the-art, “triple cation” perovskite devices with PCEs above 20%. We show that operating devices employing a spiro-MeOTAD HTL and a Au or Ag back contact at temperatures exceeding 70 °C causes irreversible changes to the devices, which results in a dramatic performance loss. By means of elemental analysis on aged devices, we observe that considerable amounts of the Au from the electrode diffuse across the HTL into the perovskite layer. We pinpoint the diffused Au to cause the irreversible loss of V_{oc} , FF, and J_{sc} in the aged devices. We further show that insertion of a thin Cr interlayer between the HTL and Au alleviates the problem of severe device degradation at elevated temperatures. This shows that neither perovskite nor spiro-MeOTAD is the primary limiting factor for high-temperature stability of PSCs in the current configuration, as it has previously been suggested. Our study creates a roadmap for high-temperature stability measurements of PSCs by taking into consideration metal migration. Therefore, it is important for the field to investigate other interlayer materials that can hinder this phenomenon.

METHODS

Device Fabrication, Perovskite Precursor Solution and Film Preparation. Nippon sheet glass ($10 \Omega \text{ cm}^{-2}$) was cleaned by sonication in a 2% Hellmanex water solution for 30 min. After being rinsed with deionized water and ethanol, the substrates were further cleaned with UV ozone treatment for 15 min. Subsequently, a 30 nm TiO_2 compact layer was deposited on FTO via spray pyrolysis at 450

°C from a precursor solution of titanium diisopropoxide bis-(acetylacetonate) in anhydrous ethanol. After being sprayed, the substrates were left at 450 °C for 45 min and left to cool to room temperature. Then, a mesoporous TiO_2 layer was deposited by spin-coating for 20 s at 4000 rpm with a ramp of 2000 rpm s^{-1} , using a 30 nm particle paste (Dyesol 30 NR-D) diluted in ethanol to achieve a 150–200 nm thick layer. After the spin-coating, the substrates were dried at 100 °C for 10 min and then sintered again at 450 °C for 30 min under dry air flow.

Li-doping of mesoporous TiO_2 , as described elsewhere,³¹ is accomplished by spin-coating a 0.1 M solution of Li-TFSI in acetonitrile at 3000 rpm for 10 s followed by another sintering step at 450 °C for 30 min. After being cooled to 150 °C, the substrates were immediately transferred in a nitrogen atmosphere glovebox to deposit the perovskite films.

Perovskite Precursor Solution and Film Preparation. The organic cations were purchased from Dyesol, the lead compounds from TCI, and CsI from abcr GmbH. The triple cation perovskite precursor solutions were prepared from a precursor solution containing FAI (1 M), PbI_2 (1.1 M), MABr (0.2 M), and $PbBr_2$ (0.2 M) in anhydrous DMF/DMSO 4:1 (v/v).^{51,52} Then CsI, which was predissolved in DMSO, was added to this perovskite precursor to achieve the 5 mol % triple cation composition. We note that this composition contains a lead excess as reported elsewhere.¹²

The perovskite solution was spin-coated in a two-step program at 1000 and 6000 rpm for 10 and 20 s, respectively. During the second step, 100 μL of chlorobenzene was poured on the spinning substrate 5 s prior to the end of the program. Films with Cs-containing perovskite turned dark immediately after spin-coating. The substrates were then annealed (at 100 °C) for 1 h in a nitrogen-filled glovebox.

Hole-Transporting Layer and Top Electrode. After the perovskite was annealed, the substrates were cooled for few minutes and a spiro-MeOTAD (Merck) solution (70 mM in chlorobenzene) was spin-coated at 4000 rpm for 20 s. Spiro-MeOTAD was doped with bis(trifluoromethylsulfonyl)imide lithium salt (Li-TFSI, Sigma-Aldrich), tris(2-(1H-pyrazol-1-yl)-4-tert-butylpyridine)cobalt(III) tris(bis(trifluoromethylsulfonyl)imide) (FK209, Dynamo), and 4-tert-butylpyridine (TBP, Sigma-Aldrich). The molar ratio of additive spiro-MeOTAD was 0.5, 0.03, and 3.3 for Li-TFSI, FK209, and TBP, respectively.

Finally, 70–80 nm of the Au top electrode was thermally evaporated under high vacuum. The active area of the device, as defined by the overlap of Au and FTO electrodes, was 0.26 cm^2 . The Cr interlayer between spiro-MeOTAD and Au was thermally evaporated. The vacuum was not broken between evaporation of Cr and Au.

J–V and Stability Measurements. The initial efficiency of the record devices was measured under AM 1.5G illumination provided by 450 W xenon lamp (Oriol) fitted with a Schott K113 Tempax filter (Präzisions Glas & Optik GmbH). The light intensity was calibrated with a Si photodiode equipped with an IR cutoff filter (KG3, Schott). All the other J–V curves were measured with a Biologic SP 300 potentiostat under a 1 sun equivalent white LED lamp. The light intensity of the LED lamp was adjusted so that the stabilized J_{sc} of the devices matched their stabilized J_{sc} measured under aforementioned calibrated xenon lamp setup. The devices were masked to 0.16 cm^2 , cooled to 20 °C, and flushed with nitrogen with an in-house developed sample holder. The stability measurements were performed by tracking the maximum power point of the devices illuminated with a white 1 sun equivalent LED lamp with a Biologic SP 300 potentiostat. The MPP was updated every 60 s by a standard perturb and observe method. The temperature of the devices was precisely controlled with a Peltier element in direct contact with the films, and the temperature was measured via a surface thermometer inserted between the Peltier element and the film. Before the beginning of each experiment, J–V curves of the devices were measured (at 10 mV s^{-1}). Additionally, J–V curves were taken every 15 min (at 100 mV s^{-1} ; only backward scan) during the aging in order to track the evolution of J–V metrics. Finally, several hours after the end of the experiment, the J–V characteristics

of the devices were remeasured (the devices being stored in the dark, at 20 °C, and under nitrogen flow between the measurements).

The experiment shown in Figure 4 with Au electrode removal was performed in the following way. Two devices (pixels) were fabricated on one substrate. J - V characteristics of both pixels were measured, and subsequently, the Au electrode was removed from one pixel. The devices were left in the dark under a nitrogen flow and at 75 °C overnight. Subsequently, the pixel aged with Au was remeasured, and then it had the electrode removed. Finally, the Au electrode was redeposited on both pixels (the process took approximately 1.5 h), and their J - V characteristics were remeasured immediately and then measured again after 7 h or recovery in the dark, under nitrogen flow and 20 °C.

ToF-SIMS Spectrometry. A dual-beam ToF-SIMS V (IONTOF) was used with Cs^+ primary ions (1 keV, 65 to 72 nA, $250 \times 250 \mu\text{m}^2$) for the erosion and a Bi^+ pulsed primary ion beam for the analysis (30 keV, 1.2 pA, $100 \times 100 \mu\text{m}^2$). The analysis area was centered inside the cesium raster area. The noninterlaced mode was used, with 2.5 s sputtering after each bismuth analysis cycle (128×128 pixels). The gold electrodes were connected to the sample holder with carbon tape for a better charge compensation using the electron flood gun. The analyzer reflectron voltage was adjusted 25 V over the cutoff voltage on the secondary ion image.

The depth profiles (Figures 3a and S7) were normalized to the SnO_2^- signal (from the FTO substrate). The SnO_2^- interface of the control devices was used as a reference for the fluence scale on each batch of samples. Indeed, the deposited layer thicknesses are similar, although small variations of the cesium sputtering current and of the interface positions are expected in the same batch of measurements. It is important to note that the relative fluence scale of the subsequent layers does not reflect their actual thickness. The apparent thickness of each layer depends on the erosion rate of the cesium primary ion beam in different materials.

Although ToF-SIMS is a sensitive analytical technique, the relative secondary ion intensities cannot be related to their relative concentration/amount because it depends on their ionization probability. For a given departing secondary ion, the ionization probability depends on factors such as the surrounding chemical element or the probability of neutralization when it escapes the surface.⁴⁹ Hence, a meaningful comparison can only be made for the same element within the same layers for different devices.

ToF-SIMS analysis was performed on devices based on $\text{FA}_{0.83}\text{MA}_{0.17}\text{Pb}(\text{I}_{0.83}\text{Br}_{0.17})_3$. However, the formulation of the later devices used for aging experiments contained a small addition of Cs. We found identical degradation patterns (Figure S10) for both types of devices, and hence, we concluded that the addition of a small amount of Cs to the perovskite blend does not affect the phenomena of metal-induced degradation of PSCs.

ICP Spectrometry. The Au electrodes of complete devices were removed from the samples with a piece of scotch tape. This step was repeated three times using a fresh piece of tape each time. Subsequently, the samples were cut into three pieces (the areas of the electrodes were cut off the central piece), and only the central region which contained the active area was taken for further processing. Next, the samples were immersed in a bath of chlorobenzene for 5 min in order to dissolve the spiro-MeOTAD layer with any remains of Au. Then, each sample was rinsed with chlorobenzene individually, dried, and, finally, placed in a vial containing 10 mL of 4:1 HCl (37%)/ HNO_3 (67%) aqua regia. The vials were subsequently sonicated for 1 min, and the samples were left overnight to dissolve. The ICP analysis was performed with Shimadzu ICPE-9000 on the aqua regia solution diluted in a 1:1 ratio with water. The detection limit for Au was ~ 1 ng in 20 mL of the solution. The active area of the device, as defined by the overlap of Au and FTO electrodes in the central part of the device, was 0.26 cm^2 .

SEM, XRD, and UV-Visible Absorption Spectrometry. A Zeiss Merlin HR-SEM was used to characterize the morphology of as-fabricated device cross sections. XRD and absorption measurements were performed on complete devices, just prior to evaporation of the Au contact. Following Au contact evaporation and subsequent aging,

the Au electrode was removed from the devices with a piece of scotch tape and XRD and absorption characterization were repeated. Hence, the aging, absorption, and XRD data shown here were obtained physically from the same devices. XRD analysis was performed using a Bruker D8 Advance X-ray diffractometer using $\text{Cu K}\alpha$ radiation ($\lambda = 0.154178 \text{ nm}$) at a scanning rate of 2° min^{-1} in the 2θ range from 11 to 40° and separately with a rate of $0.5^\circ \text{ min}^{-1}$ in the range from 12.5 to 15° . UV-visible absorption measurements were performed on a Varian Cary 5.

ASSOCIATED CONTENT

Supporting Information

The Supporting Information is available free of charge on the ACS Publications website at DOI: 10.1021/acsnano.6b02613.

Schematics of the aging program, sample preparation procedure for ICP MS, additional aging data, UV-vis and XRD spectra of fresh and aged devices, complete SIMS profiles of the aged and fresh devices (PDF)
Movie S1 (MPG)

AUTHOR INFORMATION

Corresponding Author

*E-mail: juan.correa@epfl.ch.

Notes

The authors declare no competing financial interest.

ACKNOWLEDGMENTS

Dr. Shaik M. Zakeeruddin is gratefully acknowledged for his help in handling and administration of funding. We thank S. Coudret for performing ICP MS analysis. Dr. L. Bernard is gratefully acknowledged for the first contact and discussions. We thank T. Matsui for providing devices for optimization studies. K.D. thanks the SNF for funding within the framework of Umbrella project (Grant Agreement Nos. 407040-153952 and 407040-153990). N.M. would like to thank the BNF program of the University of Bern and Prof. Dr. Hans J. Hug for his Empa affiliation. HR-SEM images were taken at the Centre for Electron Microscopy (CIME) at EPFL. A.A. has received funding from the European Union's Seventh Framework Programme for research, technological development, and demonstration under Grant Agreement No. 291771. M.S. acknowledges support from the cofunded Marie Skłodowska Curie fellowship, H2020 Grant Agreement No. 665667. M.G. thanks the SNSF-NanoTera (SYNERGY) and Swiss Federal Office of Energy (SYNERGY), CCEM-CH, in the ninth call proposal 906: CONNECT PV, the SNSF NRP70 "Energy Turnaround", and the King Abdulaziz City for Science and Technology (KACST) for financial support.

REFERENCES

- (1) NREL. Best Research-Cell Efficiencies http://www.nrel.gov/ncpv/images/efficiency_chart.jpg (accessed Mar 12, 2016).
- (2) Zhu, K.; Miyasaka, T.; Kim, J. Y.; Mora-Seró, I. Trend of Perovskite Solar Cells: Dig Deeper to Build Higher. *J. Phys. Chem. Lett.* **2015**, *6*, 2315–2317.
- (3) Leo, K. Perovskite Photovoltaics: Signs of Stability. *Nat. Nanotechnol.* **2015**, *10*, 574–575.
- (4) Tiep, N. H.; Ku, Z.; Fan, H. J. Recent Advances in Improving the Stability of Perovskite Solar Cells. *Adv. Energy Mater.* **2016**, *6*, 1501420.
- (5) Berhe, T. A.; Su, W.; Chen, C.-H.; Pan, C.-J.; Cheng, J.; Chen, H.-M.; Tsai, M.; Chen, L.-Y.; Dubale, A. A.; Hwang, B. J. Organometal Halide Perovskite Solar Cells: Degradation and Stability. *Energy Environ. Sci.* **2016**, *9*, 323–356.

- (6) Misra, R. K.; Aharon, S.; Li, B.; Mogilyansky, D.; Visoly-Fisher, I.; Etgar, L.; Katz, E. A. Temperature- and Component-Dependent Degradation of Perovskite Photovoltaic Materials under Concentrated Sunlight. *J. Phys. Chem. Lett.* **2015**, *6*, 326–330.
- (7) Yu, H.; Wang, F.; Xie, F.; Li, W.; Chen, J.; Zhao, N. The Role of Chlorine in the Formation Process of “CH₃NH₃PbI₃-xClx” Perovskite. *Adv. Funct. Mater.* **2014**, *24*, 7102–7108.
- (8) Zohar, A.; Kedem, N.; Levine, I.; Zohar, D.; Vilan, A.; Ehre, D.; Hodes, G.; Cahen, D. Impedance Spectroscopic Indication for Solid State Electrochemical Reaction in (CH₃NH₃)PbI₃ Films. *J. Phys. Chem. Lett.* **2016**, *7*, 191–197.
- (9) Noh, J. H.; Im, S. H.; Heo, J. H.; Mandal, T. N.; Seok, S. I. Chemical Management for Colorful, Efficient, and Stable Inorganic–Organic Hybrid Nanostructured Solar Cells. *Nano Lett.* **2013**, *13*, 1764–1769.
- (10) Beal, R. E.; Slotcavage, D. J.; Leijtens, T.; Bowering, A. R.; Belisle, R. A.; Nguyen, W. H.; Burkhard, G. F.; Hoke, E. T.; McGehee, M. D. Cesium Lead Halide Perovskites with Improved Stability for Tandem Solar Cells. *J. Phys. Chem. Lett.* **2016**, *7*, 746–751.
- (11) Sutton, R. J.; Eperon, G. E.; Miranda, L.; Parrott, E. S.; Kamino, B. A.; Patel, J. B.; Hörantner, M. T.; Johnston, M. B.; Haghighirad, A. A.; Moore, D. T.; Snaith, H. J. Bandgap-Tunable Cesium Lead Halide Perovskites with High Thermal Stability for Efficient Solar Cells. *Adv. Energy Mater.* **2016**, *6*, 1502458.
- (12) Saliba, M.; Matsui, T.; Seo, J.-Y.; Domanski, K.; Correa-Baena, J.-P.; Mohammad, K. N.; Zakeeruddin, S. M.; Tress, W.; Abate, A.; Hagfeldt, A.; Grätzel, M. Cesium-Containing Triple Cation Perovskite Solar Cells: Improved Stability, Reproducibility and High Efficiency. *Energy Environ. Sci.* **2016**, DOI: 10.1039/C5EE03874J.
- (13) Niu, G.; Li, W.; Meng, F.; Wang, L.; Dong, H.; Qiu, Y. Study on the Stability of CH₃NH₃PbI₃ Films and the Effect of Post-Modification by Aluminum Oxide in All-Solid-State Hybrid Solar Cells. *J. Mater. Chem. A* **2014**, *2*, 705–710.
- (14) Wei, D.; Wang, T.; Ji, J.; Li, M.; Cui, P.; Li, Y.; Li, G.; Mbengue, J. M.; Song, D. Photo-Induced Degradation of Lead Halide Perovskite Solar Cells Caused by the Hole Transport Layer/metal Electrode Interface. *J. Mater. Chem. A* **2016**, *4*, 1991–1998.
- (15) Leijtens, T.; Eperon, G. E.; Noel, N. K.; Habisreutinger, S. N.; Petrozza, A.; Snaith, H. J. Stability of Metal Halide Perovskite Solar Cells. *Adv. Energy Mater.* **2015**, *5*, 1500963.
- (16) Niu, G.; Guo, X.; Wang, L. Review of Recent Progress in Chemical Stability of Perovskite Solar Cells. *J. Mater. Chem. A* **2015**, *3*, 8970–8980.
- (17) Li, X.; Dar, M. I.; Yi, C.; Luo, J.; Tschumi, M.; Zakeeruddin, S. M.; Nazeeruddin, M. K.; Han, H.; Grätzel, M. Improved Performance and Stability of Perovskite Solar Cells by Crystal Crosslinking with Alkylphosphonic Acid Omega-Ammonium Chlorides. *Nat. Chem.* **2015**, *7*, 703–711.
- (18) Abate, A.; Paek, S.; Giordano, F.; Correa-Baena, J.-P.; Saliba, M.; Gao, P.; Matsui, T.; Ko, J.; Zakeeruddin, S. M.; Dahmen, K. H. Silolothiophene-Linked Triphenylamines as Stable Hole Transporting Materials for High Efficiency Perovskite Solar Cells. *Energy Environ. Sci.* **2015**, *8*, 2946–2953.
- (19) Li, W.; Zhang, W.; Van Reenen, S.; Sutton, R. J.; Fan, J.; Haghighirad, A. A.; Johnston, M. B.; Wang, L.; Snaith, H. J. Enhanced UV-Light Stability of Planar Heterojunction Perovskite Solar Cells with Caesium Bromide Interface Modification. *Energy Environ. Sci.* **2016**, *9*, 490–498.
- (20) You, J.; Meng, L.; Song, T.-B.; Guo, T.-F.; Yang, Y.; Chang, W.-H.; Hong, Z.; Chen, H.; Zhou, H.; Chen, Q.; Liu, Y.; De Marco, N.; Yang, Y. Improved Air Stability of Perovskite Solar Cells via Solution-Processed Metal Oxide Transport Layers. *Nat. Nanotechnol.* **2016**, *11*, 75–81.
- (21) Zhang, F.; Yang, X.; Cheng, M.; Wang, W.; Sun, L. Boosting the Efficiency and the Stability of Low Cost Perovskite Solar Cells by Using CuPc Nanorods as Hole Transport Material and Carbon as Counter Electrode. *Nano Energy* **2016**, *20*, 108–116.
- (22) Zhang, H.; Cheng, J.; Lin, F.; He, H.; Mao, J.; Wong, K. S.; Jen, A. K. Y.; Choy, W. C. H. Pinhole-Free and Surface-Nanostructured NiOx Film by Room-Temperature Solution Process for High-Performance Flexible Perovskite Solar Cells with Good Stability and Reproducibility. *ACS Nano* **2016**, *10*, 1503–1511.
- (23) Kato, Y.; Ono, L. K.; Lee, M. V.; Wang, S.; Raga, S. R.; Qi, Y. Silver Iodide Formation in Methyl Ammonium Lead Iodide Perovskite Solar Cells with Silver Top Electrodes. *Adv. Mater. Interfaces* **2015**, *2*, 1500195.
- (24) Guarnera, S.; Abate, A.; Zhang, W.; Foster, J. M.; Richardson, G.; Petrozza, A.; Snaith, H. J. Improving the Long-Term Stability of Perovskite Solar Cells with a Porous Al₂O₃ Buffer-Layer. *J. Phys. Chem. Lett.* **2015**, *6*, 432–437.
- (25) Guerrero, A.; You, J.; Aranda, C.; Kang, Y. S.; Garcia-Belmonte, G.; Zhou, H.; Bisquert, J.; Yang, Y. Interfacial Degradation of Planar Lead Halide Perovskite Solar Cells. *ACS Nano* **2016**, *10*, 218–224.
- (26) Chen, W.; Wu, Y.; Yue, Y.; Liu, J.; Zhang, W.; Yang, X.; Chen, H.; Bi, E.; Ashrafali, I.; Grätzel, M.; Han, L. Efficient and Stable Large-Area Perovskite Solar Cells with Inorganic Charge Extraction Layers. *Science* **2015**, *350*, 944–948.
- (27) Back, H.; Kim, G.; Kim, J.; Kong, J.; Kim, T. K.; Kang, H.; Kim, H.; Lee, J.; Lee, S.; Lee, K. Achieving Long-Term Stable Perovskite Solar Cells via Ion Neutralization. *Energy Environ. Sci.* **2016**, *9*, 1258–1263.
- (28) Mei, A.; Li, X.; Liu, L.; Ku, Z.; Liu, T.; Rong, Y.; Xu, M.; Hu, M.; Chen, J.; Yang, Y. A Hole-Conductor-free, Fully Printable Mesoscopic Perovskite Solar Cell with High Stability. *Science* **2014**, *345*, 295–298.
- (29) Li, X.; Tschumi, M.; Han, H.; Babkair, S. S.; Alzubaydi, R. A.; Ansari, A. A.; Habib, S. S.; Nazeeruddin, M. K.; Zakeeruddin, S. M.; Grätzel, M. Outdoor Performance and Stability under Elevated Temperatures and Long-Term Light Soaking of Triple-Layer Mesoporous Perovskite Photovoltaics. *Energy Technol.* **2015**, *3*, 551–555.
- (30) Alonso García, M. C.; Balenzategui, J. Estimation of Photovoltaic Module Yearly Temperature and Performance Based on Nominal Operation Cell Temperature Calculations. *Renewable Energy* **2004**, *29*, 1997–2010.
- (31) Giordano, F.; Abate, A.; Correa Baena, J. P.; Saliba, M.; Matsui, T.; Im, S. H.; Zakeeruddin, S. M.; Nazeeruddin, M. K.; Hagfeldt, A.; Grätzel, M. Enhanced Electronic Properties in Mesoporous TiO₂ via Lithium Doping for High-Efficiency Perovskite Solar Cells. *Nat. Commun.* **2016**, *7*, 10379.
- (32) Leyden, M. R.; Lee, M. V.; Raga, S. R.; Qi, Y. Large Formamidinium Lead Trihalide Perovskite Solar Cells Using Chemical Vapor Deposition with High Reproducibility and Tunable Chlorine Concentrations. *J. Mater. Chem. A* **2015**, *3*, 16097–16103.
- (33) Matteocci, F.; Busby, Y.; Pireaux, J.-J.; Divitini, G.; Cacovich, S.; Ducati, C.; Di Carlo, A. Interface and Composition Analysis on Perovskite Solar Cells. *ACS Appl. Mater. Interfaces* **2015**, *7*, 26176–26183.
- (34) de Quilettes, D. W.; Vorpahl, S. M.; Stranks, S. D.; Nagaoka, H.; Eperon, G. E.; Ziffer, M. E.; Snaith, H. J.; Ginger, D. S. Impact of Microstructure on Local Carrier Lifetime in Perovskite Solar Cells. *Science* **2015**, *348*, 683–686.
- (35) McGee, C.W.; Wilson, R. G. *Secondary Ion Mass Spectrometry: A Practical Handbook for Depth Profiling and Bulk Impurity Analysis*; Wiley: New York, 1989.
- (36) Baginski, T. A. An Introduction to Gold Gettering in Silicon. *Gold Bull.* **1987**, *20*, 47–53.
- (37) Lang, D. V.; Grimmeiss, H. G.; Meijer, E.; Jaros, M. Complex Nature of Gold-Related Deep Levels in Silicon. *Phys. Rev. B: Condens. Matter Phys.* **1980**, *22*, 3917–3934.
- (38) Gösele, U.; Frank, W.; Seeger, A. Mechanism and Kinetics of the Diffusion of Gold in Silicon. *Appl. Phys.* **1980**, *23*, 361–368.
- (39) Rollert, F.; Stolwijk, N.; Mehrer, H. Solubility, Diffusion and Thermodynamic Properties of Silver in Silicon. *J. Phys. D: Appl. Phys.* **1987**, *20*, 1148.
- (40) Yoshida, M.; Saito, K. Dissociative Diffusion of Nickel in Silicon and Self-Diffusion of Silicon. *Jpn. J. Appl. Phys.* **1967**, *6*, 573.

- (41) Burschka, J.; Pellet, N.; Moon, S.-J.; Humphry-Baker, R.; Gao, P.; Nazeeruddin, M. K.; Grätzel, M. Sequential Deposition as a Route to High-Performance Perovskite-Sensitized Solar Cells. *Nature* **2013**, *499*, 316–319.
- (42) Bi, D.; Tress, W.; Dar, M. I.; Gao, P.; Luo, J.; Renevier, C.; Schenk, K.; Abate, A.; Giordano, F.; Baena, J.-P. C. Efficient Luminescent Solar Cells Based on Tailored Mixed-Cation Perovskites. *Sci. Adv.* **2016**, *2*, e1501170.
- (43) Jeon, N. J.; Noh, J. H.; Yang, W. S.; Kim, Y. C.; Ryu, S.; Seo, J.; Seok, S. I. Compositional Engineering of Perovskite Materials for High-Performance Solar Cells. *Nature* **2015**, *517*, 476–480.
- (44) Domanski, K.; Tress, W.; Moehl, T.; Saliba, M.; Nazeeruddin, M. K.; Grätzel, M. Working Principles of Perovskite Photodetectors: Analyzing the Interplay Between Photoconductivity and Voltage-Driven Energy-Level Alignment. *Adv. Funct. Mater.* **2015**, *25*, 6936–6947.
- (45) Chen, H.-W.; Sakai, N.; Jena, A. K.; Sanehira, Y.; Ikegami, M.; Ho, K.-C.; Miyasaka, T. A Switchable High Sensitivity Photodetecting and Photovoltaic Device with Perovskite Absorber. *J. Phys. Chem. Lett.* **2015**, *6*, 1773–1779.
- (46) Li, D.; Dong, G.; Li, W.; Wang, L. High Performance Organic-Inorganic Perovskite-Optocoupler Based on Low-Voltage and Fast Response Perovskite Compound Photodetector. *Sci. Rep.* **2015**, *5*, 7902.
- (47) Deschler, F.; Price, M.; Pathak, S.; Klüntberg, L. E.; Jarausch, D.-D.; Högler, R.; Hüttner, S.; Leijtens, T.; Stranks, S. D.; Snaith, H. J.; Atature, M.; Phillips, R. T.; Friend, R. H. High Photoluminescence Efficiency and Optically Pumped Lasing in Solution-Processed Mixed Halide Perovskite Semiconductors. *J. Phys. Chem. Lett.* **2014**, *5*, 1421–1426.
- (48) Jaramillo-Quintero, O. A.; Sanchez, R. S.; Rincon, M.; Mora-Sero, I. Bright Visible-Infrared Light Emitting Diodes Based on Hybrid Halide Perovskite with Spiro-OMeTAD as a Hole-Injecting Layer. *J. Phys. Chem. Lett.* **2015**, *6*, 1883–1890.
- (49) Wittmaack, K. Unravelling the Secrets of Cs Controlled Secondary Ion Formation: Evidence of the Dominance of Site Specific Surface Chemistry, Alloying and Ionic Bonding. *Surf. Sci. Rep.* **2013**, *68*, 108–230.
- (50) Bush, K. A.; Bailie, C. D.; Chen, Y.; Bowring, A. R.; Wang, W.; Ma, W.; Leijtens, T.; Moghadam, F.; McGehee, M. D. Thermal and Environmental Stability of Semi-Transparent Perovskite Solar Cells for Tandems Enabled by a Solution-Processed Nanoparticle Buffer Layer and Sputtered ITO Electrode. *Adv. Mater.* **2016**, 1505279.
- (51) Correa Baena, J. P.; Steier, L.; Tress, W.; Saliba, M.; Neutzner, S.; Matsui, T.; Giordano, F.; Jacobsson, T. J.; Srimath Kandada, A. R.; Zakeeruddin, S. M.; Petrozza, A.; Abate, A.; Nazeeruddin, M. K.; Grätzel, M.; Hagfeldt, A. Highly Efficient Planar Perovskite Solar Cells through Band Alignment Engineering. *Energy Environ. Sci.* **2015**, *8*, 2928–2934.
- (52) Correa-Baena, J.-P.; Anaya, M.; Lozano, G.; Tress, W.; Domanski, K.; Saliba, M.; Matsui, T.; Jacobsson, T. J.; Calvo, M. E.; Abate, A.; Grätzel, M.; Míguez, H.; Hagfeldt, A. Unbroken Perovskite: Interplay of Morphology, Electro-optical Properties, and Ionic Movement. *Adv. Mater.* **2016**, 1600624.

Supplementary Information

Not All That Glitters Is Gold: Metal Migration-Induced Degradation In Perovskite solar cells

Konrad Domanski¹, Juan-Pablo Correa-Baena^{2}, Nicolas Mine³, Mohammad Khaja Nazeeruddin⁴, Antonio Abate^{1,5}, Michael Saliba¹, Wolfgang Tress¹, Anders Hagfeldt², Michael Grätzel¹*

¹*Laboratory for Photonics and Interfaces, Institute of Chemical Sciences and Engineering, École Polytechnique Fédérale de Lausanne, CH-1015-Lausanne, Switzerland.*

²*Laboratory of Photomolecular Science, Institute of Chemical Sciences and Engineering, École Polytechnique Fédérale de Lausanne, CH-1015-Lausanne, Switzerland.*

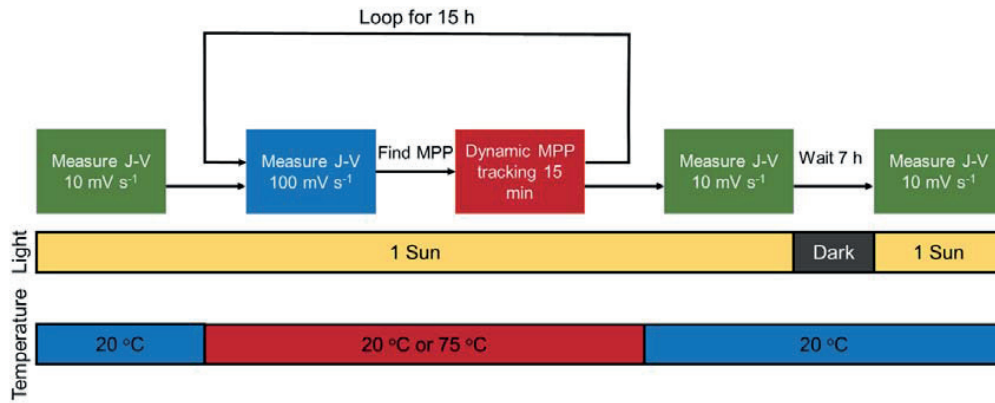
³*Laboratory for Nanoscale Materials Science, Swiss Federal Laboratories for Materials Science and Technology, CH-8600 Dübendorf, Switzerland.*

⁴*Group for Molecular Engineering of Functional Materials, Institute of Chemical Science and Engineering, École Polytechnique Fédérale de Lausanne, CH-1950 Sion, Switzerland.*

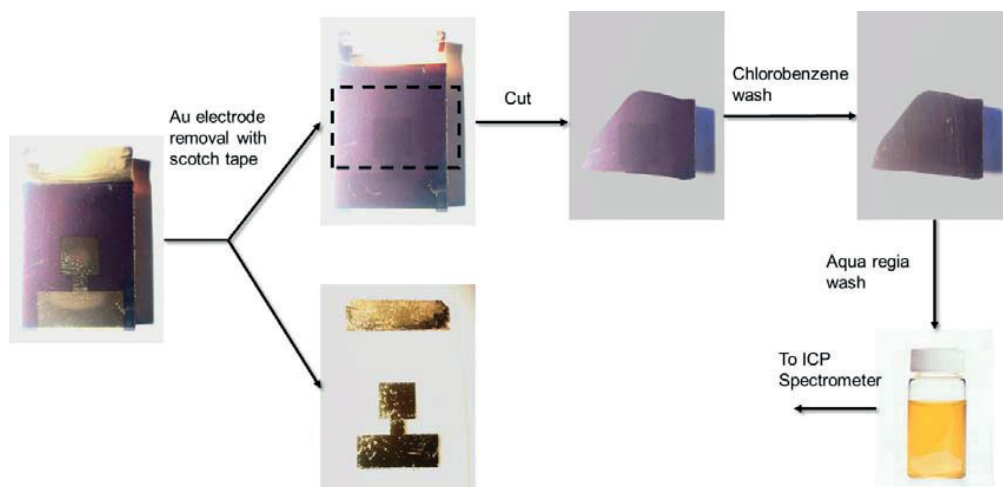
⁵*Adolphe Merkle Institute, University of Fribourg, CH-1700 Fribourg, Switzerland.*

**Corresponding author: JPCB, juan.correa@epfl.ch*

Keywords: Perovskite Solar Cells, Stability, Degradation, Secondary Ion Mass Spectrometry, Gold, Metal Electrodes, Buffer layers



Scheme S1 Schematics of the program used to age the devices.



Scheme S2 Sample preparation for ICP MS analysis.

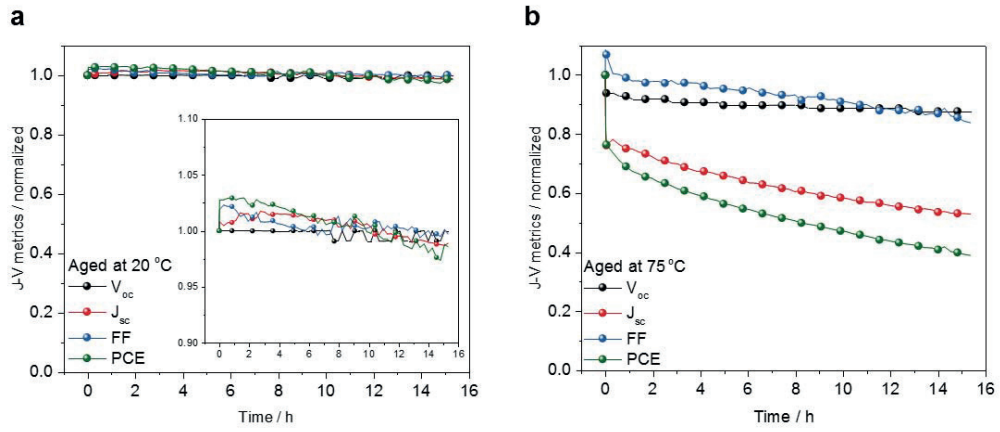


Figure S1 JV metrics evolution of devices aged at **a)** 20 °C and **b)** 75 °C. Note that the initial PCE of the device at 75 °C is considerably lower than its performance at 20 °C.

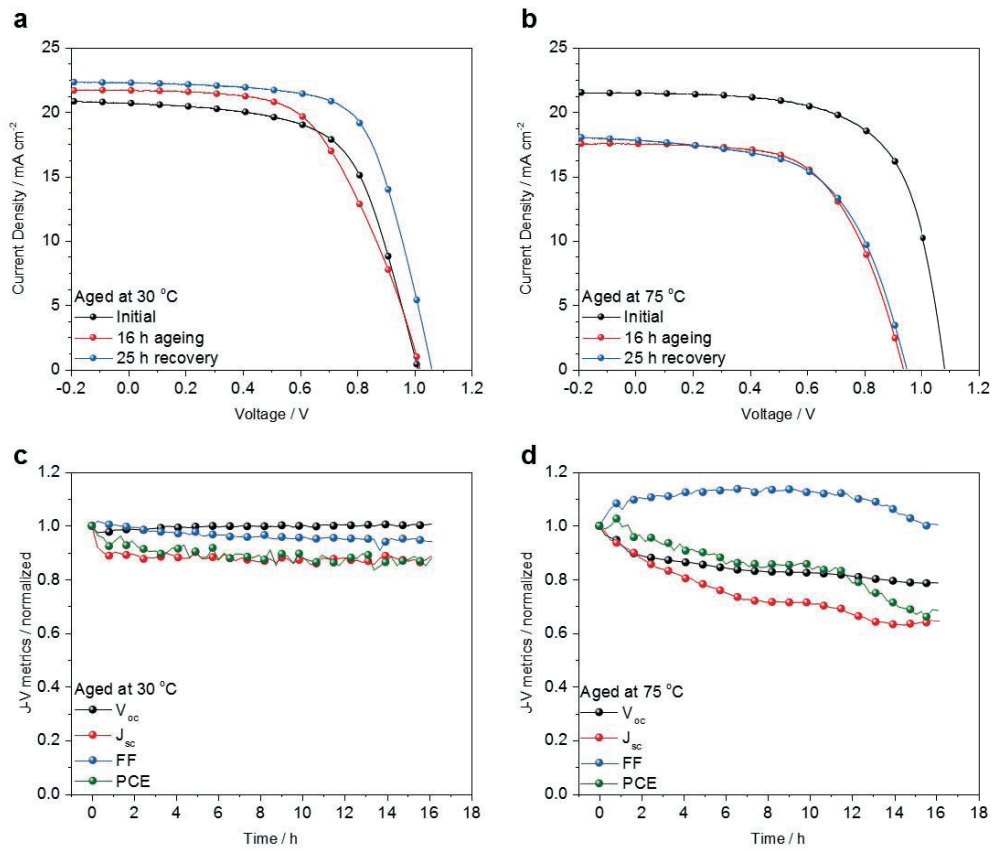


Figure S2 The repeat of the ageing experiment shown in **Figure 2. a** and **b** J-V characteristics of the devices aged at 30 °C and 75 °C respectively: before, at the end of the 16 h ageing experiment and after 25 h of recovery in the dark at 20 °C and under nitrogen flow. **c** and **d** the evolution of PCE, V_{oc} , J_{sc} and FF over the course of the ageing experiment for the respective devices. The values are normalized to the initial ones.

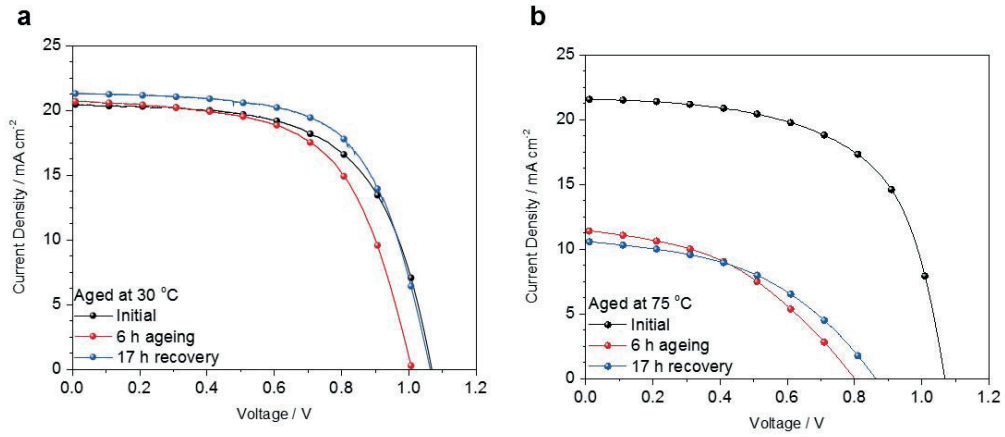


Figure S3 a and b J-V characteristics of the devices aged at 30°C and 75 °C respectively: initial, after 6 h of ageing and after 17 h of recovery in the dark. The devices were exposed to 1-Sun equivalent LED illumination while being left under nitrogen flow and open-circuit conditions. The J-V curves were measured at 20 °C with 10 mV s⁻¹ scan speed.

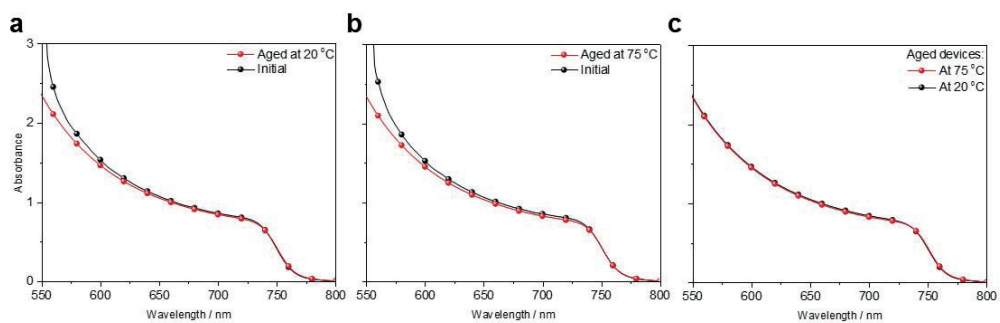


Figure S4 UV-vis absorption spectra of devices aged at **a** 20 °C and **b** 75 °C. **c** comparison of absorption spectra of the two aged devices.

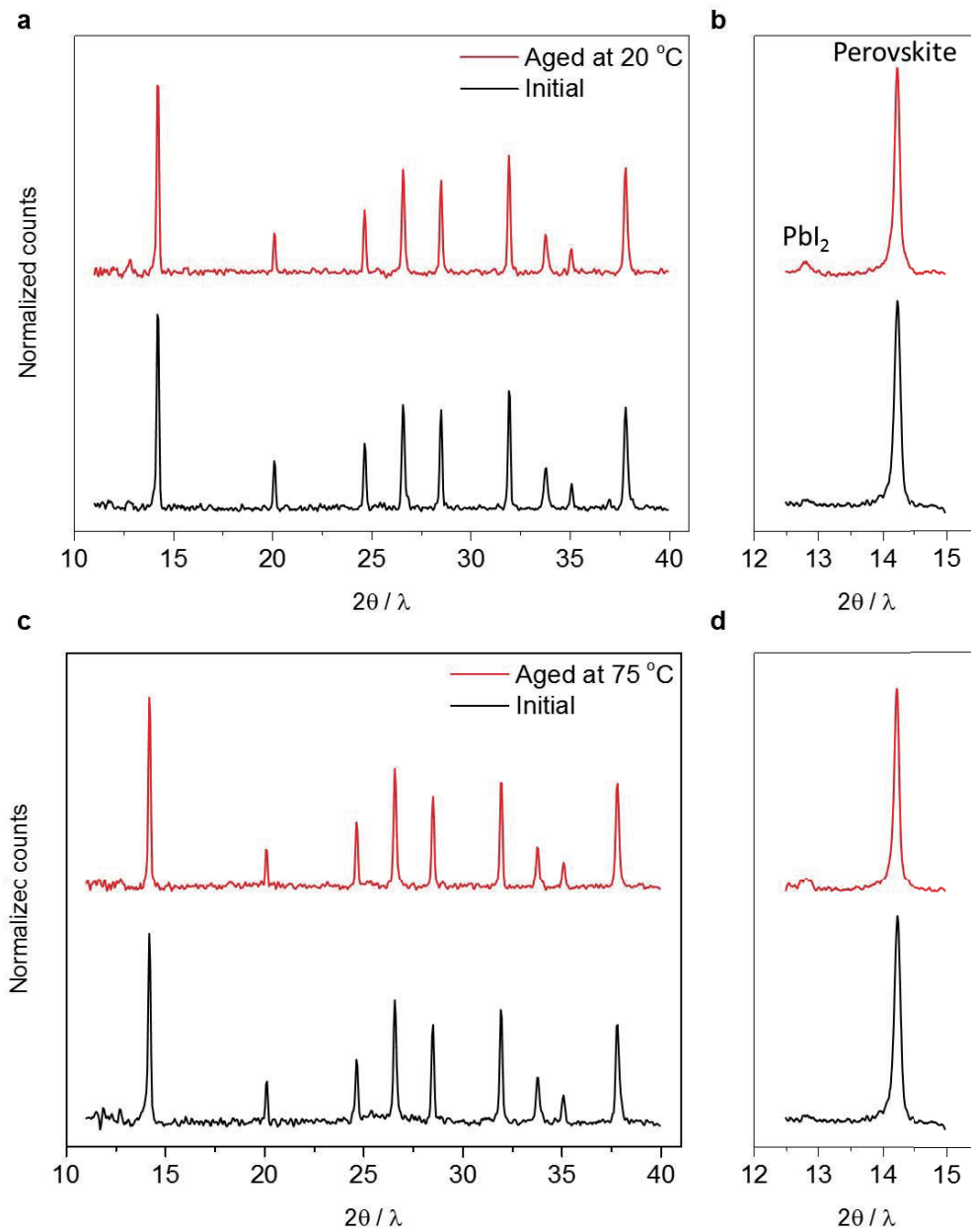


Figure S5 XRD spectra of devices aged at **a, b** 20 °C and **c, d** 75 °C. **b** and **d** show slower scans performed in the region where main PbI₂ and perovskite peaks are observed. An increase in the peak indicating the presence of PbI₂ was observed. However, since this effect is seen in both temperature experiments, it can be excluded that this small amount of PbI₂ is detrimental to device performance, given that the 20 °C sample did not degrade. Moreover, there exist multiple reports that a small amount of PbI₂ is actually beneficial for device performance.^{1,2}

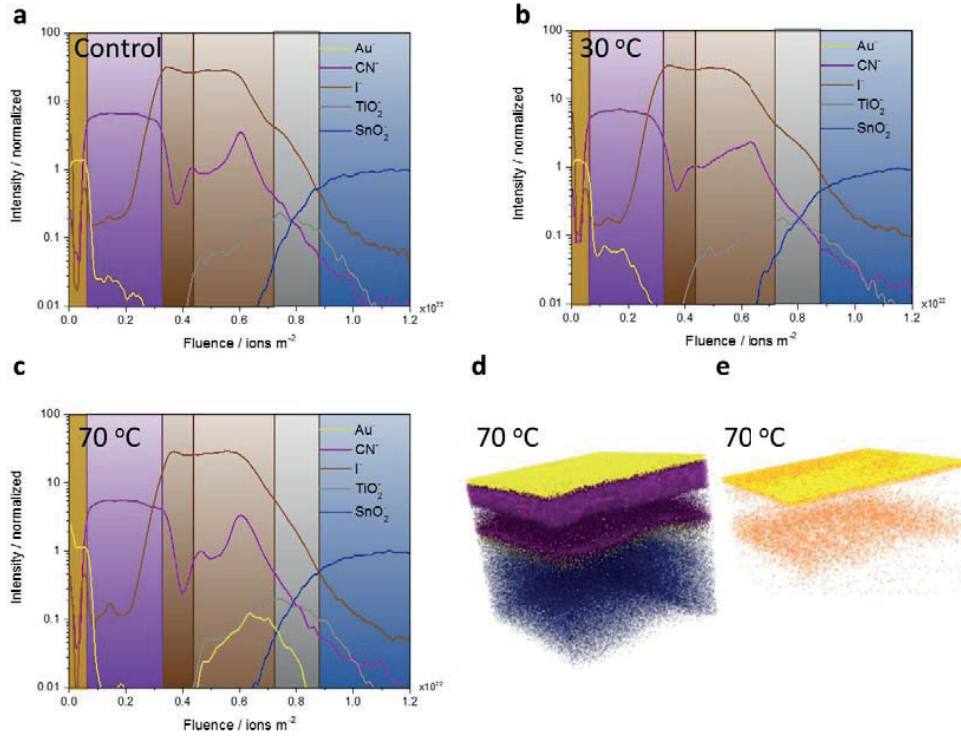


Figure S6 Full ToF-SIMS depth profile of devices shown in **Figure 3**. **a** the control device. **b** the device aged at 30°C **c** at 70 °C. **d** and **e** reconstructed elemental 3D maps of the device aged at 70 °C. The colour coding corresponds to that in the depth profiles.

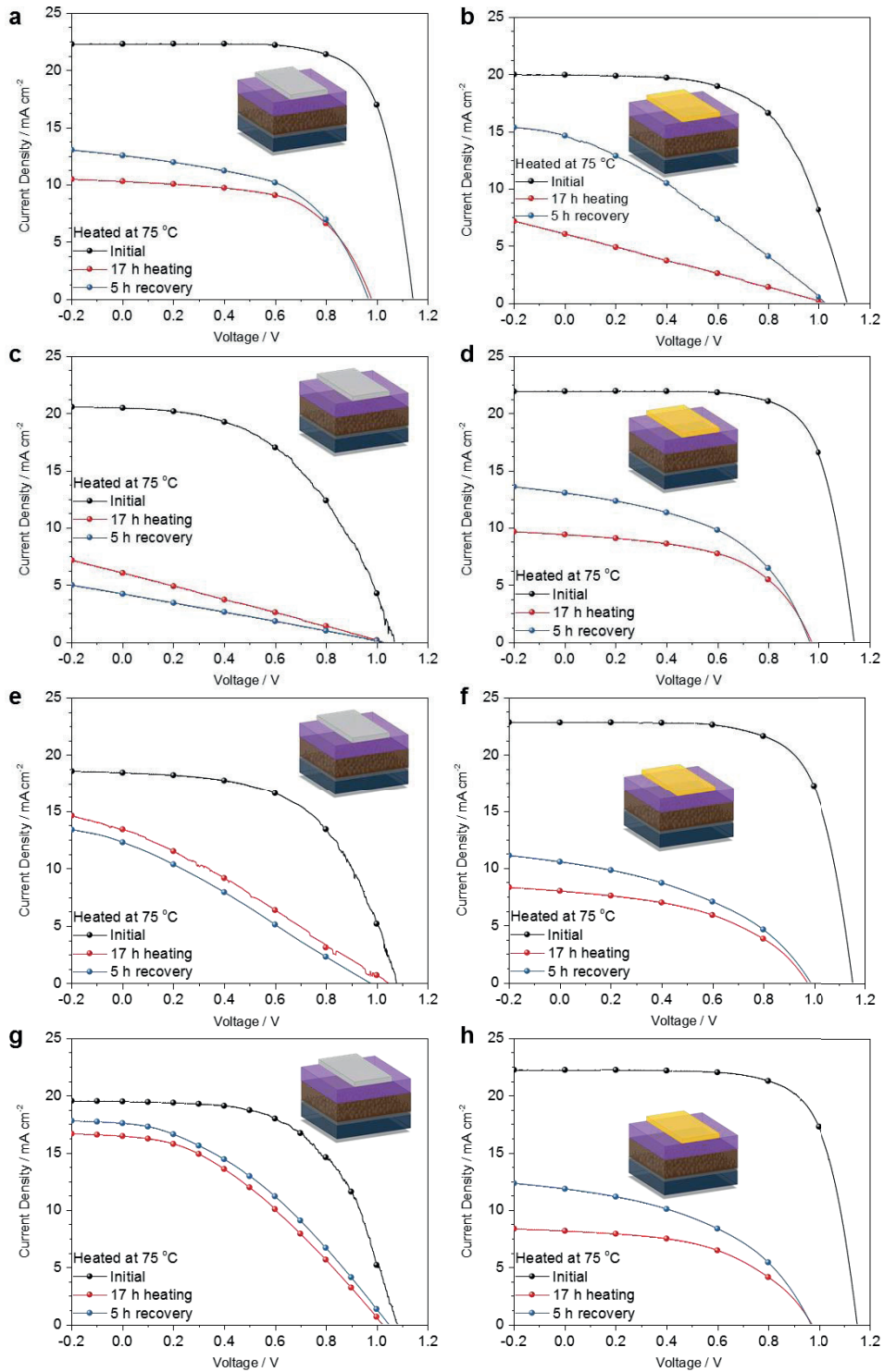


Figure S7 J-V curves of 8 identically prepared devices made within the same batch with **a, c, e, g** Ag or **b, d, f, h** Au electrodes heated in dark at 75 °C and N₂ atmosphere for 17 h. Devices were exposed to light only during J-V measurements. The J-V curves were measured at 20 °C with 10 mV s⁻¹ scan speed.

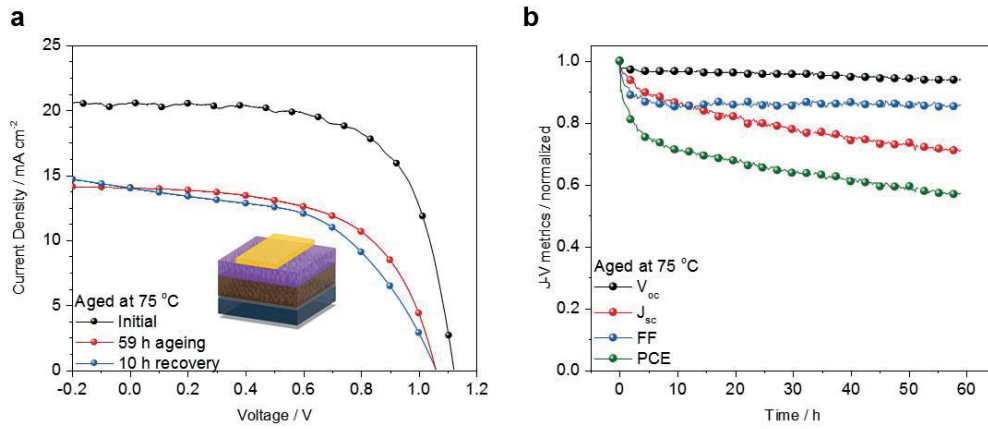


Figure S8 J-V characteristics of the device with $\text{Al}_2\text{O}_3/\text{Spiro-MeOTAD}$ HTL and Au electrode aged at 75 °C: before, at the end of the 59 h ageing experiment and after 10 h of recovery in the dark at 20 °C and under nitrogen flow. **d** the evolution of PCE, V_{oc} , J_{sc} and FF over the course of the ageing experiment for the Cr/Au device. The values are normalized to the initial ones. The recovery was in dark at 20 °C and nitrogen flow. J-V curves in **a** were recorded at 20 °C with 10 mV s^{-1} scan speed.

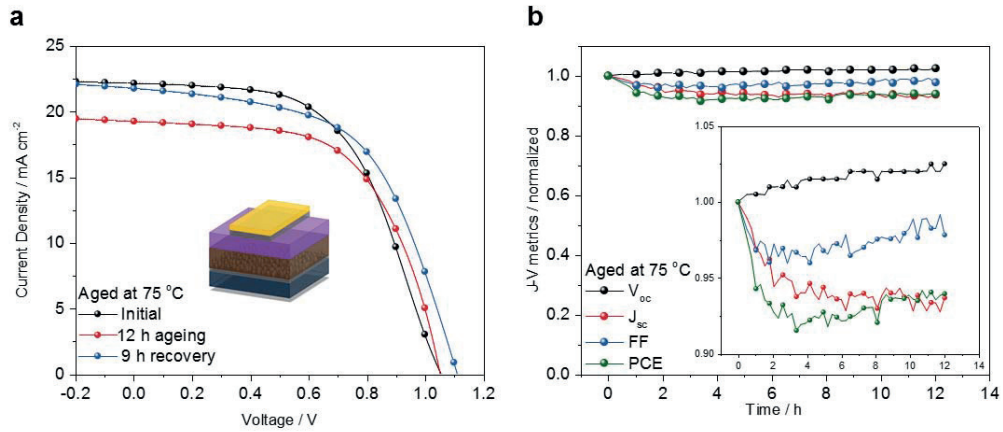


Figure S9 J-V characteristics of the device with Cr/Au electrode aged at 75 °C: before, at the end of the 12 h ageing experiment and after 9 h of recovery in the dark at 20 °C and under nitrogen flow. **d** the evolution of PCE, V_{oc} , J_{sc} and FF over the course of the ageing experiment for the Cr/Au device. The values are normalized to the initial ones. The recovery was in dark at 20 °C and nitrogen flow. J-V curves in **a** were recorded at 20 °C with 10 mV s^{-1} scan speed.

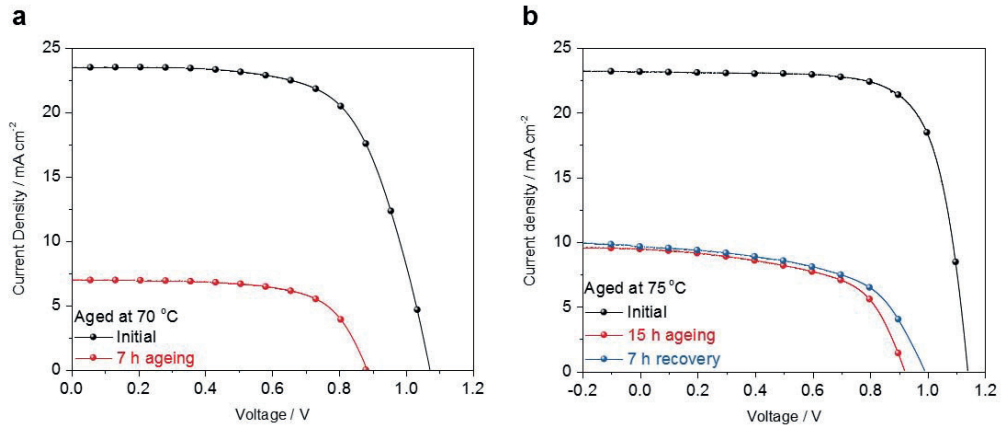


Figure S10 J-V characteristics of the devices aged at 70-75 °C: **a** $\text{FA}_{0.83}\text{MA}_{0.17}\text{Pb}(\text{I}_{0.83}\text{Br}_{0.17})_3$ -based device and **b** device based on $\text{FA}_{0.83}\text{MA}_{0.17}\text{Pb}(\text{I}_{0.83}\text{Br}_{0.17})_3$ with a small addition of CsI as outlined in the **Experimental** section at the beginning and at the end of an ageing test (MPP tracking) at elevated temperature and nitrogen atmosphere. J-V curves were recorded at 20 °C with 10 mV s⁻¹ scan speed.

Bibliography

1. Bi, D.; Tress, W.; Dar, M. I.; Gao, P.; Luo, J.; Renevier, C.; Schenk, K.; Abate, A.; Giordano, F.; Baena, J.-P. C. Efficient Luminescent Solar Cells Based on Tailored Mixed-Cation Perovskites. *Sci. Adv.* 2016, 2, e1501170.
2. Kim, Y. C.; Jeon, N. J.; Noh, J. H.; Yang, W. S.; Seo, J.; Yun, J. S.; Ho-Baillie, A.; Huang, S.; Green, M. A.; Seidel, J.; Ahn, T. K.; Seok, S. I., Beneficial Effects of PbI₂ Incorporated in Organo-Lead Halide Perovskite Solar Cells. *Adv. Energy Mater.* 2016, 6, 201502104.

Chapter 5 Incorporation of Rubidium Cations and PTAA Hole Transport Layer into Perovskite Solar Cells Improves High-Temperature Stability and Efficiency

THE CONTEXT

Using a thin layer of chromium between Au electrode and hole transporting layer in the previous work, I was able to stop Au diffusion – a trick commonly used in semiconductors industry. However, chromium does not have suitable energetics to act as an effective electrode material. Hence the high stability came at the expense of, at the time, record-breaking solar cell efficiency. Another strategy was needed to achieve high-temperature stability without sacrificing power conversion efficiency. I achieved this by replacing the state-of-the-art Spiro-MeOTAD hole transporting layer with a polymeric one – PTAA. This discovery was combined with a new perovskite composition developed in our laboratory, which further improved the efficiency.⁴²

This chapter is based on a peer-reviewed paper published in *Science* in October 2016 entitled:

Incorporation of Rubidium Cations into Perovskite Solar Cells Improves Photovoltaic Performance

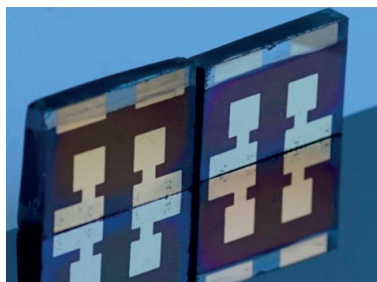
authored by:

Michael Saliba, Taisuke Matsui, **Konrad Domanski**, Ji-Youn Seo, Amita Ummadisingu, Shaik M Za-keeruddin, Juan-Pablo Correa-Baena, Wolfgang R Tress, Antonio Abate, Anders Hagfeldt and Michael Grätzel.

The version presented here is the accepted manuscript before the editorial changes.

My contribution:

Michael Saliba, Taisuke Matsui and I contributed to this work equally. In fact, this paper was realized by combining Taisuke Matsui and Michael Saliba's study on incorporation of Rb into perovskite solar cells and my separate study on blocking Au diffusion into perovskite with polymeric hole-transporting layers, which enabled high-temperature stability, while retaining record-breaking efficiency of the best-performing devices. Subsequently, I performed the stability studies, V_{oc} tracking measurements and contributed to electroluminescence measurements. I also participated in writing of the manuscript.





Incorporation of rubidium cations into perovskite solar cells improves photovoltaic performance

Michael Saliba^{1}, Taisuke Matsui^{1,2}, Konrad Domanski¹, Ji-Youn Seo¹, Amita Ummadisingu¹, Shaik M. Zakeeruddin¹, Juan-Pablo Correa-Baena³, Wolfgang R. Tress¹, Antonio Abate¹, Anders Hagfeldt³, and Michael Grätzel^{1*}*

Affiliations:

1 Laboratory of Photonics and Interfaces, École polytechnique fédérale de Lausanne, Station 6, CH-1015 Lausanne, Switzerland

2 Advanced Research Division, Materials Research Laboratory, Panasonic Corporation, 1006 Kadoma, Kadoma City, Osaka 571-8501, Japan

3 Laboratory of Photomolecular Science, École Polytechnique Fédérale de Lausanne, Station 6, CH-1015-Lausanne, Switzerland

*Correspondence to: MS michael.saliba@epfl.ch; MG michael.gratzel@epfl.ch

Abstract:

Inexpensive, highly efficient perovskite solar cells (PSCs) hold great promise towards a sustainable energy future. While the academic interest is very high, the industrial development is still hampered by poor stability in sunlight and at elevated temperatures. All currently used perovskites abide by the tolerance factor where components that seemingly do not fit into the perovskite structure are usually dismissed. Here, we introduce for the first time the small and oxidation-stable Rb⁺ into a “cation cascade” to create a new generation of perovskite materials with superior material properties. We achieved efficiencies of up to 21.6%, an electroluminescence of 4% and an outstanding open-circuit voltage of 1.24 V at a band gap of 1.63 eV entailing one of the smallest loss-in-potential of 0.39 V ever measured for any solar cell material. Furthermore, we report a breakthrough in stability at 85 °C for 500 h under full solar illumination and maximum power point tracking (during which 95% of the initial performance was retained). This provides the basis to realize 25% efficient and stable PSCs in the foreseeable future.

One Sentence Summary: The seemingly too small Rb⁺ cation was successfully integrated into perovskite solar cells resulting in remarkable electroluminescence, exceptional stability at 85 °C and astonishing open circuit voltages close to the thermodynamic limit paving the way toward an industrially deployable, new generation of perovskite photovoltaics.

Emerging low-cost perovskite solar cells (PSCs) have surged to power conversion efficiencies (PCEs) of a certified 22.1% (1) matching established photovoltaic technologies; thus holding great promise toward a sustainable energy future. The organic-inorganic perovskites used for photovoltaics (PV) have an AMX_3 formula that is comprised of a monovalent cation, A = (cesium Cs^+ ; methylammonium (MA) $CH_3NH_3^+$; formamidinium (FA) $CH_3(NH_2)_2^+$); a divalent metal M = (Pb^{2+} ; Sn^{2+}); and an anion X = (Br; I).

To date, most high efficiency perovskites are Pb-based with mixed MA/FA cations and Br/I halides (2-4). Recently, Cs was used to explore more complex cation combinations, i.e. Cs/MA, Cs/FA and Cs/MA/FA (5-9). These perovskites present more than the sum of their individual parts exhibiting unexpected properties. For example, Cs/FA mixtures suppress halide segregation enabling band gaps for perovskite/silicon tandems (10). The Cs/MA/FA based solar cells are more reproducible and thermally stable than MA/FA mixtures (9).

In general, increasing the perovskite complexity is motivated by an improved stability due to the addition of more inorganic elements and maximising entropy which can stabilize ordinarily unstable materials (like the “yellow”, non-photoactive phase of $FAPbI_3$ that can be avoided using small amounts of the otherwise unstable $CsPbI_3$) (6, 7). However, the field has now identified all single, double and triple combinations given by Cs, MA and FA. These cations were selected with the certainty that each of them forms a photoactive perovskite “black” phase dating as far back as 1893, 1978 and 1997, respectively (11-13). In order to progress further, we need a strategy to extend the circle of available cations beyond the examples that have been used for decades and centuries. Why is there such a dearth of cations?

Empirically, most monovalent cations are mismatched to sustain a photoactive $APbI_3$ perovskite with an appropriate Goldschmidt tolerance factor ($t = \frac{r_A + r_I}{\sqrt{2}(r_{Pb} + r_I)}$; r are the respective ionic radii) between 0.8 and 1.0 (14) rendering almost all elemental cations too small for consideration. We illustrate this point in **Fig. 1A** where we conduct tolerance factor calculations for the alkali metals (Li, Na, K, Rb, Cs); and MA, FA.

We selected specifically the alkali metals due to their unique position in the periodic system, with only one valence electron, providing oxidation-stable monovalent cations. This is a clear advantage over oxidation-prone Pb/Sn mixtures that have distorted material electronic properties (15).

The tolerance factor shows that only $CsPbI_3$ (as well as $MAPbI_3$ and $FAPbI_3$) fall into the range of “established perovskites” with a black phase. However, while Li, Na and K are clearly outside of the range, $RbPbI_3$ only misses by a small margin. The ionic radius of Cs and Rb is 1.67 Å and 1.52 Å, respectively. This small difference has a big impact with $RbPbI_3$ and $CsPbI_3$ drawing the demarcation line between photoactive black perovskite and photoinactive yellow non-perovskite phases. In **Fig. 1B**, we demonstrate this by heating $CsPbI_3$ and $RbPbI_3$ films at different temperatures. Both films are yellow at 28 °C. Upon heating to 380 °C, only $CsPbI_3$ turns black whereas $RbPbI_3$ remains yellow. Finally, at 460 °C both films start melting irreversibly without $RbPbI_3$ ever showing a black phase which is consistent with the observations by Trots and co-workers (16). Thus, only $CsPbI_3$ has a black phase explaining why Rb, despite its desirable oxidation stability, has so far not been used for PSCs.

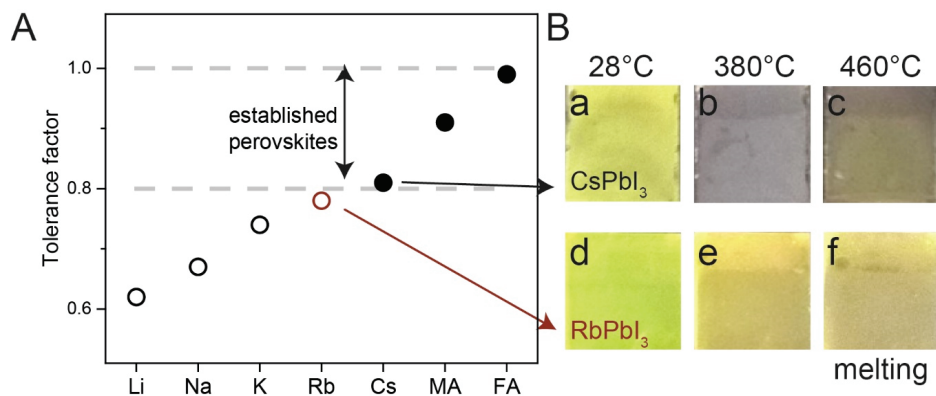


Fig. 1. Tolerance factor and perovskites at different temperatures.

(A) Tolerance factor calculation of APbI_3 perovskite with the oxidation stable $\text{A} = \text{Li, Na, K, Rb, Cs;}$ and MA, FA . Empirically, perovskites with a tolerance factor between 0.8 and 1.0 (dashed lines) show a photoactive black phase (solid circles) as opposed to non-photoactive phases (open circles). Rb (red open circle) is very close to this limit making it a candidate for integration into the perovskite lattice. (B) (a-c) CsPbI_3 (d-f) RbPbI_3 at 28 °C (a, d), 380 °C (b, e), 460 °C (c, f). Irreversible melting for both compounds occurs at 460 °C. RbPbI_3 never shows a black phase.

In this work, we propose embedding the small Rb into a photoactive perovskite phase using multiple A-cation formulations. Rb is particularly suited for this as it is only slightly smaller than Cs. We retain FA as the majority cation because of the beneficial, red-shifted band gap. We identify 4 hitherto unexplored combinations: 1 double (RbFA); 2 triple (RbCsFA , RbMAFA); and 1 quadruple (RbCsMAFA) cation doubling the 4 possible combinations given by Cs, MA and FA.

In Supplementary Note 1 (together with figs. S1 to S3), following the antisolvent approach pioneered by Jeon et al. (2, 9), we present device data on a glass/fluorine-doped tin oxide/compact TiO_2 /mesoporous TiO_2 /perovskite/spiro-OMeTAD/Au architecture (see fig. S4A for a cross sectional scanning electron microscopy (SEM) image along with an image of typical devices (fig. S4C)). All preparation details are given in the SI. For the rest of the manuscript, for convenience, we use the nomenclature of RbFA , RbCsFA , RbMAFA and RbCsMAFA to denote the entire perovskite compounds at the optimised values found in Supplementary Note 1 (usually achieved with an addition of 5-10% Rb).

Reasonable device performances were reached with RbFA (14%), RbCsFA (19.3%), RbMAFA (19.2%) comparable to CsFA (20%), CsMAFA (19.2%), as shown in figs. S1-3. We note that the CsFA result is the highest reported PCE to date on this compound showing that the devices presented here are advances over state-of-art results and thus any impact of Rb is extending the boundaries of the field. Importantly, the data reveals that the Rb can stabilize the black phase of FA perovskite providing the proof-of-concept that Rb can indeed be integrated into PSCs despite not being suitable as a pure RbPbI_3 compound. This is particularly evident for the triple cations using Rb. Surprisingly, as we go toward 4-cation mixtures (see fig. S3), we find that RbCsMAFA (with 5% of Rb) results in PCEs close to 21% with an open-circuit voltage (V_{oc}) of 1186 mV outperforming the CsMAFA triple cation controls (that are close to ~20%). Hence, in the

remainder of this discussion, we focus on RbCsMAFA in order to substantiate and explore the beneficial impact of our novel cation integration approach for PSCs.

As a first step, we investigate the starting condition of the crystallisation process for the RbCsMAFA compound upon annealing at 100 °C, which is needed to fully crystallize the perovskite films. In **Fig. 2A**, we present the UV-vis and PL data of the unannealed MAFA and RbCsMAFA films. The PL reveals that MAFA shows several photoluminescence (PL) peaks with maxima ranging from 670 – 790 nm, while the RbCsMAFA film has a narrow peak at 770 nm, which is attributable to perovskite. The insets are fluorescence microscopy maps of the surface of the unannealed films showing that the MAFA films are comprised of various emissive species forcing the pre-annealed film to crystallise with inhomogeneous starting conditions. This is in stark contrast to RbCsMAFA films, which are emissive in a narrow range and thus start crystallizing from more homogeneous conditions. Thus, the addition of the inorganic cations enforces a crystallisation that starts with a photoactive perovskite phase (close to the final emission after annealing) instead of a mixture of varying emissions that need to converge towards the final emission (see **Fig. 2C**). This is consistent with the high reproducibility and lack of yellow phase in the RbCsMAFA films. Furthermore, in **Fig. 2B**, we collect the corresponding XRD data of the unannealed films showing a pronounced perovskite peak for RbCsMAFA as compared to MAFA films. In **Fig. 2C** and **Fig. 2D**, we show analogous data after annealing including UV-vis, PL and XRD data revealing a RbCsMAFA band gap of ~1.63 eV (which is slightly blue shifted compared to MAFA at ~1.62 eV) containing neither a PbI₂ nor a yellow δ -phase peak. The low-angle perovskite peak for MAFA and RbCsMAFA occurs at 14.17° and 14.25°, respectively, revealing that Rb indeed modifies the crystal lattice. In addition, the top view SEM images indicate large crystals in the RbCsMAFA devices (see fig. S5), which has been shown to be beneficial for the PV metrics (17).

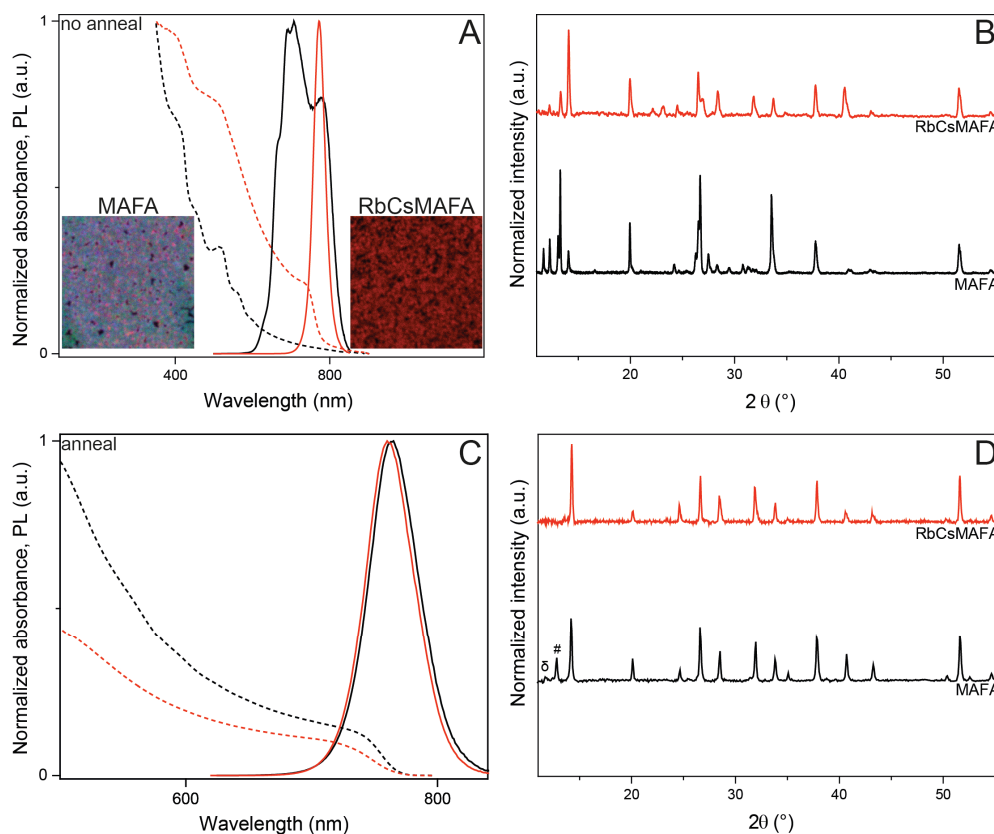


Fig. 2. Characterisation of unannealed and annealed films.

(A) UV-vis (dashed lines) and photoluminescence (solid lines) of unannealed MAFA (black) and RbCsMAFA (red) films.

The inset images show fluorescence microscopy measurements (image size $\sim 26 \times 26 \mu\text{m}^2$) of MAFA (left) and RbCsMAFA (right image) films. The image is an overlay of three emission ranges sampled from 640 – 650 nm, assigned as green; from 680 – 690 nm (blue); and 725 – 735 nm (red). The colors were chosen to ensure easily discernible features. (B) XRD data of the unannealed MAFA and RbCsMAFA films. (C) UV-vis (dashed) and photoluminescence (solid lines) of annealed (at 100 $^\circ\text{C}$ for 1 h) MAFA (black) and RbCsMAFA (red) films. (D) XRD data of the annealed MAFA and RbCsMAFA films. The PbI_2 and yellow phase peak is denoted as # and δ , respectively.

Hence, we proceed with collecting statistical data on RbCsMAFA devices (see fig. S6) which we find to exhibit superior performance compared to CsMAFA. Remarkably, the average open-circuit voltage (V_{oc}) is increased from 1120 to 1158 mV and the fill factor from 0.75 to 0.78. In **Fig. 3A**, we show the RbCsMAFA champion cell reaching a stabilized power output of 21.6% with a fill factor of 81% and 1180 mV open-circuit voltage. The measured J_{sc} matches the incident-photon-to-current-efficiency (IPCE) measurement in fig. S7. We also achieve a stabilized PCE of 19.0% on a large-area 0.5 cm² device (see fig. S8).

To correctly determine the V_{oc} , we investigate RbCsMAFA devices with the active area being fully illuminated, held at room temperature and under an inert nitrogen atmosphere. This permits for an accurate V_{oc} value without heating or degradation effects (from moisture for example). In **Fig. 3B**, for one of our highest performing devices, we measure an outstanding V_{oc} of 1240 mV confirmed by the inset that is tracking the V_{oc} over time. The “loss-in-potential” (difference between V_{oc} and band gap) is only ~ 0.39 V, which is one of the lowest recorded for any PV material, implying very small non-radiation recombination losses (18). The high V_{oc} is particularly intriguing because this is the major parameter left preventing PSCs from reaching their thermodynamic limit (since the J_{sc} and FF are already approaching their maximal values). Theoretically, in very pure, defect-free materials with only radiative recombination, the loss-in-potential can be as small as 0.23 (band gap of 1 eV) to 0.3 V (band gap of 2 eV). In particular silicon, the main industrial PV material, cannot approach this limit because of its indirect band gap and Auger recombination exhibiting a loss-in-potential of ~ 0.4 V for the most efficient devices (18).

The non-radiative recombination losses can be quantified measuring the external electroluminescence quantum efficiency (EQE_{EL}), which is larger than 1 % at a driving current that is equal to the short circuit current (see **Fig. 3C**). Following the approach in (19-21) (see for a more detailed discussion in Supplementary Note 2 together with fig. S9), we can use the EQE_{EL} and the emission spectrum to predict a V_{oc} of 1240 mV confirming independently the value measured from the JV curve.

Furthermore, for higher driving currents, the EQE_{EL} in **Fig. 3C** approaches 4%, making the solar cell one of the most efficient perovskite LEDs as well, emitting in the near IR/red spectral range (see inset image). We also present a video in the SI showing a RbCsMAFA device mounted in our custom-made device holder. As we tune towards maximum emission and back, we observe bright electroluminescence in ambient light. This is particularly remarkable as efficient LEDs commonly require specific architectures including thin active layers, which are not suited for efficient light harvesting in solar cells (22). Our EQE_{EL} is larger than for any (commercially) available solar cell (e.g. for Si EQE_{EL} $\approx 0.5\%$) (18). This indicates that all major sources of non-radiative recombination are strongly suppressed and the material has very low bulk and surface defect density. These results are consistent with the improved crystallinity discussed in **Fig. 2**.

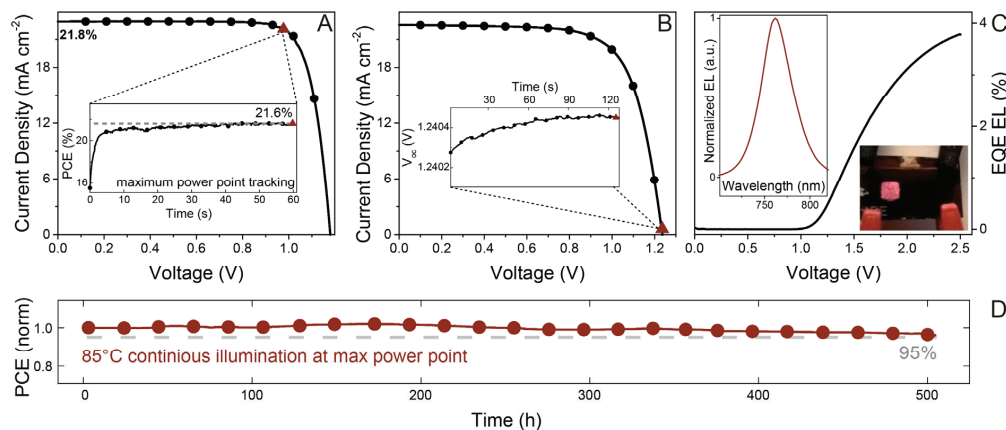


Fig. 3. Champion efficiency, open-circuit voltage, electroluminescence and high temperature stability.

(A) Current-density/voltage (JV) curve, taken at 10 mV s^{-1} scan rate, of the best performing solar cell at 21.8% efficiency ($V_{oc} = 1180 \text{ mV}$, $J_{sc} = 22.8 \text{ mA cm}^{-2}$, and a fill factor of 81%). The inset shows the scan rate independent maximum power point (MPP) tracking for 60 s resulting in a stabilized efficiency of 21.6% at 977 mV and 22.1 mA cm^{-2} (displayed as the red triangles in the JV and MPP scan, respectively).

(B) JV curve of the highest open-circuit voltage device. The inset shows the V_{oc} over 120 s resulting in 1240 mV (displayed as the red triangles in the JV and V_{oc} scan, respectively).

(C) EQE electroluminescence (EL) as a function of voltage. The left inset shows the corresponding EL spectrum over wavelength. The image in the inset is a solar cell with 2 active areas. The left area is operated as an LED displaying a clearly visible red emission even under ambient light. At the same time, the right area can be operated as a solar cell or a photodetector underlining the versatility of the perovskite material.

(D) Thermal stability test of a perovskite solar cell. The device is aged for 500 hours at $85 \text{ }^\circ\text{C}$ under continuous full sun illumination and maximum power point tracking in a nitrogen atmosphere (red curve, circles). This aging routine exceeds industry norms. During the $85 \text{ }^\circ\text{C}$ step, the device retains 95% (dashed line) of its initial performance.

With efficiencies close to 22% and an outstanding EL, this perovskite material has the potential to be highly attractive for large scale industrial deployment. It already outcompetes most PV materials and could very plausibly go above 25% if all the best performing parameters were achieved in one device.

However, to make a real impact, the next mandatory breakthrough must be in the area of long-term stability. Simply put, after having reached record efficiencies, V_{oc} 's and electroluminescence, we must aspire to reach high stability.

This is not a trivial task as from the very beginning, the hygroscopic nature of perovskite films, phase instabilities and light sensitivity have raised major concerns (23). This is especially disconcerting because industrial norms mandate prolonged testing at a) full sun illumination, maximum power point tracking at $60 \text{ }^\circ\text{C}$ and b) at $85 \text{ }^\circ\text{C}$ in the dark, among others.

Interestingly, as we have realized recently the, Achilles' heel of PSCs is not necessarily the perovskite itself but rather the commonly used spiro-OMeTAD hole transporter material (HTM)

that becomes permeable (at elevated temperature) to metal electrode diffusion into the perovskite causing irreversible degradation (24, 25). This effect can be mitigated using buffer layers or by avoiding the usage of metal electrodes (24-26). Alternatively, for the heating tests in this work, we find a thin layer of PTAA (see SEM image in fig. S4B) to work equally well for high temperature stability testing (27).

We impose the above protocols simultaneously aging devices for 500 hours at 85 °C under continuous illumination with full solar intensity and maximum power point tracking in a nitrogen atmosphere. This compounded stress test exceeds industrial standards (28). We show the result in **Fig. 3D** (red curve, circles). The device started with > 17% efficiency at room temperature before the aging protocol was applied. During the 85 °C step (in which the V_{oc} is inevitably lowered), the device retains 95% of its initial performance. To our knowledge, this is one of the industrially most relevant reports on PSC stability to date providing concrete evidence that the Rb compositions reported here are not only highly efficient but also compatible with the much “softer” industrial aging protocols.

Our findings make a convincing case that the integration of the small, oxidation-stable Rb via the multiple cation approach results in a new generation of perovskites with one of the smallest ever measured loss-in-potentials of 0.39 V and a record electroluminescence. The new material is stable under elevated temperature even exceeding standards imposed by industry. Hence, this approach could enable a new generation of highly efficient (beyond 25%), highly emissive perovskites for photovoltaics and photoemission applications (lasers and light emitting devices (LEDs)).

Acknowledgments:

M.S., T.M. and K.D. contributed equally. M. S. conceived and designed the overall project. J.-Y. S., A.U., J.-P. C.-B. conducted SEM, PL and XRD experiments on the perovskite films. A.U. conducted confocal laser scanning fluorescence microscopy for PL mapping. M.S., K. D. and W. T. conducted long-term aging tests on the devices. M. S., T. M., J.-P. C.-B. and A. A. prepared and characterised PV devices. M.G. directed and supervised the research. M. S. wrote the first draft of the paper. All authors contributed to the discussion and writing of the paper.

M. S. acknowledges support from the co-funded Marie Skłodowska Curie fellowship, H2020 Grant agreement no. 665667. A. A. received funding from the European Union's Seventh Framework Programme for research, technological development and demonstration under grant agreement no. 291771. Financial support is acknowledged from the Swiss National Science Foundation (SNSF), funding from the framework of Umbrella project (Grant Agreement Nos. 407040-153952 and 407040-153990); the NRP 70 "Energy Turnaround"; the in the 9th call proposal 906: CONNECT PV as well as from SNF-NanoTera and Swiss Federal Office of Energy (SYNERGY). M. G. and S. M. Z. thank the King Abdulaziz City for Science and Technology (KACST) for financial support under a joint research project.

References and Notes

1. NREL chart, accessed 07/18/2016
2. N. J. Jeon *et al.*, Compositional engineering of perovskite materials for high-performance solar cells. *Nature* **517**, 476 (Jan 22, 2015).
3. M. Saliba *et al.*, A molecularly engineered hole-transporting material for efficient perovskite solar cells. *Nature Energy* **1**, 15017 (01/18/online, 2016).
4. X. Li *et al.*, A vacuum flash-assisted solution process for high-efficiency large-area perovskite solar cells. *Science*, (2016-06-09 00:00:00, 2016).
5. H. Choi *et al.*, Cesium-doped methylammonium lead iodide perovskite light absorber for hybrid solar cells. *Nano Energy* **7**, 80 (Jul, 2014).
6. J. W. Lee *et al.*, Formamidinium and Cesium Hybridization for Photo- and Moisture-Stable Perovskite Solar Cell. *Adv Energy Mater* **5**, (Oct 21, 2015).
7. C. Yi *et al.*, Entropic stabilization of mixed A-cation ABX₃metal halide perovskites for high performance perovskite solar cells. *Energy Environ. Sci.* **9**, 656 (2016).
8. Z. Li *et al.*, Stabilizing Perovskite Structures by Tuning Tolerance Factor: Formation of Formamidinium and Cesium Lead Iodide Solid-State Alloys. *Chemistry of Materials* **28**, 284 (2015/12/18, 2016).
9. M. Saliba *et al.*, Cesium-containing triple cation perovskite solar cells: improved stability, reproducibility and high efficiency. *Energy & Environmental Science* **9**, 1989 (2016).
10. D. P. McMeekin *et al.*, A mixed-cation lead mixed-halide perovskite absorber for tandem solar cells. *Science* **351**, 151 (Jan 8, 2016).
11. H. L. Wells, Über die Cäsium- und Kalium-Bleihalogenide. *Zeitschrift für anorganische Chemie* **3**, 195 (1893).
12. D. Weber, $\text{CH}_3\text{NH}_3\text{PbX}_3$, a Pb(Ii)-System with Cubic Perovskite Structure. *Zeitschrift Fur Naturforschung Section B-a Journal of Chemical Sciences* **33**, 1443 (1978).
13. D. B. Mitzi, K. Liang, Synthesis, resistivity, and thermal properties of the cubic perovskite $\text{NH}_2\text{CH} = \text{NH}_2\text{SnI}_3$ and related systems. *Journal of Solid State Chemistry* **134**, 376 (Dec, 1997).
14. G. Kieslich, S. J. Sun, A. K. Cheetham, Solid-state principles applied to organic-inorganic perovskites: new tricks for an old dog. *Chemical Science* **5**, 4712 (2014).
15. F. Hao, C. C. Stoumpos, D. H. Cao, R. P. H. Chang, M. G. Kanatzidis, Lead-free solid-state organic-inorganic halide perovskite solar cells. *Nature Photonics* **8**, 489 (Jun, 2014).
16. D. M. Trots, S. V. Myagkota, High-temperature structural evolution of caesium and rubidium triiodoplumbates. *Journal of Physics and Chemistry of Solids* **69**, 2520 (Oct, 2008).
17. J.-P. Correa-Baena *et al.*, Unbroken Perovskite: Interplay of Morphology, Electro-optical Properties, and Ionic Movement. *Advanced Materials* **28**, 5031 (2016).
18. M. A. Green, Radiative efficiency of state-of-the-art photovoltaic cells. *Progress in Photovoltaics* **20**, 472 (Jun, 2012).
19. U. Rau, Reciprocity relation between photovoltaic quantum efficiency and electroluminescent emission of solar cells. *Physical Review B* **76**, (Aug, 2007).
20. R. T. Ross, Some Thermodynamics of Photochemical Systems. *Journal of Chemical Physics* **46**, 4590 (1967).
21. W. Tress *et al.*, Predicting the Open-Circuit Voltage of $\text{CH}_3\text{NH}_3\text{PbI}_3$ Perovskite Solar Cells Using Electroluminescence and Photovoltaic Quantum Efficiency Spectra: the Role of Radiative and Non-Radiative Recombination. *Adv Energy Mater* **5**, (Feb 4, 2015).
22. G. R. Li *et al.*, Highly Efficient Perovskite Nanocrystal Light-Emitting Diodes Enabled by a Universal Crosslinking Method. *Advanced Materials* **28**, 3528 (May 11, 2016).

23. N. H. Tiep, Z. L. Ku, H. J. Fan, Recent Advances in Improving the Stability of Perovskite Solar Cells. *Adv Energy Mater* **6**, (Feb 4, 2016).
24. K. Domanski *et al.*, Not All That Glitters Is Gold: Metal-Migration-Induced Degradation in Perovskite Solar Cells. *ACS Nano* **10**, 6306 (2016/06/28, 2016).
25. K. A. Bush *et al.*, Thermal and Environmental Stability of Semi-Transparent Perovskite Solar Cells for Tandems Enabled by a Solution-Processed Nanoparticle Buffer Layer and Sputtered ITO Electrode. *Advanced Materials*, n/a (2016).
26. A. Y. Mei *et al.*, A hole-conductor-free, fully printable mesoscopic perovskite solar cell with high stability. *Science* **345**, 295 (Jul 18, 2014).
27. J. H. Heo *et al.*, Efficient inorganic-organic hybrid heterojunction solar cells containing perovskite compound and polymeric hole conductors. *Nature Photonics* **7**, 487 (Jun, 2013).
28. Y. G. Rong, L. F. Liu, A. Y. Mei, X. Li, H. W. Han, Beyond Efficiency: the Challenge of Stability in Mesoscopic Perovskite Solar Cells. *Adv Energy Mater* **5**, (Oct 21, 2015).
29. R. D. Shannon, Revised Effective Ionic-Radii and Systematic Studies of Interatomic Distances in Halides and Chalcogenides. *Acta Crystallographica Section A* **32**, 751 (1976).
30. J. P. C. Baena *et al.*, Highly efficient planar perovskite solar cells through band alignment engineering. *Energy & Environmental Science* **8**, 2928 (2015).
31. W. Shockley, H. J. Queisser, Detailed Balance Limit of Efficiency of P-N Junction Solar Cells. *Journal of Applied Physics* **32**, 510 (1961).



www.sciencemag.org/cgi/content/full/science.aah5557/DC1

Supplementary Materials for

Incorporation of rubidium cations into perovskite solar cells improves photovoltaic performance

Michael Saliba,* Taisuke Matsui, Konrad Domanski, Ji-Youn Seo, Amita Ummadisingu, Shaik M. Zakeeruddin, Juan-Pablo Correa-Baena, Wolfgang R. Tress, Antonio Abate, Anders Hagfeldt, Michael Grätzel*

*Corresponding author. E-mail: michael.saliba@epfl.ch (M.S.); michael.gratzel@epfl.ch (M.G.)

Published 29 September 2016 on *Science* First Release
DOI: 10.1126/science.aah5557

This PDF file includes:

Materials and Methods

Supplementary Text

Figs. S1 to S16

Tables S1 and S2

Caption for movie S1

References

Other supplementary material for this manuscript includes the following:

Movie S1

Materials and Methods

Substrate preparation and Li-doping TiO₂

Nippon Sheet Glass 10 Ω /sq was cleaned by sonication in 2% Hellmanex water solution for 30 minutes. After rinsing with deionised water and ethanol, the substrates were further cleaned with UV ozone treatment for 15 min. Then, 30 nm TiO₂ compact layer was deposited on FTO via spray pyrolysis at 450°C from a precursor solution of titanium diisopropoxide bis(acetylacetonate) in anhydrous ethanol. After the spraying, the substrates were left at 450°C for 45 min and left to cool down to room temperature. Then, mesoporous TiO₂ layer was deposited by spin coating for 20 s at 4000 rpm with a ramp of 2000 rpm s⁻¹, using 30 nm particle paste (Dyesol 30 NR-D) diluted in ethanol to achieve 150-200 nm thick layer. After the spin coating, the substrates were immediately dried at 100°C for 10 min and then sintered again at 450°C for 30 min under dry air flow.

Li-doping of mesoporous TiO₂ was accomplished by spin coating a 0.1 M solution of Li-TFSI in acetonitrile at 3000 rpm for 30 s followed by another sintering step at 450°C for 30 minutes. After cooling down to 150°C the substrates were immediately transferred in a nitrogen atmosphere glove box for depositing the perovskite films.

Perovskite precursor solution

The organic cation iodide salts were purchased from Dyesol; the lead compounds from TCI and the CsI and RbI from abcr GmbH. The following formulations were composed by mixing appropriate amounts of FAI, MAI, CsI, RbI, PbI₂, MABr and PbBr₂.

Rb perovskite

RbPbI₃ was prepared from a precursor solution containing 1.2 M RbI and 1.3 M PbI₂ in anhydrous DMF:DMSO 4:1 (v:v).

Cs perovskite

CsPbI₃ was prepared from a precursor solution containing 1.2 M CsI and 1.3 M PbI₂ in anhydrous DMF:DMSO 4:1 (v:v).

MA/FA perovskite

The “mixed” perovskite precursor solutions were deposited from a precursor solution containing FAI (1 M), PbI₂ (1.1 M), MABr (0.2 M) and PbBr₂ (0.22 M) in anhydrous DMF:DMSO 4:1 (v:v).

Cs/FA perovskite

3 perovskite solutions were mixed; CsPbI₃ (containing 1.2 M CsI and 1.3 M PbI₂ in anhydrous DMF:DMSO 4:1 (v:v)); FAPbI₃ (containing 1.2 M FAI, 1.3 M PbI₂ in anhydrous DMF:DMSO 4:1 (v:v)); and FAPbBr₃ (containing 1.2 M FAI and 1.3 M FABr₂ in anhydrous DMF:DMSO 4:1 (v:v)). Then the 3 solutions are mixed to obtain the desired composition.

Rb/FA perovskite

3 perovskite solutions were mixed; RbPbI₃ (containing 1.2 M RbI and 1.3 M PbI₂ in anhydrous DMF:DMSO 4:1 (v:v)); FAPbI₃ (containing 1.2 M FAI, 1.3 M PbI₂ in anhydrous DMF:DMSO

4:1 (v:v)); and FAPbBr₃ (containing 1.2 M FAPbBr and 1.3 M PbBr₂ in anhydrous DMF:DMSO 4:1 (v:v)). Then the 3 solutions are mixed to obtain the desired composition.

Cs/MA/FA perovskite

Then CsI, predissolved as a 1.5 M stock solution in DMSO, was added to the mixed perovskite (MA/FA) precursor to achieve the desired triple cation composition.

Rb/MA/FA perovskite

This follows the same procedure as Cs/FA/MA except RbI was added instead of CsI. RbI was predissolved as a 1.5 M stock solution in DMF:DMSO 4:1 (v:v).

Rb/Cs/FA perovskite

4 perovskite solutions were mixed: CsPbI₃ (containing 1.2 M CsI and 1.3 M PbI₂ in anhydrous DMF:DMSO 4:1 (v:v)); RbPbI₃ (containing 1.2 M RbI and 1.3 M PbI₂ in anhydrous DMF:DMSO 4:1 (v:v)); FAPbI₃ (containing 1.2 M FAI, 1.3 M PbI₂ in anhydrous DMF:DMSO 4:1 (v:v)); and FAPbBr₃ (containing 1.2 M FAPbBr and 1.3 M PbBr₂ in anhydrous DMF:DMSO 4:1 (v:v)). Then the 4 solutions were mixed to obtain the desired composition.

Rb/Cs/MA/FA perovskite

RbI, predissolved as a 1.5 M stock solution in DMF:DMSO 4:1 (v:v), was added to the Cs/FA/MA triple cation perovskite to achieve the desired quadruple composition.

Perovskite deposition

The perovskite solution was spin coated in a two steps program at 1000 and 4000 rpm for 10 and 30 s respectively. During the second step, 200 μ L of chlorobenzene was poured on the spinning substrate 20 s prior to the end of the program. The substrates were then annealed (at 100 °C unless stated otherwise) for 1 h in a nitrogen filled glove box.

Hole transporting layers

After the perovskite annealing, the substrates were cooled down for few minutes and a *spiro-OMeTAD* (Merck) solution (70 mM in chlorobenzene) was spin coated at 4000 rpm for 20 s. Spiro-OMeTAD was doped with bis(trifluoromethylsulfonyl)imide lithium salt (Li-TFSI, Sigma-Aldrich), tris(2-(1H-pyrazol-1-yl)-4-tert-butylpyridine)-cobalt(III) tris(bis(trifluoromethylsulfonyl)imide) (FK209, Dynamo) and 4-tert-Butylpyridine (tBP, Sigma-Aldrich). The molar ratio of additives for spiro-OMeTAD was: 0.5, 0.03 and 3.3 for Li-TFSI, FK209 and tBP respectively.

PTAA. 1 ml of PTAA (EM-Index), dissolved in toluene at a concentration of 10 mg ml⁻¹, was mixed with 2.0 μ l of tBP and 1.6 μ l of 1.8M LiTFSI solution (dissolved in ACN). Then the solution was spin coated at 4000 rpm for 20 s

Finally, 70-80 nm of gold *top electrode* was thermally evaporated under high vacuum.

Photovoltaic device testing

The solar cells were measured using a 450 W xenon light source (Oriel). The spectral mismatch between AM1.5G and the simulated illumination was reduced by the use of a Schott K113 Tempax

filter (Präzisions Glas & Optik GmbH). The light intensity was calibrated with a Si photodiode equipped with an IR-cutoff filter (KG3, Schott), and it was recorded during each measurement. Current-voltage characteristics of the cells were obtained by applying an external voltage bias while measuring the current response with a digital source meter (Keithley 2400). The voltage scan rate was 10 mV s^{-1} and no device preconditioning, such as light soaking or extended forward voltage biasing in the dark, was applied before starting the measurement. The cells were masked with a black metal mask to fix the active area and avoid artifacts produced by scattered light. The devices for the statistical (champion) measurement was conducted without (with) antireflective coating and on a 0.16 cm^2 (0.1225 cm^2) mask. The large area device was measured on a 0.5 cm^2 mask. The incident light intensity was adjusted to 1000 W/m^2 in accordance with standard AM 1.5 reporting conditions.

Stability measurements

Stability measurements were performed with a Biologic MPG2 potentiostat under a full AM 1.5 Sun-equivalent white LED lamp. The devices were masked (0.16 cm^2) and flushed with nitrogen for several hours before the start of the experiment in order to remove residual oxygen and water from the environment of an in-house developed sample holder. Then, the devices were measured with a maximum power point (MPP) tracking routine under continuous illumination (and nitrogen). The MPP was updated every 10 s by a standard perturb and observe method. The temperature of the devices was controlled with a Peltier element in direct contact with the films. The temperature was measured with a surface thermometer located between the Peltier element and the film. Every 30 minutes a JV curve was recorded in order to track the evolution of individual JV parameters.

V_{oc} and electroluminescence

V_{oc} and electroluminescence measurements were performed using the above LED setup. The devices were left unmasked, at room temperature and under constant nitrogen flow in order to prevent degradation during operation.

Electroluminescence yield

Electroluminescence yield was measured by applying either constant current or by applying varying potential to the device and by recording the emitted photon flux with a calibrated, large area (1 cm^2) Si photodiode (Hamamatsu S1227-1010BQ) placed directly on top of the sample. The driving voltage or current were applied using a Bio-Logic SP300 potentiostat, which was also used to measure the short-circuit current of the detector at a second channel.

UV-vis

UV-vis measurements were performed on a Varian Cary 5.

Scanning electron microscopy

Scanning electron microscopy (SEM) was performed on a ZEISS Merlin HR-SEM. Secondary electron images were acquired with an EDX detector.

X-ray powder diffraction

X-ray powder diffractions (XRD) were recorded on an X'Pert MPD PRO (Panalytical) equipped with a ceramic tube (Cu anode, $\lambda = 1.54060 \text{ \AA}$), a secondary graphite (002) monochromator and a RTMS X'Celerator (Panalytical) in an angle range of $2\theta = 5^\circ$ to 60° .

Photoluminescence spectra

Photoluminescence spectra were obtained with Fluorolog 322 (Horiba Jobin Yvon Ltd) with the range of wavelength from 620 nm to 850 nm by exciting at 460 nm. The samples were mounted at 60° and the emission recorded at 90° from the incident beam path.

Confocal laser scanning fluorescence microscopy

Confocal laser scanning fluorescence microscopy (CLSM) images were captured using a confocal laser scanning microscope (Leica TCS SP8) with a HC PL APO oil objective (63x/1.40). We used a 440 nm pulsed diode laser (pulsed at 40 MHz) for excitation and a HyD detector for imaging. Fiji was used for image processing.

Quantum yield measurements

Quantum yield measurements were conducted as reported elsewhere (35) using a 102 mm diameter integration sphere (Horiba F-3018) and a Fluorolog 322 (Horiba Jobin Yvon Ltd. Spectrofluorometer). The perovskite films were deposited on non-quenching substrates.

Intensity modulated photocurrent spectroscopy

Intensity modulated photocurrent spectroscopy (IMPS) was conducted with an Autolab potentiostat (PGSTAT30) driven by NOVA software: Using a red LED, light intensity was modulated while short-circuit current variation was recorded.

Goldschmidt tolerance factor calculations

The Goldschmidt tolerance factor for an AMX_3 perovskite was calculated using $t = \frac{r_A + r_X}{\sqrt{2}(r_M + r_X)}$, with r_A , r_M and r_X being the ionic radii as taken from (14, 36). Table S1 provides all details.

Supplementary Note 1.

We prepare Rb compounds using the antisolvent approach developed recently for CsMAFA triple perovskite (9). In that work, we abbreviated “ $\text{Cs}_x(\text{MA}_{0.17}\text{FA}_{0.83})_{(100-x)}\text{Pb}(\text{I}_{0.83}\text{Br}_{0.17})_3$ ” for convenience as Cs_xM (x is in percentage), where M stands for “mixed perovskite”. i.e. Cs_0M means no Cs, is the basic composition our state-of-the-art devices. We note that these compositions refer to the precursor that also contains a lead excess as reported elsewhere (36). Including Rb complicates a convenient way of writing down these compounds.

We chose the following conventions (denoting only the precursor solutions).

For double perovskites and triple perovskites that contain Rb and Cs at the same time, we use stoichiometric ratios of the corresponding RbPbI_3 and CsPbI_3 perovskites instead of simply adding the salts.

We show these series in fig. S1. The optimum $\text{Cs}_x\text{FA}_{(100-x)}$ ratio was reached at $\text{Cs}_{15}\text{FA}_{85}$ which we call CsFA from here. The optimum for $\text{Rb}_x\text{FA}_{(100-x)}$ was reached for $\text{Rb}_{10}\text{FA}_{90}$ which we call RbFA. The optimum $\text{Rb}_x\text{Cs}_y\text{FA}_{(100-x-y)}$ composition was reached at $\text{Rb}_5\text{Cs}_{10}\text{FA}_{85}$ which we call RbCsFA.

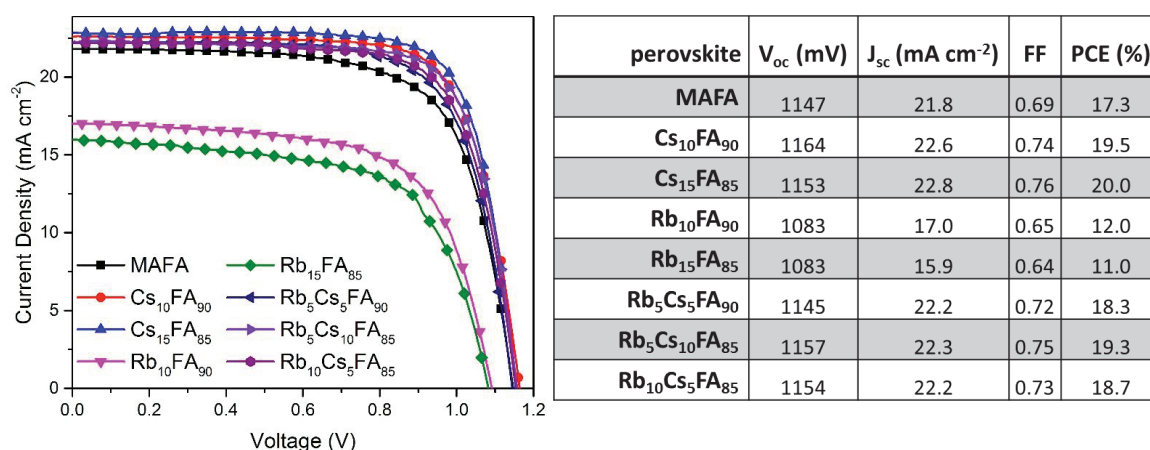
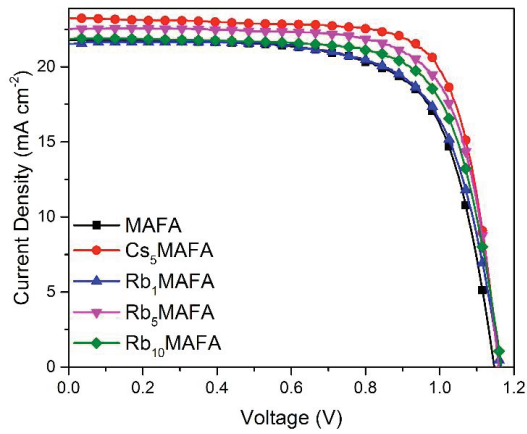


Fig. S1. Optimization of the CsFA, RbFA and RbCsFA compounds.

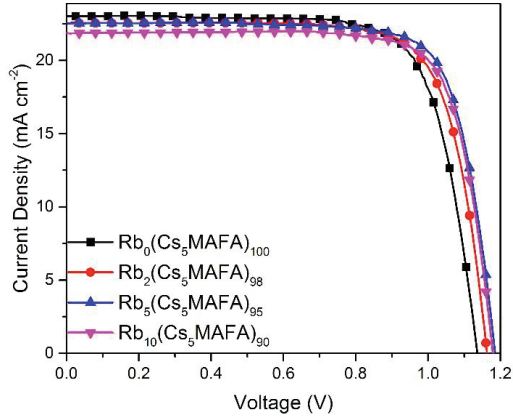
The triple perovskites that contain both MA and FA are labelled according to the Cs_xM formalism but we now write Cs_xMAFA instead of Cs_xM . Rb then simply replaces Cs, i.e. Rb_xMAFA is the analogous triple perovskite to Cs_xMAFA . We show this series in fig. S2. Optimization of the CsMAFA and RbMAFA. The optimum Rb concentration for Rb_xMAFA was reached at Rb_5MAFA .



perovskite	V_{oc} (mV)	J_{sc} (mA cm^{-2})	FF	PCE (%)
MAFA	1147	21.8	0.69	17.3
Cs ₅ MAFA	1182	23.3	0.75	20.6
Rb ₁ MAFA	1163	21.6	0.70	17.5
Rb ₅ MAFA	1159	22.5	0.74	19.2
Rb ₁₀ MAFA	1166	21.9	0.72	18.5

Fig. S2. Optimization of the CsMAFA and RbMAFA.

For the quadruple compounds, we chose to add the RbI to the Cs₅M triple. We use the same formalism as above and label the new series as Rb_x(Cs₅M)_(100-x). We refer to the series as Rb_xCsMAFA as shown in fig. S3. Finally, the best performing devices were recorded at x=5 which we subsequently call RbCsMAFA throughout the manuscript.



perovskite	V_{oc} (mV)	J_{sc} (mA cm^{-2})	FF	PCE (%)
Rb ₀ (Cs ₅ MAFA) ₁₀₀	1138	23.0	0.75	19.6
Rb ₂ (Cs ₅ MAFA) ₉₈	1163	22.5	0.76	19.9
Rb ₅ (Cs ₅ MAFA) ₉₅	1186	22.5	0.77	20.6
Rb ₁₀ (Cs ₅ MAFA) ₉₀	1179	21.9	0.78	20.1

Fig. S3. Optimization of the RbCsMAFA compounds.

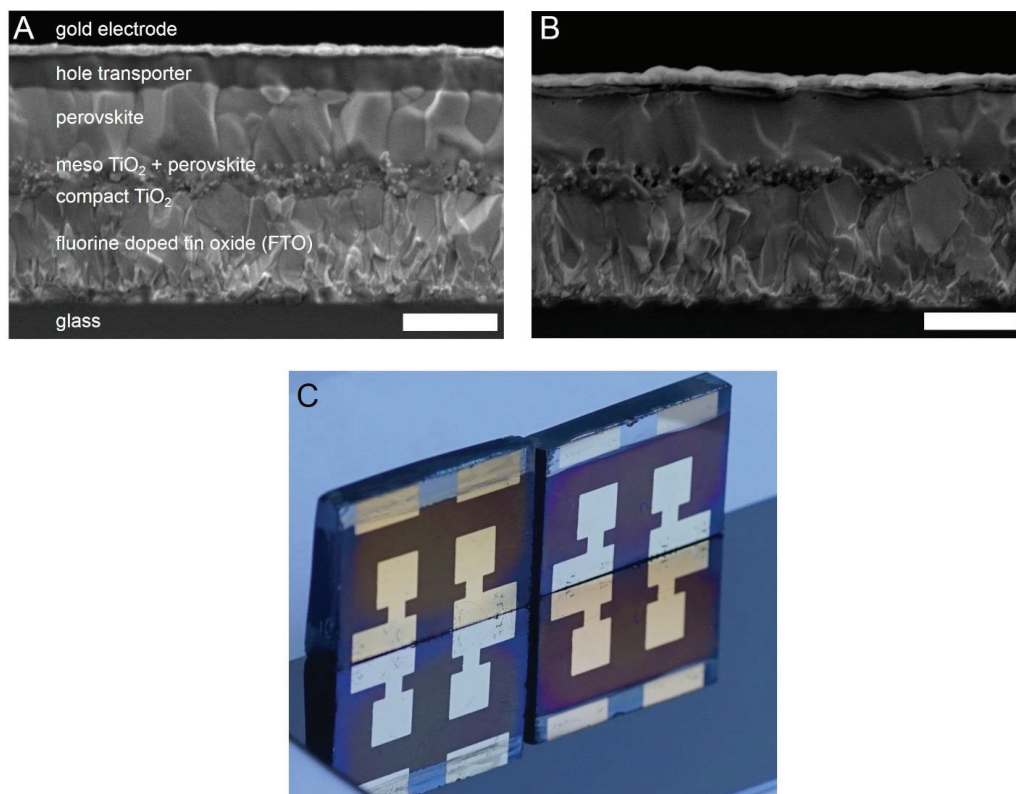


Fig. S4. Cross sectional scanning electron microscope (SEM) images of an Rb₅CsMAFA perovskite solar cell with the hole transporter material (A) spiro-OMeTAD (thickness 200-250 nm) and (B) PTAA (thickness 30-50 nm). The scale bars are 500 nm. (C) Image of typical devices.

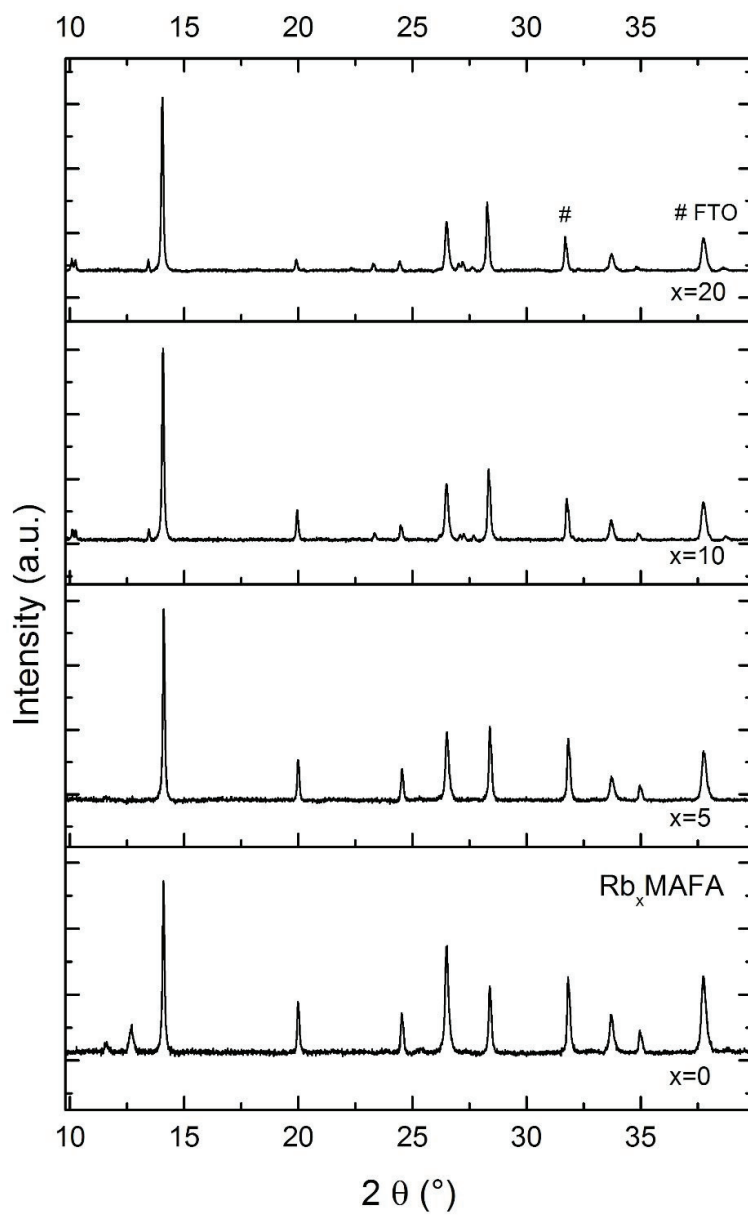


Fig. S5. XRD of the Rb_xMAFA series.

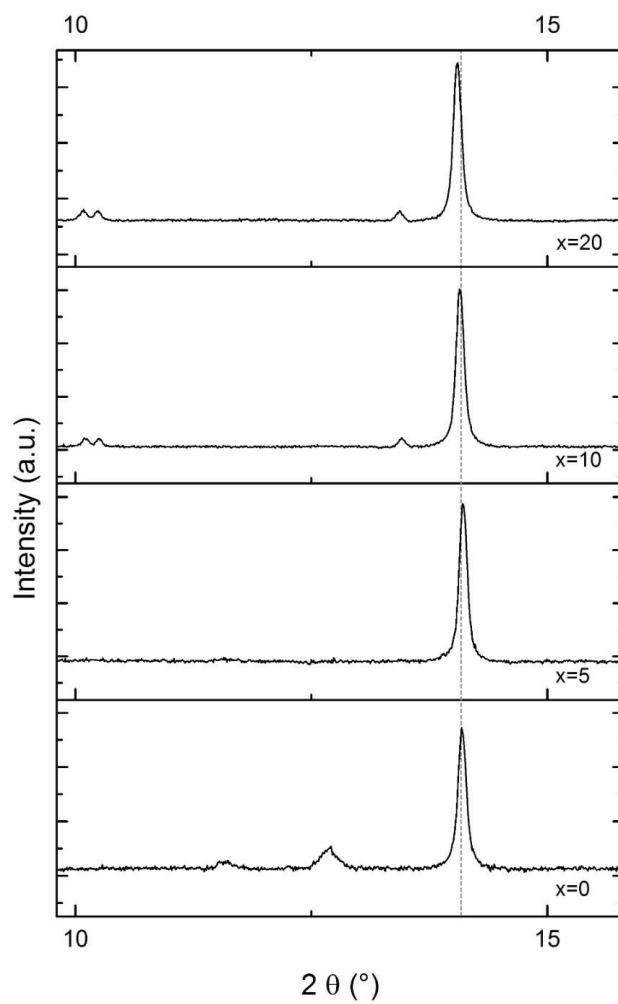


Fig. S6. Magnified view of Rb_xMAFA series.

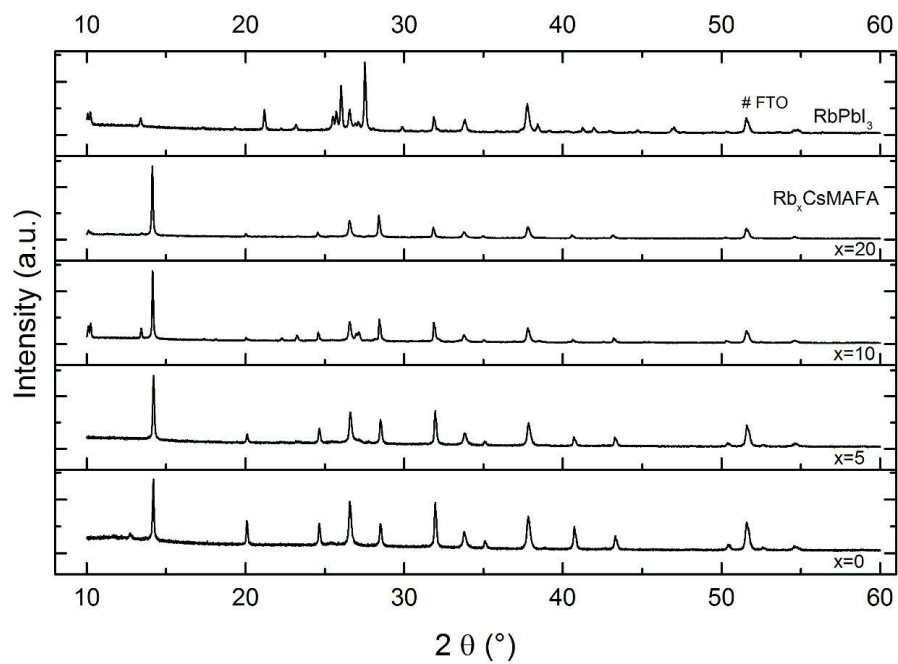


Fig. S7. Rb_xCsMAFA series together with a RbPbI_3 reference.

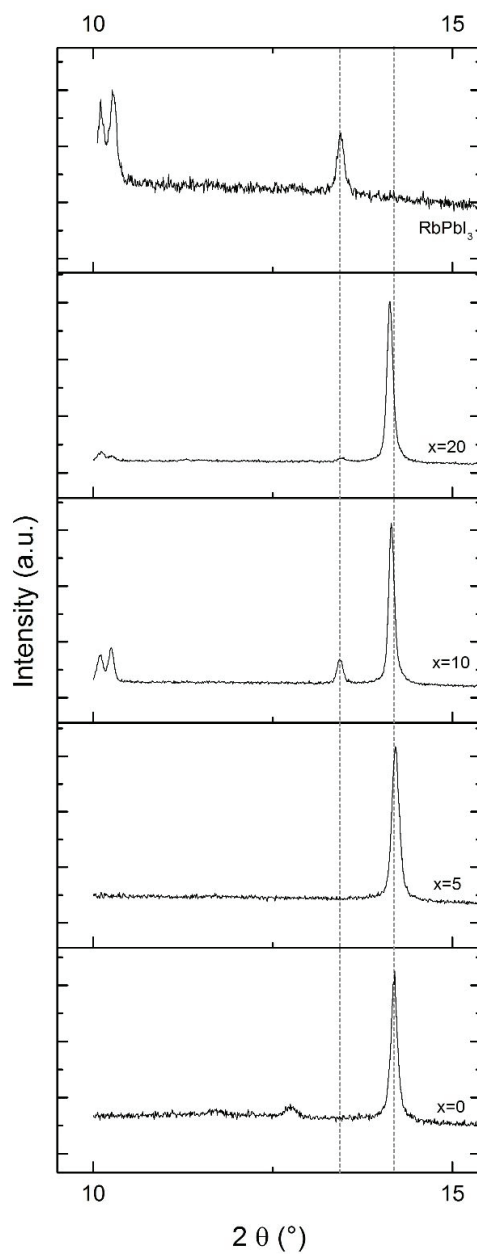


Fig. S8. Magnified view of Rb_xCsMAFA series together with a RbPbI_3 reference.

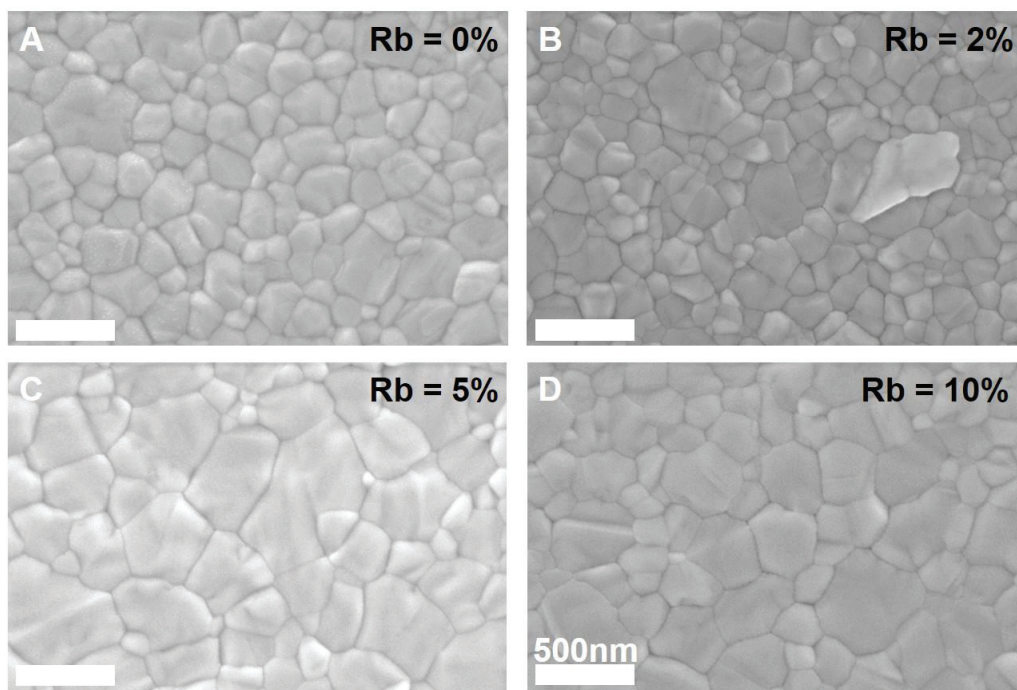


Fig. S9. Top view scanning electron microscope (SEM) images of $Rb_xCsMAFA$ series with (A) 0% (B) 2% (C) 5% and (D) 10% Rb. The scale bars are 500 nm.

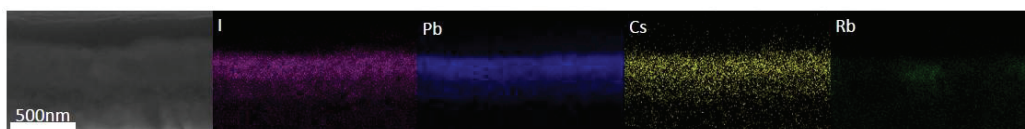


Fig. S10. SEM image and energy-dispersive X-ray spectroscopy (EDX) mapping of I, Pb, Cs and Rb.

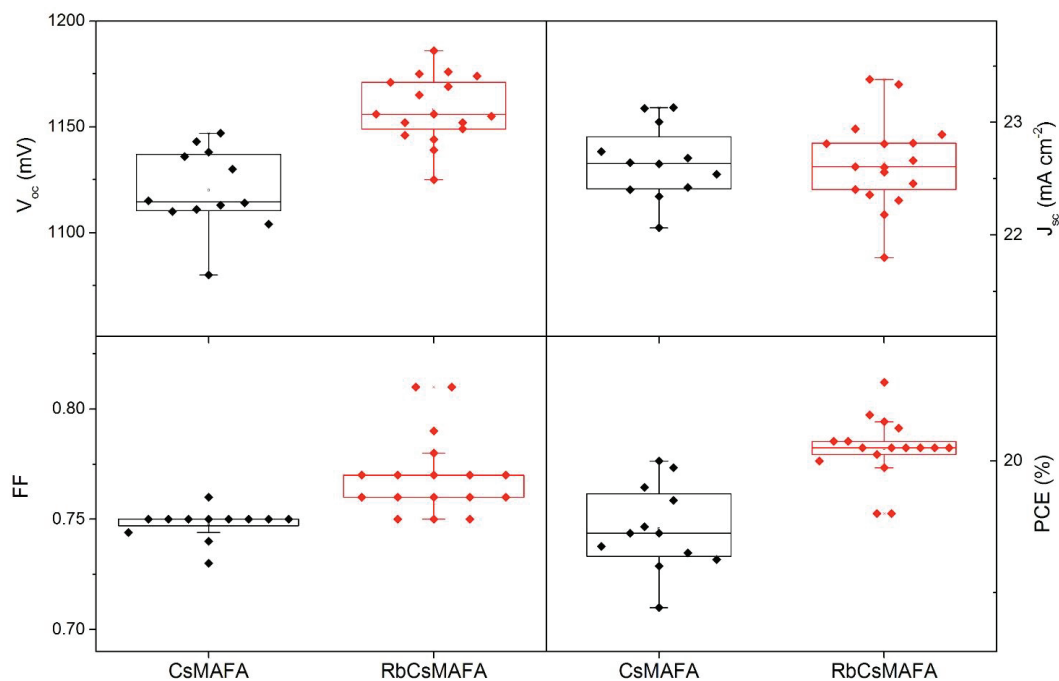


Fig. S11. V_{oc} , J_{sc} , FF and PCE statistics of 12 CsMAFA and 17 RbCsMAFA devices measured with a scan rate of 10 mV s^{-1} without preconditioning, such as light soaking or long-term forward voltage biasing. We note that the V_{oc} improved from 1120 to 1158 mV, the FF from 0.75 to 0.77, and the PCE from 18.9 to 20.2%. 2 RbCsMAFA devices showed fill factors of 81%.

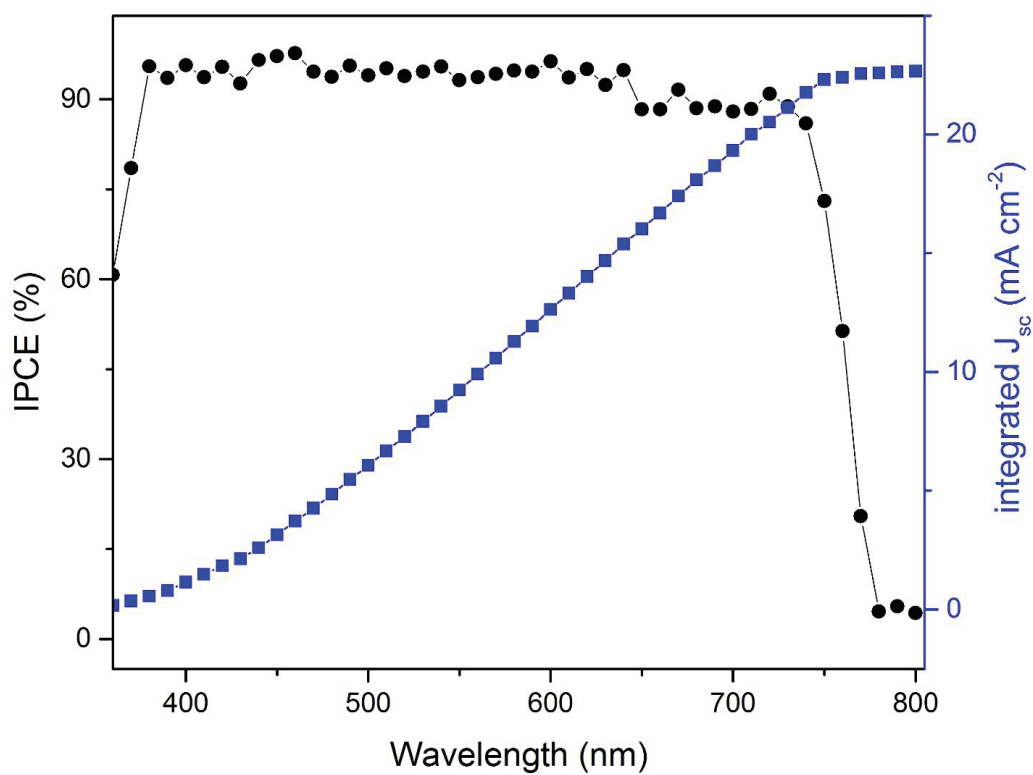


Fig. S12. External quantum efficiency of the champion device. The integrated short circuit current density of 22.7 mA cm^{-2} follows the JV scans from the solar simulator.

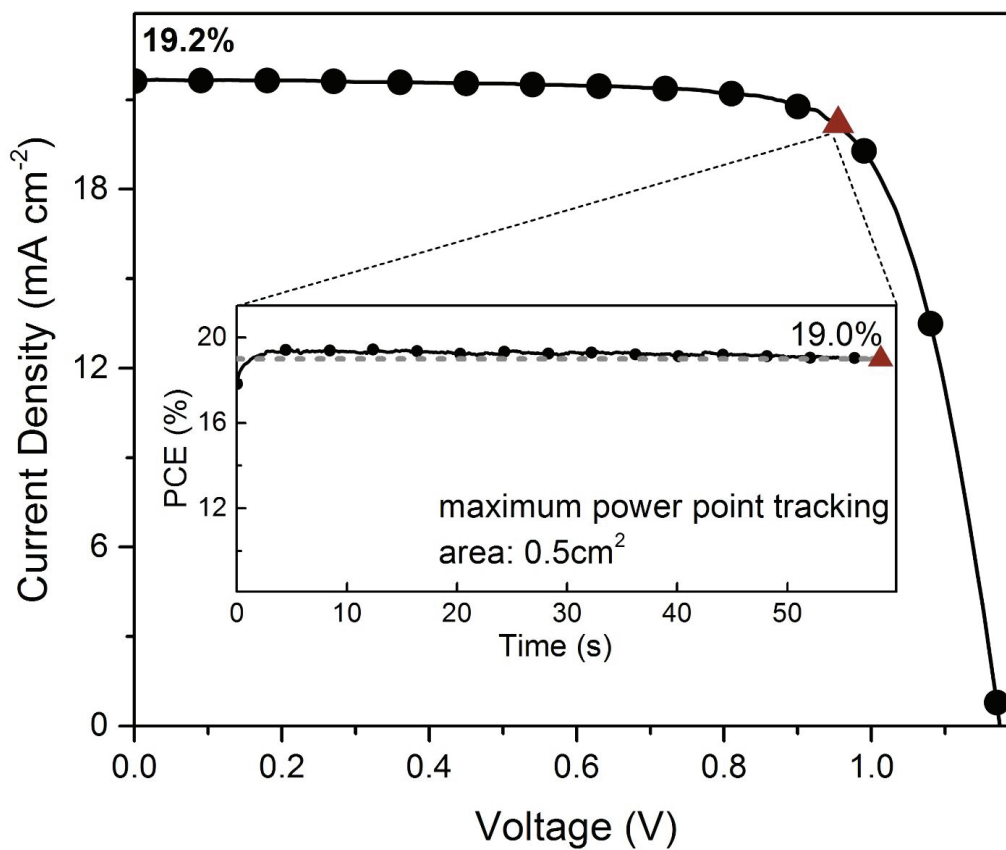


Fig. S13. JV curve, taken at 10 mV s^{-1} scan rate, for a RbCsMAFA device showing 19.2% with an active area of 0.5 cm^2 . The inset shows the scan rate independent maximum power point (MPP) tracking for 60 s resulting in a stabilized efficiency of 19.0% at 949 mV and 20.0 mA cm^{-2} (displayed as the red triangles in the JV and MPP scan, respectively).

Supplementary Note 2.Electroluminescence and prediction of V_{oc}

Using the emission spectrum (inset of **Fig. 3C**), the IPCE and the reciprocity relation (23), we determine the theoretical radiative limit of the V_{oc} ($V_{oc,rad}$) to be ~ 1.34 - 1.35 V. Due to the sharp emission peak and the concomitant low Urbach energy of ~ 14 meV, $V_{oc,rad}$ comes very close to what is expected from the Shockley Queisser limit for a band edge absorber with a band gap of 1.63 eV. However, in a real device additional non-radiative losses need to be considered according to

$$V_{oc} = V_{oc,rad} - \Delta V_{oc,nonrad} = V_{oc,rad} + \frac{kT}{e} \ln EQE_{EL} \approx V_{oc,rad} + 60 \text{ mV} \log EQE_{EL}|_{T=300 \text{ K}}$$

where EQE_{EL} is the external quantum efficiency of electroluminescence (21, 23-25). From this equation, we expect an $EQE_{EL} > 1\%$ for a $\Delta V_{oc,nonrad}$ of ~ 0.10 V. We can measure EQE_{EL} by operating the solar cell as an LED, i.e. by applying a forward voltage and detecting the emitted photon flux, which is then divided by the injected electron flux. In fig. S14, we show the current-voltage (JV) curve, emitted photon flux and the calculated EQE_{EL} . In **Fig. 3C**, we present the calculated EQE_{EL} as a function of voltage (along with an electroluminescence spectrum showing a peak at ~ 1.63 eV) with an emission that can be detected from ~ 900 mV. The EQE_{EL} to match the above equation is chosen such that the injection current equals the photocurrent of $\sim 22 \text{ mA cm}^{-2}$. We measure an EQE_{EL} of 1.4% resulting in $\Delta V_{oc,rad} = 0.11$ V and therefore in a predicted V_{oc} of 1240 mV confirming the value measured from the JV curve.

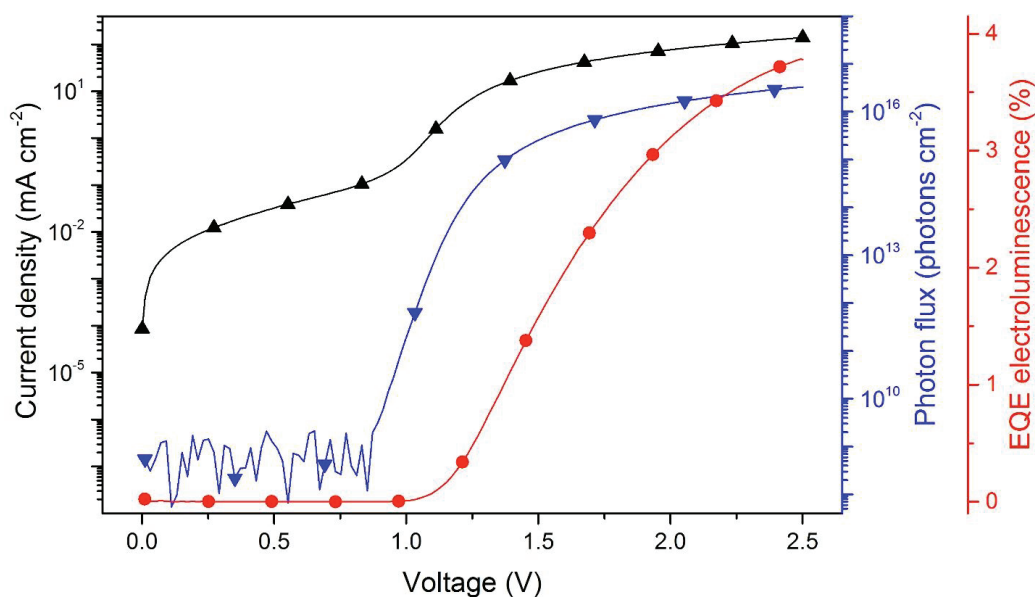


Fig. S14. JV curve (black), emitted photon flux (blue) and the calculated EQE_{EL} (red).

Supplementary Note 3.

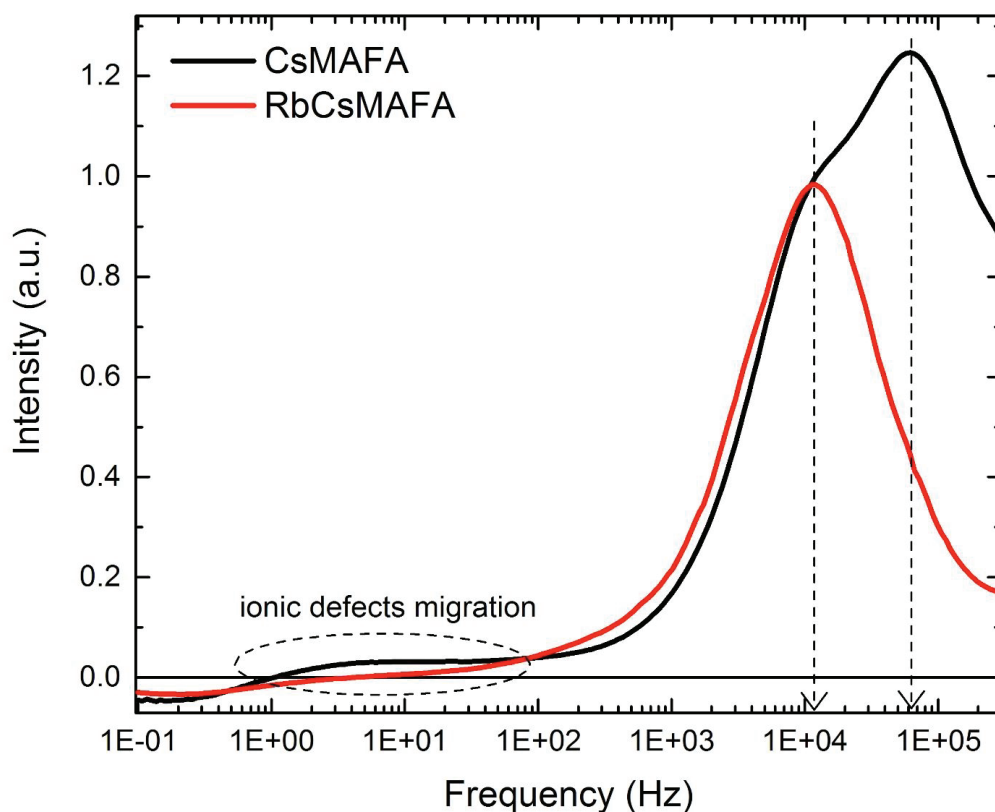


Fig. S15. Imaginary component frequency spectra of the current response to the red LED light modulated (10% of the stationary value) around 1 sun equivalent intensity for the CsMAFA and RbCsMAFA based devices at short circuit condition. Data were normalized to the intensity of 12.11 kHz.

To give further insight to the charge transfer dynamics, we used intensity modulated photocurrent spectroscopy (IMPS) within a working perovskite solar cell (38).

The photocurrent was allowed to settle for 300 s before the frequency scan. In fig. S15, we show the imaginary component of the IMPS frequency spectra for CsMAFA and RbCsMAFA devices. The CsMAFA trace shows two features around 1E+4 and 6E+4 Hz. In our previous work, we have assigned these to the resonant frequencies of the charge dynamics within the perovskite active layer and the electron/hole charge selective materials, respectively (19, 39). Notably, the trace of RbCsMAFA clearly shows only the low-frequency feature at 1E+4 Hz with no indication of any other feature up to the instrument resolution at 5E+5 Hz. This is consistent with an improved charge transport within the RbCsMAFA perovskite layer compared to CsMAFA which already is much faster than MAFA (19). The feature at 1E+4 Hz is identical for CsMAFA and RbCsMAFA, suggesting that the charge transport in the electron/hole charge selective materials is not affected by the perovskite.

Moving from higher to lower frequencies (below $1\text{E}+2$ Hz), the trace of RbCsMAFA rapidly goes to zero, while CsMAFA displays a signal that persists up to 1 Hz. We associated this resonant frequency window ($1\text{E}-1$ to $1\text{E}+3$ Hz) with the migration of ionic defects within the perovskite layer (40). The difference between CsMAFA and RbCsMAFA in this frequency region may be interpreted two ways: *i.* RbCsMAFA has no apparent ionic defect as compared to CsMAFA (detectable in this frequency range), *ii.* ionic defects within the RbCsMAFA lattice are less likely to migrate. Both cases are highly desired to reduce the detrimental impact of the ion migration on the device performance and long-term stability.

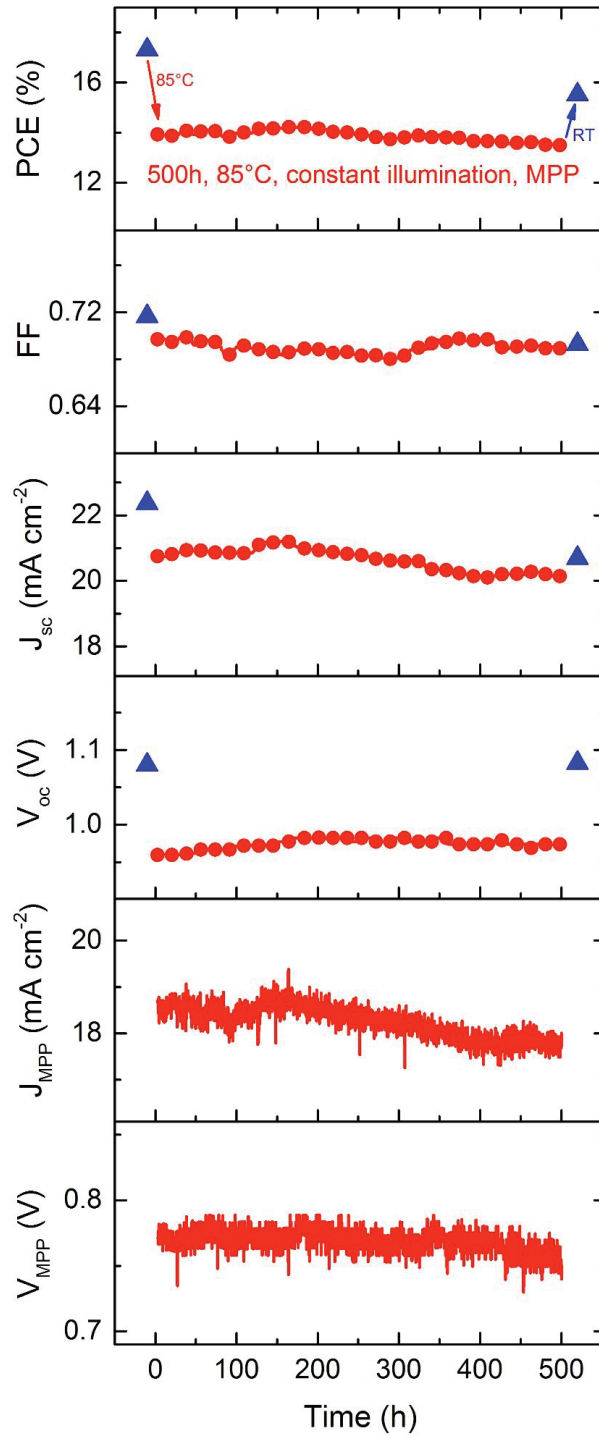


Fig. S16. PCE, FF, J_{sc} , V_{oc} , J_{MPP} and V_{MPP} of a PTAA-based RbCsMAFA device aged for 500 hours at 85 °C under continuous full sun illumination and maximum power point tracking in a nitrogen atmosphere (red curve, circles). During the 85 °C step, the device retains 95% of its initial PCE. The blue triangles indicate the device performance at room temperature (RT) before and after the aging protocol is applied. A small rise in PCE of 0.3% can be observed within the 200 h which could stem from a reorganized polymeric PTAA under heat.

Table S1. Tolerance factor calculations for APbI₃ calculated from $t = \frac{r_A + r_I}{\sqrt{2}(r_{Pb} + r_I)}$ with $r_{Pb} = 119$ pm (36) and $r_I = 220$ pm (36). The cationic radii for Li, Na, K, Rb, Cs were taken from (36); and for MA, FA from (14). The octahedral factor $\mu = r_{Pb}/r_I = 0.541$ for all these compounds is within the $0.414 < \mu < 0.732$ range for perovskite formation (41).

A-cation	radius (pm)	tolerance factor for APbI ₃
Li	76	0.62
Na	102	0.67
K	138	0.75
Rb	152	0.78
Cs	167	0.81
MA	217	0.91
FA	253	0.99

Table S2. Open-circuit voltage (V_{oc}), short circuit current-density (J_{sc}), fill factor (FF) and power conversion efficiency (PCE) of the champion device in Fig. 3A. The curves were recorded at a scan rate of 10 mV s^{-1} from forward bias (FB) to the short circuit condition (SC), and the other way around. No device preconditioning, such as light soaking or forward voltage bias applied for long time, was used before starting the measurement.

Scan direction	J_{sc} (mA cm ⁻²)	V_{oc} (mV)	FF	PCE (%)
FB to SC	22.8	1180	0.81	21.8
SC to FB	22.8	1173	0.80	21.3

Movie S1

Perovskite solar cell mounted in a custom-made device holder. A bright electroluminescence is observed in day light conditions as the signal is tuned towards maximum emission and back.

References

1. National Renewable Energy Laboratory, Best Research-Cell Efficiencies chart; www.nrel.gov/ncpv/images/efficiency_chart.jpg.
2. N. J. Jeon, J. H. Noh, W. S. Yang, Y. C. Kim, S. Ryu, J. Seo, S. I. Seok, Compositional engineering of perovskite materials for high-performance solar cells. *Nature* **517**, 476–480 (2015). [Medline doi:10.1038/nature14133](https://doi.org/10.1038/nature14133)
3. M. Saliba, S. Orlandi, T. Matsui, S. Aghazada, M. Cavazzini, J.-P. Correa-Baena, P. Gao, R. Scopelliti, E. Mosconi, K.-H. Dahmen, F. De Angelis, A. Abate, A. Hagfeldt, G. Pozzi, M. Graetzel, M. K. Nazeeruddin, A molecularly engineered hole-transporting material for efficient perovskite solar cells. *Nat. Energy* **1**, 15017 (2016). [doi:10.1038/nenergy.2015.17](https://doi.org/10.1038/nenergy.2015.17)
4. X. Li, D. Bi, C. Yi, J. D. Décoppet, J. Luo, S. M. Zakeeruddin, A. Hagfeldt, M. Grätzel, A vacuum flash-assisted solution process for high-efficiency large-area perovskite solar cells. *Science* **353**, 58–62 (2016). [Medline doi:10.1126/science.aaf8060](https://doi.org/10.1126/science.aaf8060)
5. H. Choi, J. Jeong, H.-B. Kim, S. Kim, B. Walker, G.-H. Kim, J. Y. Kim, Cesium-doped methylammonium lead iodide perovskite light absorber for hybrid solar cells. *Nano Energy* **7**, 80–85 (2014). [doi:10.1016/j.nanoen.2014.04.017](https://doi.org/10.1016/j.nanoen.2014.04.017)
6. J. W. Lee, D.-H. Kim, H.-S. Kim, S.-W. Seo, S. M. Cho, N.-G. Park, Formamidinium and cesium hybridization for photo- and moisture-stable perovskite solar cell. *Adv. Energy Mater.* **5**, 1501310 (2015). [doi:10.1002/aenm.201501310](https://doi.org/10.1002/aenm.201501310)
7. C. Yi, J. Luo, S. Meloni, A. Boziki, N. Ashari-Astani, C. Grätzel, S. M. Zakeeruddin, U. Röthlisberger, M. Grätzel, Entropic stabilization of mixed A-cation ABX₃ metal halide perovskites for high performance perovskite solar cells. *Energy Environ. Sci.* **9**, 656–662 (2016). [doi:10.1039/C5EE03255E](https://doi.org/10.1039/C5EE03255E)
8. Z. Li, M. Yang, J.-S. Park, S.-H. Wei, J. J. Berry, K. Zhu, Stabilizing perovskite structures by tuning tolerance factor: Formation of formamidinium and cesium lead iodide solid-state alloys. *Chem. Mater.* **28**, 284–292 (2016). [doi:10.1021/acs.chemmater.5b04107](https://doi.org/10.1021/acs.chemmater.5b04107)
9. M. Saliba, T. Matsui, J. Y. Seo, K. Domanski, J. P. Correa-Baena, M. K. Nazeeruddin, S. M. Zakeeruddin, W. Tress, A. Abate, A. Hagfeldt, M. Grätzel, Cesium-containing triple cation perovskite solar cells: Improved stability, reproducibility and high efficiency. *Energy Environ. Sci.* **9**, 1989–1997 (2016). [Medline doi:10.1039/C5EE03874J](https://doi.org/10.1039/C5EE03874J)
10. D. P. McMeekin, G. Sadoughi, W. Rehman, G. E. Eperon, M. Saliba, M. T. Hörantner, A. Haghighirad, N. Sakai, L. Korte, B. Rech, M. B. Johnston, L. M. Herz, H. J. Snaith, A mixed-cation lead mixed-halide perovskite absorber for tandem solar cells. *Science* **351**, 151–155 (2016). [Medline doi:10.1126/science.aad5845](https://doi.org/10.1126/science.aad5845)

11. H. L. Wells, Über die Cäsium- und Kalium-Bleihalogenide. *Z. Anorg. Chem.* **3**, 195–210 (1893). [doi:10.1002/zaac.18930030124](https://doi.org/10.1002/zaac.18930030124)
12. D. Weber, $\text{CH}_3\text{NH}_3\text{PbX}_3$, a Pb(II)-system with cubic perovskite structure. *Z. Naturforsch. B* **33**, 1443 (1978). [doi:10.1515/znb-1978-1214](https://doi.org/10.1515/znb-1978-1214)
13. D. B. Mitzi, K. Liang, Synthesis, resistivity, and thermal properties of the cubic perovskite $\text{NH}_2\text{CH}=\text{NH}_2\text{SnI}_3$ and related systems. *J. Solid State Chem.* **134**, 376–381 (1997). [doi:10.1006/jssc.1997.7593](https://doi.org/10.1006/jssc.1997.7593)
14. G. Kieslich, S. J. Sun, A. K. Cheetham, Solid-state principles applied to organic-inorganic perovskites: New tricks for an old dog. *Chem. Sci.* **5**, 4712–4715 (2014). [doi:10.1039/C4SC02211D](https://doi.org/10.1039/C4SC02211D)
15. M. R. Filip, G. E. Eperon, H. J. Snaith, F. Giustino, Steric engineering of metal-halide perovskites with tunable optical band gaps. *Nat. Commun.* **5**, 5757 (2014). [doi:10.1038/ncomms6757](https://doi.org/10.1038/ncomms6757)
16. F. Hao, C. C. Stoumpos, D. H. Cao, R. P. H. Chang, M. G. Kanatzidis, Lead-free solid-state organic-inorganic halide perovskite solar cells. *Nat. Photonics* **8**, 489–494 (2014). [doi:10.1038/nphoton.2014.82](https://doi.org/10.1038/nphoton.2014.82)
17. D. M. Trots, S. V. Myagkota, High-temperature structural evolution of caesium and rubidium triiodoplumbates. *J. Phys. Chem. Solids* **69**, 2520–2526 (2008). [doi:10.1016/j.jpcs.2008.05.007](https://doi.org/10.1016/j.jpcs.2008.05.007)
18. See supplementary materials on Science Online.
19. J. P. Correa-Baena, M. Anaya, G. Lozano, W. Tress, K. Domanski, M. Saliba, T. Matsui, T. J. Jacobsson, M. E. Calvo, A. Abate, M. Grätzel, H. Míguez, A. Hagfeldt, Unbroken perovskite: Interplay of morphology, electro-optical properties, and ionic movement. *Adv. Mater.* **28**, 5031–5037 (2016). [Medline doi:10.1002/adma.201600624](https://doi.org/10.1002/adma.201600624)
20. M. A. Green, Radiative efficiency of state-of-the-art photovoltaic cells. *Prog. Photovolt. Res. Appl.* **20**, 472–476 (2012). [doi:10.1002/pip.1147](https://doi.org/10.1002/pip.1147)
21. K. Tvingstedt, O. Malinkiewicz, A. Baumann, C. Deibel, H. J. Snaith, V. Dyakonov, H. J. Bolink, Radiative efficiency of lead iodide based perovskite solar cells. *Sci. Rep.* **4**, 6071 (2014). [Medline doi:10.1038/srep06071](https://doi.org/10.1038/srep06071)
22. D. Bi, W. Tress, M. I. Dar, P. Gao, J. Luo, C. Renevier, K. Schenk, A. Abate, F. Giordano, J. P. Correa Baena, J. D. Decoppet, S. M. Zakeeruddin, M. K. Nazeeruddin, M. Grätzel, A. Hagfeldt, Efficient luminescent solar cells based on tailored mixed-cation perovskites. *Sci. Advances* **2**, e1501170 (2016). [Medline doi:10.1126/sciadv.1501170](https://doi.org/10.1126/sciadv.1501170)
23. U. Rau, Reciprocity relation between photovoltaic quantum efficiency and electroluminescent emission of solar cells. *Phys. Rev. B* **76**, 085303 (2007). [doi:10.1103/PhysRevB.76.085303](https://doi.org/10.1103/PhysRevB.76.085303)

24. R. T. Ross, Some thermodynamics of photochemical systems. *J. Chem. Phys.* **46**, 4590 (1967). [doi:10.1063/1.1840606](https://doi.org/10.1063/1.1840606)
25. W. Tress, N. Marinova, O. Inganäs, M. K. Nazeeruddin, S. M. Zakeeruddin, M. Graetzel, Predicting the open-circuit voltage of CH₃NH₃PbI₃ perovskite solar cells using electroluminescence and photovoltaic quantum efficiency spectra: The role of radiative and non-radiative recombination. *Adv. Energy Mater.* **5**, 1400812 (2015). [doi:10.1002/aenm.201400812](https://doi.org/10.1002/aenm.201400812)
26. H. Cho, S. H. Jeong, M. H. Park, Y. H. Kim, C. Wolf, C. L. Lee, J. H. Heo, A. Sadhanala, N. Myoung, S. Yoo, S. H. Im, R. H. Friend, T. W. Lee, Overcoming the electroluminescence efficiency limitations of perovskite light-emitting diodes. *Science* **350**, 1222–1225 (2015). [Medline doi:10.1126/science.aad1818](https://doi.org/10.1126/science.aad1818)
27. L. Gil-Escrig, G. Longo, A. Pertegás, C. Roldán-Carmona, A. Soriano, M. Sessolo, H. J. Bolink, Efficient photovoltaic and electroluminescent perovskite devices. *Chem. Commun.* **51**, 569–571 (2015). [Medline doi:10.1039/C4CC07518H](https://doi.org/10.1039/C4CC07518H)
28. G. Li, F. W. Rivarola, N. J. Davis, S. Bai, T. C. Jellicoe, F. de la Peña, S. Hou, C. Ducati, F. Gao, R. H. Friend, N. C. Greenham, Z. K. Tan, Highly efficient perovskite nanocrystal light-emitting diodes enabled by a universal crosslinking method. *Adv. Mater.* **28**, 3528–3534 (2016). [Medline doi:10.1002/adma.201600064](https://doi.org/10.1002/adma.201600064)
29. N. H. Tiep, Z. L. Ku, H. J. Fan, Recent advances in improving the stability of perovskite solar cells. *Adv. Energy Mater.* **6**, 1501420 (2016). [doi:10.1002/aenm.201501420](https://doi.org/10.1002/aenm.201501420)
30. K. Domanski, J. P. Correa-Baena, N. Mine, M. K. Nazeeruddin, A. Abate, M. Saliba, W. Tress, A. Hagfeldt, M. Grätzel, Not all that glitters is gold: Metal-migration-induced degradation in perovskite solar cells. *ACS Nano* **10**, 6306–6314 (2016). [Medline doi:10.1021/acsnano.6b02613](https://doi.org/10.1021/acsnano.6b02613)
31. K. A. Bush, C. D. Bailie, Y. Chen, A. R. Bowring, W. Wang, W. Ma, T. Leijtens, F. Moghadam, M. D. McGehee, Thermal and environmental stability of semi-transparent perovskite solar cells for tandems enabled by a solution-processed nanoparticle buffer layer and sputtered ITO electrode. *Adv. Mater.* **28**, 3937–3943 (2016). [Medline doi:10.1002/adma.201505279](https://doi.org/10.1002/adma.201505279)
32. A. Mei, X. Li, L. Liu, Z. Ku, T. Liu, Y. Rong, M. Xu, M. Hu, J. Chen, Y. Yang, M. Grätzel, H. Han, A hole-conductor-free, fully printable mesoscopic perovskite solar cell with high stability. *Science* **345**, 295–298 (2014). [Medline doi:10.1126/science.1254763](https://doi.org/10.1126/science.1254763)
33. J. H. Heo, S. H. Im, J. H. Noh, T. N. Mandal, C.-S. Lim, J. A. Chang, Y. H. Lee, H.- Kim, A. Sarkar, M. K. Nazeeruddin, M. Grätzel, S. I. Seok, Efficient inorganic-organic hybrid heterojunction solar cells containing perovskite compound and polymeric hole conductors. *Nat. Photonics* **7**, 487 (2013). [doi:10.1038/nphoton.2013.80](https://doi.org/10.1038/nphoton.2013.80)

34. Y. G. Rong, L. F. Liu, A. Y. Mei, X. Li, H. W. Han, Beyond efficiency: The challenge of stability in mesoscopic perovskite solar cells. *Adv. Energy Mater.* **5**, 1501066 (2015). [doi:10.1002/aenm.201501066](https://doi.org/10.1002/aenm.201501066)
35. N. Pellet, J. Teuscher, J. Maier, M. Gratzel, Transforming hybrid organic inorganic perovskites by rapid halide exchange. *Chem. Mater.* **27**, 2181–2188 (2015). [doi:10.1021/acs.chemmater.5b00281](https://doi.org/10.1021/acs.chemmater.5b00281)
36. R. D. Shannon, Revised effective ionic radii and systematic studies of interatomic distances in halides and chalcogenides. *Acta Crystallogr. A* **32**, 751–767 (1976). [doi:10.1107/S0567739476001551](https://doi.org/10.1107/S0567739476001551)
37. J. P. C. Correa Baena, L. Steier, W. Tress, M. Saliba, S. Neutzner, T. Matsui, F. Giordano, T. J. Jacobsson, A. R. Srimath Kandada, S. M. Zakeeruddin, A. Petrozza, A. Abate, M. K. Nazeeruddin, M. Grätzel, A. Hagfeldt, Highly efficient planar perovskite solar cells through band alignment engineering. *Energy Environ. Sci.* **8**, 2928–2934 (2015). [doi:10.1039/C5EE02608C](https://doi.org/10.1039/C5EE02608C)
38. E. Guillén, F. J. Ramos, J. A. Anta, S. Ahmad, Elucidating transport-recombination mechanisms in perovskite solar cells by small-perturbation techniques. *J. Phys. Chem. C* **118**, 22913–22922 (2014). [doi:10.1021/jp5069076](https://doi.org/10.1021/jp5069076)
39. F. Giordano, A. Abate, J. P. Correa Baena, M. Saliba, T. Matsui, S. H. Im, S. M. Zakeeruddin, M. K. Nazeeruddin, A. Hagfeldt, M. Graetzel, Enhanced electronic properties in mesoporous TiO₂ via lithium doping for high-efficiency perovskite solar cells. *Nat. Commun.* **7**, 10379 (2016). [Medline doi:10.1038/ncomms10379](https://doi.org/10.1038/ncomms10379)
40. J.-Y. Seo *et al.*, Ionic liquid control crystal growth to enhance planar perovskite solar cells efficiency. *Adv. Energy Mater.* 10.1002/aenm.201600767 (2016). [doi:10.1002/aenm.201600767](https://doi.org/10.1002/aenm.201600767)
41. C. Li, X. Lu, W. Ding, L. Feng, Y. Gao, Z. Guo, Formability of ABX₃ (X = F, Cl, Br, I) halide perovskites. *Acta Crystallogr. B* **64**, 702–707 (2008). [Medline doi:10.1107/S0108768108032734](https://doi.org/10.1107/S0108768108032734)

Chapter 6 High Temperature-Stable Perovskite Solar Cells Based on Low-Cost Carbon Nanotube Hole Contact

THE CONTEXT

With high efficiency and high stability, our perovskite solar cells were checking two out of three components of the “holy grail of photovoltaics” (which additionally includes cheap production on large scale). However, the resultant devices employed two very expensive materials: Au and PTTA, making them potentially very expensive to produce on a large scale (material cost is significant and vacuum processing is required for depositing Au). In this work, I replaced both materials by a combination of potentially inexpensive carbon contact impregnated with Spiro-MeOTAD (a significantly cheaper material than PTAA). This way, I achieved good high-temperature stability with relatively inexpensive materials, which can be deposited inexpensively, while sacrificing only around 25% (relatively) of the initial efficiency of similar devices based on metal contacts.⁹¹

This chapter is based on a peer-reviewed paper published in *Advanced Materials* in January 2017 entitled:

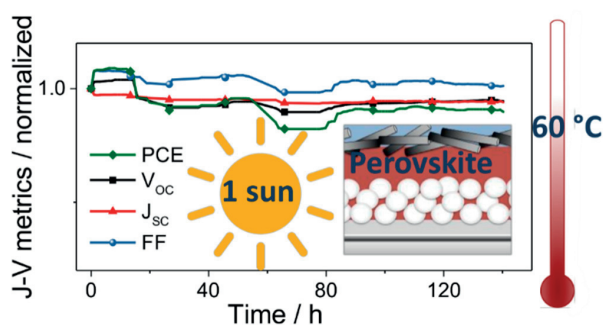
High Temperature-Stable Perovskite Solar Cell Based on Low-Cost Carbon Nanotube Hole Contact

authored by:

Kerttu Aitola, **Konrad Domanski**, Juan-Pablo Correa-Baena, Kári Sveinbjörnsson, Michael Saliba, Antonio Abate, Michael Grätzel, Esko Kauppinen, Erik MJ Johansson, Wolfgang Tress, Anders Hagfeldt and Gerrit Boschloo.

My contribution:

Kerttu Aitola and I contributed to this work equally. I discovered the way to achieve high-temperature stable perovskite solar cells by using carbon back-contacted devices. I performed all measurements presented in this work, analysed the data, plotted the figures and wrote about half of the manuscript, while Kerttu Aitola wrote the remaining part of the manuscript and prepared the carbon electrodes.



High Temperature-Stable Perovskite Solar Cell Based on Low-Cost Carbon Nanotube Hole Contact

Kerttu Aitola,* Konrad Domanski, Juan-Pablo Correa-Baena,* Kári Sveinbjörnsson, Michael Saliba, Antonio Abate, Michael Grätzel, Esko Kauppinen, Erik M. J. Johansson, Wolfgang Tress, Anders Hagfeldt, and Gerrit Boschloo

Mixed ion perovskite solar cells (PSC) are manufactured with a metal-free hole contact based on press-transferred single-walled carbon nanotube (SWCNT) film infiltrated with 2,2,7,7-tetrakis(*N,N*-di-*p*-methoxyphenylamine)-9,9,0-spirobifluorene (Spiro-OMeTAD). By means of maximum power point tracking, their stabilities are compared with those of standard PSCs employing spin-coated Spiro-OMeTAD and a thermally evaporated Au back contact, under full 1 sun illumination, at 60 °C, and in a N₂ atmosphere. During the 140 h experiment, the solar cells with the Au electrode experience a dramatic, irreversible efficiency loss, rendering them effectively nonoperational, whereas the SWCNT-contacted devices show only a small linear efficiency loss with an extrapolated lifetime of 580 h.

Perovskite solar cells^[1] (PSCs) are a relatively new type of photovoltaic devices, which are based on light absorbing materials with the general formula of ABX₃, where A is a monovalent

cation (methylammonium (MA), formamidinium (FA), Cs, or Rb), B is Pb or Sn, and X is a halide.^[2–4] PSCs have recently attracted a lot of attention, owing to their very high power conversion efficiency (PCE; up to 22.1%),^[5] cheap starting materials, and ease of fabrication. However, their poor stability, which has been linked to the sensitivity of the organometallic absorber toward humidity,^[6] and their overall poor long-term thermal stability^[7] have been the major factors hindering their fast commercialization. It has been proposed that the Cs-containing “triple cation” perovskites of the form Cs/FA/MA are structurally more stable than the MAPbI₃ and the mixed ion FAPbI₃:MAPbBr₃^[8] perovskites, due to the smaller ionic radius of the Cs than those of the FA and MA cations.^[3] This approach has been further advanced by the incorporation of Rb into the mixture to form the so-called “quadruple cation” PSCs.^[2]

We have previously reported a crucial instability factor in PSCs operating at elevated temperatures related to Au from the back hole contact (HC) migrating through the entire solar cell structure and interacting with the perovskite, causing dramatic loss of solar cell performance.^[9] Although the Au migration could be circumvented via the use of Cr interlayer between the Au contact and the hole transporting material (HTM; 2,2,7,7-tetrakis(*N,N*-di-*p*-methoxyphenylamine)-9,9,0-spirobifluorene, Spiro-OMeTAD), this came at the expense of a considerable efficiency decrease. In a subsequent work, we have shown that the problem of Au migration can be also circumvented by substituting Spiro-OMeTAD with the poly(triaryl amine) (PTAA) HTM.^[2] However, this approach still involves the use of expensive Au contacts, and the PTAA polymer is currently also considerably more costly than the Spiro-OMeTAD HTM.

Different carbon-based alternative materials have been introduced as HTMs and HCs, such as carbon nanotube films with^[10–12] and without^[13] additional metal layers and carbon black composite contacts.^[14,15] In our previous study, we demonstrated that a potentially cost-effective single-walled carbon nanotube (SWCNT) film deposited directly onto the FAPbI₃:MAPbBr₃ perovskite layer and processed further with a small amount of drop-cast Spiro-OMeTAD yielded high solar cell efficiencies of around 15%.^[16] SWCNT-based contacts offer also other important advantages, such as extremely high flexibility^[17] (which is a prerequisite for industrial roll-to-roll

Dr. K. Aitola, K. Sveinbjörnsson,
Prof. E. M. J. Johansson, Prof. G. Boschloo
Department of Chemistry – Ångström Laboratory
Physical Chemistry
Uppsala University
Box 523, 75120 Uppsala, Sweden
E-mail: kerttu.aitola@kemi.uu.se

K. Domanski, Dr. M. Saliba, Prof. M. Grätzel, Dr. W. Tress
Laboratory for Photonics and Interfaces
Institute of Chemical Sciences and Engineering
École Polytechnique de Fédérale de Lausanne
CH-1015 Lausanne, Switzerland

Dr. J.-P. Correa-Baena
Massachusetts Institute of Technology
77 Massachusetts Avenue, Cambridge, MA 02139, USA
E-mail: jpcorrea@mit.edu

Dr. A. Abate
Adolphe Merkle Institute
University of Fribourg
CH-1700 Fribourg, Switzerland

Prof. E. Kauppinen
Department of Applied Physics
Aalto University
P.O. Box 15100, 00076 Aalto, Finland

Prof. A. Hagfeldt
Laboratory of Photomolecular Science
Institute of Chemical Sciences and Engineering
École Polytechnique Fédérale de Lausanne
CH-1015 Lausanne, Switzerland

DOI: 10.1002/adma.201606398



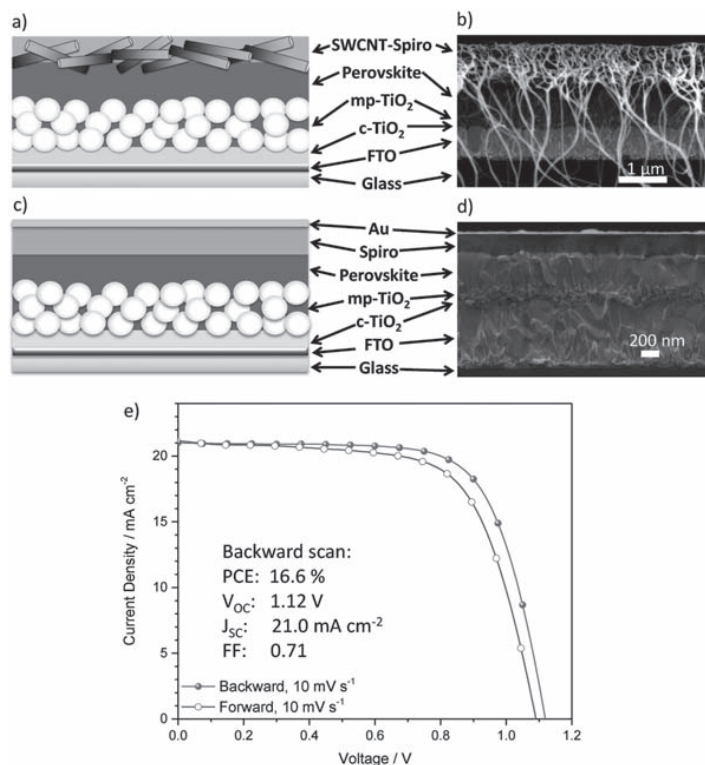


Figure 1. a) Schematics and b) cross-sectional SEM image of the SWCNT-contacted device. The carbon nanotube “whiskers” in front of the SEM image are due to sample preparation. c) Schematics and d) cross-sectional SEM image of the standard Au contacted device (with spin-coated Spiro-OMeTAD HTM). e) The J - V curve of a device that yielded a 16.0% average efficiency (average of the backward and forward scans).

deposition processes) and semitransparency,^[18] which is required in, e.g., bifacial solar cells. Snaith and co-workers have also suggested that a SWCNT-poly(methyl methacrylate) (PMMA) composite may protect the perovskite films from ambient humidity even more efficiently than PMMA alone due to the hydrophobic nature of SWCNTs.^[11]

In this work, we show that PSCs employing a SWCNT-based HTM-HC have superior long-term stability at elevated temperatures (60 °C—temperature commonly used for solar cell stability testing^[19]), as compared to that of the standard configuration with an evaporated Au contact with Spiro-OMETAD HTM. We fabricated devices based on fluorine-doped tin oxide (FTO)/compact TiO₂/mesoporous TiO₂/perovskite/Spiro-OMETAD/HC architecture, with Cs₅(MA_{0.17}FA_{0.83})₉₅Pb(I_{0.83}Br_{0.17})₃ perovskite as the active layer (from here on referred to as “mixed ion perovskite”). Two types of HTM-HC configurations were used: (1) spin-coated Spiro-OMETAD and evaporated Au contact and (2) SWCNT:Spiro-OMETAD composite HTM-HC^[16] manufactured by a simple press transfer of the SWCNT film

on the perovskite layer and infiltrating the SWCNT film with Spiro-OMETAD (i.e., no additional Au or Ag contact or a separate Spiro-OMETAD layer is utilized in the structure; the latter configuration is depicted in **Figure 1a,b** and the standard one in **Figure 1c,d**).

In this study, both the short-circuit current density (J_{SC}) and the open circuit voltage (V_{OC}) were, on average, similar for the both types of cells (cf. **Figures 1c** and **3a,b**). While the similar V_{OC} is in line with our previous findings,^[16] we note no mismatch in J_{SC} s of the Au and SWCNT contacted devices, as we did in the previous study (where the J_{SC} was lower for the SWCNT devices as compared to the Au devices). In this work, the currents for the SWCNT devices are overall a bit higher (21–22 mA cm⁻²) than in the previous study (\approx 20 mA cm⁻²). This suggests that in the currently used perovskite films’ case, the film absorbs most of the incoming light and Au back reflection does not contribute to the current generation. This is due to the thicker perovskite film (500 nm)^[20] compared to what was used in our previous work (300–400 nm).^[16] Finally, the

relatively lower fill factor (FF) in the SWCNT devices (compared to spin-coated Spiro-OMeTAD-perovskite interface) is most likely related to the somewhat unoptimized contact between the SWCNT-Spiro-OMeTAD composite and the perovskite layer.^[16] The higher sheet resistance of the SWCNT-Spiro-OMeTAD composite film ($\approx 15 \Omega \square^{-1}$ compared to $<1 \Omega \square^{-1}$ for Au layer) further reduces the FF. Nevertheless, high efficiency ($>16\%$) PSCs can be manufactured with the SWCNT-based HTM-HC, without the use of costly metal electrodes.

The results from the 140 h maximum power point (MPP) tracking of the Au and SWCNT-contacted devices under white light-emitting diode (LED) illumination with an intensity equivalent to 1 sun, carried out in N_2 atmosphere, can be seen in **Figure 2**. A Au-contacted device yielding a PCE of 18.4% (18.0% stabilized) and a SWCNT device yielding 15.0% PCE (14.3% stabilized) were used in the stability testing. The lower performance of the latter, as compared to the device in **Figure 1c**, was due to its slightly lower V_{OC} (1.03 V) and FF (0.63). The cells were kept at the temperature of 20 °C for the first 14 h of the ageing experiment, and one can see that the Au-contacted device has shown pronounced changes within this period. We added also results from a 90 h MPP tracking of an Au device conducted in 20 °C in **Figure 2a** to highlight the initial degradation of PSCs in lower temperatures, followed by a stabilization period, which is not seen in high temperature experiments, where Au devices undergo an irreversible degradation process. We have previously shown that the changes occurring in 20 °C experiments are due to slow cation migration in the devices happening in the timescale of hours and they are mostly of reversible nature and the cells recover most of their performance if they are allowed to relax 7–8 h in the dark.^[9,21] Curiously, the SWCNT device exhibits only a small efficiency drop in this region. According to our practical experience, this initial

efficiency loss phenomenon is not usually so pronounced for lower efficiency ($<18\%$) solar cells, like the SWCNT cells, and we believe that in the lower efficiency cells' case it is masked by for instance initially higher series resistances.

After the temperature was increased to 60 °C, the degradation of the Au-based device accelerated dramatically. The device showed an exponential decay, losing 20% of the remaining PCE within only 8 h of ageing. This is expected and has been shown by us to be due to Au migration-induced degradation of the device.^[9] In contrast, the SWCNT-contacted device showed a slow decay which can be approximated with a linear function yielding a slope of $-0.005\% \text{ h}^{-1}$. Assuming that this trend continues, we extrapolate a very conservative estimate of the predicted lifetime (defined as the point, where 20% of initial PCE is lost, T_{80}) of 580 h. With a simplistic assumption that the degradation rate is directly proportional to the light intensity, this value corresponds to half a year of operation given an average of three sun shine hours a day—typical value for central Europe.^[22]

We further investigated the nature of degradation of the two devices by tracking the evolution of the $J-V$ curves and the $J-V$ metrics over the course of the ageing experiment (**Figure 3**). The Au-based device degraded significantly including a significant worsening of all the main $J-V$ parameters. Notably, the considerable loss of V_{OC} has been previously demonstrated to be an indication of Au-induced degradation of the perovskite layer.^[9] Importantly, the SWCNT device showed only a minor decrease in V_{OC} and J_{SC} , which could be due to, e.g., perovskite phase transition, slow degradation due to residual water or oxygen in the perovskite film, light induced trap states or ionic movement—degradation mechanisms of perovskite films employed in photovoltaic devices are not well known yet thus all the aforementioned reasons are so far only speculative. However, our work shows that a carbon nanotube film, deposited by simple nonvacuum means and with the use of which the metal migration issue can be avoided completely, is a promising option for hole contact in stable PSCs.

In this work, we have shown that perovskite solar cells employing a mixed ion perovskite absorber and a single-walled carbon nanotube-based hole-transporting material and hole contact are good candidates for durable and efficient photovoltaic devices. During the experiment conducted at 60 °C in N_2 atmosphere and 1 sun equivalent white LED illumination, the devices showed only a modest linear efficiency loss (slope: $-0.005\% \text{ h}^{-1}$), which led to an estimated lifetime (T_{80}) of 580 h. At the same time, the standard PCSs with a Au back contact experienced a dramatic and rapid efficiency loss; likely due to the Au ion migration in the structure.

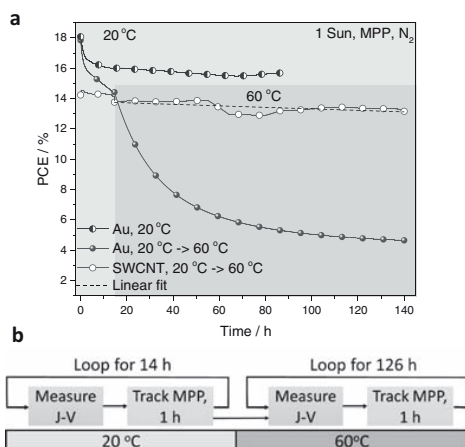


Figure 2. a) The result of MPP tracking of Au and SWCNT-contacted devices at elevated temperatures. b) The temperature of the devices was changed from initial 20 to 60 °C after 14 h into the experiment. MPP tracking of an Au device at 20 °C is shown for 90 h.

Experimental Section

SWCNT Synthesis: The SWCNTs were synthesized by a floating catalyst-chemical vapor deposition procedure described in ref. [18]. Shortly, ferrocene containing CO:CO₂ (99:1 ratio) carrier gas was directed into a hot furnace reactor kept at 880 °C. The ferrocene decomposed in the temperature gradient between the gas injector and the reactor forming catalytic iron nanoparticles, that acted as catalysts for the CO:CO₂ gas decomposition and SWCNTs started forming on the nanoparticles. The formed SWCNTs were collected from the gas phase

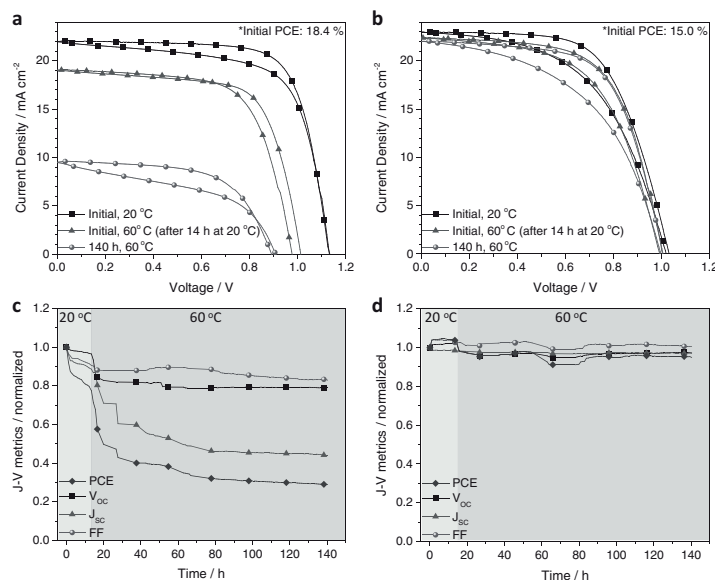


Figure 3. *J*-*V* curves of a) Au and b) SWCNT-contacted devices at the beginning of the experiment at 20 °C, at 60 °C after the temperature increase, and at the end of the experiment (at 60 °C). c, d) The evolution of individual *J*-*V* metrics (PCE, V_{OC} , J_{SC} , and FF) over the course of the experiment.

on a porous filter membrane at the reactor outlet and the formed film could be transferred from the filter paper on the desired substrate.

Fabrication of Perovskite Solar Cells: FTO glass sheets (Nippon Sheet Glass 10) were etched with zinc powder and HCl (4 M). Substrates were ultrasonically cleaned by a sequential 15 min 2% Hellmanex water solution, deionized water, ethanol, and acetone. Substrates were treated under UV-ozone for 15 min to remove the last traces of organic residues. A 30–50 nm thin compact TiO_2 layer was then deposited on to the clean preheated substrates by spray pyrolysis from a precursor solution of titanium diisopropoxide bis(acetylacetonate) in anhydrous ethanol, using oxygen as the carrier gas on a hot plate set to 450 °C, followed by annealing at 450 °C, for 30 min in air. A mesoporous TiO_2 layer was deposited by spin coating for 20 s at 4000 rpm with a ramp of 2000 rpm, using 30 nm particle paste (Dyesol 30 NR-D) diluted in ethanol to achieve a 200 nm layer thickness (150 mg mL^{-1}). After the spin coating, the substrates were immediately dried at 100 °C for 10 min and then sintered again at 450 °C for 30 min under dry air flow.

Li-doping of mesoporous TiO_2 ^[23] was accomplished by spin coating a 0.1 M solution of Li-TFSI in acetonitrile at 3000 rpm with a ramp of 1000 rpm for 10 s, followed by another sintering step at 450 °C for 30 min. After cooling down to 150 °C, the substrates were immediately transferred to a nitrogen atmosphere glove box for depositing the perovskite films.

The mixed triple-cation lead mixed-halide perovskite solution was prepared from a precursor solution made of formamimidinium iodide (FAI) (1 M, Dyesol), PbI_2 (1.1 M, TCI), MABr (0.2 M, Dyesol), and $PbBr_2$ (0.22 M, TCI) in a 4:1 (V:V) mixture of anhydrous dimethylformamide:dimethylsulfoxide (DMSO) (Acros). Then, a 1.5 M stock solution of CsI (abc GmbH) in DMSO was added to the above solution in 5:95 volume ratio. The mixed ion perovskite solution was deposited through a two-step spin coating program (10 s at 1000 rpm and 20 s at 6000 rpm). During the second step, 200 μL of chlorobenzene was poured on the

spinning substrate 5 s before the end of the procedure. The substrates were then placed on a hotplate for annealing at 100 °C for 1 h in a nitrogen filled glove box.

After the perovskite annealing, the substrates were cooled down for a few minutes and a Spiro-OMeTAD (Merck) solution ($70 \times 10^{-3} \text{ M}$ in chlorobenzene) was spin coated at 4000 rpm for 20 s. Spiro-OMeTAD was doped with bis(trifluoromethylsulphonyl)imide lithium salt (Li-TFSI, Sigma-Aldrich), tris(2-(1H-pyrazol-1-yl)-4-*tert*-butylpyridine)cobalt(III) tris(bis(trifluoromethylsulphonyl)imide) (FK209, Dyanamo), and 4-*tert*-butylpyridine (TBP, Sigma-Aldrich). The molar ratio of additives for Spiro-OMeTAD was 0.5, 0.03, and 3.3 for Li-TFSI, FK209, and TBP, respectively.

In the reference “standard” solar cells case, an 80 nm thick gold top electrode was deposited on the Spiro-OMeTAD layer as top contact electrode by thermal evaporation under high vacuum.

The SWCNT solar cells were prepared by cutting the SWCNT film on filter paper to around 5 mm \times 10 mm size piece and transferred on the perovskite substrate using some pressure, after which the filter paper was peeled off the SWCNT film. The SWCNT film was “densified”^[16] with a small amount of chlorobenzene. After that another SWCNT film was transferred on the first film in order to reach lower sheet resistance than with the single film layer.^[16] Finally, $2 \times 2 \mu\text{L}$ drops of Spiro-OMeTAD solution were drop cast on the SWCNT film.

***J*-*V* Measurements:** *J*-*V* measurements were performed with a Newport Solar Simulator, model 91160, equipped with a Keithley 2400 source meter, and providing a 1000 W m^{-2} AM 1.5G illumination intensity, as measured by means of a certified reference silicon solar cell (Fraunhofer - Institut für Solare Energiesysteme ISE). A slow (10 mV s^{-1}) scan speed was used in the initial *J*-*V* measurements.

Stability Measurements: Stability measurements were performed with a Biologic MPG2 potentiostat under white LED lamp (Lumileds LXM3-PW51) with 1 sun equivalent intensity. The devices were masked

(0.16 cm²) and flushed with nitrogen for several hours before the start of the experiment in order to remove residual oxygen and water from the environment of an in-house developed sample holder. Then, the *J*-*V* curves of the devices were measured at 100 mV s⁻¹ (high scan speed was chosen to maximize the time that the devices spend at MPP) followed by MPP tracking routine under continuous illumination (and N₂). The MPP was updated every 10 s by a standard perturb and observe method and continued for 1 h before the procedure was repeated starting with measuring the *J*-*V* curve again. The temperature of the devices was controlled with a Peltier element in direct contact with the films. The temperature was measured with a surface thermometer located between the Peltier element and the film. While the initial temperature was set to 20 °C, it was changed to 60 °C after 14 h into the experiment without disturbing the ongoing data collection. The temperature equilibration time was below 1 min. All devices were tested at the same time inside one sample holder—hence being exposed to identical environmental conditions: temperature, illumination, and atmosphere.

Electron Microscopy Analysis: Scanning electron microscopy (SEM) characterization of the device stack was performed with a ZEISS Merlin high resolution SEM.

Acknowledgements

K.A. and K.D. contributed equally to this work. K.A. is grateful for the Wallenberg foundation, Swedish Research Council FORMAS, Swedish Energy Agency and the Solar-era.net project "CNT-PV" for the financial support. K.D. thanks the Fonds national suisse for funding within the framework of Umbrella project (Grant Agreement Nos. 407040-153952 and 407040-153990). We thank Benjamin Le Geyt, Supardi Sujito, Christophe Clement and Andre Fattet for their help in setting up infrastructure used for this work.

Received: November 25, 2016
Published online: February 23, 2017

- [1] M. M. Lee, J. Teuscher, T. Miyasaka, T. N. Murakami, H. J. Snaith, *Science* **2012**, 338, 643.
- [2] M. Saliba, T. Matsui, K. Domanski, J.-Y. Seo, A. Ummadisingu, S. M. Zakeeruddin, J.-P. Correa-Baena, W. R. Tress, A. Abate, A. Hagfeldt, M. Grätzel, *Science* **2016**, 354, 206.
- [3] M. Saliba, T. Matsui, J.-Y. Seo, K. Domanski, J.-P. Correa-Baena, M. K. Nazeeruddin, S. M. Zakeeruddin, W. Tress, A. Abate, A. Hagfeldt, M. Grätzel, *Energy Environ. Sci.* **2016**, 9, 1989.
- [4] N. J. Jeon, J. H. Noh, Y. C. Kim, W. S. Yang, S. Ryu, S. Il Seok, *Nat. Mater.* **2014**, 13, 1.
- [5] NREL Best Research Cell Efficiencies, <http://www.nrel.gov/pv/assets/images/efficiency-chart.png>, (accessed: January 2017).
- [6] J. Yang, B. D. Siempelkamp, D. Liu, T. L. Kelly, *ACS Nano* **2015**, 9, 1955.
- [7] B. Conings, J. Drijkoningen, N. Gauquelin, A. Babayigit, J. D'Haen, L. D'Olieslaeger, A. Ethirajan, J. Verbeeck, J. Manca, E. Mosconi, F. De Angelis, H.-G. Boyen, *Adv. Energy Mater.* **2015**, 5, 1500477.
- [8] N. J. Jeon, J. H. Noh, W. S. Yang, Y. C. Kim, S. Ryu, J. Seo, I. Sang, *Nature* **2015**, 517, 476.
- [9] K. Domanski, J.-P. Correa-Baena, N. Mine, M. K. Nazeeruddin, A. Abate, M. Saliba, W. Tress, A. Hagfeldt, M. Grätzel, *ACS Nano* **2016**, 10, 6306.
- [10] S. N. Habisreutinger, T. Leijtens, G. E. Eperon, S. D. Stranks, R. J. Nicholas, H. J. Snaith, *J. Phys. Chem. Lett.* **2014**, 5, 4207.
- [11] S. N. Habisreutinger, T. Leijtens, G. E. Eperon, S. D. Stranks, R. J. Nicholas, H. J. Snaith, *Nano Lett.* **2014**, 14, 5561.
- [12] R. Ihly, A.-M. Dowgiallo, M. Yang, P. Schulz, N. Stanton, O. G. Reid, A. Ferguson, K. Zhu, J. J. Berry, J. Blackburn, *Energy Environ. Sci.* **2016**, 9, 1439.
- [13] Z. Li, S. A. Kulkarni, P. P. Boix, E. Shi, A. Cao, K. Fu, S. K. Batabyal, J. Zhang, Q. Xiong, L. H. Wong, N. Mathews, S. G. Mhaisalkar, *ACS Nano* **2014**, 8, 6797.
- [14] A. Mei, X. Li, L. Liu, Z. Ku, T. Liu, Y. Rong, M. Xu, M. Hu, J. Chen, Y. Yang, M. Grätzel, H. Han, *Science* **2014**, 345, 295.
- [15] H. Zhou, Y. Shi, Q. Dong, H. Zhang, Y. Xing, K. Wang, Y. Du, T. Ma, *J. Phys. Chem. Lett.* **2014**, 5, 3241.
- [16] K. Aitola, K. Sveinbjörnsson, J. P. Correa Baena, A. Kaskela, A. Abate, Y. Tian, E. M. J. Johansson, M. Grätzel, E. Kauppinen, A. Hagfeldt, G. Boschloo, *Energy Environ. Sci.* **2016**, 9, 461.
- [17] N. Saran, K. Parikh, D.-S. Suh, E. Muñoz, H. Kolla, S. K. Manohar, *J. Am. Chem. Soc.* **2004**, 126, 4462.
- [18] A. Kaskela, A. G. Nasibulin, M. Y. Timmermans, B. Aitchison, A. Papadimitratos, Y. Tian, Z. Zhu, H. Jiang, D. P. Brown, A. Zakhidov, E. I. Kauppinen, *Nano Lett.* **2010**, 10, 4349.
- [19] M. O. Reese, S. A. Gevorgyan, M. Jørgensen, E. Bundgaard, S. R. Kurtz, D. S. Ginley, D. C. Olson, M. T. Lloyd, P. Morvillo, E. A. Katz, A. Elschner, O. Haillant, T. R. Currier, V. Shrotriya, M. Hermenau, M. Riede, K. R. Kirov, G. Trimmel, T. Rath, O. Inganäs, F. Zhang, M. Andersson, K. Tvingstedt, M. Lira-Cantu, D. Laird, C. McGuinness, S. Gowrisanker, M. Pannone, M. Xiao, J. Hauch, R. Steim, D. M. DeLongchamp, R. Röscher, H. Hoppe, N. Espinosa, A. Urbina, G. Yaman-Uzunoglu, J.-B. Bonekamp, A. J. J. M. Van Breemen, C. Girotto, E. Voroshazi, F. C. Krebs, *Sol. Energy Mater. Sol. Cells* **2011**, 95, 1253.
- [20] J. P. Correa-Baena, M. Anaya, G. Lozano, W. Tress, K. Domanski, M. Saliba, T. Matsui, T. J. Jacobsson, M. E. Calvo, A. Abate, M. Grätzel, H. Miguez, A. Hagfeldt, *Adv. Mater.* **2016**, 7, 5031.
- [21] E. H. Anaraki, A. Kermanpur, L. Steier, K. Domanski, T. Matsui, W. Tress, M. Saliba, A. Abate, M. Grätzel, A. Hagfeldt, J.-P. Correa-Baena, *Energy Environ. Sci.* **2016**, 9, 3128.
- [22] PVWatts Calculator, <http://pvwatts.nrel.gov/>, n.d (accessed: 18 August 2016).
- [23] F. Giordano, A. Abate, J. Pablo, C. Baena, M. Saliba, T. Matsui, S. H. Im, S. M. Zakeeruddin, M. K. Nazeeruddin, A. Hagfeldt, M. Graetzel, *Nat. Commun.* **2016**, 7, 1.

Chapter 7 Migration of Cations Induces Reversible Performance Losses over Day/Night Cycling in Perovskite Solar Cells

THE CONTEXT

While pursuing high stability for perovskite solar cells, I discovered that perovskite devices degrade in a rather peculiar way, which is not necessarily typical for any other photovoltaic technology. I observed that very often, when devices are left in dark following ageing, they recover a large part of the lost performance. I identified two characteristic regimes of degradation: an initial, exponential one (mostly reversible) and a slower, linear one (mostly irreversible). After an in-depth analysis, I concluded that very slow cation migration in the perovskite is responsible for this behaviour.¹²⁶

This chapter is based on a peer-reviewed paper published in *Energy Environmental Science* in January 2017 entitled:

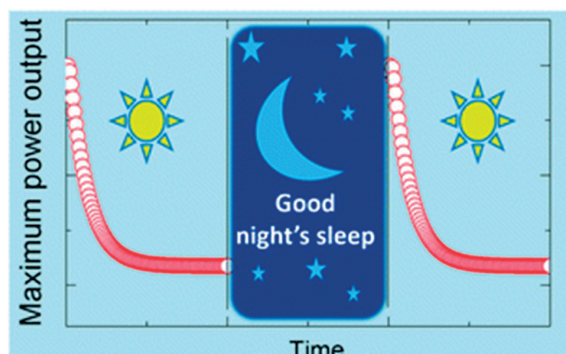
Migration of Cations Induces Reversible Performance Losses over Day/Night Cycling in Perovskite Solar Cells

authored by:

Konrad Domanski, Bart Roose, Taisuke Matsui, Michael Saliba, Silver-Hamill Turren-Cruz, Juan-Pablo Correa-Baena, Cristina Roldan Carmona, Giles Richardson, Jamie M Foster, Filippo De Angelis, James M Ball, Annamaria Petrozza, Nicolas Mine, Mohammad K Nazeeruddin, Wolfgang Tress, Michael Grätzel, Ullrich Steiner, Anders Hagfeldt and Antonio Abate.

My contribution:

I performed about half of the measurements presented in this work, prepared part of the figures, coordinated part of the collaborations in this project and wrote about half of the manuscript. Indeed, this work was a very large collaborative effort involving combination of many complimentary techniques and involvement of many people with diverse expertise, which was coordinated mostly by Antonio Abate.





Cite this: *Energy Environ. Sci.*,
2017, 10, 604

Migration of cations induces reversible performance losses over day/night cycling in perovskite solar cells†

Konrad Domanski,^a Bart Roose,^b Taisuke Matsui,^c Michael Saliba,^a Silver-Hamill Turren-Cruz,^d Juan-Pablo Correa-Baena,^d Cristina Roldan Carmona,^e Giles Richardson,^f Jamie M. Foster,^g Filippo De Angelis,^{hi} James M. Ball,^j Annamaria Petrozza,^j Nicolas Mine,^k Mohammad K. Nazeeruddin,^e Wolfgang Tress,^a Michael Grätzel,^a Ullrich Steiner,^b Anders Hagfeldt^d and Antonio Abate^{*ab}

Perovskites have been demonstrated in solar cells with a power conversion efficiency of well above 20%, which makes them one of the strongest contenders for next generation photovoltaics. While there are no concerns about their efficiency, very little is known about their stability under illumination and load. Ionic defects and their migration in the perovskite crystal lattice are some of the most alarming sources of degradation, which can potentially prevent the commercialization of perovskite solar cells (PSCs). In this work, we provide direct evidence of electric field-induced ionic defect migration and we isolate their effect on the long-term performance of state-of-the-art devices. Supported by modelling, we demonstrate that ionic defects, migrating on timescales significantly longer (above 10^3 s) than what has so far been explored (from 10^{-1} to 10^2 s), abate the initial efficiency by 10–15% after several hours of operation at the maximum power point. Though these losses are not negligible, we prove that the initial efficiency is fully recovered when leaving the device in the dark for a comparable amount of time. We verified this behaviour over several cycles resembling day/night phases, thus probing the stability of PSCs under native working conditions. This unusual behaviour reveals that research and industrial standards currently in use to assess the performance and the stability of solar cells need to be adjusted for PSCs. Our work paves the way for much needed new testing protocols and figures of merit specifically designed for PSCs.

Received 17th November 2016,
Accepted 10th January 2017

DOI: 10.1039/c6ee03352k

www.rsc.org/ees

Broader context

Perovskite solar cells have been recently demonstrated as a potential new photovoltaic technology. Better than any previous photovoltaic material, perovskite combines the advantage of low processing and high power conversion efficiency. Furthermore, perovskite solar cells can be used in tandem with market dominating silicon solar cells to increase their efficiency and thus to lower the price of solar energy. While there are no concerns about their efficiency, very little is known about the stability of perovskite solar cells under illumination and load, *i.e.* under real working conditions. So far, discussion about stability has been mainly focused on external factors, such as oxygen, water and UV light exposure, which are well-known causes of rapid performance degradation. However, performance losses occur even ruling out any external source of degradation. This work provides a step improvement in our knowledge of this phenomenon and it paves the way towards stable perovskite solar cells.

^a Laboratory for Photonics and Interfaces, Institute of Chemical Sciences and Engineering, École Polytechnique Fédérale de Lausanne, CH-1015-Lausanne, Switzerland.

E-mail: antonioabate83@gmail.com, Antonio.abate@unifr.ch

^b Adolphe Merkle Institute, University of Fribourg, Chemin des Verdiers 4, CH-1700 Fribourg, Switzerland

^c Advanced Research Division, Panasonic Corporation, 1006, (Oaza Kadoma), Kadoma City, Osaka 571-8501, Japan

^d Laboratory of Photomolecular Science, Institute of Chemical Sciences and Engineering, École Polytechnique Fédérale de Lausanne, CH-1015-Lausanne, Switzerland

^e Group for Molecular Engineering of Functional Materials, Institute of Chemical Sciences and Engineering, École Polytechnique Fédérale de Lausanne, CH-1015-Lausanne, Switzerland

^f Mathematical Sciences, University of Southampton, SO17 1BJ, UK

^g Department of Mathematics, University of Portsmouth, Portsmouth, PO1 2UP, UK

^h Computational Laboratory for Hybrid/Organic Photovoltaics (CLHYO), CNR-ISTM, Via Elce di Sotto 8, 06123 Perugia, Italy

ⁱ CompuNet, Istituto Italiano di Tecnologia, Via Morego 30, 16163 Genova, Italy

^j Center for Nano Science and Technology @Polimi, Istituto Italiano di Tecnologia, via, Giovanni Pascoli 70/3, 20133 Milan, Italy

^k Laboratory for Nanoscale Materials Science, Empa, Swiss Federal Laboratories for Material Science and Technology, Ueberlandstr. 129, 8600 Dübendorf, Switzerland

† Electronic supplementary information (ESI) available. See DOI: 10.1039/c6ee03352k

Introduction

Perovskite solar cells (PSCs) have the potential to become a new generation of photovoltaics with the shortest energy payback time and the lowest CO₂ emission factor among the existing technologies.¹ In only a few years, unprecedented progress in preparation procedures and material compositions has delivered lab-scale devices that have now reached power conversion efficiencies (PCEs) of up to 22.1%.² However, this impressive improvement of the PCE has not been matched by an equal advancement in the knowledge of the performance losses under standard working conditions (illumination and load).^{3–7}

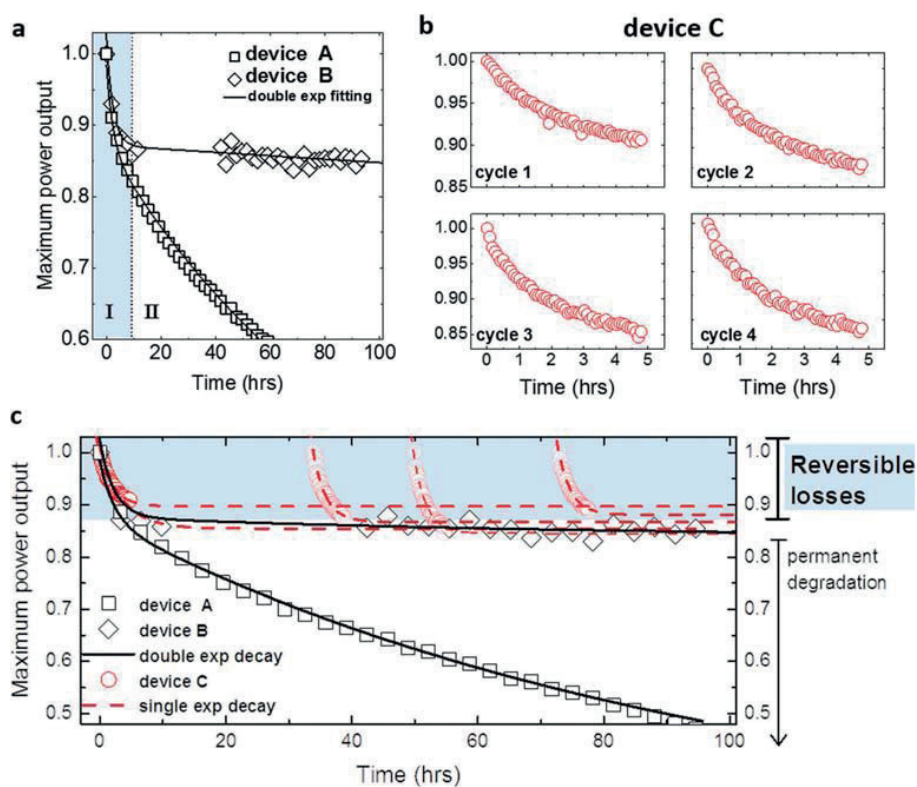
So far, discussion on the stability of PSCs has been mainly focused on oxygen,⁸ water⁵ and UV light exposure⁹ as causes of rapid performance degradation in PSCs. These extrinsic factors have been associated with a number of degradation mechanisms that can be retarded using the sealing technologies industrialised for organic electronics, which provide oxygen and humidity barriers and protection against UV light.^{10,11} Conversely, prolonged exposure to solar cell operational temperatures (above 50 °C) can cause severe degradation, which cannot be avoided by sealing the PSCs. These, so called intrinsic losses have been mostly associated with the degradation of organic materials and metal contacts within PSCs.^{3,12,13} Indeed, significant progress has been made by replacing the organic components with their inorganic counterparts and passivating the interfaces between the different layers composing the device.^{13–18} Nonetheless, temperature activated formation and migration of ionic defects within the organic–inorganic ABX₃ perovskite lattice remain potential sources of instability for perovskite photovoltaics.^{19–22} Halide anion (X) vacancies have been calculated to show the lowest formation energies,²³ with bromide vacancies being favoured over iodide.²⁴ Correspondingly, X vacancies (together with interstitial X) have been shown to be the most mobile defects, followed by cation A and B vacancies.^{25–27} Several studies indicated that, regardless of particular architectures and constituents within the PSCs, X defects migrate and reversibly accumulate within the perovskite lattice in narrow Debye layers at the interfaces with the charge selective contacts.^{19,28–34} Depending on voltage and light bias conditioning, accumulation of ions (and their vacancies) partially screens the built-in electric field and possibly creates interfacial electronic trap states, which reduce the charge extraction efficiency.^{25,30,31,34–43} Ion migration on timescales from 10^{–1} to 10² s has been widely investigated to explain the hysteresis of current density–voltage (*J*–*V*) curves.^{36,37,40,44–48} However, the impact of X and potentially A and/or B defect formation and migration on PSC performance on timescales above 10³ s, which are indicative of long-term stability, remains unknown.⁴⁹ Little experimental evidence exists on this subject since separating reversible ion migration from any non-reversible long-term degradation is complex under real device working conditions, *i.e.* prolonged exposure to continuous light and voltage bias.^{29,39,50–55}

In this work, we provide direct evidence of electric field-induced ion migration and its effects on the long-term performance

of perovskite solar cells working under different loads. By cooling *in situ* the active area of working PSCs, we are able to inhibit thermally induced, non-reversible degradation, thereby exposing fully reversible performance losses. Within several hours of operation at the maximum power point (MPP), the reversible losses decrease a significant fraction of the initial PCE, which is followed by a period of stabilization. Supported by modelling and elemental depth profiling, we correlate the reversible performance losses in PSCs to the migration of ion vacancies on timescales (above 10³ s) that are significantly longer than those explored so far (from 10^{–1} to 10² s). These unusually slow dynamics reveal that academic and industrial standards currently in use to assess the performance and stability of solar cells need to be adjusted for PSCs, which exhibit phenomena previously unknown to the photovoltaics community. Importantly, we show that over natural day/night cycles, PSCs that reversibly degrade during the day recover overnight to “start fresh” every morning. Our work paves the way towards developing specific testing protocols, definition of new figures of merits and calculation of energy payback time that are needed to characterize PSCs.

Results and discussion

To study the impact of the long-term ion migration on device performance and stability, we prepared state-of-the-art PSCs, using the mixed halide–cation perovskite composition CH₃NH₃/CH(NH₂)₂Pb Br/I and the antisolvent deposition method on mesoporous TiO₂ substrates,⁵⁶ which enabled the realization of power conversion efficiencies above 20% (see device characterization in ESI†). We tracked the maximum power output of 3 identically prepared devices (device A, B and C in Fig. 1). During the experiment, the devices were kept under 1 Sun-equivalent white LED illumination at MPP (around 0.85 V) and under a N₂ atmosphere. Devices A and B were continuously tracked for over 100 hours. As previously reported,^{3,7,13} the maximum power output traces can be described with a double exponential decay function showing an initial rapid (I in Fig. 1a) and a subsequent slower decay regime (II in Fig. 1a).^{3,7,13} We have previously shown that the latter (regime II) is due to degradation involving one or more device components, while the early decay (regime I) remains unexplained so far and it will be the main object of this study.^{3,7} We selected two devices exhibiting very different II regimes: a rather unstable device A (residual power output *J*₀ = 25%, Table 1) and device B showing particularly good stability (residual power output *J*₀ = 84%, Table 1). Since long-term degradation is a convolution of several mechanisms that may abruptly impact the performance,⁵⁷ it is not surprising that identically prepared devices age differently. However, it is rather unexpected that they have identical time constants for the decay regime I (*t*₁ in Table 1). To isolate regime I from the subsequent degradation (regime II), the maximum power point tracking (MPPT) for device C was stopped after only 5 hours and repeated periodically after leaving the device resting in the dark for a varying number of hours (Fig. 1b). Surprisingly, the initial



Published on 10 January 2017. Downloaded by ECOLE POLYTECHNIC FED DE LAUSANNE on 29/06/2017 16:22:24.

Fig. 1 Maximum power output tracking for 3 identically prepared perovskite solar cells (device A, B and C) measured under UV-filtered 1 Sun equivalent light. Devices were continuously kept at the maximum power point using the standard “perturb and observe” method. The efficiency of all freshly made devices was above 20% (see ESI†) and it dropped to around 17–18% after 2–3 weeks, when the stability data were recorded. Data were normalized to the maximum value, which was usually reached within several minutes of tracking. (a) Devices A and B were continuously tracked for over 100 hours. (b) Device C was cyclically tracked 4 times for 5 hours and it was left in the dark at open circuit in between the consecutive measurements. (c) Experimental data were fitted to an exponential decay (single or double) and the fitting parameters are reported in Table 1.

Table 1 Fitting parameters of the exponential decay functions used in Fig. 1. The device A and B curves were fitted with a double exponential decay function $J = A_1 \exp(-x/t_1) + A_2 \exp(-x/t_2) + J_0$, where t is the time constant, J_0 is the residual power output and A is the pre-exponential factor. The device C curves were fitted with a single exponential decay function $J = A_1 \exp(-x/t_1) + J_0$

	t_1 (h)	J_0 (residual power %)
Device A	2.3 ± 0.2	25 ± 1
Device B	2.3 ± 0.2	84 ± 2
Device C, cycle 1	2.1 ± 0.05	90 ± 0.1
Device C, cycle 2	2.0 ± 0.04	87 ± 0.1
Device C, cycle 3	1.9 ± 0.04	85 ± 0.1
Device C, cycle 4	2.0 ± 0.04	88 ± 0.1

power output at each cycle was similar or even slightly higher to the previous one, demonstrating that the initial performance losses are fully reversible (regime I) and are thus separated from the subsequent permanent degradation (regime II). The decay traces and exponential fits of devices A, B and C are summarized in Fig. 1c. The residual power output for device C

at each cycle (dashed line in Fig. 1c, J_0 in Table 1) lies between 0.85 and 0.9, similar to what was extracted for the more stable device B after 100 hours of MPPT. This confirms that the performance losses in device B are mostly reversible, with a marginal contribution of permanent degradation. We repeated this experiment for devices with planar and inverted architectures, varying the electron and hole selective contact materials (see ESI†), with similar conclusions. While we collected data for PSCs prepared with mixed halide-cation perovskites, reversible losses have been observed for a broad range of perovskite compositions.^{18,52–54,58} Therefore, we confidently conclude that reversible losses are intrinsic to the perovskite as a photovoltaic material and not to specific material composition or device architecture.

It is worth noting that the characteristic times for the reversible degradation/recovery are representative of the native working conditions for solar cells, *i.e.* day/night cycles. Therefore, a PSC producing energy during the day will have time to recover during the night to “start fresh” every morning. This finding has

an important practical implication for establishing industrial benchmarks for ageing and cost/operation time calculations of PSCs.

Reversible performance degradation as a result of light soaking has been previously investigated by Bag *et al.*⁵² and Nie *et al.*⁵⁴ In both the studies, the authors concluded that the heat from sunlight is responsible for lattice strain and consequent defect formation. In contrast to the existing literature, we studied the reversible losses under real device working conditions, *i.e.* prolonged exposure to continuous light and voltage bias around MPP. We postulated that the migration of ions and ion defects is the cause of reversible losses. In order to provide direct evidence of ion migration, we deposited a PbI_2 layer on top of a $\text{CH}_3\text{NH}_3\text{PbBr}_3$ perovskite layer in capacitor-like devices, as represented in the schematic in Fig. 2a. These devices were heated to 70 °C in a nitrogen atmosphere and one of the pixels was cyclically biased at +2 and -2 V every 30 minutes (leakage current remained below $\pm 1 \text{ mA cm}^{-2}$). After 16 hours, we found that the biased pixel had changed its colour to black, while the unbiased pixel (also kept at 70 °C) remained yellow, as clearly visible in Fig. 2b. Notably, the colouring of the biased pixel accurately follows the overlap between the top (gold) and the bottom (FTO) electrodes. This suggests that, in response to the

electric field, ions migrate between the yellow $\text{CH}_3\text{NH}_3\text{PbBr}_3$ and PbI_2 layers to form the black $\text{CH}_3\text{NH}_3\text{PbI}_x\text{Br}_{(3-x)}$ perovskite. We made use of time of flight secondary ion mass spectrometry (ToF-SIMS) to measure the effective elemental changes within the layers.⁵⁹ From the I_2^- and Br_2^- elemental depth profiles shown in Fig. 2c and d, we found that the iodine and bromine distributions are significantly changed in the biased pixel compared to the control one. In particular, we observe strong halide mixing, which results in the formation of black $\text{CH}_3\text{NH}_3\text{PbI}_x\text{Br}_{(3-x)}$. This constitutes strong direct evidence that halides can indeed migrate within the perovskite driven by an electric field and not due to thermal activation or electric current.^{52,60-62}

We also analysed the ToF-SIMS depth profiles looking for an indication of organic cation diffusion (by tracing CN^- signal). Unfortunately, the depth profiles did not qualitatively correspond to the expected CN^- distribution in the control sample (see figure in ESI†) and hence we deemed the analysis inconclusive (we also found a large amount of organic contamination on the surface of the sample). Additionally, we performed energy-dispersive X-ray (EDX) spectroscopy on the cross-section of the same device (see figure in ESI†). However, again we could not conclude whether the cations are mobile, largely due to the fact that the technique is not suited for tracing lightweight elements constituting CH_3NH_3^+

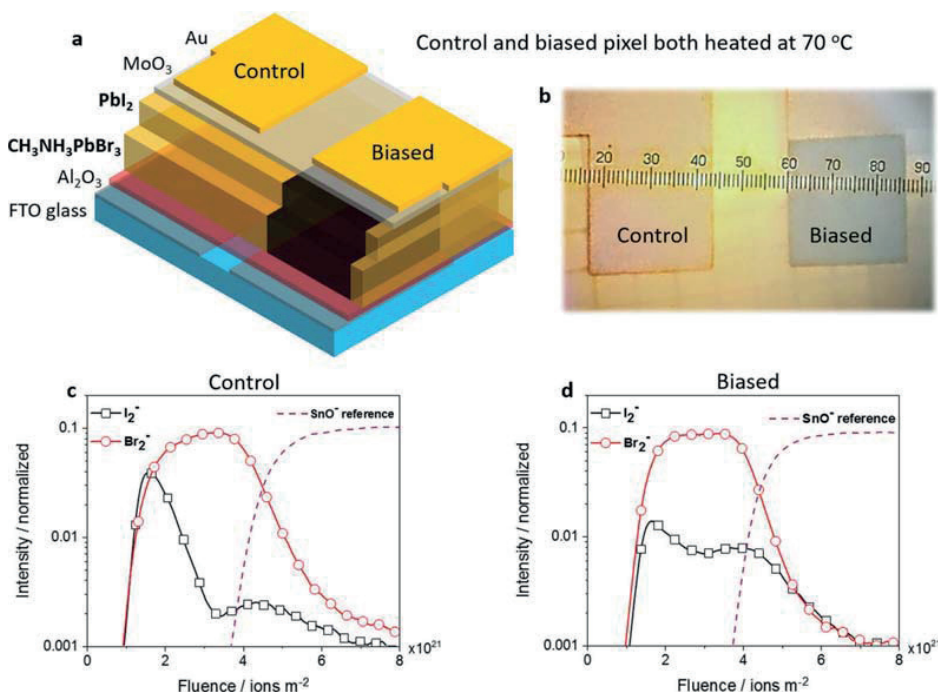


Fig. 2 (a) Schematics of the sample prepared for the biasing experiment, consisting of two electronically-separated pixels on the same substrate. Both pixels were heated to 70 °C in a N_2 atmosphere. Only one pixel was cyclically biased at +2 and -2 V every 30 minutes for 16 hours (biased pixel). (b) Top view image of the sample after biasing (scale in millimetre). Time of flight secondary ion mass spectrometry (ToF-SIMS) depth profiles of the control (c) and biased (d) pixels showing the relative secondary ion intensity of iodine and bromine clusters across the film depth. The SnO^- signals coming from the fluorine doped SnO_2 (FTO glass) are used as a reference, to which all traces in the respective graph are normalized.

ions (the fact that the devices had to be coated with C prior to the analysis, made the analysis even more challenging). Given that it is not trivial to provide direct evidence of organic cation migration, we made use of electric measurements supported by modelling to prove it indirectly.

We used intensity modulated photocurrent spectroscopy (IMPS) to monitor ion migration during device operation at the voltages highlighted in the J - V curve in the inset in Fig. 3a.⁶³ The photocurrent was allowed to settle at each voltage for 300 s before the frequency scan. Fig. 3a shows the imaginary component of the IMPS frequency spectra. The traces show two features in the high frequency region, which we assign to the resonant frequencies of the charge dynamics within the perovskite layer (above 10^5 Hz) and the electron/hole charge selective materials (between 10^4 and 10^5 Hz).⁶⁴ The spectra are similar in this region, which suggests that charge transport is not significantly

affected by the voltage applied. An additional feature at around 10^2 Hz is clearly visible in the low frequency region. We have previously associated the 10^{-1} - 10^3 Hz (or 10^{-3} - 10 s) resonant frequency window with the ion defect migration within the perovskite crystal lattice.^{64,65} The migration and accumulation of ionic defects at the interfaces with the charge selective contacts result in the formation of two narrow Debye layers (DLs).³⁴ The qualitative relation between the DL capacitance and the applied voltage was recently derived from the drift diffusion model proposed by Richardson *et al.*³⁴ Different from the previous report, here we are taking into account processes occurring on both the relatively short timescale of the spectroscopic oscillations (10^{-3} - 10 s) and on the longer settling time (300 s) before the start of the frequency scan (Fig. 3b, see the ESI† for more details). Based on the calculations of activation energies for migration of different ionic defects in $\text{CH}_3\text{NH}_3\text{PbI}_3$, negatively-charged cation vacancies show significantly lower mobility than positively-charged halide vacancies.^{20,25,26,66-68} Given that cation vacancies are slower than the halide ones, three different scenarios are possible: (I) only halide vacancies are mobile on both spectroscopic (10^{-3} - 10 s) and settling (300 s) timescales, while all the other defects remain effectively frozen; (II) cation vacancies are sufficiently mobile to equilibrate within the DLs during the settling time, but they are effectively immobile on the spectroscopic timescale; and (III) both halide and cation vacancies are sufficiently mobile to equilibrate within the DLs on the spectroscopic timescale. We found that the experimental trend in Fig. 3a was best reproduced by the model that accounts for halide vacancy migration, but does not directly account for the slowly moving cation vacancies even on the 300 s settling timescale. This observation suggests that if cation vacancies are effectively mobile, they should migrate over a timescale of hours.

To provide evidence that cation vacancies are effectively mobile we measured the current transient dynamics at short circuit after preconditioning the device at either forward (0.85 V) or reverse (-0.3 V) bias (Fig. 4a). Under each biasing condition, we waited for the current to stabilize for about 20 minutes at 20°C , before cooling the device to -20°C and switching it abruptly to short circuit conditions. By cooling down the device, we aimed to retard ion migration and capture the transient dynamics resulting from the initial non-equilibrium ion distribution. Following forward bias preconditioning, the short circuit current (J_{sc}) rapidly decreased from over 23 mA cm^{-2} towards a value of around 14 mA cm^{-2} . In contrast, subsequent to preconditioning at reverse bias, J_{sc} increases from 4 mA cm^{-2} to around 13 mA cm^{-2} . Notably, in these two experiments J_{sc} does not relax to the same value over the 100 s over which the transient is measured; there is a secondary slow timescale process which we attribute to the slow motion of cation vacancies. In order to back up this assertion, we calculate the short circuit current based on (I) a model of the perovskite layer in which only halide vacancies are mobile (Fig. 4b, left-hand panel) and (II) a model in which both halide and cation vacancies are mobile (Fig. 4b, right-hand panel) but where cation vacancies move 100 times more slowly than halide vacancies (see the ESI† for further details). It can be seen from Fig. 4 that while the model with immobile cation

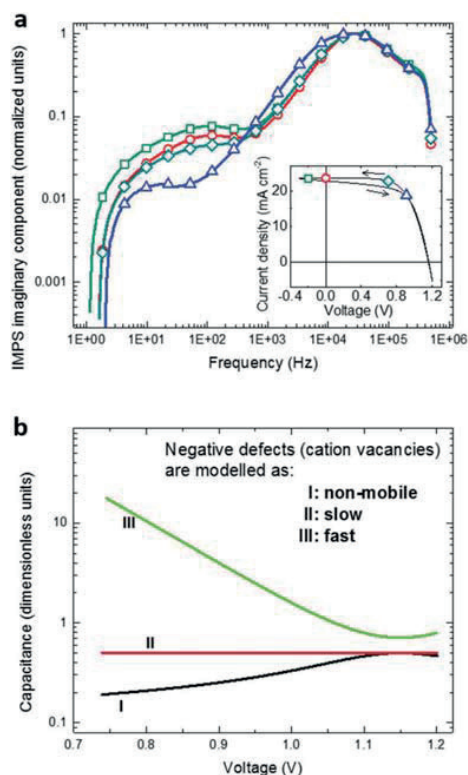


Fig. 3 (a) Imaginary component frequency spectra of the current response to the light modulated (10% of the stationary value) ~ 1 Sun equivalent intensity under different applied voltage biases. Data were normalized to the maximum value corresponding to the peak between 10 and 100 kHz. The inset shows the J - V curve recorded for the same devices at 100 mV s^{-1} scan rate. (b) Model calculation of the capacitance per unit surface area at the edge of the perovskite layer as a function of the forward applied voltage bias, assuming the negative defects (cation vacancies) as non-mobile, slow or fast, compared to the timescale of the spectroscopic oscillations in the low frequency region (10^{-1} - 10^3 Hz).

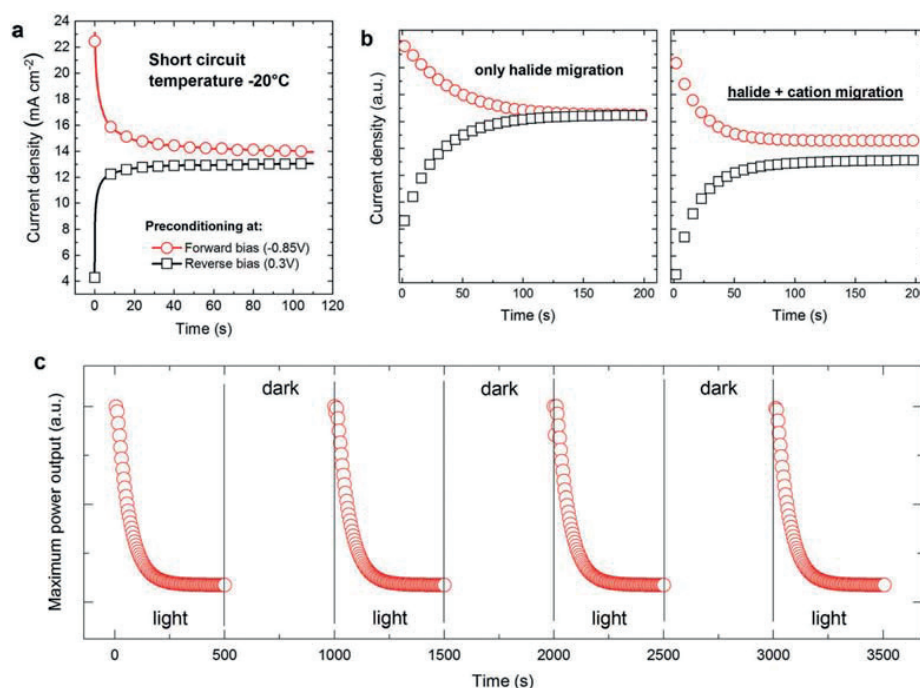


Fig. 4 (a) Current transient dynamics collected from the same device pre-condition for about 20 minutes under forward (0.85 V) or reverse (-0.3 V) bias and cooled to -20 °C before to abruptly switch to short circuit conditions. (b) Modelled current transient dynamics as predicted by the evolution of the potential (left panel – considering only halide vacancy migration, and right panel – considering fast halide and slow cation vacancy migration). (c) The modelled maximum power conversion efficiency (with fast halide and slow cation vacancy migration) over 4 cycles of light and dark shows similar (non-quantitative) reversible performance losses to the experiment in Fig. 1.

Published on 10 January 2017. Downloaded by ECOLE POLYTECHNIC FED DE LAUSANNE on 29/06/2017 16:22:24.

vacancies is able to qualitatively predict the initial part of the transients, it fails to capture the slow timescale decay. However, the inclusion of slow moving cation vacancies into the model (Fig. 4b, right-hand panel) gives a picture closer to the reality (Fig. 4a) in which there is an initial rapid transient, over tens of seconds, followed by a much longer timescale decay.

In order to investigate the conjecture that the reversible decay in efficiency shown in Fig. 1 (which occurs over a timescale of around 1 hour) is due to the slow motion of cation vacancies, we simulate the current produced by the device as the light is switched on and off a number of times; the results are shown in Fig. 4c and qualitatively reproduce the behaviour seen in Fig. 1c for device C (plotted in red circles). We conclude, by remarking, that slow cation vacancy motion thus provides a theory that is capable of explaining both the slow timescale decay in transient short circuit current measurements (Fig. 4a) and the reversible decay in efficiency observed in PSCs after prolonged exposure to light (Fig. 1c).

To summarize, we have observed that PSCs degrade reversibly on the timescale of hours regardless of the device architecture. We have also proven that both halide and cation vacancies are mobile (albeit the latter are considerably slower than the former) and their distribution in the perovskite layer can considerably affect charge extraction and, in consequence, the PCE of the device.

Fig. 5 shows a simplistic schematic to condense the results of the experiments and model calculations discussed here. The images represent the halide lattice within the perovskite with ionic vacancies. The initial condition (a) describes a stoichiometric amount of anion and cation vacancies, which are randomly distributed in the perovskite lattice as proposed by Walsh *et al.*⁶⁹ (b) Up to 10^2 s (*i.e.* minutes) after the device was exposed to light and switched to MPP, halide vacancies migrate to form a Debye layer at the interface with hole selective contact, leaving the relatively immobile cation vacancies behind. (c) For timescales longer than 10^3 s (*i.e.* hours), cation vacancies form an additional Debye layer at the interface with the electron selective contact, which in turn inhibits charge extraction from the device. Hence we come back to the original experiment shown in Fig. 1. When PSCs are exposed to real operating conditions, slow cation migration is responsible for the reversible losses in the device on the timescale of hours. However, when the device is given several hours to recover in the dark, the ionic distribution returns to the initial state and the device appears to be “fresh”. The strong asymmetry in the activation energy for migration of halide and cation vacancies implies that stabilization times on the order of hours (not minutes as widely believed) are required for PSCs to reach true steady-state working conditions. This implies that traditional solar cell characterization methods,

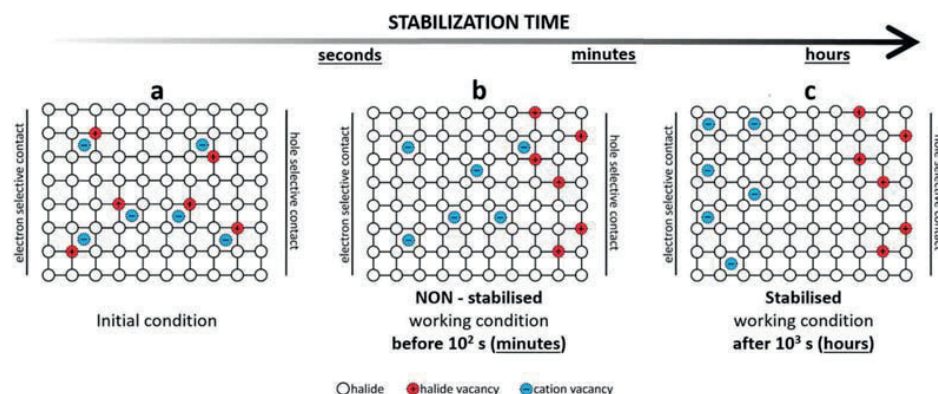


Fig. 5 Schematics of the evolution of the ion distribution within the perovskite layer sandwiched between the electron and hole selective contacts under solar cell working conditions: (a) initial conditions, (b) non-stabilized conditions on the timescale of minutes and (c) the stabilized condition on the timescale of hours.

such as measurements of standard $J-V$ curves and incident photon to current efficiency (IPCE) spectra, are usually performed on non-stabilized devices. We propose the maximum power point tracking for several hours as the most reliable method to determine the initial efficiency and the stability of PSCs.

Conclusions

In this work, we investigated the impact of the ionic defect migration on the performance and stability of state-of-the-art perovskite solar cells (PSCs). We provide direct evidence of halide migration within the perovskite as a result of the applied electric field. In line with previous reports, we found that halide vacancies migrate and accumulate at the interface with the hole selective contact on timescales between 10^{-1} and 10^2 s. The accumulation of interfacial halide vacancies increases as the applied voltage moves from forward to reverse bias, which results in the occurrence of the well-known hysteresis in the current density–voltage curves of PSCs. In addition to what has been explored previously, we propose that cation vacancies migrating on significantly longer timescales (above 10^3 s) than halide vacancies play a key role in the long-term performance of PSCs. We show that the accumulation of cation vacancies at the electron contact induces reversible performance losses that abate the initial efficiency of state-of-the-art PSCs by about 10–15% over several hours of operation at the maximum power point. Although these losses are not negligible, the initial efficiency is fully recovered when leaving the device in the dark for a comparable amount of time. We verified this behaviour for devices with different architectures over several cycles resembling day/night phases. We show that PSCs recover their initial efficiency during the night and deliver, every morning, the same efficiency as freshly made devices. This unusual behaviour reveals that research and industry standards currently in use to assess the performance and the stability of solar cells need to be reconsidered for PSCs. Our work provides indications

for the much needed new testing protocols and figures of merits specifically designed for PSCs.

Methods section

General methods

All the chemicals were purchased from commercial sources and used without further purification. All the solvents were anhydrous and high purity grade.

Solar cells fabrication

Devices were fabricated on fluorine doped tin oxide (FTO) coated glass substrates. The substrates were cleaned sequentially with Hellmanex in an ultrasonic bath for 30 min, then washed with acetone and isopropanol, and finally cleaned with oxygen plasma for 5 min. An about 30 nm TiO_2 compact layer was deposited on about 150 cm^2 of FTO *via* spray pyrolysis at 450°C from a precursor solution prepared with 0.4 mL of acetyl acetone (Aldrich), 0.6 mL of titanium diisopropoxide bis(acetylacetonate) solution (Aldrich, 75% in 2-propanol) and 9 mL of ethanol. After spraying, the substrates were left at 450°C for 5 min, then they were slowly cooled down to room temperature. A mesoporous TiO_2 layer was deposited by spin coating for 10 s at 4000 rpm with a ramp of 2000 rpm s^{-1} , using 30 nm particle paste (18NR-T Dyesol) diluted in ethanol to achieve about 150 nm thick layer. After spin coating, the substrate was immediately dried at 100°C for 10 min and then sintered again at 500°C for 30 min under dry air flow. Mesoporous TiO_2 was doped with lithium by spin coating a 0.1 M solution of Li-TFSI in acetonitrile at 3000 rpm for 30 s. After spin coating, the substrate was dried at 100°C for 10 min and then sintered again at 500°C for 30 min, under dry air flow. To minimize water absorption from the atmosphere, after cooling down to 150°C the substrates were immediately transferred to a nitrogen filled glove box and then kept for further cooling down to room temperature.

The perovskite films were deposited from a precursor solution containing formamidinium iodide (1 M), lead iodide (1.1 M), methylammonium bromide (0.2 M) and lead bromide (0.2 M) in a mixture of anhydrous dimethylformamide:dimethylsulfoxide 4:1 (v:v). The perovskite solution was spin coated using a two-step program at 1000 and 4000 rpm for 10 and 30 s, respectively. During the second step, 100 μ L of chlorobenzene was poured on the spinning substrate 15 s prior to the end of the program. The substrates were then annealed at 100 °C for 1 hour in a nitrogen filled glove box.

After perovskite annealing the substrates were cooled down for 1 minute and a spirofluorene linked methoxy triphenylamine (spiro-OMeTAD, from Merck) solution was spun at 4000 rpm for 20 s. The spiro-OMeTAD solution was prepared in chlorobenzene at a concentration of 70 mM, and doped with 50 mol% of bis(trifluoromethanesulfonyl)imide (Li-TFSI, Aldrich) from a stock solution of 1.8 M Li-TFSI in acetonitrile, 330 mol% of *tert*-butylpyridine (Aldrich) and 3 mol% of Tris(2-(1*H*-pyrazol-1-yl)-4-*tert*-butylpyridine)-cobalt(III) Tris(bis(trifluoromethylsulfonyl)-imide) (Co-complex, Dyesol) from a 0.25 M stock solution of Co-complex in acetonitrile. Finally, 80 nm of gold was deposited by thermal evaporation under high vacuum, using shadow masking to pattern the electrodes.

Solar cell characterisation

The solar cells were measured using a 450 W xenon light source (Oriel). The spectral mismatch between AM1.5G and the simulated illumination was reduced by the use of a Schott K113 Tempax filter (Präzisions Glas & Optik GmbH). The light intensity was recorded using a Si photodiode equipped with an IR-cutoff filter (KG3, Schott) before each measurement. Current density–voltage (*J*-*V*) characteristics of the cells were obtained by applying an external voltage bias while measuring the current response using a digital source meter (Keithley 2400). The cells were masked with a black metal mask (0.16 cm²) to estimate the active area and reduce the influence of scattered light. The devices were stored in dry air and under dark conditions, and they were characterized two days after perovskite film deposition.

The solar cell current transient dynamics (potentiostatic) and the maximum power point tracking data were measured under 1 Sun equivalent white LED illumination using an SP300 biologic potentiostat. Maximum point tracking was done using a home-developed program, which would keep the devices at the maximum power point by creeping oscillation in voltage and which would measure a full *J*-*V* curve every 60 minutes. The devices were placed inside an in-house-developed airtight sample holder, which allowed them to be kept under an inert, nitrogen atmosphere. Additionally, the backside metal electrode of the devices was placed against a Peltier element, which with the use of a PID controller would keep the actual temperature of the device at 20 °C regardless of the illumination or ambient temperature.

Intensity modulated photocurrent spectroscopy was performed using Autolab PGSTAT302N according to the procedures reported previously.⁶⁵

Time of flight secondary ion mass spectrometry (ToF-SIMS)

Samples were prepared with the following configuration: on top of patterned FTO glass, 10 nm of a compact Al₂O₃ layer was deposited. Subsequently, a 500 nm layer of CH₃PbBr₃ was deposited by spin-coating and a 200 nm-thick layer of PbI₂ was thermally evaporated. Finally, a 50 nm layer of MoO₃ and the Au electrode were thermally evaporated. Two electronically separated devices (pixels) were fabricated on each substrate. Both pixels were heated to 70 °C under nitrogen atmosphere and ambient light conditions. One pixel was cycling biased (± 2 V with 1 hour period) for 16 hours. During biasing the currents flowing through the pixel remained below 1 mA cm⁻². ToF-SIMS was performed on biased and control pixels according to the method previously reported.¹³

Drift diffusion simulations

The complete drift diffusion model was published by Richardson *et al.* elsewhere.³⁴ The details of the calculation are reported in the ESI.†

Acknowledgements

A. A. received funding from the European Union's Seventh Framework Programme for research, technological development and demonstration under grant agreement no. 291771. K. D. thanks the SNF for funding within the framework of Umbrella project (Grant agreement no. 407040-153952 and 407040-153990). M. S. acknowledges support from the co-funded Marie Skłodowska Curie fellowship, H2020 Grant agreement no. 665667. N. M. acknowledges support from the BNF program of the University of Bern. Prof. Dr Hans J. Hug, Dr Laetitia Bernard and Prof. Dr Arnaud Delcorte are gratefully acknowledged, respectively, for N. M. EMPA affiliation and access to the ToF-SIMS software. U. S., A. A. and B. R. thank the Adolphe Merkle Foundation and the NRP 70 Energy Turnaround – SNF.

References

- J. Gong, S. B. Darling and F. You, *Energy Environ. Sci.*, 2015, **8**, 1953–1968.
- NationalRenewableEnergyLaboratory, Best research-cell efficiencies, http://www.nrel.gov/ncpv/images/efficiency_chart.jpg.
- A. Abate, S. Paek, F. Giordano, J.-P. Correa-Baena, M. Saliba, P. Gao, T. Matsui, J. Ko, S. M. Zakeeruddin and K. H. Dahmen, *Energy Environ. Sci.*, 2015, **8**, 2946–2953.
- J. You, L. Meng, T.-B. Song, T.-F. Guo, Y. M. Yang, W.-H. Chang, Z. Hong, H. Chen, H. Zhou and Q. Chen, *Nat. Nanotechnol.*, 2016, **11**, 75–81.
- Z. Song, A. Abate, S. C. Watthage, G. K. Liyanage, A. B. Phillips, U. Steiner, M. Graetzel and M. J. Heben, *Adv. Energy Mater.*, 2016, **6**, 1600846.
- R. J. Sutton, G. E. Eperon, L. Miranda, E. S. Parrott, B. A. Kamino, J. B. Patel, M. T. Hörlantner, M. B. Johnston, A. A. Haghighirad and D. T. Moore, *Adv. Energy Mater.*, 2016, **6**, 1502458.

- 7 M. Saliba, T. Matsui, J.-Y. Seo, K. Domanski, J.-P. Correa-Baena, M. K. Nazeeruddin, S. M. Zakeeruddin, W. Tress, A. Abate and A. Hagfeldt, *Energy Environ. Sci.*, 2016, **9**, 1989–1997.
- 8 D. Bryant, N. Aristidou, S. Pont, I. Sanchez-Molina, T. Chotchunangatchaval, S. Wheeler, J. R. Durrant and S. A. Haque, *Energy Environ. Sci.*, 2016, **9**, 1655–1660.
- 9 B. Roose, J. P. Correa Baena, K. C. Gödel, M. Graetzel, A. Hagfeldt, U. Steiner and A. Abate, *Nano Energy*, 2016, **30**, 517–522.
- 10 F. Bella, G. Griffini, J.-P. Correa-Baena, G. Saracco, M. Grätzel, A. Hagfeldt, S. Turri and C. Gerbaldi, *Science*, 2016, aah4046.
- 11 T. J. Wilderspin, F. De Rossi and T. M. Watson, *Sol. Energy*, 2016, **139**, 426–432.
- 12 A. Calloni, A. Abate, G. Bussetti, G. Berti, R. Yivlialin, F. Ciccacci and L. Duò, *J. Phys. Chem. C*, 2015, **119**, 21329–21335.
- 13 K. Domanski, J.-P. Correa-Baena, N. Mine, M. K. Nazeeruddin, A. Abate, M. Saliba, W. Tress, A. Hagfeldt and M. Grätzel, *ACS Nano*, 2016, **10**, 6306–6314.
- 14 A. Mei, X. Li, L. Liu, Z. Ku, T. Liu, Y. Rong, M. Xu, M. Hu, J. Chen and Y. Yang, *Science*, 2014, **345**, 295–298.
- 15 K. A. Bush, C. D. Bailie, Y. Chen, A. R. Bowering, W. Wang, W. Ma, T. Leijtens, F. Moghadam and M. D. McGehee, *Adv. Mater.*, 2016, **28**, 3937–3943.
- 16 S. Guarnera, A. Abate, W. Zhang, J. M. Foster, G. Richardson, A. Petrozza and H. J. Snaith, *J. Phys. Chem. Lett.*, 2015, **6**, 432–437.
- 17 B. Roose, K. C. Gödel, S. Pathak, A. Sadhanala, J. P. C. Baena, B. D. Wilts, H. J. Snaith, U. Wiesner, M. Grätzel and U. Steiner, *Adv. Energy Mater.*, 2016, **6**, 1501868.
- 18 M. Saliba, T. Matsui, K. Domanski, J.-Y. Seo, A. Ummadisisingu, S. M. Zakeeruddin, J.-P. Correa-Baena, W. R. Tress, A. Abate and A. Hagfeldt, *Science*, 2016, **354**, 206–209.
- 19 Z. Xiao, Y. Yuan, Y. Shao, Q. Wang, Q. Dong, C. Bi, P. Sharma, A. Gruverman and J. Huang, *Nat. Mater.*, 2015, **14**, 193–198.
- 20 Y. Yuan and J. Huang, *Acc. Chem. Res.*, 2016, **49**, 286–293.
- 21 Y. Shao, Y. Fang, T. Li, Q. Wang, Q. Dong, Y. Deng, Y. Yuan, H. Wei, M. Wang and A. Gruverman, *Energy Environ. Sci.*, 2016, **9**, 1752–1759.
- 22 Y. Zou and R. J. Holmes, *Adv. Energy Mater.*, 2016, **5**, 1500019.
- 23 W.-J. Yin, T. Shi and Y. Yan, *Appl. Phys. Lett.*, 2014, **104**, 063903.
- 24 A. Buin, R. Comin, J. Xu, A. H. Ip and E. H. Sargent, *Chem. Mater.*, 2015, **27**, 4405–4412.
- 25 J. M. Azpiroz, E. Mosconi, J. Bisquert and F. De Angelis, *Energy Environ. Sci.*, 2015, **8**, 2118–2127.
- 26 C. Eames, J. M. Frost, P. R. Barnes, B. C. O'regan, A. Walsh and M. S. Islam, *Nat. Commun.*, 2015, **6**, 7497.
- 27 J. Haruyama, K. Sodeyama, L. Han and Y. Tateyama, *J. Am. Chem. Soc.*, 2015, **137**, 10048–10051.
- 28 V. W. Bergmann, Y. Guo, H. Tanaka, I. M. Hermes, D. Li, A. Klasen, S. A. Bretschneider, E. Nakamura, R. Berger and S. A. Weber, *ACS Appl. Mater. Interfaces*, 2016, **8**, 19402–19409.
- 29 R. Cao, F. Xu, J. Zhu, S. Ge, W. Wang, H. Xu, R. Xu, Y. Wu, Z. Ma and F. Hong, *Adv. Energy Mater.*, 2016, **6**, 1600814.
- 30 S. Chen, X. Wen, R. Sheng, S. Huang, X. Deng, M. A. Green and A. Ho-Baillie, *ACS Appl. Mater. Interfaces*, 2016, **8**, 5351–5357.
- 31 P. Calado, A. M. Telford, D. Bryant, X. Li, J. Nelson, B. C. O'Regan and P. R. Barnes, arXiv preprint arXiv:1606.00818, 2016.
- 32 O. Hentz, Z. Zhao and S. Gradecak, *Nano Lett.*, 2016, **16**, 1485–1490.
- 33 I. Zarazua, J. Bisquert and G. Garcia-Belmonte, *J. Phys. Chem. Lett.*, 2016, **7**, 525–528.
- 34 G. Richardson, S. E. O'Kane, R. G. Niemann, T. A. Peltola, J. M. Foster, P. J. Cameron and A. B. Walker, *Energy Environ. Sci.*, 2016, **9**, 1476–1485.
- 35 S. D. Stranks, V. M. Burlakov, T. Leijtens, J. M. Ball, A. Goriely and H. J. Snaith, *Phys. Rev. Appl.*, 2014, **2**, 034007.
- 36 W. Tress, N. Marinova, T. Moehl, S. Zakeeruddin, M. K. Nazeeruddin and M. Grätzel, *Energy Environ. Sci.*, 2015, **8**, 995–1004.
- 37 W. Tress, J. P. Correa Baena, M. Saliba, A. Abate and M. Graetzel, *Adv. Energy Mater.*, 2016, **6**, 1600396.
- 38 S. van Reenen, M. Kemerink and H. J. Snaith, *J. Phys. Chem. Lett.*, 2015, **6**, 3808–3814.
- 39 J. Carrillo, A. Guerrero, S. Rahimnejad, O. Almora, I. Zarazua, E. Mas-Marza, J. Bisquert and G. Garcia-Belmonte, *Adv. Energy Mater.*, 2016, **6**, 1502246.
- 40 H. Yu, H. Lu, F. Xie, S. Zhou and N. Zhao, *Adv. Funct. Mater.*, 2016, **26**, 1411–1419.
- 41 S. Meloni, T. Moehl, W. Tress, M. Franckevičius, M. Saliba, Y. H. Lee, P. Gao, M. K. Nazeeruddin, S. M. Zakeeruddin and U. Rothlisberger, *Nat. Commun.*, 2016, **7**, 10334.
- 42 T. S. Ripolles, A. K. Baranwal, K. Nishinaka, Y. Ogomi, G. Garcia-Belmonte and S. Hayase, *Phys. Chem. Chem. Phys.*, 2016, **18**, 14970–14975.
- 43 O. Almora, C. Aranda, I. Zarazua, A. Guerrero and G. Garcia-Belmonte, *ACS Energy Lett.*, 2016, **1**, 209–215.
- 44 H. J. Snaith, A. Abate, J. M. Ball, G. E. Eperon, T. Leijtens, N. K. Noel, S. D. Stranks, J. T.-W. Wang, K. Wojciechowski and W. Zhang, *J. Phys. Chem. Lett.*, 2014, **5**, 1511–1515.
- 45 E. Unger, E. Hoke, C. Bailie, W. Nguyen, A. Bowering, T. Heumüller, M. Christoforo and M. McGehee, *Energy Environ. Sci.*, 2014, **7**, 3690–3698.
- 46 I. Levine, P. K. Nayak, J. T.-W. Wang, N. Sakai, S. Van Reenen, T. M. Brenner, S. Mukhopadhyay, H. J. Snaith, G. Hodes and D. Cahen, arXiv preprint arXiv:1604.03907, 2016.
- 47 T. Zhang, H. Chen, Y. Bai, S. Xiao, L. Zhu, C. Hu, Q. Xue and S. Yang, *Nano Energy*, 2016, **26**, 620–630.
- 48 Y. Zhao, W. Zhou, W. Ma, S. Meng, H. Li, J. Wei, R. Fu, K. Liu, D. Yu and Q. Zhao, *ACS Energy Lett.*, 2016, **1**, 266–272.
- 49 K. C. Kwon, K. Hong, Q. Van Le, S. Y. Lee, J. Choi, K. B. Kim, S. Y. Kim and H. W. Jang, *Adv. Funct. Mater.*, 2016, **26**, 4213–4222.

- 50 O. Almora, A. Guerrero and G. Garcia-Belmonte, *Appl. Phys. Lett.*, 2016, **108**, 043903.
- 51 S. Bae, S. Kim, S.-W. Lee, K. Cho, S. Park, S. Lee, Y. Kang, H.-S. Lee and D. Kim, *J. Phys. Chem. Lett.*, 2016, **7**, 3091–3096.
- 52 M. Bag, L. A. Renna, R. Y. Adhikari, S. Karak, F. Liu, P. M. Lahti, T. P. Russell, M. T. Tuominen and D. Venkataraman, *J. Am. Chem. Soc.*, 2015, **137**, 13130–13137.
- 53 F. Huang, L. Jiang, A. R. Pascoe, Y. Yan, U. Bach, L. Spiccia and Y.-B. Cheng, *Nano Energy*, 2016, **27**, 509–514.
- 54 W. Nie, J.-C. Blancon, A. J. Neukirch, K. Appavoo, H. Tsai, M. Chhowalla, M. A. Alam, M. Y. Sfeir, C. Katan and J. Even, *Nat. Commun.*, 2016, **7**, 11574.
- 55 J. S. Yun, J. Seidel, J. Kim, A. M. Soufiani, S. Huang, J. Lau, N. J. Jeon, S. I. Seok, M. A. Green and A. Ho-Baillie, *Adv. Energy Mater.*, 2016, **6**, 1600330.
- 56 N. J. Jeon, J. H. Noh, Y. C. Kim, W. S. Yang, S. Ryu and S. I. Seok, *Nat. Mater.*, 2014, **13**, 897–903.
- 57 X. Zhao and N.-G. Park, *Photonics*, 2015, **2**, 1139–1151.
- 58 E. H. Anaraki, A. Kermanpur, L. Steier, K. Domanski, T. Matsui, W. Tress, M. Saliba, A. Abate, M. Grätzel and A. Hagfeldt, *Energy Environ. Sci.*, 2016, **9**, 3128–3134.
- 59 A. M. Belu, D. J. Graham and D. G. Castner, *Biomaterials*, 2003, **24**, 3635–3653.
- 60 C. Li, S. Tscheuschner, F. Paulus, P. E. Hopkinson, J. Kießling, A. Köhler, Y. Vaynzof and S. Huettnner, *Adv. Mater.*, 2016, **28**, 2446–2454.
- 61 D. Li, H. Wu, H.-C. Cheng, G. Wang, Y. Huang and X. Duan, *ACS Nano*, 2016, **10**, 6933–6941.
- 62 S. J. Yoon, S. Draguta, J. S. Manser, O. Sharia, W. F. Schneider, M. Kuno and P. V. Kamat, *ACS Energy Lett.*, 2016, **1**, 290–296.
- 63 E. Guillén, F. J. Ramos, J. A. Anta and S. Ahmad, *J. Phys. Chem. C*, 2014, **118**, 22913–22922.
- 64 J. Y. Seo, T. Matsui, J. Luo, J. P. Correa-Baena, F. Giordano, M. Saliba, K. Schenk, A. Ummadisingu, K. Domanski and M. Hadadian, *Adv. Energy Mater.*, 2016, **6**, 1600767.
- 65 J. P. Correa-Baena, M. Anaya, G. Lozano, W. Tress, K. Domanski, M. Saliba, T. Matsui, T. J. Jacobsson, M. E. Calvo and A. Abate, *Adv. Mater.*, 2016, **28**, 5031–5037.
- 66 E. Mosconi and F. De Angelis, *ACS Energy Lett.*, 2016, **1**, 182–188.
- 67 D. Yang, W. Ming, H. Shi, L. Zhang and M.-H. Du, *Chem. Mater.*, 2016, **28**, 4349–4357.
- 68 W. Ming, S. Chen and M.-H. Du, *J. Mater. Chem. A*, 2016, **4**, 16975–16981.
- 69 A. Walsh, D. O. Scanlon, S. Chen, X. Gong and S. H. Wei, *Angew. Chem.*, 2015, **127**, 1811–1814.

Electronic Supplementary Material (ESI) for Energy & Environmental Science.
This journal is © The Royal Society of Chemistry 2017

Migration of cations induces reversible performance losses over day/night cycling in perovskite solar cells

*Corresponding author: AA antoniobate83@gmail.com

TABLE OF CONTENT

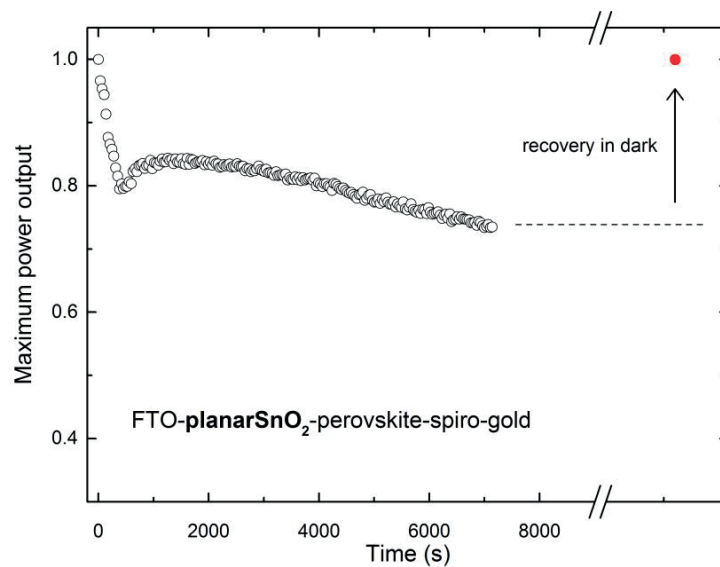
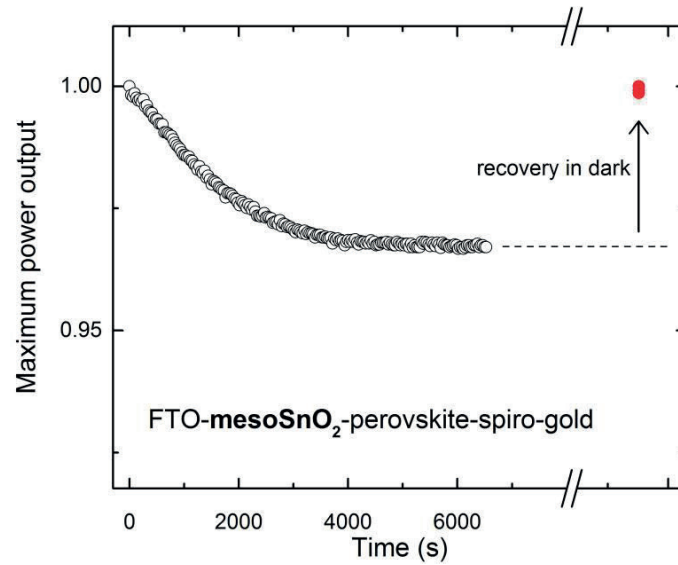
- Perovskite solar cells performance parameters
- Reversible losses in SnO₂-based mesoporous and planar perovskite solar cells
- Reversible losses in inverted perovskite solar cells
- Organic cation depth profiles by time of flight secondary ion mass spectrometry (ToF-SIMS)
- Energy dispersive X-ray spectroscopy (EDX) depth profiles
- Stabilized power output
- Incident Photon to Current Conversion Efficiency
- Equivalent circuit representation of the PSC based on drift diffusion modelling
- Model Poisson drift-diffusion equations

Perovskite solar cells performance parameters

Device	Voc (V)	Jsc (mA cm⁻²)	FF	PCE (%)
1	1134	23.4	0.75	20.3
2	1140	23.3	0.76	19.8
3	1104	22.4	0.78	20.2
4	1117	22.8	0.76	20.1
5	1116	23.0	0.74	19.8
6	1117	22.8	0.76	20.2
7	1109	23.5	0.75	20.2
8	1103	22.6	0.77	19.8
9	1083	22.2	0.74	18.8
10	1107	23.2	0.77	20.7
11	1106	23.0	0.76	20.4
12	1107	23.1	0.73	19.4
13	1092	23.3	0.75	19.7
14	1110	23.2	0.73	19.4
15	1097	23.2	0.73	19.3
16	1110	23.1	0.75	20.0

We selected the best performing devices prepared over a period of 6 months following the same preparation procedure described in the Experimental Section of the main text. Device open-circuit voltage (Voc), short circuit current (Jsc), fill factor (FF) and power conversion efficiency (PCE) were extracted from the current density-voltage (J-V) curves collected under simulated solar light. The light source was a 450 W xenon lamp (Oriel) equipped with a SchottK113 Tempax sunlight filter (Prazisions Glas & Optik GmbH) to match the emission spectrum of the lamp to the AM1.5G standard. Before each measurement, the exact light intensity was determined using a calibrated Si reference diode equipped with an infrared cut-off filter (KG-3, Schott). The J-V curves were recorded by scanning the voltage at 0.01 V s⁻¹ rate from forward bias to short circuit conditions with no preconditioning such as light soaking or holding the device under forward voltage bias beforehand. The cells were masked with a black metal mask (0.16 cm²) to estimate the active area and reduce the influence of the scattered light.

Reversible losses in SnO₂-based mesoporous and planar perovskite solar cells

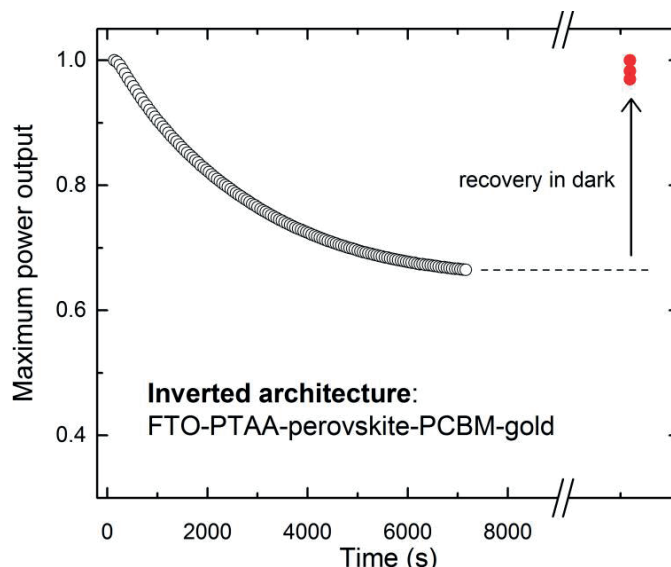


Similar to what reported in the main text for mesoporous TiO₂-based device, the reversible losses can be measured also for mesoporous and planar SnO₂-based perovskite solar cells.

Mesoporous and planar SnO₂-based perovskite solar cells preparation: aluminum doped zinc oxide coated glass slides (Zhuhai Kaivo Optoelectronic Technology Co.) were cleaned by sonication in deionized water for 15 minutes. After rinsing with ethanol the substrates were again sonicated with isopropanol and rinsed with acetone. The substrates were treated with UV-ozone for 5 minutes and a 30 nm thick SnO₂ was deposited by spray pyrolysis at 450°C from a precursor solution of butyltin trichloride (250 mM) in anhydrous ethanol. For planar SnO₂ devices perovskite was spincoated directly on top of the SnO₂ compact layer. Mesoporous SnO₂ electrodes were synthesized using a structure directing block-copolymer. A tin oxide precursor sol was prepared by dissolving poly(1,4-isoprene-*b*-ethylene oxide) (25 mg,

Polymer Source, Mn: PIP(50000)-PEO(12000), Mw/Mn: 1.05) in tetrahydrofuran (1 mL), after which tin(IV) chloride pentahydrate was added (80 mg) and stirred for 30 minutes. The resulting solution was spin-coated (4000 rpm, 10 s) onto the substrate. The films were annealed on a programmable hotplate (2000 W, Harry Gestigkeit GmbH) using a 45 minutes ramp to 450 °C followed by a dwell time of 30 minutes to remove the block-copolymer template and crystallize SnO₂. Perovskite films were deposited from a precursor solution containing FAI (1 M), PbI₂ (1.1 M), MABr (0.2 M), PbBr₂ (0.2 M) and CsI (0.075 M) in anhydrous DMF:DMSO 4:1 (v:v). The perovskite solution was spin-coated in a two-step program at 1000 and 6000 rpm for 10 and 20 s respectively. During the second step, 100 µL of chlorobenzene was poured onto the spinning substrate 5 seconds prior the end of the program. The substrates were then annealed at 100 °C for 1 hour in a nitrogen glove box. Subsequently, the substrates were cooled down for a few minutes and a spiro-OMeTAD (Luminescence Technology) solution (70 mM in chlorobenzene) doped with bis(trifluoromethylsulfonyl)imide lithium salt (Li-TFSI, Aldrich), tris(2-(1H-pyrazol-1-yl)-4-tert-butylpyridine)-cobalt(III)tris(bis(trifluoromethylsulfonyl)imide) (FK209, Dyenamo) and 4-tert-butylpyridine (TBP, Aldrich) was spun at 4000 rpm for 20 s. The molar ratios of additives for spiro-OMeTAD were: 0.5, 0.03 and 3.3 for Li-TFSI, FK209 and TBP, respectively. Finally, 80 nm of gold was thermally evaporated under high vacuum on top of the device.

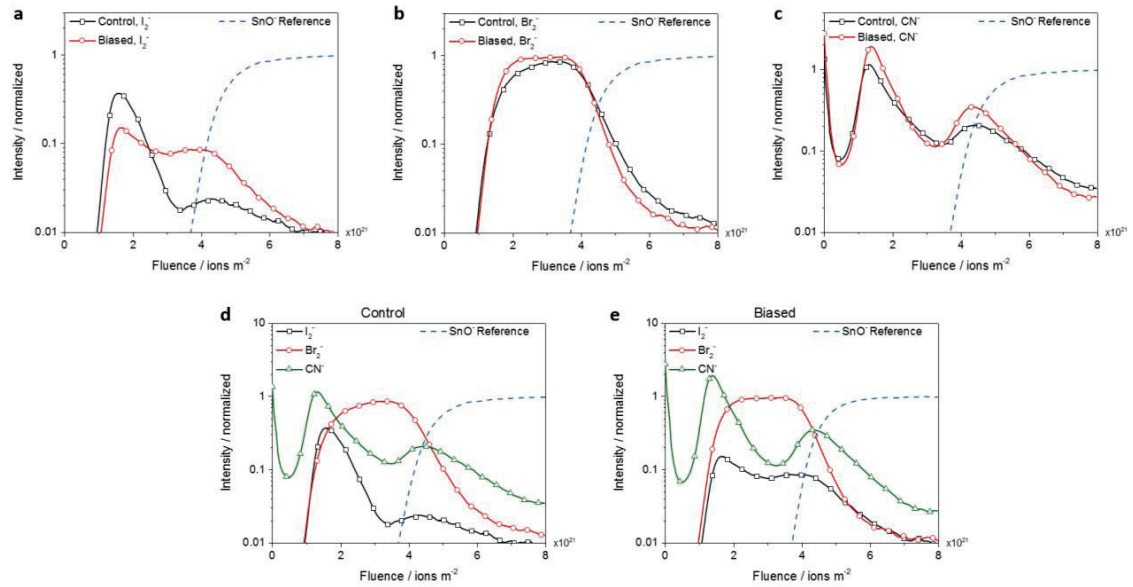
Reversible losses in inverted perovskite solar cells



Similar to what reported in the main text for mesoporous TiO₂-based device, the reversible losses can be measured also for so called inverted perovskite solar cells.

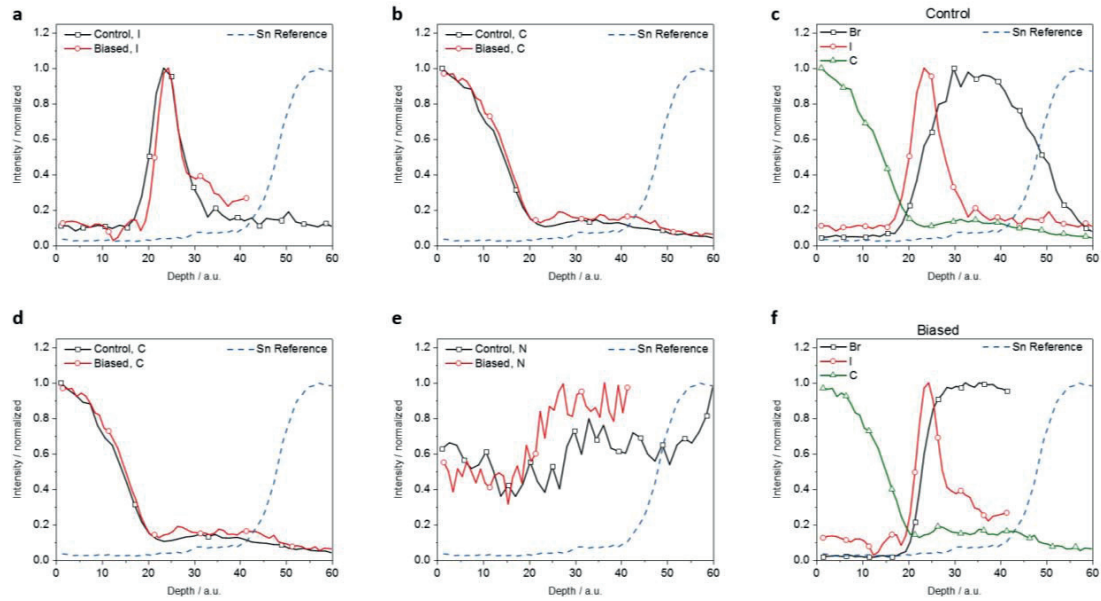
Inverted perovskite solar cells preparation: fluorine doped tin oxide (FTO) coated glass slides (Sigma-Aldrich) were cleaned by sonication in 2% Hellmanex soap solution for 15 minutes. After rinsing with deionized water and ethanol the substrates were again sonicated with isopropanol and rinsed with acetone. The substrates were then treated with UV-ozone for 5 minutes and brought into a nitrogen filled glovebox. A PTAA (EM Index, 15 mg/ml in toluene) solution doped with bis(trifluoromethylsulfonyl)imide lithium salt (Li-TFSI, Aldrich) and 4-tert-butylpyridine (TBP, Aldrich) was spincoated on top of the FTO at 2000 rpm for 30 s. Perovskite films were deposited from a precursor solution containing FAI (1 M), PbI₂ (1.1 M), MABr (0.2 M), PbBr₂ (0.2 M) and CsI (0.075 M) in anhydrous DMF:DMSO 4:1 (v:v). The perovskite solution was spin-coated in a two-step program at 1000 and 6000 rpm for 10 and 20 s respectively. During the second step, 100 μ L of diethyl ether was poured onto the spinning substrate 5 s prior to the end of the program. The substrates were then annealed at 100 $^{\circ}$ C for 1 hour in a nitrogen glove box. Subsequently, the substrates were cooled down for a few minutes and a PCBM solution (20 mg/mL in chlorobenzene) was spun at 2000 rpm for 60 s. Finally, 80 nm of gold was thermally evaporated on top of the device.

Organic cation depth profiles by time of flight secondary ion mass spectrometry (ToF-SIMS)



Time of flight secondary ion mass spectrometry (ToF-SIMS) depth profiles comparing traces of **a** I_2^- , **b** Br_2^- , **c** CN^- ions for biased and control pixels of the sample shown in **Figure 2** in the main text. **d** and **e** show the same traces plotted in separate graphs for control and biased pixels respectively. The SnO^- ions coming from the fluorine doped SnO_2 (FTO glass) are used as a reference and all traces are normalized to their maxima.

Energy dispersive X-ray spectroscopy (EDX) depth profiles



Energy dispersive X-ray spectroscopy (EDX) depth profiles showing the traces of a I, b Br, d C and e N in biased and control pixels of the sample shown in Figure 2. c and f show the same traces plotted in separate graphs for control and biased pixels respectively. The Sn signal coming from the fluorine doped SnO₂ (FTO glass) is used as a reference. The traces are normalized to their maxima. Some of the traces from the biased pixel are interrupted. EDX was performed with Zeiss Merlin. Prior to cutting the sample was coated with carbon to avoid charging effect.



Cell Name: TM_6_3_MPPT_Feb_21#01

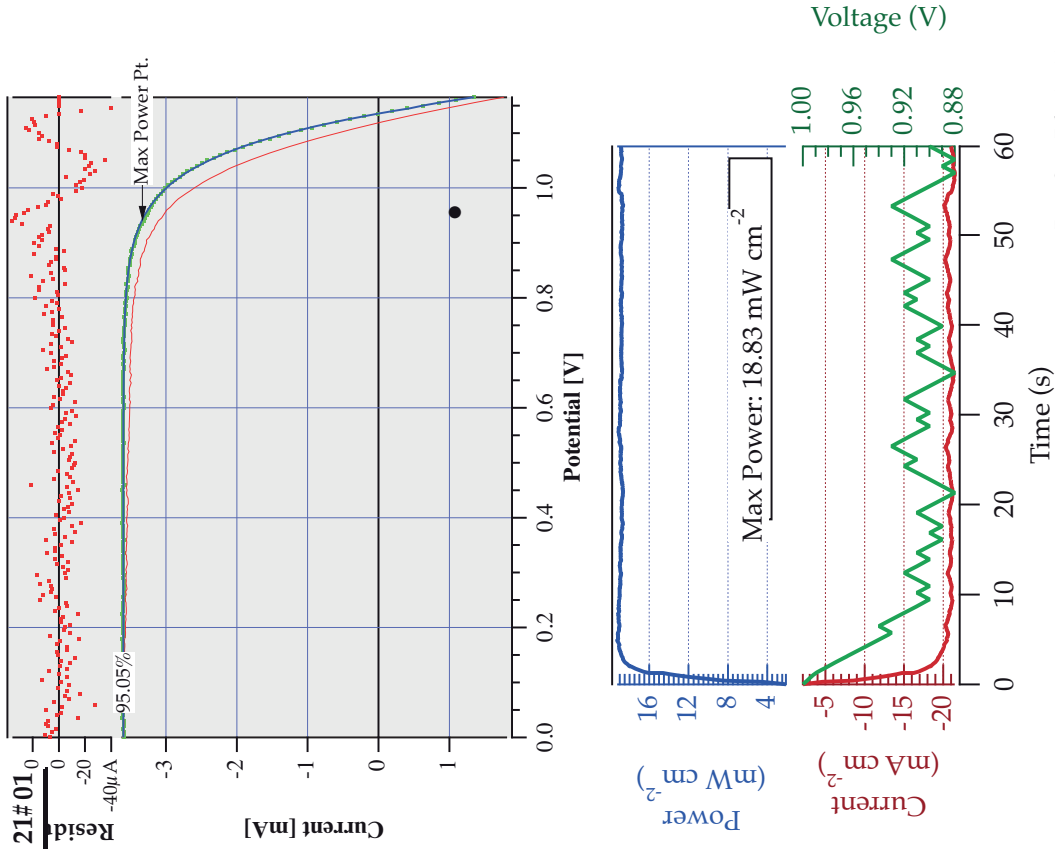
Measurement Date : Wed, Feb 10, 2016 / 12:47:41 PM
 Type of cell : PC
 Cell Active Area : 0.16 cm²
 Light Source : Xe 450W @ AM1.5G
 Dye Sensitiser :
 Additional Remarks :
 Electrolyte Z960 :
 Working Temperature : 298 K
 SemiConductor Layer : Double (PC) 12 / 4, sc., + TiCl4
 Layer Thickness, Porosity :
 Working Electrode Glass :
 Counter Electrode Type : TEC-7
 Data File Name : TM_6_3_MPPT_Feb 21#01
 Current Compliance : 2 mA
 Settling Time, ΔU, Meas. Delay : 0.01 s, -5 mV, 0s

Thermopile _{ref}	95% Sun	95% Sun
Current _{ref}	-2.786 mSun	-2.786 mSun
Power _{in}	95.049 mW/cm ²	95.049 mW/cm ²
Norm. Std. Dev.	0.29	0.21
Module U _{oc}	1.135 V	1.118 V
Cell U _{oc}	1.135 V	1.118 V
I _{sc}	-3.598 mA	-3.611 mA
I _{sc}	-22.485 mA/cm ²	-22.567 mA/cm ²
U _{pmax}	932.80 mV	903.91 mV
I _{pmax}	-20.9 mA/cm ²	-20.5 mA/cm ²
Power _{out}	19.54 mW/cm ²	18.52 mW/cm ²
Total Power _{out}	3.13 mW	2.96 mW
Fill Factor	0.765	0.734
Efficiency η	20.56%	19.48%

IPCE @ 550 nm : 66.444 %
 Slope $\partial V_{oc} / \partial \log(I_{sc})$: NaN mV
 Ideality Factor @ 1 Sun : 2.69
 Series Resistance @ 1 Sun 4.15 Ω ± 4.7 %, (25.96 Ω/cm²)

Calibration File: KIDACX: Ref Cell#9, Thu, Aug 29, 2013

© RAHB: KIDAQX_Modif Measured by Visitor on IV old

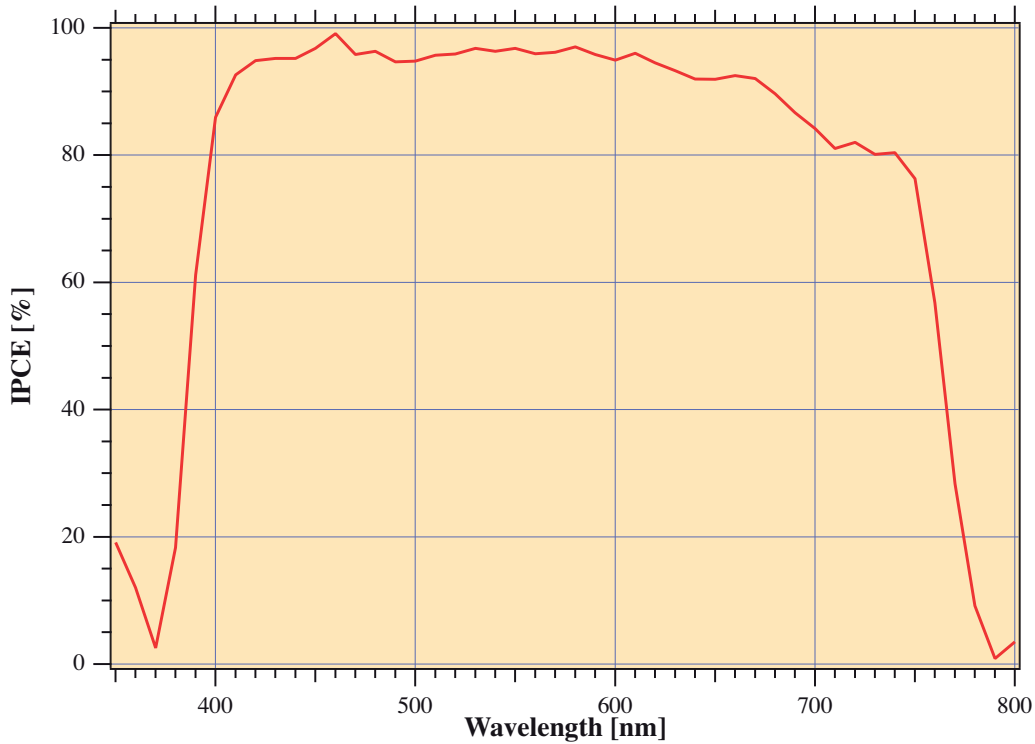


Date: Sun, Feb 21, 2016



Incident Photon to Current Conversion Efficiency

Measurement Date : Tue, Sep 13, 2016/10:31:14 AM
 Type of cell : Si diode
 Cell Active Area : 0.16 cm²
 Light Source : Xe 300W, Coaxial @ 4Hz, with 1% LED bias Intensity
 Dye Sensitiser :
 Additional Remarks :
 Electrolyte Solution :
 Semiconductor Layer :
 Layer Thickness, Porosity :
 Working Electrode Glass :
 Counter Electrode Type : PT-ST-1JJ-1_Sep 13, 2016#01
 Data File Name : From 350 nm to 800 nm in 10 nm steps
 IPCE Spectrum
 Lock-in Freq.(Time Const), Gain : 4 Hz (0.03s), x1000/500 mV
 Calibration File : MacIntosh HD:Igor Applications:DataScan Data:cal_Mon 9 May 2016



IPCE @ 540 nm (init) is 99.7 %
IPCE @ 550 nm (meas) is 96.8 %
PCE @ 700 nm (meas) is 84.2 %

At 0 mV bias, with 1% Light Bias the Integrated Current from 350 to 800 nm for:

Solar AM 1.5 G : 1000 W / m² is 22.09 mA/cm²
 Xe lamp: 450W/113 : 1000W is 22.20 mA/cm²; Estimated Mismatch; 1.29 %
 Osram: 18W/T8/840 @500lx is 70.7 μA/cm²
 Osram: 18W/T8/827 @500lx is 53.1 μA/cm²
 Osram: 18W/T8/930 @500lx is 55.6 μA/cm²
 White LED M111: 1000W is 263.6 mA/cm²; Estimated Mismatch:-7.93 %
 Date: Tue, Sep 13, 2016

1. Equivalent circuit representation of the PSC based on drift diffusion modelling

The purpose of this section is to predict the capacitance of the perovskite layer in a PSC, based on three different hypotheses for ion vacancy motion, and to use the results to compare to experimentally generated spectroscopy data. This comparison will, in turn, allow a comparison of hypotheses for ion vacancy motion. Based on DFT calculations [3] it is usually assumed that the most mobile vacancy species in the perovskite methylammonium-lead-trihalide are the positively charged halide vacancies and it is suspected that the motion of negatively charged methylammonium vacancies, though considerably less mobile than the halides, may still influence processes occurring on timescales of the order of 1s-10000s. In Richardson *et al.* [5] drift-diffusion models of vacancy motion are used to show that charge resides in narrow Debye layers, of the width around 2nm, at the edge of the perovskite layer and that away from these layers, in the perovskite bulk, there is almost exact charge neutrality with a balance between positive and negative vacancies. Charge neutrality in the perovskite bulk means that, with the exception of the Debye layers, the electric field is uniform (but may vary in time) throughout the perovskite. Significant charge densities in the Debye layers (caused by disparities in the concentrations of positive and negative ion vacancies) lead to rapid changes in the electric potential within these narrow regions and corresponding potential drops from one side of the Debye layer to the other. The behaviour of the device is thus almost entirely controlled by ion vacancy motion into and out of the Debye Layers.

If the mobile ion vacancies can redistribute themselves within the Debye layers more rapidly than changes occur to the external conditions (*e.g.* the applied potential) then, to a good approximation, the behaviour of the Debye layer can be characterised by a nonlinear capacitance relation [5], of the form $Q = \mathcal{Q}_{dl}(\mathcal{V}_{dl})$, which relates the charge Q stored in the layer to the potential drop \mathcal{V}_{dl} across it: defined as the potential in the perovskite, just inside the Debye layer, minus the potential in the adjacent blocking layer. Denoting the potential drop across the Debye layer at the interface with the electron transport layer (ETL) as \mathcal{V}_- and that across the Debye layer at the interface with the hole transport layer (HTL) as \mathcal{V}_+ we see that the total potential drop across the two capacitances is $\mathcal{V}_+ - \mathcal{V}_-$. If the charge in HTL Debye layer is defined as Q then charge conservation implies the charge stored in the ETL Debye layer is $-Q$. In order to determine the capacitance of the entire perovskite layer we need to consider the capacitance of both Debye layers in series. It follows that

$$Q = \mathcal{Q}_{dl}(\mathcal{V}_+), \quad \text{and} \quad -Q = \mathcal{Q}_{dl}(\mathcal{V}_-)$$

By defining the inverse of the function $\mathcal{Q}_{dl}(\mathcal{V})$ as $\mathcal{V}_{dl}(Q)$ it is possible to see that the total potential drop across both Debye layers $\mathcal{V}_c = \mathcal{V}_+ - \mathcal{V}_-$ is

$$\mathcal{V}_c(Q) = \mathcal{V}_{dl}(Q) - \mathcal{V}_{dl}(-Q). \quad (1)$$

The Debye layer capacitance C is then given by $C(Q) = 1/\mathcal{V}'_c(Q)$, where the prime denotes the derivative of the function $\mathcal{V}_c(Q)$.

The electrical behaviour of the cell can be described by the equivalent circuit shown in figure 1. Here the lower branch of the circuit (in red) provides the description of the vacancy motion within the perovskite and consists of a nonlinear capacitor (accounting for charge accumulation within both Debye layers) in series with a linear resistor which accounts for the resistance to vacancy motion within the perovskite.

Different capacitance relations are obtained depending on the assumptions made about the vacancy mobilities. At one extreme the assumption made in Richardson *et al.* [5] (which we term hypothesis (a)) is that, on the timescales of concern, the negatively charged methylammonium ions are completely immobile while the positively charged halide vacancies redistribute quickly within the narrow Debye layers into quasi-equilibrium configurations. These assumptions are backed up by the estimates of Eames *et al.* [3] for the activation energies required to move vacancies from one site on the perovskite crystal to an adjacent one (which suggest a much higher mobility for halide vacancies than for methylammonium vacancies). In [5] it is shown that this hypothesis leads to the following capacitance relation for a single Debye layer:

$$Q_{dl}(\mathcal{V}_{dl}) = \frac{A\varepsilon V_T}{L_d} \text{sign}(\mathcal{V}_{dl}) \left[2 \left(e^{\mathcal{V}_{dl}/V_T} - 1 - \frac{\mathcal{V}_{dl}}{V_T} \right) \right]^{1/2}, \quad \text{Hypothesis (a)} \quad (2)$$

where \mathcal{V}_{dl} is the potential drop across the Debye layer, ε the permittivity of the perovskite, V_T the thermal voltage, A the area of the cell and L_d the Debye length. In order to determine the capacitance of both Debye layers in series this relation is inverted to obtain $\mathcal{V}_{dl}(Q)$ which in turn is substituted into the relation (1) to obtain the total potential drop across both Debye layers \mathcal{V}_c as a function of the charge Q stored in them.

At the other extreme is the hypothesis that both sets of vacancies are sufficiently mobile so that they can redistribute quickly in the Debye layers into quasi-equilibrium configurations (which we term hypothesis (c)). This leads to a capacitance relation (as shown, for example, in [4]) for a single Debye layer of the form

$$Q_{dl}(\mathcal{V}_{dl}) = 2\sqrt{2} \frac{A\varepsilon V_T}{L_d} \sinh \left(\frac{\mathcal{V}_{dl}}{2V_T} \right), \quad \text{Hypothesis (c)}. \quad (3)$$

Once again the total potential drop across both Debye layers \mathcal{V}_c can be determined as a function of the stored charge Q by inverting this relation (to obtain $\mathcal{V}_{dl}(Q)$) and substituting into (1).

The spectroscopy experiments conducted in this work require that both the external illumination and the applied voltage are changed to their base values and then left for a period of 300s, in order to allow the vacancy distributions time to settle to an equilibrium within the PSC (it is somewhat doubtful whether 300s is sufficient to allow both sets of vacancy distributions to fully equilibrate). After this settling period a small oscillatory oscillation to the illumination is applied, with frequency in the range 10-10⁵Hz, and the oscillatory response of the current flow to this perturbation in the illumination is measured and used to infer the dependence of the capacitance of the device on the base applied voltage V . The experiment is thus conducted on two very different timescales: the settling timescale

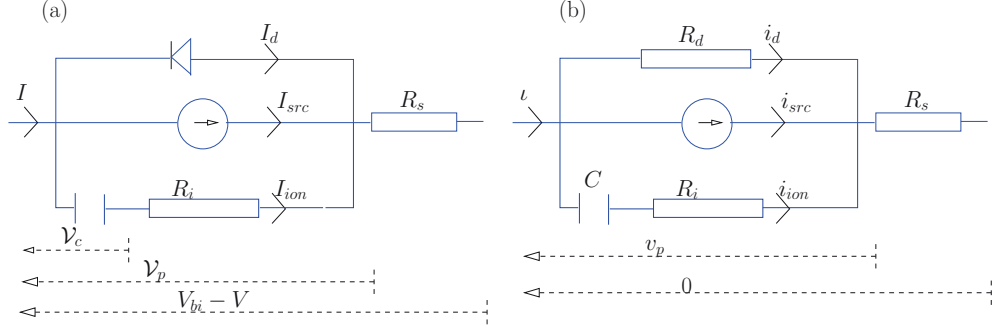


Figure 1: (a) The full nonlinear equivalent circuit (with nonlinear capacitor). (b) The linear equivalent circuit used to calculate the response to the addition of a small perturbation $i_{src}(t)$ to the photovoltaic generated current. Potential drops across various segments of the circuits shown by dashed lines with arrows.

of 300s and the spectroscopic timescale of less than 0.1s. This disparity in the experimental timescales leads us to pose an alternative vacancy motion hypothesis that may be appropriate to the spectroscopic experiments (we term this hypothesis (b)) and which is intermediate between hypotheses (a) and (c). In this scenario it is assumed that both vacancy species (halide and methylammonium) are sufficiently mobile so that they equilibrate within the Debye layers within the 300s settling period, but that on the much shorter spectroscopic timescale the methylammonium vacancies are effectively immobile (being frozen into the configuration obtained after the 300s settling period) while the more mobile halide vacancies are still mobile enough to equilibrate within the Debye layers, even on this short timescale. This hypothesis leads to the following linear capacitance relation relating the charge Q stored in the Debye layers to the total potential drop $\mathcal{V}_c = \mathcal{V}_+ - \mathcal{V}_-$ across both layers

$$Q(\mathcal{V}_c) = \frac{1}{2} \frac{A\varepsilon V_T}{L_d} \mathcal{V}_c, \quad \text{Hypothesis (b)}. \quad (4)$$

In figure 2(c) (main text) the total capacitance of both Debye layers, as defined by $C(Q) = 1/\mathcal{V}'_c(Q)$, is plotted for all three hypotheses as a function of V the potential drop across the cell at steady-state (here \mathcal{V}_c , the total potential drop across both layers, is equal to the total drop across the cell so that $\mathcal{V}_c = V_{bi} - V$). Notably hypothesis (a) gives a capacitance that increases with V while hypothesis (c) gives one that sharply decays with increases in V .

1.1 Derivation of the linearised equations describing the spectroscopy measurements

In the light intensity modulated spectroscopy experiments conducted whose results are plotted in figure 2(b) a steady source of illumination is applied to the cell at constant applied

voltage V_{ap} and only after the experiment has been running for 300s is a small oscillatory perturbation to this light source applied. The aim of the following discussion is to predict the small oscillatory response of the current I produced by the device in response to the perturbation of the light source as a function both of the applied voltage V_{ap} and of the frequency ω of the perturbation. In order to do this we first consider the response of the device to the initial steady illumination source before linearising about this base state to derive a set of linear equations that can be used to analyse the response of the device to the oscillatory perturbation in light intensity.

A nonlinear equivalent circuit model for the PSC. An equivalent circuit description of the device, which is based on the asymptotic solution of a charge transport model for ion vacancy motion and electron and hole transport within a PSC given in [5], is shown in figure 1(a). In this description there are three components in parallel (i) the current source arising from photovoltaic generation, (ii) a diode that models recombination between electron and holes within the device and (iii) two nonlinear capacitors in series with a resistor that represent the flow of ion vacancies through the perovskite layer and in (and out of) the Debye layers on its edge.¹ The resistor in series with these three components can be assigned to the resistance of the contacts and the blocking layers. The total current I flowing through the circuit is thus the the sum of the currents flowing through the 3 components in parallel

$$I = I_{src} + I_d + I_{ion}, \quad (5)$$

where $I_{src}(t)$ is the current source (a known quantity), I_d the current flowing thorough the diode and I_{ion} that flowing through the nonlinear capacitors and resistor in series. We characterise the two nonlinear capacitors in series by a single capacitance relation, as in (2)-(4) above, of the form

$$Q = \mathcal{Q}(\mathcal{V}_c) \quad \text{or equivalently by its inverse} \quad \mathcal{V}_c = \mathcal{V}(Q). \quad (6)$$

Here Q is the charge stored on the capacitors and $\mathcal{V}_c = \mathcal{V}_p - I_{ion}R_i$ is the total potential drop across the capacitors (in figure 1(a) a single capacitor with the properties of both capacitors in series is shown). On denoting the potential drop across the components in parallel by \mathcal{V}_p we obtain the following current voltage relations between I_{ion} and \mathcal{V}_p :

$$\mathcal{V}_p = \mathcal{V}(Q) + I_{ion}R_i, \quad (7)$$

$$\frac{dQ}{dt} = I_{ion}, \quad (8)$$

representing a sum of the potential drops across this arm of the circuit and conservation of charge within the capacitors, respectively. The current-voltage relation for the branch of the

¹It is relatively straightforward to see how the first and third of these components ((i) and (iii)) can be related to the asymptotic solution to the charge transport model give in [5], it is less clear that the electron-hole recombination can be described by a single diode (as in (ii)) but this is the usual way to represent this phenomenon in an equivalent circuit.

circuit containing the diode we model with a standard diode equation, namely

$$I_d = -\mathcal{I}_0 \left(\exp \left(-\frac{\mathcal{V}_p}{\mathcal{N}V_T} \right) - 1 \right), \quad (9)$$

where here V_T is the thermal voltage, \mathcal{I}_0 is the reverse saturation current and \mathcal{N} the ideality factor of the diode. Finally we sum the potential drop across the series resistor (resistance R_s) and that across the components in parallel and equate this to the total potential drop across the device $V_{bi} - V$ to obtain

$$\mathcal{V}_p + IR_s = V_{bi} - V, \quad (10)$$

where here V_{bi} is the built in voltage and V the applied potential (this terminology follows the convention in [5]). Equations (5)-(10) comprise five equations for the five unknowns \mathcal{V}_p , I_{ion} , I_d , I and Q (here I_{src} and V are specified).

The steady-state. We start by looking for a steady solution to the equivalent circuit model (which we denote by a tilde) for the situation when both the voltage V and the photovoltaic generated current I_{src} are held constant before linearising about this steady solution in order to model the situation in which there is a small sinusoidal perturbation is added to the photovoltaic generation term. At steady state the ionic current flow through the lower branch of the circuit is zero

$$\tilde{I}_{ion} \equiv 0. \quad (11)$$

The potential difference across the components in parallel $\tilde{\mathcal{V}}_p$, and across the capacitor $\tilde{\mathcal{V}}_c$, can be determined from (10) and (11), and are given by

$$\tilde{\mathcal{V}}_p(\tilde{I}) = V_{bi} - V - \tilde{I}R_s, \quad \tilde{\mathcal{V}}_c = \tilde{\mathcal{V}}_p. \quad (12)$$

It follows, from (5) and (9), that the steady-state current \tilde{I} is determined by the solution to the following equation

$$\tilde{I} = I_{src} - \mathcal{I}_0 \left(\exp \left(-\frac{\tilde{\mathcal{V}}_p(\tilde{I})}{\mathcal{N}V_T} \right) - 1 \right). \quad (13)$$

The steady state charge on the capacitor \tilde{Q} , obtained from the capacitance relation (6), is

$$\tilde{Q} = \mathcal{Q}(\tilde{\mathcal{V}}_p(\tilde{I})). \quad (14)$$

Linearising about the steady-state for small perturbations to the photovoltaic generation. Linearising the governing equations (5)-(10) about the steady-state solution leads to simplified equations for the perturbation induced by a small oscillation $i_{src}(t)$ to the photovoltaic generation term of the form

$$I_{src} = \tilde{I}_{src} + i_{src}(t). \quad (15)$$

This linearisation is achieved by writing the solution in the form

$$\begin{aligned} I_d &= -\mathcal{I}_0 \left(\exp \left(\frac{\tilde{\mathcal{V}}_p(\tilde{I})}{\mathcal{N}V_T} \right) - 1 \right) + i_d, & I_{ion} &= i_{ion}, & I &= \tilde{I} + \iota, \\ Q &= \mathcal{Q}(\tilde{\mathcal{V}}_p(\tilde{I})) + q, & \mathcal{V}_p &= \tilde{\mathcal{V}}_p(\tilde{I}) + v_p, \end{aligned}$$

where the quantities i_d , i_{ion} , q , v_p and ι (all denoted by small letters) are small perturbations to the steady solution induced by $i_{src}(t)$. Substituting (16) into the equivalent circuit model (5)-(10) and linearising about the steady solution leads to the model

$$\iota = i_{src} + i_{ion} + i_d, \quad v_p + \iota R_s = 0, \quad v_p = i_d R_d(\tilde{\mathcal{V}}_p(\tilde{I})), \quad (16)$$

$$R_i \frac{di_{ion}}{dt} + \frac{1}{C(\tilde{\mathcal{V}}_p(\tilde{I}))} i_{ion} = \frac{dv_p}{dt}. \quad (17)$$

This model is equivalent to the linear equivalent circuit depicted in figure 1(b). Here the linear resistance R_d and the linear capacitance C are both functions of the steady state potential across the components in parallel $\tilde{\mathcal{V}}_p(\tilde{I}) = V_{bi} - V - \tilde{I}R_s$ and are defined by

$$R_d(\tilde{\mathcal{V}}_p(\tilde{I})) = \frac{\mathcal{N}V_T}{\mathcal{I}_0} \exp \left(\frac{\tilde{\mathcal{V}}_p(\tilde{I})}{\mathcal{N}V_T} \right), \quad C(\tilde{\mathcal{V}}_p(\tilde{I})) = \mathcal{Q}'(\tilde{\mathcal{V}}_p(\tilde{I})). \quad (18)$$

where $\mathcal{Q}'(\cdot)$ is the derivative of the function $\mathcal{Q}(\cdot)$.

1.2 Solution of the linear model for sinusoidal perturbations to the photovoltaic generation

In order to mimic the light intensity modulated spectroscopy experiments carried out in the experimental part of this work we seek a solution to the linear equations (16)-(17) in which the perturbation to the photovoltaic generation is sinusoidal with the form

$$i_{src}(t) = i_0 \exp(i\omega t).$$

Substituting this forcing term into (16)-(17) and solving leads to the solution

$$i_{ion} = -i_0 M(\omega, V) \exp(i\omega t), \quad v_p = -i_0 \frac{R_s R_d}{R_s + R_d} (1 - M(\omega, V)) \exp(i\omega t), \quad (19)$$

$$i_d = -i_0 \frac{R_s}{R_s + R_d} (1 - M(\omega, V)) \exp(i\omega t), \quad \iota = i_0 (1 - M(\omega, V)) \frac{R_d}{R_s + R_d} \exp(i\omega t), \quad (20)$$

where

$$M(\omega, V) = \frac{(R_i + \mathcal{R}_{ef}) \mathcal{R}_{ef} \omega^2 C^2}{1 + (R_i + \mathcal{R}_{ef})^2 \omega^2 C^2} + i \frac{\mathcal{R}_{ef} \omega C}{1 + (R_i + \mathcal{R}_{ef})^2 \omega^2 C^2}, \quad (21)$$

where the capacitance C and the effective resistance \mathcal{R}_{ef} , as defined by

$$\mathcal{R}_{ef}(\tilde{V}_p) = \frac{R_s R_d(\tilde{V}_p)}{R_s + R_d(\tilde{V}_p)}, \quad (22)$$

are both functions of $\tilde{V}_p = V_{bi} - V - \tilde{I}(V)R_s$, and thus of V .

The key part of the solution required to compare to the experimental results (plotted in figure 2(b)) is the imaginary part of $\iota \exp(-i\omega t)$, which on using (20b), can be written

$$\text{Im}(\iota \exp(-i\omega t)) = - \left(\frac{i_0}{R_s} \right) \frac{\mathcal{R}_{ef}^2 \omega C}{1 + (R_i + \mathcal{R}_{ef})^2 \omega^2 C^2}. \quad (23)$$

This function has

$$\text{a maximum modulus of } \frac{i_0 \mathcal{R}_{ef}^2}{2R_s (R_i + \mathcal{R}_{ef})} \quad \text{for } \omega = \frac{1}{C (R_i + \mathcal{R}_{ef})}. \quad (24)$$

The maximum of the imaginary part of the perturbation to the current only depends on the applied voltage V through \mathcal{R}_{ef} , via (12), (18) and (22). It is clear that as V increases from zero to the built in voltage V_{bi} so the linear resistance of the diode R_d decreases extremely rapidly (as expected). Typically the linear resistance of the diode is very large near short-circuit ($V = 0$) but become comparable with the series resistance R_s near open-circuit (close to $V = V_{bi}$). Thus for sufficiently small V the effective resistance $\mathcal{R}_{ef} \approx R_s$ since $R_d \gg R_s$. As V increases there is then a small region of voltage in which R_d is comparable to R_s and then for larger applied voltages (where $R_d \ll R_s$) the effective resistance is approximated by $\mathcal{R}_{ef} \approx R_d$. The function $\mathcal{R}_{ef}(V)$ is thus a smoothed off step function which transitions from values close to R_s , for small enough V , to values close to zero, as V increases beyond a certain critical size. This type of behaviour is reflected in the experimental results plotted in the main paper figure 3(a). Here the maxima at $V = -0.2, 0.2, 0.7$ Volts are all very similar (presumably because $\mathcal{R}_{ef} \approx R_s$ for smaller values of V) however that for $V = 0.9$ Volts, which is close to $V = V_{bi}$, is about a factor of 10 smaller which could be explained by a considerably smaller value of \mathcal{R}_{ef} at this higher voltage. According to this theory the dependence of the experimental results on the capacitance of the Debye layers C , as the applied voltage V is changed, is reflected only through the position of the maximum as a function of frequency ω . In figure 3(a) of the main paper it can be seen that for the lower applied voltages ($V = -0.2, 0.2, 0.7$ Volts) the position of this maximum changes little but for $V = 0.9$ Volts it is considerably decreased below that of the other voltages. This suggest that C must be an increasing function of V (since $(R_i + \mathcal{R}_{ef})$ decreases, albeit probably only marginally, with V). The only hypothesis consistent with this is hypothesis (a), reflected in the capacitance relation (2) and plotted in figure 3(b), which asserts that even on the long settling timescale of 300s there is minimal movement of methylammonium vacancies.

Model Poisson drift-diffusion equations

The model cell is made up of a n-type layer in $x < -1$, a perovskite layer in $-1 < x < 1$ and a p-type layer in $x > 1$. The central assumptions used in the model will be: (i) that the blocking layers are sufficiently highly doped that their Fermi levels are flat (this justifies the use of Ohmic boundary conditions on the hole density at $x = 1$ and electron density at $x = -1$), and; (ii) that the electric field/potential is determined by the solely by the ion distribution and not the electrons/holes (this justified by the observation that there are orders of magnitude more ions than electronic charge carriers).

The ion problem: The equations that determine the distribution of positively charged defects (e.g. halide vacancies), P , and the electric potential, ϕ , are

$$\frac{\partial P}{\partial t} = D_0 \frac{\partial}{\partial x} \left(\frac{\partial P}{\partial x} + P \frac{\partial \phi}{\partial x} \right), \quad (1)$$

$$\frac{\partial^2 \phi}{\partial x^2} = \frac{N_0 - P}{\lambda^2}, \quad (2)$$

where, N_0 is the (fixed) density of the immobile negative vacancies (e.g. cation vacancies), λ is a small (dimensionless) parameter which we term the normalised Debye length and D_0 is the (dimensionless) diffusivity of negative defects.

Suitable boundary and initial conditions specify zero flux of positive defects at each boundary of the perovskite layer, a specified change in potential across the perovskite layer and that the initial density of positive and negative defects should be the same (thus ensuring net charge neutrality of the material). We therefore write

$$-D_0 \left(\frac{\partial P}{\partial x} + P \frac{\partial \phi}{\partial x} \right) \Big|_{x=-1,+1} = 0, \quad (3)$$

$$\phi|_{x=-1} = (V_{bi} - V)/2, \quad (4)$$

$$\phi|_{x=+1} = -(V_{bi} - V)/2, \quad (5)$$

$$P|_{t=0} = N_0. \quad (6)$$

Here, V_{bi} and V are the built-in and applied voltages respectively, and (roughly speaking) $0 < V < V_{bi}$ corresponds to the power-generating regime.

The electronic problem: Once the ion problem, (1)-(6), has been solved we then determine the electronic current by solving the following system for the electron, n , and hole concentrations, p . The electric potential is, for the purposes of the solution of this system, taken to be a known function that was determined previously by solving the ionic problem. Since we are primarily interested in the dynamics on the timescale of ionic motion (much longer than the timescale for electron and hole motion), it is sufficient to solve only for the steady-state distribution of charge carriers. The equations are

$$D_+ \left(\frac{\partial p}{\partial x} + p \frac{\partial \phi}{\partial x} \right) + G(x) - R(n, p, N, P) = 0, \quad (7)$$

$$D_- \left(\frac{\partial n}{\partial x} - n \frac{\partial \phi}{\partial x} \right) + G(x) - R(n, p, N, P) = 0, \quad (8)$$

where D_+ and D_- are the (dimensionless) diffusivities of holes and electrons respectively, $R(n, p, P)$ is the recombination rate (which we will specify later), and $G(x)$ is the photo-generation rate. Suitable boundary conditions are Ohmic conditions on n and p at $x = -1$ and $x = 1$ respectively, accompanied by no flux conditions on n and p at $x = 1$ and $x = -1$ respectively:

$$n|_{x=-1} = n_0, \quad (9)$$

$$-D_+ \left(\frac{\partial p}{\partial x} + p \frac{\partial \phi}{\partial x} \right) \Big|_{x=-1} = 0, \quad (10)$$

$$p|_{x=1} = p_0, \quad (11)$$

$$-D_- \left(\frac{\partial n}{\partial x} - n \frac{\partial \phi}{\partial x} \right) \Big|_{x=1} = 0. \quad (12)$$

The current, J , is then give by the hole flux minus the electron flux; that is

$$J = D_- \left(\frac{\partial n}{\partial x} - n \frac{\partial \phi}{\partial x} \right) - D_+ \left(\frac{\partial p}{\partial x} + p \frac{\partial \phi}{\partial x} \right). \quad (13)$$

The sum of equations (7) and (8) implies that this current is constant through the perovskite layer, and so the value of J may be determined by evaluating the right-hand side of (13) at any $-1 < x < 1$.

Recombination rate: The results shown here were computed for a recombination rate $R(n, p, N, P) = \gamma_1 np + \gamma_2 nN$, where γ_1 and γ_2 are constants. The model therefore accounts for two different recombination pathways. The first corresponds to traditional bimolecular recombination, at a rate proportional to np , whilst the second account for electron-dominated recombination via the cation vacancies at a rate proportional to nN . It is worth noting that qualitatively similar solutions are obtained for any recombination rate has the form $R(n, p, N, P) = \hat{\gamma}_1 R_1(n, p) + \hat{\gamma}_2 nN$, where R_1 could he Shockley-Reid-Hall, bimolecular, or direct recombination rates.

Computations: Solutions of the model equations were obtained using the chebfun software. More details on the using this software to solve similar Poission drift-diffusion systems can be found in [Foster et. al., SIAM J. Appl. Math, 74(6):1935–1966 (2014)].

Results — short circuit current decay: The model results in figure 4 were obtained by first solving (1)-(6) with: (i) the applied voltage V held fixed in either forward or reverse bias long enough for the P and ϕ to reach a steady-state; (ii) V was abruptly switched to zero and the resulting transients of P and ϕ were solved for, then; (iii) the equations for the electrons and holes, (7)-(12) were then solved taking ϕ as predicted by solving the transient problem in stage (ii). Finally; (iv) the current is computed (as a function of time) using (13).

References

- [1] J. M. Azpiroz, E. Mosconi, J. Bisquert and F. De Angelis, “Defect migration in methylammonium lead iodide and its role in perovskite solar cell operation”. *Energy Environ. Sci.*, **8**, 2118-2127 (2015).
- [2] L. Han, N. Koide & T. Mitate “Modeling of an equivalent circuit for dye-sensitized solar cells”. *App. Phys. Lett.* **84**, 2433 (2004).
- [3] C. Eames, J.M. Frost, P.R.F. Barnes, B.C. O’Regan, A. Walsh & M. S. Islam, “Ionic transport in hybrid lead iodide perovskite solar cells”. *Nature Comms.*, **6**, 7497, (2015).
- [4] K.B. Oldham, “A Gouy-Chapman-Stern model of the double layer at a (metal)/(ionic liquid) interface”. *J. Electroanal. Chem.* **613**, 131-138 (2008).
- [5] G. Richardson, S.E.J. O’Kane, R.G. Niemann, T.A. Peltola, J.M. Foster, P.J. Cameron & A.B. Walker, “Can slow-moving ions explain hysteresis in the current-voltage curves of perovskite solar cells?” *Energy Environ. Sci.* **9**, 1476-1485 (2016).
- [6] G. Richardson, “A multiscale approach to modelling electrochemical processes occurring across the cell membrane with application to transmission of action potentials”. **26**, 201-224, (2009).

Chapter 8 Mobile Ions Explain Workings of Perovskite Photodetectors: Analyzing the Interplay between Photoconductivity and Voltage-Driven Energy-Level Alignment

THE CONTEXT

The discovery of mobile cations and reversible degradation added another perovskite-specific feature alongside the already well-documented current-voltage hysteresis, which is now widely believed to be caused mostly by mobile ions in the perovskite.^{129,130} In this work I discovered that mobile anions, that migrate to the perovskite/FTO interface, can alter its energetics allowing for a direct hole injection into perovskite under reverse bias. This behaviour enables the devices to work as a photoconductive diodes with a high internal gain.¹³¹

This chapter is based on a peer-reviewed paper published in *Advanced Functional Materials* in November 2015 entitled:

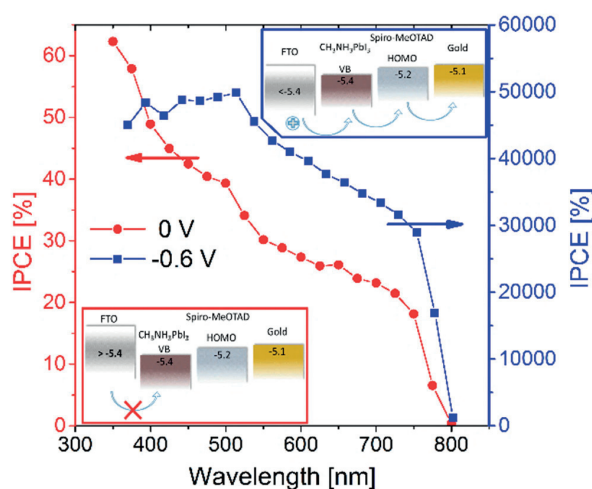
Working Principles of Perovskite Photodetectors: Analyzing the Interplay between Photoconductivity and Voltage-Driven Energy-Level Alignment

authored by:

Konrad Domanski, Wolfgang Tress, Thomas Moehl, Michael Saliba, Mohammad Khaja Nazeeruddin and Michael Grätzel.

My contribution:

I led the project, performed all measurements, prepared the figures, wrote the manuscript and made most of the devices used for this study.



Working Principles of Perovskite Photodetectors: Analyzing the Interplay Between Photoconductivity and Voltage-Driven Energy-Level Alignment

Konrad Domanski, Wolfgang Tress,* Thomas Moehl,* Michael Saliba, Mohammad Khaja Nazeeruddin, and Michael Grätzel

Organic–inorganic lead halide perovskites have recently received significant attention as active materials for high-performance photovoltaics and photodetectors. However, the understanding of their operation mechanism remains limited. High-gain, low-voltage $\text{CH}_3\text{NH}_3\text{PbI}_3$ photodetectors in various architectures are demonstrated herein. Photomultiplication in all structures with direct contact of fluorine-doped tin oxide (FTO) and perovskite with the highest responsivity 208 A W^{-1} corresponding to an incident photon-to-current efficiency of 47 000% is observed. Studying the dynamics and temperature dependence, a slow process with an activation energy of $420 \pm 90 \text{ meV}$ in the time scale of seconds is found, which is essential to photocurrent multiplication. A model based on ion migration to explain the observed transients and the photomultiplication is developed. The accumulation of negative ionic charge at the FTO/perovskite interface under reverse bias lowers the FTO work function allowing for direct hole injection into the perovskite valence band. Under illumination, the conductivity of perovskite is increased and the device behaves similar to a photoconductor.

conversion efficiencies of 20.1% have been achieved within only five years of development.^[25] Recently, it has been demonstrated that organic–inorganic lead halide perovskites are also suitable candidates for high-performance photodetectors.^[11,26] Photodetectors, which convert incident optical signals to electrical signals, are key components for optical communication, photography, environmental sensing, medical analysis, astronomy, and safety equipment.^[27] An important class of photodetectors are those exhibiting intrinsic photocurrent amplification (gain) meaning that an incident photon triggers an electrical current flow provided by numerous electrons. Gain increases the sensitivity of the detector making it suitable for applications such as receivers in optical fiber communication, high-resolution imaging, single photon counting, and laser microscopy.^[28]

1. Introduction

Solution-processable organic–inorganic lead halide perovskites with the formula $\text{CH}_3\text{NH}_3\text{PbX}_3$ (where X is Cl, Br, or I) have attracted significant attention as new optoelectronic materials for photovoltaics,^[1–8] photodetectors,^[9–19] phototransistors,^[13,20] light emitting diodes (LEDs),^[21] and lasers.^[22,23]

The perovskite materials were shown to possess favorable properties for photovoltaic applications,^[24] and electrical power

Hu et al. demonstrated the first embodiment of a $\text{CH}_3\text{NH}_3\text{PbI}_3$ -based photodetector by employing a lateral geometry with a perovskite-filled channel between a pair of conductive contacts.^[12,14] This photodetector architecture exhibited gain of several tens under illumination and reverse bias. The authors suggested that a modified Schottky barrier at the gold/perovskite interface gave rise to electron injection resulting in the observed gain.^[12] More recently, Lee et al. presented a hybrid perovskite–graphene photodetector employing field effect transistor geometry, which despite the slow dynamics and a non-linear response, exhibited gain of several hundreds.^[13] Adding further to this, Dong et al. introduced a vertical stack geometry device and showed a high gain of ≈ 500 along with fast response time.^[11] The observed photomultiplication was suggested to originate from trapped photogenerated holes inducing band bending, which reduces the Schottky junction thickness at the MoO_3 /perovskite interface and allows the electrons to tunnel through the barrier.

While previous work has focused on the performance metrics of perovskite photodetectors, the understanding of their operating principles is still limited. In this work, we present a vertical stack geometry $\text{CH}_3\text{NH}_3\text{PbI}_3$ -based photodetector operated at a very low voltage (-0.6 V), which is characterized by a very high average gain of 1300 and a peak incident photon-to-current efficiency (IPCE) of 50 000%. We demonstrate that the

K. Domanski, Dr. W. Tress, Dr. M. Saliba,
Prof. M. K. Nazeeruddin
Group for Molecular Engineering
of Functional Materials
Institute of Chemical Science and Engineering
École Polytechnique Fédérale de Lausanne
Station 6, CH-1015 Lausanne, Switzerland
E-mail: wolfgang.tress@epfl.ch

K. Domanski, Dr. W. Tress, Dr. T. Moehl, Prof. M. Grätzel
Laboratory of Photonics and Interfaces
Institute of Chemical Science and Engineering
École Polytechnique Fédérale de Lausanne
Station 6, CH-1015 Lausanne, Switzerland
E-mail: thomas.moehl@epfl.ch

DOI: 10.1002/adfm.201503188



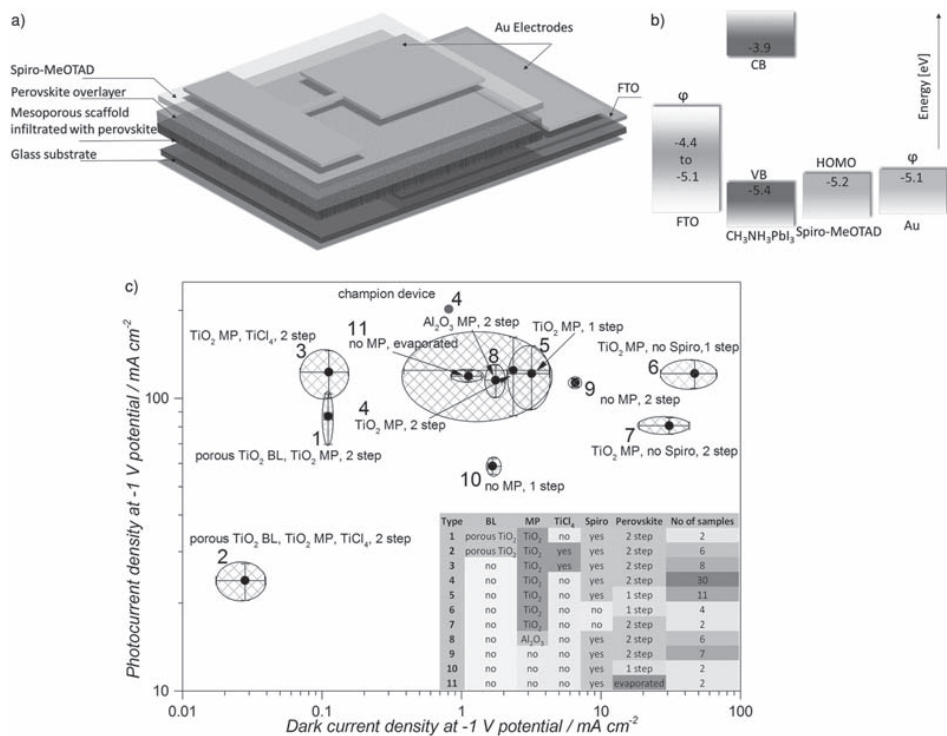


Figure 1. a) Structure of the model device and b) schematic energy diagram of the hybrid perovskite photodetector.^[30] The work function of FTO is not fixed, and it can be changed by interface modification as well as surface treatments.^[31] ϕ : work function, CB: conduction band, VB: valence band, HOMO: highest occupied molecular orbital. c) Dark and photocurrent density under 1 sun illumination as measured under -1 V for devices with different architectures. The ellipses represent standard deviation. Devices with 11 different architectures and an overall more than 100 devices were fabricated. BL: blocking layer; MP: mesoporous scaffold. The data can be found in Table S1 in the Supporting Information.

only prerequisite to obtain high gain in this type of devices is a direct contact between $\text{CH}_3\text{NH}_3\text{PbI}_3$ and fluorine-doped tin oxide (FTO), which shows the versatility of perovskite as a material for high-performance photodetectors.

We investigate steady-state and dynamic behavior of the photodetector with respect to illumination and operating voltage. We find that both, a reduction of the hole injection barrier at the FTO/perovskite interface under reverse bias and an enhancement of conductivity of the perovskite film under illumination (photoconductivity) are essential for the working mechanism. By investigating the temperature dependent dynamics, we find a characteristic activation energy of 420 ± 90 meV for the process dominating the dynamics of the current response. Our findings are consistent with the movement of ionic species alongside electronic charge carriers within perovskite. By assuming that these ions modify the electronic properties of the FTO/perovskite interface, we provide a model for the operation principles of the photodetector.

2. Investigated Architectures

We investigated devices with an architecture similar to our previous design (Figure 1a).^[26] On top of FTO-patterned glass, a TiO_2 blocking layer (BL) was deposited by spin-coating, spray-pyrolysis or atomic layer deposition (ALD). This was followed by deposition of a mesoporous (MP) metal oxide scaffold (conductive TiO_2 or insulating Al_2O_3). Optionally, TiCl_4 treatment was employed at this stage of device fabrication. The $\text{CH}_3\text{NH}_3\text{PbI}_3$ film was deposited using several different methods: interdiffusion of two perovskite precursors (PbI_2 and $\text{CH}_3\text{NH}_3\text{I}$),^[4] orthogonal solvent quenching,^[2] or perovskite precursor coevaporation.^[29] Finally, the hole transporting material (HTM), Spiro-MeOTAD, was spin-coated and Au contacts were thermally evaporated. Employment of a BL, an MP scaffold, or an HTM was optional and devices in various configurations were studied. A schematic energy diagram of the model devices is shown in Figure 1b. We note that the work function of FTO is not fixed. Depending on the on the surface treatment, or more

precisely, on the surface adsorbates/ dipoles values between -4.4 eV and -5.1 eV are reported. We used a UV-ozone pretreatment of the FTO, which typically results in a work function of -5.1 eV.^[31] However, we show later in this report that the work function can be further shifted as a result of ions accumulated at FTO/perovskite interface.

We compared the devices by analyzing their current density–voltage (J – V) characteristics. A standard procedure involved measuring dark J – V characteristics of the devices from 0 to -1 V (reverse), to $+1$ V (forward), back to 0 V with 200 mV s^{-1} scan rate. This was followed by an analogous measurement under white, 100 mW cm^{-2} LED illumination. A desirable combination of parameters for the photodetectors was low dark and high photocurrent under reverse bias conditions. We used dark and photocurrent density values at -1 V potential as benchmark parameters to compare fabricated devices and to select the best performers for an in-depth analysis. The summary of our findings is presented in Figure 1c.

The J – V studies showed that devices with pinhole-free compact, spray-pyrolyzed, or ALD-deposited TiO_2 BL do not exhibit photocurrent amplification under reverse bias and hence they do not work as photodetectors with gain. We note that already 2 nm thick compact BL deposited on TiO_2 MP completely suppressed photocurrent amplification under reverse bias conditions. Thus, creating an interface between FTO and perovskite proves critical for the photodetector to exhibit gain. We found that replacing a compact BL with a porous one with the same thickness (deposited via spin-coating) introduced photocurrent amplification (gain) under reverse bias conditions. The gain was further increased when the BL was removed completely, which is consistent with an increased FTO/perovskite contact area. On the other hand, the dark currents also increased when the compact BL was replaced with a porous one and they further increased when the BL was removed completely (Figure 2a). Interestingly, dark currents of devices with 2 nm thick ALD-deposited BL were very similar to dark currents of devices employing no BL despite the fact that the former did not show photocurrent amplification. Correspondingly, the

shunt resistance (calculated from the slope of the dark current at 0 V) decreased from ≈ 1 $M\Omega$ cm^2 for devices with a compact BL to ≈ 50 $k\Omega$ cm^2 for devices with a porous BL, to ≈ 10 $k\Omega$ cm^2 for devices with ALD or without BL. This indicates that the BL is sufficiently thin for electrons to tunnel through while at the same time a direct contact between FTO and perovskite is prohibited (due to the pinhole-free, conformal BL obtained from ALD even for very thin films). This underlines once again the importance of the FTO/perovskite interface for photocurrent amplification.

The $TiCl_4$ treatment, which creates a 1 – 3 nm thick porous layer of TiO_2 , was found to considerably reduce both dark and photocurrent under reverse bias when applied on samples with a porous TiO_2 BL. However, when applied on devices without a BL and with MP TiO_2 , it reduced dark currents while not affecting the photocurrent significantly, which again is in line with the FTO–perovskite interface being responsible for a functioning photodetector.

Furthermore, we compared devices with TiO_2 or Al_2O_3 MP scaffolds. Both scaffolds showed very similar J – V characteristics. However, devices without MP scaffold suffered from much increased dark currents (≈ 8 times increase at -1 V bias) while still showing only slightly lower photocurrents. In order to exclude that the photocurrent amplification phenomena originates from the perovskite/HTM interface, devices without Spiro-MeOTAD layer (and without BL) were fabricated. Such devices still functioned as photodetectors with gain (albeit the gain was much lower than that for devices employing an HTM). However, they suffered from ≈ 13 times increased dark currents as compared to the devices with an HTM, which can be explained by increased shunting due to a direct contact of MP TiO_2 with gold.

Thus, we conclude that as soon as an intimate contact between FTO and perovskite is present, the device can be operated as a photodetector with gain, regardless of the device architecture or the perovskite deposition method.

We found large variation in photodetector performance of the devices with the same architecture not only between

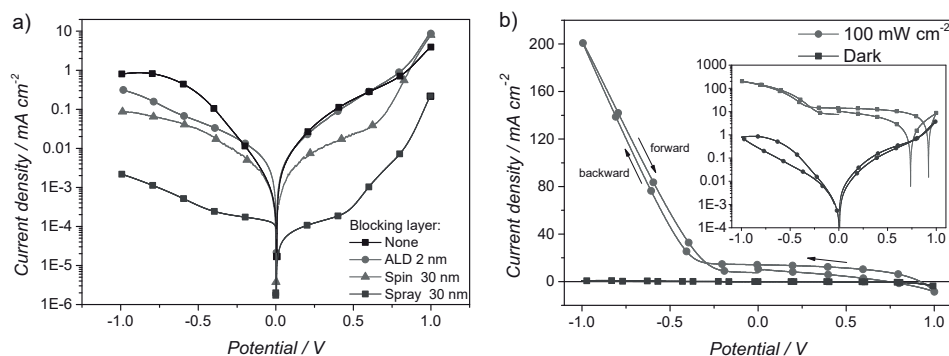


Figure 2. a) Dark J – V characteristics of devices with no BL, 2 nm thick ALD compact BL ≈ 30 nm thick spin-coated porous BL, with ≈ 30 nm thick spray-pyrolyzed compact one. b) J – V characteristics of a champion device (without a BL) in the dark and under simulated 1 sun illumination. Scan rate: 200 mV s^{-1} .

different batches of devices but also within each batch (the standard error on the photocurrent density at -1 V of 30 model devices was 30%). However, we have not observed any instances of devices without a compact BL, which would not function as photodetectors with gain. Devices employing $\text{CH}_3\text{NH}_3\text{PbI}_3$ can suffer from low reproducibility, which has been a subject of an intense discussion within the photovoltaic community.^[32] In general, we observed the highest reproducibility with devices employing no BL and no MP scaffold, although their photodetector performance was limited because of high dark currents from shunting.

Following these findings, we fixed our device architecture for the remainder of this study to a stack of FTO/ TiO_2 MP scaffold/ $\text{CH}_3\text{NH}_3\text{PbI}_3$ /Spiro-MeOTAD HTM/Au (Figure 1a). The $\text{CH}_3\text{NH}_3\text{PbI}_3$ film was deposited via two-step interdiffusion method. We note that this particular architecture yielded the highest-performing devices, however the average performance was not the highest.

3. Device Characterization

3.1. Basic Steady-State Characterization

Measured in the dark, the perovskite photodetector exhibits rectifying behavior. A solar to power conversion efficiency of

6.2% is achieved under 100 mW cm^{-2} simulated solar radiation (Figure 2b). However, when the device under illumination is biased in reverse direction, a strong increase in photocurrent is observed, which allows the device to work as both a photovoltaic cell and a high-gain photodetector depending on the direction of the applied bias.

The spectral response of the detector was characterized under 0 and -0.6 V reverse bias. As shown in Figure 3a,b, the detector exhibits high performance across the broad spectrum covering near UV and stretching the entire visible range, while being IR-blind. The IPCE of the device at short circuit conditions falls from $\approx 60\%$ under 350 nm to $\approx 30\%$ under 550 nm and $\approx 20\%$ under 750 nm illumination, which follows the absorbance of the perovskite film (Figure S1, Supporting Information).

Another important parameter for photodetectors is responsivity, which describes the ability of a device to respond to optical signals and it is defined as the ratio of the photogenerated current and the incident light power (P_{in})

$$R = \frac{I_{\text{photo}}}{P_{\text{in}}} = \frac{I_{\text{illuminated}} - I_{\text{dark}}}{P_{\text{in}}} \quad (1)$$

Under short-circuit conditions the detector is characterized by low responsivity of $0.18\text{--}0.11 \text{ A W}^{-1}$ in 350–750 nm region.

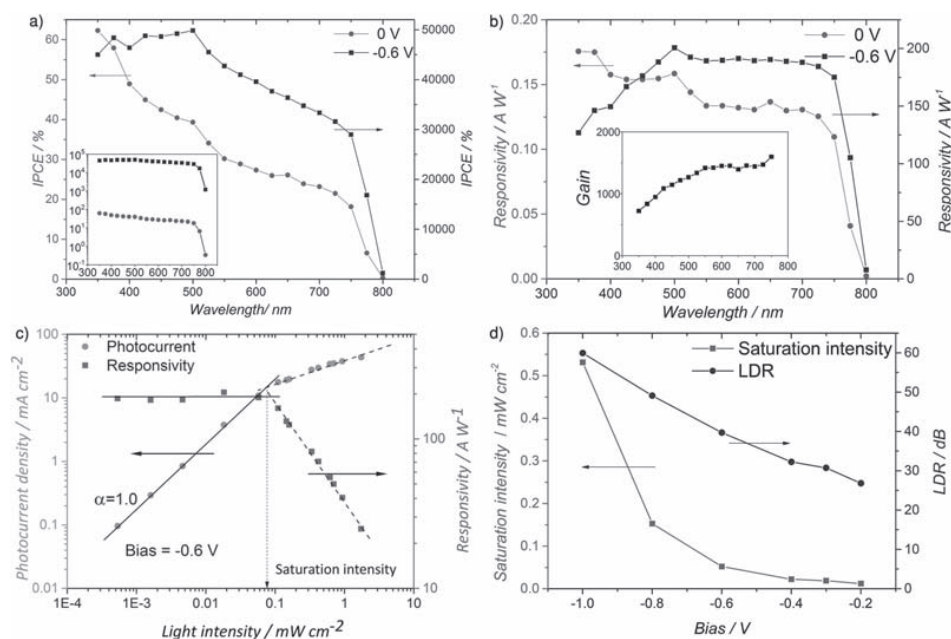


Figure 3. Optoelectronic response of the perovskite photodetector. a) IPCE of the perovskite photodetector (the inset in logarithmic scale), b) responsivity at short-circuit conditions and under -0.6 V reverse bias. The inset shows the gain spectrum of the photodetector. c) Photocurrent and responsivity dependence on light intensity. The lines are fits to a power law. d) Dependence of saturation intensity and LDR on the operating voltage.

To contrast this, when the detector is operated under -0.6 V reverse bias, a peak responsivity up to 200 A W^{-1} and IPCE of 50 000% is observed under 500 nm illumination. The gain spectrum of the detector can be calculated as the ratio of responsivity at -0.6 V bias and at 0 V (short-circuit condition) bias: $\text{gain} = \frac{R_{-0.6\text{V}} - R_{sc}}{R_{sc}}$. Gain of 1 indicates that for every pair of photogenerated carriers, there is one additional carrier injected to the perovskite and the overall current flowing through the external circuit is doubled. The gain of the photodetector is found to increase steadily from ≈ 720 to ≈ 1600 between 350 nm and 750 nm. This can be attributed to the more homogeneous carrier generation within the perovskite layer at longer illumination wavelengths due to a larger penetration depth of the light, which decreases the resistivity of the perovskite more homogeneously.

Linear dynamic range (LDR) describes an illumination intensity range within which the current response of the detector scales linearly with light intensity. It can be obtained as

$$\text{LDR} = 20 \log \frac{I_{\text{upper}} - I_{\text{dark}}}{I_{\text{lower}} - I_{\text{dark}}} \quad (2)$$

where I_{upper} is the current value at which the response of the detector deviates from linearity and I_{lower} is the lower resolution limit. For practical applications, it is desirable for a photodetector to have high LDR. However, the device can also be operated outside LDR if its behavior is well characterized.

Below the onset for the photocurrent amplification around -0.2 V, the response of the detector is linear from $0.5 \mu\text{W cm}^{-2}$ (noise limited) up to at least 100 mW cm^{-2} , which results in LDR of at least 106 dB (Figure S2, Supporting Information). However, when the device is operated under photocurrent amplification conditions, the signal starts to saturate already below the mW cm^{-2} regime (Figure 3c). Photocurrent saturation in photoconductors is known to be related to filling of sensitizing centers.^[33] Sensitizing centers are localized states that are empty in the dark and that can capture one type of photogenerated charges, which at low light intensities, increases the overall conductivity of the semiconductor. Under saturation (at higher light intensities), all sensitizing centers are effectively filled. However, the saturation may not be complete either due to the finite lifetime of charges generated above the saturation, or because recombination centers are able to additionally capture some of the photogenerated charges.^[33] The saturation intensity of our detector was found to increase substantially under higher operating bias (red line in Figure 3d). Consequently, since the noise limit on the lower end of the linear region ($\approx 0.5 \mu\text{W cm}^{-2}$) does not considerably vary with operating voltage, LDR increases when the device is operated under higher reverse bias showing an approximately linear scaling with reverse bias (blue line).

Under -0.6 V reverse bias, we have measured a responsivity of 208 A W^{-1} (IPCE of 47 000%), which is among the highest values reported for perovskite photodetectors.^[11,13,19,20] The current response of the device was found to be linear with irradiance up to $80 \mu\text{W cm}^{-2}$ resulting in a LDR of 44 dB.

We note a broad variability for the saturation intensity from 20 to $110 \mu\text{W cm}^{-2}$ with an average value of $58 \mu\text{W cm}^{-2}$ measured for six identically fabricated devices under -0.6 reverse bias. The average responsivity of those devices was found as $135 \pm 55 \text{ A W}^{-1}$. The high variation in the performance of the detectors is not unusual for optoelectronic devices employing $\text{CH}_3\text{NH}_3\text{PbI}_3$ and it shows that a robust method to fabricate perovskite photodetectors is still subject to ongoing research.

3.2. Transient Light Intensity and Scan-Rate-Dependent Response

The transient photocurrent response of the device was investigated by biasing the device in reverse direction and exposing it to 60 s long pulses of 550 nm monochromatic light. Below the onset for photocurrent amplification (also at J_{sc} and under forward bias), the transient response of the detector is relatively fast (<10 ms) and thus not resolved in the investigated timescale of seconds. When the device is biased beyond the photocurrent amplification onset, i.e. when the device is operated under photocurrent amplification conditions, the dynamics become considerably slower and an initial overshoot in current is observed when the light is switched-on (Figure 4a,b). This overshoot becomes less pronounced and it peaks later when the voltage is further increased in reverse direction. Although we have observed this overshoot under any bias past the amplification onset, at higher reverse bias the overshoot may not be distinct enough to be identified easily. Subsequently, when light is switched-off, the current decay is composed of two components—a very fast one (not resolvable on the investigated timescale of 10 ms) and a very slow one (on the order of seconds). The nature of these two components is likely to be fundamentally different and we hypothesize that the slow component arises due to the movement of ionic species in the perovskite.^[34,35] This transient behavior is fully reproducible (Figure S3, Supporting Information) and the bandwidth of the detector is determined to be in the sub-Hz region due to the very slow dynamics.

The current decay is slower when the light is switched-off and the devices are operated under higher reverse voltage. The amount of charge flowing through the device, after light is switched-off can be calculated by fitting the decay curves and integrating the area under them. We determine the charge to be in the range of $\approx \text{mC cm}^{-2}$ (Figure 4c). This is significantly higher than can be expected from the extraction of trapped photogenerated electronic carriers (the trapped charge carrier density would exceed the atomic density of the material) and it implies a photoinduced long-lived rise in injection current from the contacts, which decays on the timescale of seconds after the light is switched-off. These slow transient phenomena are due to a slow change either of the conductivity of the perovskite or of the charge carrier injection rates at the contacts (or a combination of both), which can be interpreted as a signature of movement of ionic species within the perovskite layer and will be analyzed later in this work.

The photodetector exhibits gain and can be operated as such under any reverse bias greater than the photocurrent amplification onset. However, the responsivity of the device is highly dependent on the operating voltage. Figure 4d shows that below the photocurrent amplification onset at around

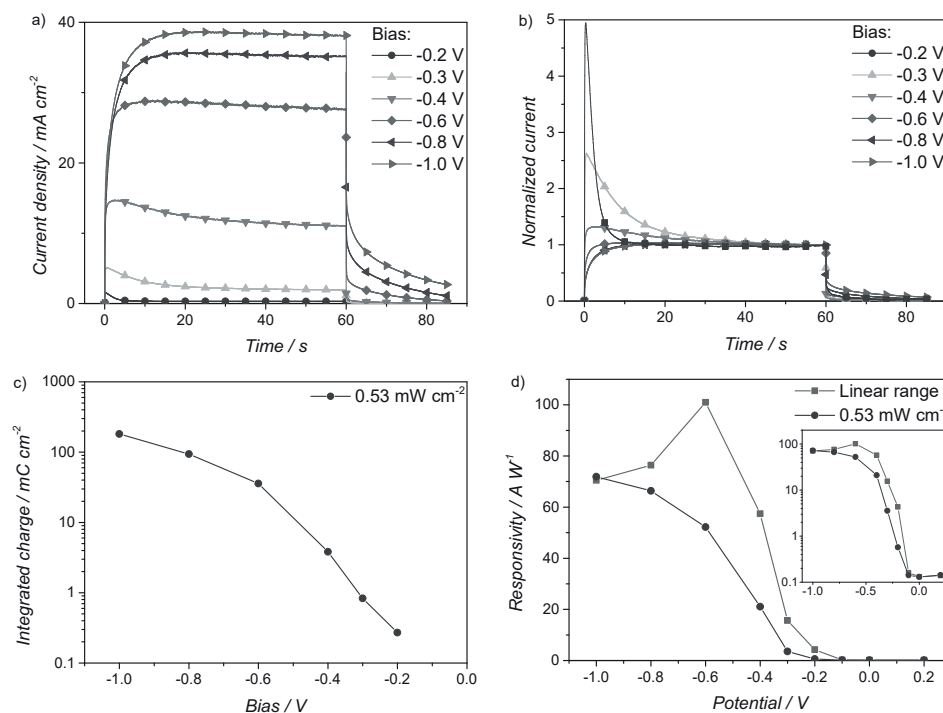


Figure 4. Light-transient response of the perovskite photodetector. a) Transient current response to 60 s long 0.53 mW cm^{-2} pulses of 550 nm light under different reverse bias. The steady-state dark currents are subtracted for each bias; b) transient current response normalized to the steady-state value at 60 s; c) integrated charge flowing after light is switched-off and d) dependence of responsivity on operating bias: under 0.53 mW cm^{-2} illumination and under illumination within LDR the inset in logarithmic scale.

-0.2 V , the responsivity of the device remains very low, which translates to IPCEs below unity. Under higher reverse bias, the responsivity measured within the LDR peaks at -0.6 V before decreasing slightly. The decrease is due to the larger relative contribution of the dark current under higher reverse bias. Under higher illumination intensities ($\geq 0.1 \text{ mW cm}^{-2}$) the decrease is not observed since the relative contribution of the dark current is lower. Interestingly, the responsivity of the device and the total charge flowing through it after light is switched-off follow a very similar trend as a function of operating bias. This may suggest that a photoinduced long-lived rise in injection current is the common origin of both photocurrent amplification and the large amount of post-illumination charge flowing through the device.

The onset of photocurrent amplification at around -0.2 V is found to be independent of light intensity, light spectrum, scan rate, or temperature. However, under reverse bias, past the onset for photocurrent amplification, the slope and the shape of the J - V curves are heavily dependent on the illumination intensity (Figure 5), scan rate (Figure 6), and temperature (Figure 7), as will become clear further down.

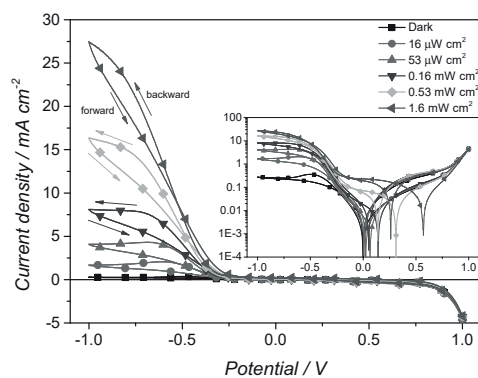


Figure 5. Light intensity dependent J - V characteristics of the perovskite photodetector. The inset shows the results in logarithmic scale. Scan rate: 10 mV s^{-1} .

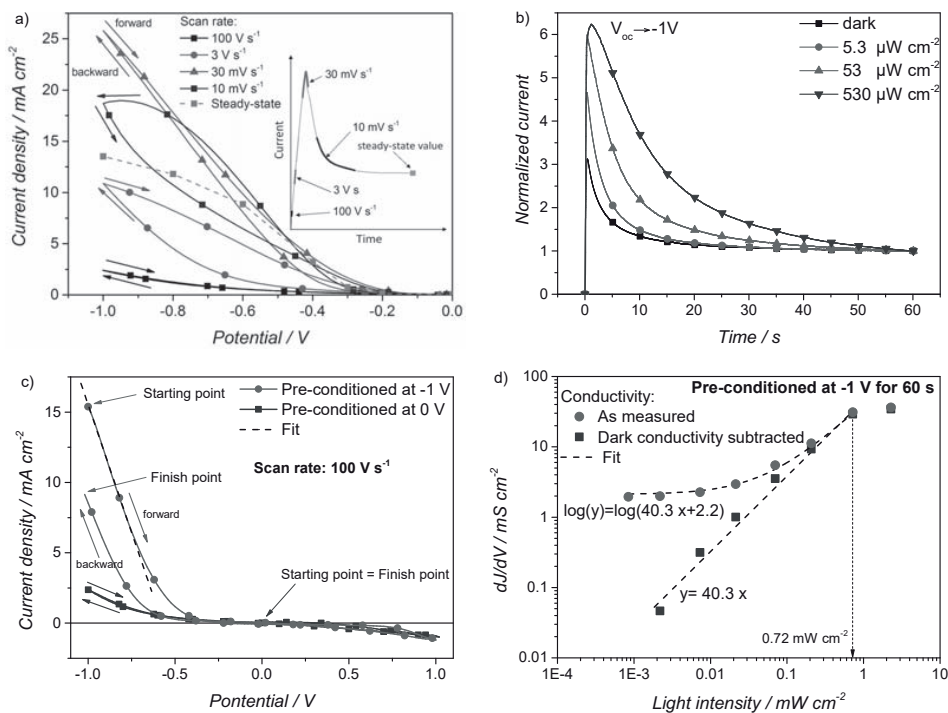


Figure 6. a) The effect of the scan rate on the J - V hysteresis of the photodetector (illumination: 550 nm, $530 \mu\text{W cm}^{-2}$). The inset shows a schematic voltage transient. b) The response of the device when the potential is step-changed from V_{oc} to -1 V for different light intensities and normalized to the steady-state photocurrent at 60 s. c) J - V characteristics of the detector following 60 s of preconditioning at different potentials; illumination: 0.72 mW cm^{-2} for -1 V and 0.53 mW cm^{-2} for 0 V preconditioned data. d) dJ/dV is found constant between -1 V and -0.6 V in forward scan d) dJ/dV in the linear region as a function of illumination intensity when the detector is preconditioned at -1 V for 60 s. The linearity of conductivity with light intensity indicates photoconductive behavior.

When scanning in backward direction, past the amplification onset, the photocurrent increases sharply with voltage. As the voltage is increased further, the photocurrent saturates and starts to decrease. Scanning beyond this point results in a large J - V hysteresis when the scan is then continued in forward direction (cf. curves for intermediate light intensities in Figure 5). In general, the further past the current peak the scan is performed, the larger the hysteresis becomes. The trend was found to hold for all of the devices tested and it is also observed in the dark scans suggesting the independence of the phenomena from light. On the other hand, the point at which the photocurrent starts to saturate is dependent on the illumination intensity. In general, the higher the light intensity, the further the saturation voltage shifts towards reverse bias direction (Figure 5).

The slow photocurrent transients and the hysteresis in the J - V curves of Figure 5 anticipate a strong dependence on voltage sweep rate. Thus, we measure the J - V curves at different scan rates and following a defined preconditioning point

(0 V). Figure 6a shows J - V curves measured from 0 V to -1 V and back. When the scan rate is varied, large differences in J - V characteristics of the devices are observed. Again, the most pronounced differences are observed when the device is operated under reverse bias. When very high scan rates are employed (order of tens to hundreds V s^{-1}) the photocurrent amplification under reverse bias is almost completely suppressed. Correspondingly, the observed hysteresis is very low. We observe a substantial increase in photocurrent amplification and even higher increase in hysteresis for slightly lower scan rates (several V s^{-1}). The highest photocurrent amplification as well as the lowest hysteresis is obtained when intermediate scan rates are used (30 – 100 mV s^{-1}). Decreasing the scan rate further to 10 mV s^{-1} results in both lower photocurrent amplification and higher hysteresis. Overlaying these results with steady-state current values (dashed) reveals that even lower scan rates would be required to achieve hysteresis-free curves.

These seemingly anomalous results of the light intensity and scan rate influence on the J - V characteristics can

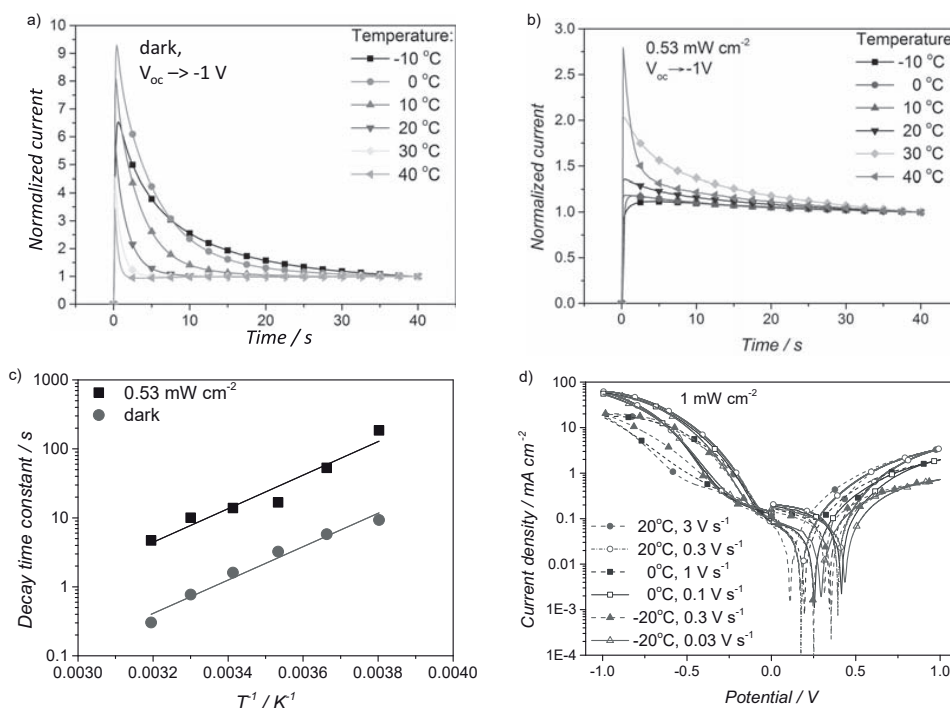


Figure 7. The effect of temperature on the behavior of perovskite photodetector. Transient response of the device when the potential is step-changed from V_{oc} to -1 V at different temperatures normalized to current value at 40 s a) in the dark, b) under 0.53 mW cm^{-2} illumination, and c) the corresponding decay time constants (τ_{decay}) of the transient data fitted to Equation (3). d) Scan rate and temperature dependent J - V characteristics of the detector under 1 mW cm^{-2} illumination. Scan rates are selected to visualize the similarity of J - V curves measured at an approximately three times lower rate when the temperature was decreased by 20 K.

be explained by investigating the transient behavior of the detector. Figure 6b shows the response of the device when it is subjected to a potential step-change from V_{oc} under corresponding light intensity to -1 V (V_{oc} of the devices was found between 90 mV for $530 \mu\text{W cm}^{-2}$ and 0 mV in the dark). Interestingly, immediately after the bias is changed to -1 V, almost no current flows through the device neither in the dark nor under light. A relatively slow process is responsible for enabling the current to flow and for photocurrent amplification. However, the same process seems to be responsible for the subsequent overshoot in current, which is followed by a slow decay to a saturation value. The dynamics of this behavior are light intensity dependent and slow down at higher light intensities.

It is possible to model the response of the device to a potential step with two exponential terms, a positive and a negative one

$$J(t) = A_1(1 - e^{-t/\tau_{rise}}) + A_2e^{-t/\tau_{decay}} + B \quad (3)$$

The negative term gives rise to the overshoot in current, while the positive term is responsible for the subsequent decay. By fitting the data to this model (Figure S4, Supporting Information) and by analyzing the time constants of the two processes, we have found that light intensity has no apparent influence on the current rise time, which remains below 0.01 s. At the same time, the time constant for current decay decreases from ≈ 20 s at 1.6 mW cm^{-2} to ≈ 4 s at $0.53 \mu\text{W cm}^{-2}$ following closely a power law relationship (Figure S5, Supporting Information). The observed time scale for current decay is comparable to time scales for hysteresis as reported for $\text{CH}_3\text{NH}_3\text{PbI}_3$ -based solar cells.^[36,37]

The inset in Figure 6a explains how photocurrent amplification and hysteresis are related to the transient behavior presented in Figure 6b. We note that the device does not have sufficient time to establish photocurrent amplification when performing a very fast J - V scan. The hysteresis is low since the time interval between forward and reverse scans is very short, which does not permit for significant changes of device's electronic properties; higher current is measured during forward

scan (from -1 V to 0 V). At slower scan rates there is more time to establish photocurrent amplification but consequently the hysteresis increases since the time between backward and forward scans is larger. We “probe the tip” of the transient overshoot by choosing the appropriate scan rate. This way it is possible to achieve nearly hysteresis-free J - V curves. When J - V scans are performed at a lower rate, the device has sufficient time to reach the “postovershoot” region. Hence the hysteresis becomes higher and now, contrary to the faster measurements, the backward scan yields the higher current value. Based on this, we can explain the shape of the light intensity dependent J - V curves presented in Figure 5 under reverse bias and slow scan rates. We have shown that the response of the device to the varying voltage becomes slower when the intensity of the incident illumination is higher. Thus, the hysteresis is lower for larger intensities analogously to the lower hysteresis for intermediate scan rates. This behavior is a consequence of the effect of photogenerated charges on the slow process in the device.

Finally, in Figure 6c, we measured J - V characteristics of the device following 60 s of preconditioning at different potentials. Clearly, during a very fast scan, the device cannot respond quickly enough to establish photocurrent amplification. Thus, suppressing the dominance of the slow process for the device response can be achieved by employing a fast 100 V s^{-1} scan rate (40 ms for the complete scan). When the scan is preconditioned at -1 V for 60 s, we observe high photocurrent amplification under reverse bias conditions. Since the contribution of the slow process on the 40 ms timescale is still not negligible, the forward and backward scans do not overlap. Scanning in forward direction, the J - V curve is linear between -1 and -0.6 V, which is an indication of photoconductivity as the mechanism responsible for photocurrent amplification. Figure 6d shows how the dJ/dV slope in this linear regime depends on light intensity. The conductivity of the sample is found to be directly proportional to light intensity which is another indication of photoconductivity. However, when plotted in logarithmic scale the relationship is evidently linear only when constant, dark conductivity is subtracted. We note that the response of the detector saturates beyond 0.72 mW cm^{-2} illumination intensity, which is consistent with the value shown in Figure 3 for corresponding operating conditions (0.53 mW cm^{-2}).

3.3. Temperature Dependence

To further analyze the origin of the slow response times, we perform J - V and transient measurements as a function of temperature. Figure 7a,b show how the response of the device to a potential step from V_{oc} to -1 V varies at temperatures between -10 and 40 °C (V_{oc} under 0.53 mW cm^{-2} illumination varied with temperature from 150 mV at -10 °C to 50 mV at 40 °C). We investigated the effect of temperature on the dynamics of the device by again fitting the data with the two exponentials model as presented in Equation (3) (Figures S6 and S7, Supporting Information). While the influence of temperature on the current rise time constant was not fully conclusive, we have found that the current decay becomes considerably slower at lower temperatures both in the dark and under illumination (Figure 7c).

Combined analysis of three independent datasets has revealed an Arrhenius-type relationship. Independently of illumination, we derived an activation energy of 420 ± 90 meV for the slow process responsible for the current decay. This value is consistent with the recently reported activation energy for the movement of iodine defects in $CH_3NH_3PbI_3$.^[34,35,38]

Subsequently, we observed a strong temperature effect on the J - V characteristics of the perovskite photodetector (Figure S8, Supporting Information). In reverse bias direction, photocurrent amplification is found to be heavily dependent both on scan rate and temperature. On the other hand, while the J - V characteristics in forward direction are less influenced by the scan rate, the influence of temperature is even more pronounced. The latter is likely due to the reduced conductivity of Spiro-MeOTAD at lower temperatures (Figure S9, Supporting Information). Interestingly, in reverse direction almost identical (rate dependent) J - V curves can be obtained when simultaneously changing the scan rate and the temperature (Figure 7d). We have found that decreasing the temperature by 20 K is equivalent to performing the J - V scans approximately three times faster (see Figure S8 in the Supporting Information for more examples). This proves once again that the shape of the reverse J - V curve describing photocurrent amplification is mainly governed by a temperature-activated slow process. This observation is consistent with the effect of temperature on the transient behavior. Using a first order approximation $\propto \exp(-E_a/kT)$, we determine the activation energy to be between 300 and 400 meV, which is remarkably close to the value found above.

In summary, we have found that:

- Direct contact between FTO/perovskite is essential for the device to exhibit photomultiplication.
- Photomultiplication is enabled by slow processes with time constants on the order of seconds established by biasing the device in reverse direction.
- Photomultiplication is a consequence of photoconductivity of $CH_3NH_3PbI_3$. The response of the device becomes slower under illumination.
- The device reacts slower at lower temperatures. Matching J - V curves can be obtained by either changing the scan rate or temperature in a controlled way.

4. Results and Discussion

The characteristics of the photodetector are dominated by processes that occur on the time scale of seconds and that are strongly temperature activated. These observations coincide with results from studies on the J - V hysteresis in perovskite solar cells. Recently, clear evidence has been presented linking hysteresis with the relatively slow movement of ionic species within the material.^[34,35,37,39] Iodine defects (interstitials and vacancies) were shown to have the lowest formation and activation energies for ionic point defects which are suggested to be the mobile species in $CH_3NH_3PbI_3$.^[40] Guided by these results, we propose a model explaining the photomultiplication effect in our system.

Figure 8 visualizes how the transient current response to a step-change in potential (from 0 V to negative voltages) arises

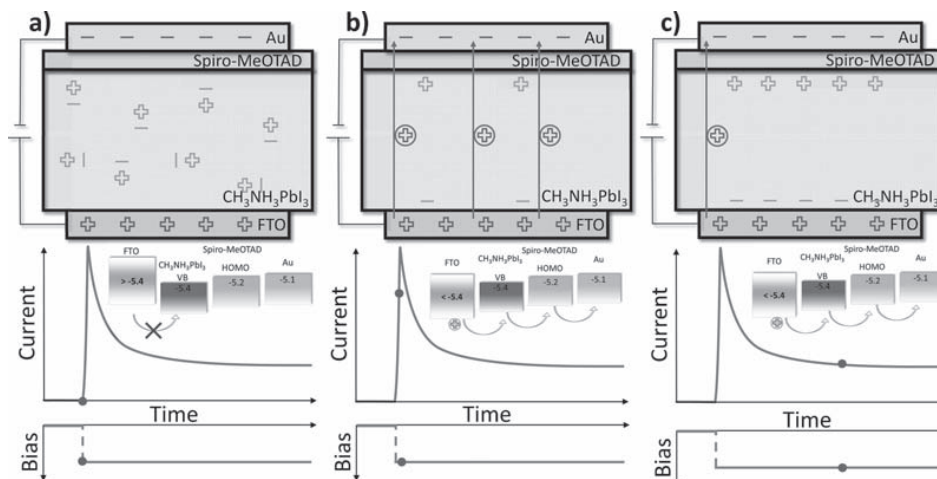


Figure 8. The emergence of transient behavior when the device is kept in dark and it is subjected to a step-change in potential. a) Immediately after applying reverse bias, no current flows through the device since the work function of FTO is too low for hole injection. b) Ions travel to FTO/perovskite interface downshifting FTO work function and enabling hole injection into perovskite. c) As ions accumulate at the interface, they screen the electric field, which results in the decrease of the current. Dark grey charges represent the electric charges on electrodes, light grey mobile ions (in the perovskite), and grey with circle represent the holes injected from FTO. The current–time as well as the distribution of the ions plots are schematic.

due to the movement of mobile ionic species. When the device is kept in the dark, immediately after reverse bias is applied, an (additional) electric field is established across the device but current does not flow due to the unfavorable alignment of FTO work function and CH₃NH₃PbI₃ valence band (Figure 8a). Mobile ionic species in CH₃NH₃PbI₃ respond to the established electric field and travel towards the respective interfaces where they “pile up.” The accumulation of negative ions at CH₃NH₃PbI₃/FTO interface causes a downshift of the FTO work function, which enables hole injection into CH₃NH₃PbI₃ and results in a flow of dark current across the device (Figure 8b). However, as large amount of ions accumulate at the interfaces, they screen the electric field in the perovskite, which results in the decrease of dark current until equilibrium is reached (Figure 8c).

The effect of temperature on the transient behavior of the detector expresses itself as a modulation in dynamics. We have shown that the time constant of the current decay increases with temperature following an Arrhenius-type relationship (Figure S7, Supporting Information). This is caused by faster diffusion of ionic species at higher temperatures.

Under illumination additional screening effects and interactions of ionic defects with photogenerated charges have to be taken into account. This additional charge can effectively reduce the electric field in the perovskite layer and hence the driving force for ionic species to move; therefore, resulting in slower response times with increased light intensity (Figure 6b). Alternatively, photogenerated charges can compensate the ionic charge accumulated at the interfaces. When the device is kept under constant, reverse bias (past the photocurrent amplification onset) and the light is switched-on, photogenerated charges are attracted to the respective electrodes by the electric

field, which is largely screened by the accumulated ions. The transit time of electrons is assumed to be longer than that of holes,^[41] which results in fast hole collection and multiple re-injection before the electrons are collected. This way photomultiplication is obtained and thus the device behaves similar to a photoconductor. Additionally, photogenerated charges establish an electric field, which is opposite to the field applied across the device. This induces the diffusion of ions away from the interface, which reduces the screening and results in a slow current increase. Under low reverse operating voltage, a large amount of ions is able to diffuse away from the interface, which in turn results in unfavorable conditions for hole injection.

When the light is switched-off, the relatively low density of ions at the interfaces leads to lower screening and a long-lived rise in injection current from the contacts as compared to the preillumination state (Figure 4c). Essentially, the mechanism responsible for the remnant large injection current after light is switched-off is the same as the one shown in Figure 8. The effect is even more pronounced when the device is operated under higher reverse bias, since the electric field remains largely unscreened and hole injection is more efficient.

5. Conclusions

We have fabricated high-gain, low-voltage CH₃NH₃PbI₃ photodetectors in various architectures. We observed photomultiplication in all structures having direct contact of FTO and perovskite, i.e. devices with either a porous or without any TiO₂ hole BL. Devices based on FTO/TiO₂ MP scaffold/CH₃NH₃PbI₃/Spiro-MeOTAD HTM/Au showed the

highest responsivity of 208 A W^{-1} under 550 nm illumination, which corresponds to an IPCE of 47 000%. These high values of photomultiplication were reached for light intensities in the range of $0.5\text{--}80 \mu\text{W cm}^{-2}$ when the device was biased in reverse (-0.6 V).

During $J\text{--}V$ scans in the potential range of -1 V and 1 V a strong dependence of the current response on scan rate and preconditioning was observed, showing the highest current values with least hysteresis at moderate scan rate (30 mV s^{-1}). This observation is explained by a slow process in the time scale of seconds found when studying the transient current response upon changing illumination intensity or applied voltage. Having performed temperature dependent studies, we observed a strong dependence of the response time on temperature, yielding an activation energy of $420 \pm 90 \text{ meV}$ for the slow process. As the values for activation energy and response time are characteristic for ionic motion in these perovskite materials, we develop a model based on ion migration that can explain the observed transients and the photomultiplication. Essential is the pile-up of negative ionic charge at the FTO/perovskite interface under reverse bias. This charge lowers the FTO work function allowing for direct hole injection into the perovskite valence band. Due to an overall increase in conductivity, the hole current is enhanced upon illumination, and the device behaves similar to a photoconductor.

These results on the performance of our photodetector encourage the application of $\text{CH}_3\text{NH}_3\text{PbI}_3$ for low-cost, and highly sensitive photodetectors with high gain. The proposed working principle leads to a better understanding of phenomena such as hysteresis in perovskite-based optoelectronic devices in general and the perovskite interface formation in particular.

6. Experimental Section

Blocking Layer: FTO-patterned glass (Nippon sheet glass, NSG 10 Ω) was cleaned in an ultrasonic bath containing Hellmanex solution for 20 min, and subsequently in isopropanol. This was followed by a UV ozone treatment for 10 min. For devices employing a spin-coated BL, a 0.15 M titanium diisopropoxide bis(acetylacetonate) (TAA) solution (in ethanol) was spin-coated on the FTO at 1000 rpm for 10 s and 2000 rpm for 30 s. This was followed by drying at $125 \text{ }^\circ\text{C}$ for 5 min and then annealing at $500 \text{ }^\circ\text{C}$ for 15 min to produce a layer of about 30 nm in thickness. The 30 nm thick TiO_2 compact BL was deposited by spray-pyrolysis of diluted TAA solution (Sigma-Aldrich) at an FTO substrate at $450 \text{ }^\circ\text{C}$. The solution for spray-pyrolysis was prepared by mixing 1 mL of TAA (30% in 2-propanol) and 25 mL of ethanol. 1–3 nm thick TiO_2 compact BL was deposited by ALD on top of MP TiO_2 scaffolds.

Mesoporous Scaffold: The TiO_2 and Al_2O_3 solutions were prepared by dispersing 1 and 2 g of paste (Dyesol) respectively in 10 mL ethanol and stirring them overnight before use. The solutions were sonicated for 5 min and then spin-coated on the substrates at 2000 rpm for 10 s. The films were dried at $125 \text{ }^\circ\text{C}$ for 10 s and then annealed at $550 \text{ }^\circ\text{C}$ for 30 min. This resulted in scaffold thickness of around 100 nm.

TiCl_4 Treatment: An optional TiCl_4 treatment was performed by immersing the as-prepared scaffolds in a 0.15 M aqueous TiCl_4 solution at $70\text{--}80 \text{ }^\circ\text{C}$ for 30 min and then washing them with deionized water and drying. The films were then annealed at $500 \text{ }^\circ\text{C}$ for 20 min.

$\text{CH}_3\text{NH}_3\text{PbI}_3$ Layer: $\text{CH}_3\text{NH}_3\text{PbI}_3$ films were deposited via several different methods.

Two-step spin-coating: The films were prepared under ambient air atmosphere. 1 M PbI_2 solution was prepared by dissolving 462 mg of PbI_2 (Sigma-Aldrich) in 1 mL N,N -dimethylformamide (DMF) under stirring at $70 \text{ }^\circ\text{C}$. The hot solution (30 μL) was loaded onto the substrate (10 s loading time) and then spin-coated at 3000 rpm for 5 s and

6000 rpm for 5 s. Subsequently, the films were transferred to a hotplate at $100 \text{ }^\circ\text{C}$ for 10 min. After cooling down to room temperature, 200 μL of 0.044 M $\text{CH}_3\text{NH}_3\text{I}$ solution (in isopropanol) was loaded onto the substrate (30 s loading time) and spun at 3000 rpm for 20 s and dried at $100 \text{ }^\circ\text{C}$ for 5 min.

One-step orthogonal spin-coating: The films were deposited in a nitrogen-filled glove box. A 1.1 M precursor solution of $\text{CH}_3\text{NH}_3\text{PbI}_3$ was prepared by dissolving stoichiometric amounts of PbI_2 and $\text{CH}_3\text{NH}_3\text{PbI}_3$ in dimethylsulfoxide (DMSO). The precursor solution was spin-coated on MP TiO_2 scaffold at 1000 rpm for 10 s, immediately followed by 6000 rpm for 30 s. 10 s before the end of the spin-coating program, chlorobenzene was dropped on the spinning substrate. The substrate was then heated at $90 \text{ }^\circ\text{C}$ for 1 h.

Evaporation: The evaporation was performed in a vacuum chamber. The perovskite film was coevaporated from PbI_2 and $\text{CH}_3\text{NH}_3\text{I}$ sources through a shadow mask. Both precursors were heated simultaneously to their corresponding sublimation temperatures and the perovskite film was deposited at a substrate placed above the sources.

Hole Transporting Layer and Backside Electrode: A $70 \times 10^{-3} \text{ M}$ spiro-MeOTAD solution was prepared by dissolving 72.3 mg of spiro-MeOTAD in 1 mL of chlorobenzene to which 28.8 μL of 4-*tert*-butyl pyridine and 17.5 μL of 1.8 M lithium(trifluoromethanesulfonyl)imide (Li-TFSI) solution in acetonitrile were added. The hole transporting layer was prepared by spin-coating the as prepared spiro-MeOTAD solution at 4000 rpm for 30 s. Finally, 80 nm of gold was thermally evaporated through a shadow mask to complete the device.

Device Characterization: The absorption spectrum of the devices was measured using a Hewlett Packard HP 8453 spectrometer. Current–voltage characteristics of the devices were recorded using BioLogic SP200 potentiostat. The source of monochromatic light was a monochromator-filtered xenon lamp. Neutral density filters were used to attenuate the light and a mechanical chopper was used to control the sample illumination. The 100 mW cm^{-2} white light was generated by an array of white LEDs. A heating/cooling sample holder employing a Peltier element was built in order to control the temperature of devices. A thermocouple was used for temperature feedback. The geometry was arranged so that the thermocouple was placed between the Peltier element and the backside of the device. A 0.5 mm thick thermal pad separated the device and the thermocouple.

Supporting Information

Supporting Information is available from the Wiley Online Library or from the author.

Acknowledgements

This work was made possible by the NPRP award [NPRP 6-175-2-070] from the Qatar National Research Fund (a member of The Qatar Foundation). The statements made herein are solely the responsibility of the authors. The authors thank Paul Gratia and Dr. Cristina Roldán Carmona for preparing the evaporated devices, Dr. Juan Pablo Correa for preparing ALD-deposited BL, Agata Mosinska for help with data fitting, and Heidi Francelet for administrative support. W.T. thanks the European Union for funding within the Seventh Framework Program (FP7/2007-2013) under Grant Agreement No. 604032 of the MESO project. T.M. thanks the SNF for financial support through the Nano-tera Synergy project and European Research Council (ERC) for financial support under the Advanced Research Grant (ARG no. 247404) funded under the “Mesolight” project. M.G. thanks the Swiss National Science Foundation for financial support under the Grant No. 200021_157135/1.

Received: July 31, 2015

Revised: August 28, 2015

Published online: October 20, 2015

- [1] J. Burschka, N. Pellet, S.-J. Moon, R. Humphry-Baker, P. Gao, M. K. Nazeeruddin, M. Grätzel, *Nature* **2013**, 499, 316.
- [2] N. J. Jeon, J. H. Noh, Y. C. Kim, W. S. Yang, S. Ryu, S. I. Seok, *Nat. Mater.* **2014**, 13, 897.
- [3] A. Kojima, K. Teshima, Y. Shirai, T. Miyasaka, *J. Am. Chem. Soc.* **2009**, 131, 6050.
- [4] J.-H. Im, I.-H. Jang, N. Pellet, M. Grätzel, N.-G. Park, *Nat. Nano.* **2014**, 9, 927.
- [5] N. J. Jeon, J. H. Noh, W. S. Yang, Y. C. Kim, S. Ryu, J. Seo, S. I. Seok, *Nature* **2015**, 517, 476.
- [6] K. Wojciechowski, M. Saliba, T. Leijtens, A. Abate, H. J. Snaith, *Energ. Environ. Sci.* **2014**, 7, 1142.
- [7] O. Malinkiewicz, A. Yella, Y. H. Lee, G. M. Espallargas, M. Graetzel, M. K. Nazeeruddin, H. J. Bolink, *Nat. Photo.* **2014**, 8, 128.
- [8] D. Liu, T. L. Kelly, *Nat. Photo.* **2014**, 8, 133.
- [9] Y. Guo, C. Liu, H. Tanaka, E. Nakamura, *J. Phys. Chem. Lett.* **2015**, 5, 1748.
- [10] D. Li, G. F. Dong, W. Z. Li, L. D. Wang, *Sci. Rep.* **2015**, 5, 7902.
- [11] R. Dong, Y. Fang, J. Chae, J. Dai, Z. Xiao, Q. Dong, Y. Yuan, A. Centrone, X. C. Zeng, J. Huang, *Adv. Mater.* **2015**, 27, 1912.
- [12] X. Hu, X. D. Zhang, L. Liang, J. Bao, S. Li, W. L. Yang, Y. Xie, *Adv. Funct. Mater.* **2014**, 24, 7373.
- [13] Y. Lee, J. Kwon, E. Hwang, C. H. Ra, W. J. Yoo, J. H. Ahn, J. H. Park, J. H. Cho, *Adv. Mater.* **2015**, 27, 41.
- [14] H.-R. Xia, J. Li, W.-T. Sun, L.-M. Peng, *Chem. Commun.* **2014**, 50, 13695.
- [15] Q. Lin, A. Armin, D. M. Lyons, P. L. Burn, P. Meredith, *Adv. Mater.* **2015**, 27, 1969.
- [16] Y. Fang, J. Huang, *Adv. Mater.* **2015**, 27, 2804.
- [17] S. Zhuo, J. Zhang, Y. Shi, Y. Huang, B. Zhang, *Angew. Chem. Int. Ed.* **2015**, 127, 5785.
- [18] L. Dou, Y. Yang, J. You, Z. Hong, W.-H. Chang, G. Li, Y. Yang, *Nat. Commun.* **2014**, 5, 5404.
- [19] H.-W. Chen, N. Sakai, A. K. Jena, Y. Sanehira, M. Ikegami, K.-C. Ho, T. Miyasaka, *J. Phys. Chem. Lett.* **2015**, 6, 2622.
- [20] F. Li, C. Ma, H. Wang, W. Hu, W. Yu, A. D. Sheikh, T. Wu, *Nat. Commun.* **2015**, 6, 8238.
- [21] Z.-K. Tan, R. S. Moghaddam, M. L. Lai, P. Docampo, R. Higler, F. Deschler, M. Price, A. Sadhanala, L. M. Pazos, D. Credgington, F. Hanusch, T. Bein, H. J. Snaith, R. H. Friend, *Nat. Nano.* **2014**, 9, 687.
- [22] F. Deschler, M. Price, S. Pathak, L. E. Klintberg, D.-D. Jarausch, R. Higler, S. Hüttner, T. Leijtens, S. D. Stranks, H. J. Snaith, M. Atatüre, R. T. Phillips, R. H. Friend, *J. Phys. Chem. Lett.* **2014**, 5, 1421.
- [23] G. Xing, N. Mathews, S. S. Lim, N. Yantara, X. Liu, D. Sabba, M. Grätzel, S. Mhaisalkar, T. C. Sum, *Nat. Mater.* **2014**, 13, 476.
- [24] G. Xing, N. Mathews, S. Sun, S. S. Lim, Y. M. Lam, M. Grätzel, S. Mhaisalkar, T. C. Sum, *Science* **2013**, 342, 344.
- [25] W. S. Yang, J. H. Noh, N. J. Jeon, Y. C. Kim, S. Ryu, J. Seo, S. I. Seok, *Science* **2015**, 348, 1234.
- [26] T. Moehl, J. H. Im, Y. H. Lee, K. Domanski, F. Giordano, S. M. Zakeeruddin, M. I. Dar, L.-P. Heiniger, M. K. Nazeeruddin, N.-G. Park, *J. Phys. Chem. Lett.* **2014**, 5, 3931.
- [27] S. Donati, *Photodetectors: Devices, Circuits, and Applications*, Prentice-Hall PTR, Upper Saddle River, NJ, USA **2000**.
- [28] R. McIntyre, *Measurement* **1985**, 3, 146.
- [29] M. Liu, M. B. Johnston, H. J. Snaith, *Nature* **2013**, 501, 395.
- [30] H.-S. Kim, C.-R. Lee, J.-H. Im, K.-B. Lee, T. Moehl, A. Marchioro, S.-J. Moon, R. Humphry-Baker, J.-H. Yum, J. E. Moser, *Sci. Rep.* **2012**, 2, 591.
- [31] M. Helander, M. Greiner, Z. Wang, W. Tang, Z. Lu, *J. Vac. Sci. Technol. A* **2011**, 29, 011019.
- [32] D. A. Egger, E. Edri, D. Cahen, G. Hodes, *J. Phys. Chem. Lett.* **2015**, 6, 279.
- [33] R. H. Bube, C. T. Ho, *J. Appl. Phys.* **1966**, 37, 4132.
- [34] T. Y. Yang, G. Gregori, N. Pellet, M. Grätzel, J. Maier, *Angew. Chem. Int. Ed.* **2015**, 127, 8016.
- [35] E. T. Hoke, D. J. Slotcavage, E. R. Dohner, A. R. Bowring, H. I. Karunadasa, M. D. McGehee, *Chem. Sci.* **2015**, 6, 613.
- [36] E. Unger, E. Hoke, C. Bailie, W. Nguyen, A. Bowring, T. Heumüller, M. Christoforo, M. McGehee, *Energ. Environ. Sci.* **2014**, 7, 3690.
- [37] W. Tress, N. Marinova, T. Moehl, S. Zakeeruddin, M. K. Nazeeruddin, M. Grätzel, *Energ. Environ. Sci.* **2015**, 8, 995.
- [38] Y. Yuan, J. Chae, Y. Shao, Q. Wang, Z. Xiao, A. Centrone, J. Huang, *Adv. Energy Mater.* **2015**, 27, 1912.
- [39] Z. Xiao, Y. Yuan, Y. Shao, Q. Wang, Q. Dong, C. Bi, P. Sharma, A. Gruverman, J. Huang, *Nat. Mater.* **2015**, 14, 193.
- [40] J. M. Aspiroz, E. Mosconi, J. Bisquert, F. De Angelis, *Energ. Environ. Sci.* **2015**, 8, 2118.
- [41] Q. Dong, Y. Fang, Y. Shao, P. Mulligan, J. Qiu, L. Cao, J. Huang, *Science* **2015**, 347, 967.

Copyright WILEY-VCH Verlag GmbH & Co. KGaA, 69469 Weinheim, Germany, 2015.

ADVANCED FUNCTIONAL MATERIALS

Supporting Information

for *Adv. Funct. Mater.*, DOI: 10.1002/adfm.201503188

Working Principles of Perovskite Photodetectors: Analyzing
the Interplay Between Photoconductivity and Voltage-Driven
Energy-Level Alignment

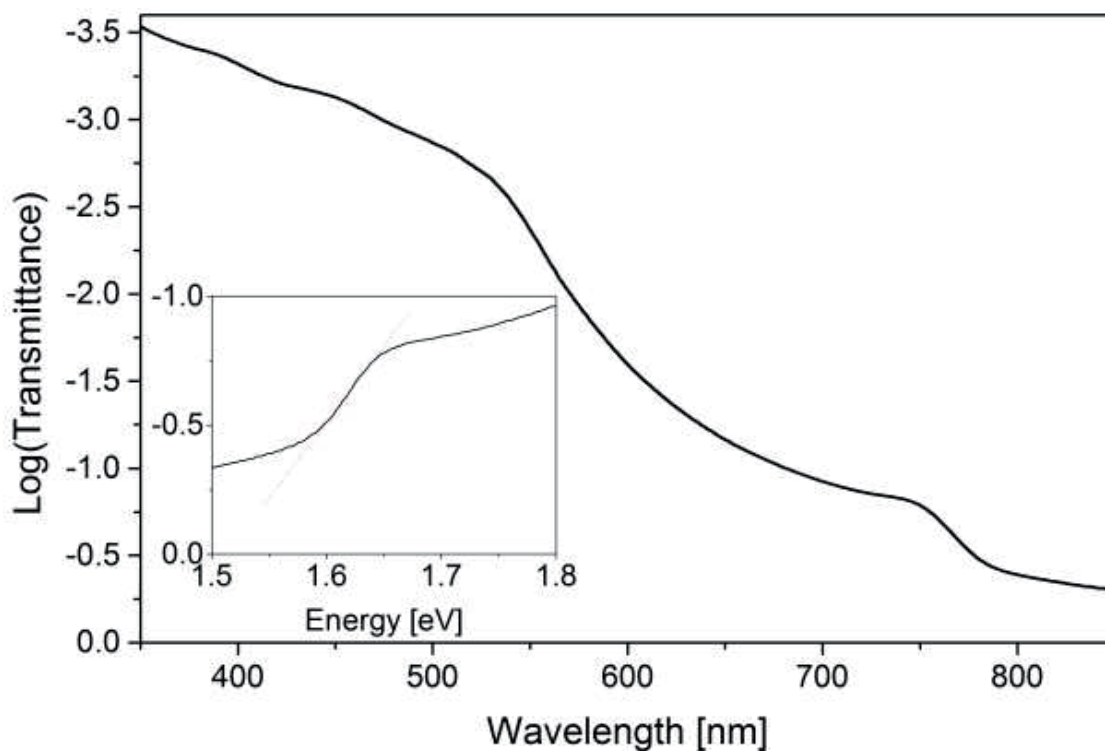
Konrad Domanski, Wolfgang Tress, Thomas Moehl,* Michael
Saliba, Mohammad Khaja Nazeeruddin, and Michael Grätzel*

Supporting Information

Working Principles of Perovskite Photodetectors: Analyzing the Interplay Between Photoconductivity and Voltage-Driven Energy Level Alignment

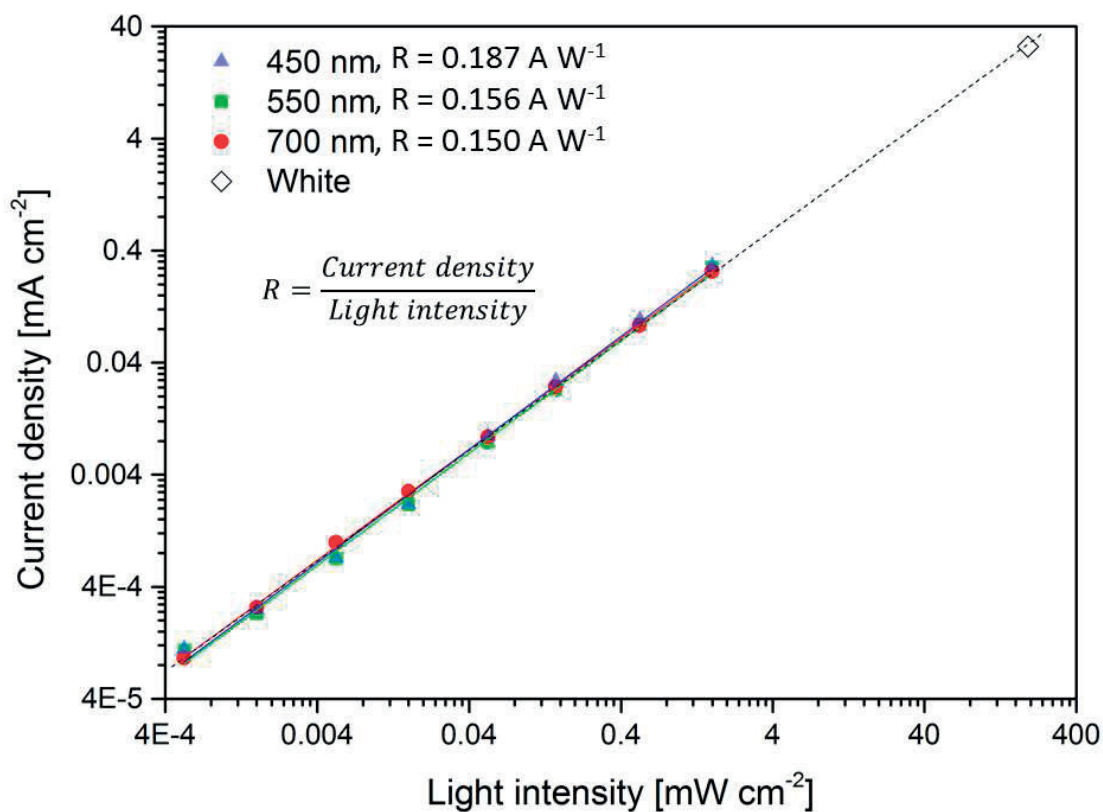
Konrad Domanski, Wolfgang Tress, Thomas Moehl*, Michael Saliba, Mohammad Khaja Nazeeruddin, Michael Grätzel*

$\text{CH}_3\text{NH}_3\text{PbI}_3$ is shown to possess a broadband absorption spectrum stretching the entire visible range with the absorption edge around 780 nm (1.59 eV; **Supporting Figure 1**). The contribution below the absorption edge is caused by strong scattering by the rough perovskite film.



Supporting Figure 1. Transmittance spectrum of the perovskite photodetector. The absorption edge of the detector is found around 780 nm (1.59 eV).

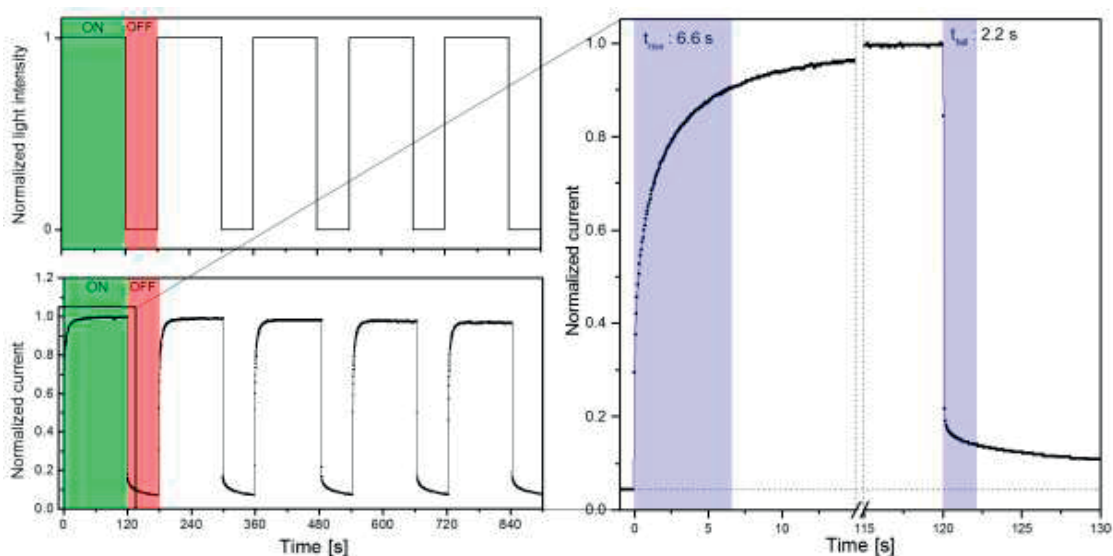
The response of the detector at short circuit conditions was found to be linear with respect to illumination intensity within the range of interest (**Supporting Figure 2**). The variation in photoresponse caused by using light of different wavelengths is reflected in respective responsivity values obtained under illumination with different wavelengths.



Supporting Figure 2. Photoresponse of the photodetector at short circuit conditions under different illumination wavelengths. The measurement at 100 mW cm⁻² was done under white LED light.

The on-off behavior of the photodetector was examined by shining 120 s - long pulses of 0.53 mW cm^{-2} , 550 nm monochromatic light (**Supporting Figure 3**). The time between the pulses was 60 s. The time that it takes the device to switch between 10% and 90% of the saturation current (with dark current subtracted) after light is switched-on is termed rise time, t_{rise} . Consequently, fall time, t_{fall} describes the transition from 90% to 10% of the response after the light is switched-off.

The photodetector is characterized by rise and fall times on the order of several seconds, which result in sub-Hz bandwidth. The pattern consists of a fast response, which is followed by a slow saturation or decay. The unusually slow response of the device is ascribed to slow processes within the perovskite, which is consistent with the idea of the movement of ionic species.

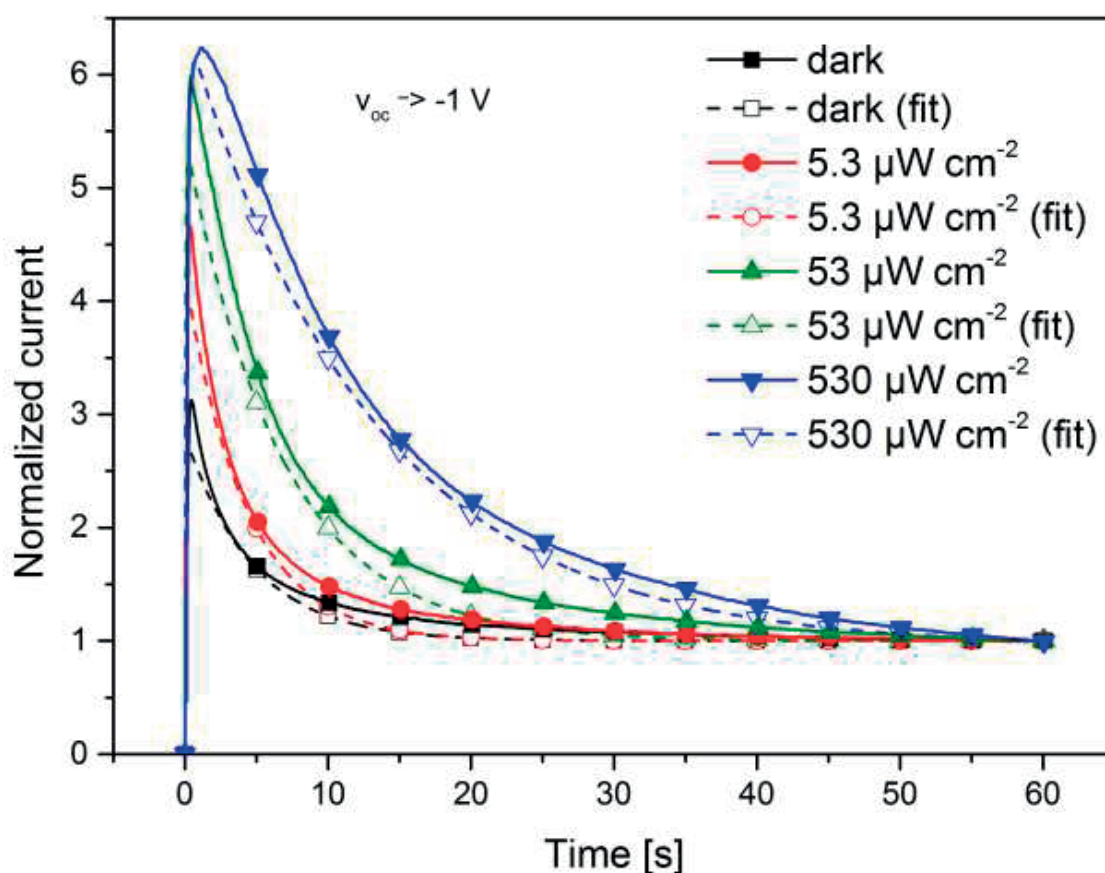


Supporting Figure 3. On-off dynamics of the perovskite photodetector. Illumination: 0.53 mW cm^{-2} , 550 nm monochromatic light.

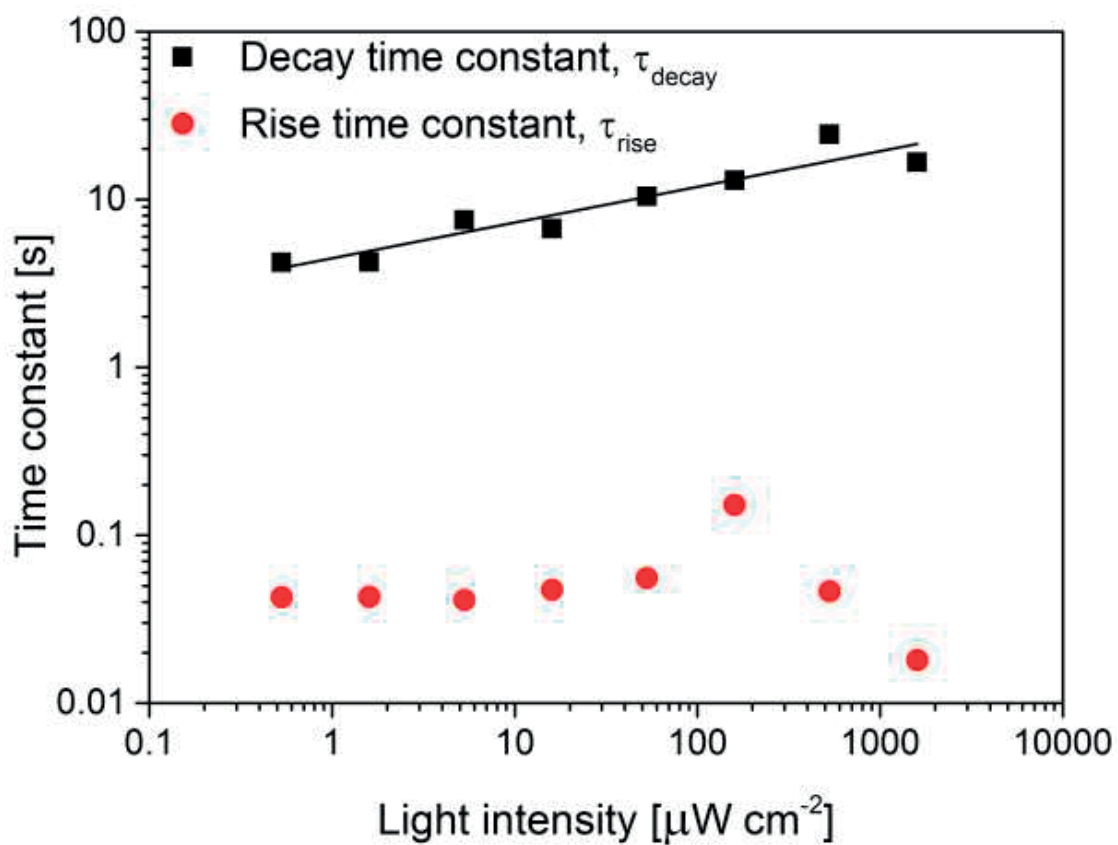
The current response of the device when it is subjected to a potential step change from V_{oc} to -1 V was modelled with two exponential terms:

$$J = -A_1 e^{-t/\tau_{rise}} + A_2 e^{-t/\tau_{decay}} + B \quad (S1)$$

The negative term is responsible for the initial rise in current, while the positive term is responsible for its subsequent decay. **Supporting Figure 4** shows how the model fits the experimental data and **Supporting Figure 5** shows how the current decay and rise time constants depend on the illumination intensity. One can see that at higher illumination intensities, the current decay becomes slower. The decay time constant is related to the illumination intensity through a power law, while no apparent influence of illumination intensity on the current rise time constant was found.

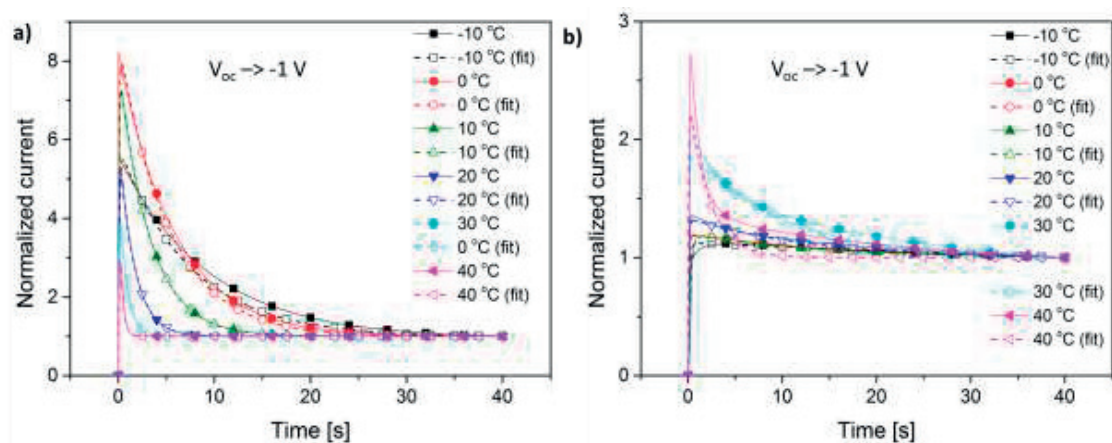


Supporting Figure 4. The response of the device when the potential is step-changed from V_{oc} to -1 V for different light intensities. Normalized to the steady-state photocurrent. Recorded data and fits to the **Supporting equation (1)** are presented.



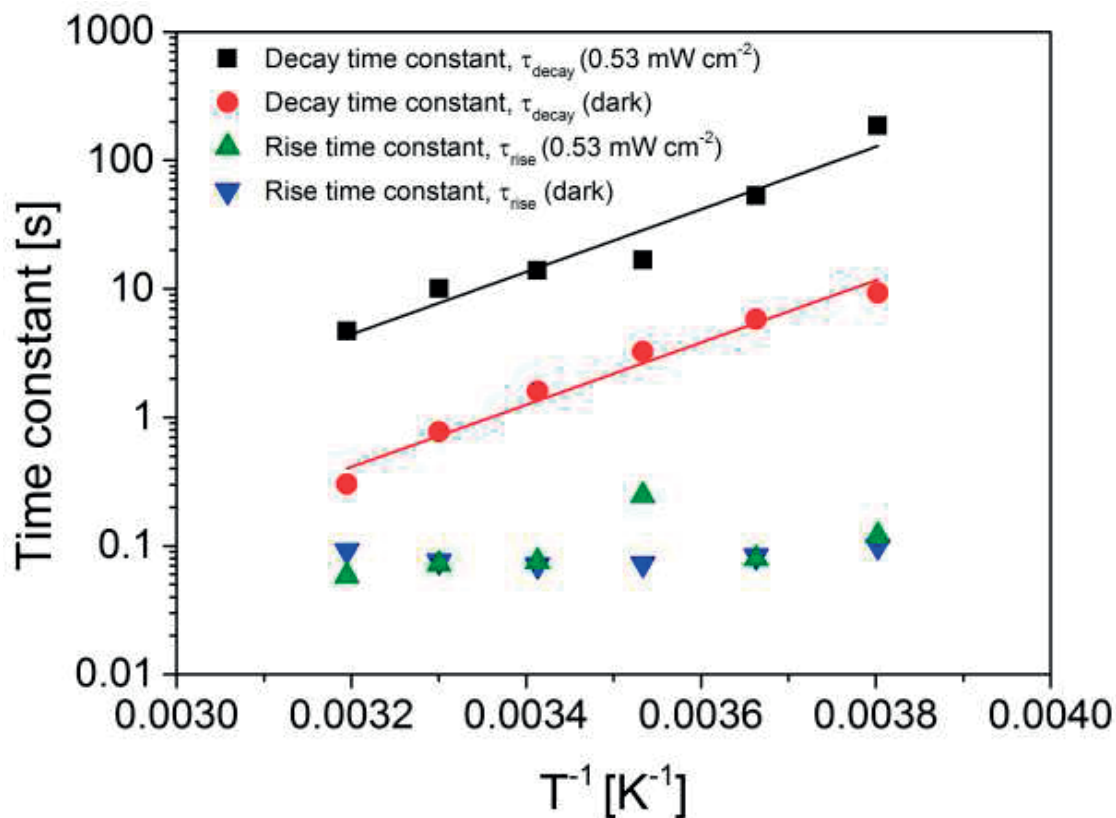
Supporting Figure 5. Time constants of current rise and decay (Supporting equation (1)) as a function of illumination intensity.

Supporting Figure 6 shows the transient current response of the device when it is subjected to a potential step change from V_{oc} to -1 V. The recorded data is fitted to the model presented in **Supporting equation (1)**.



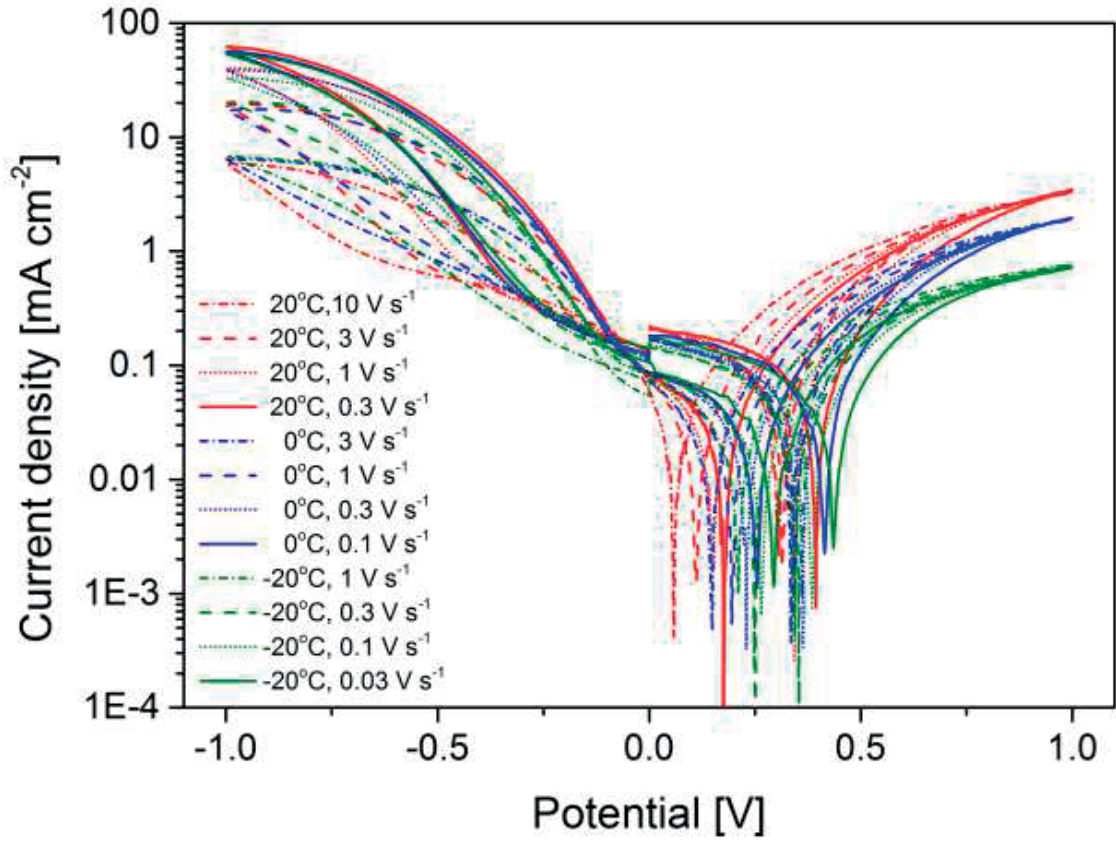
Supporting Figure 6. The transient response of the device when the potential is step-changed from V_{oc} to -1 V at different temperatures. a) in the dark, b) under 0.53 mW cm^{-2} illumination. Recorded data and fits to the **Supporting equation (1)** are presented.

Supporting Figure 7 shows how the current decay and rise time constants depend on temperature. One can see that at lower temperatures the current decay becomes slower. The decay time constant is related to the temperature through an Arrhenius-type relationship. No apparent influence of temperature on the current rise time constant was found.



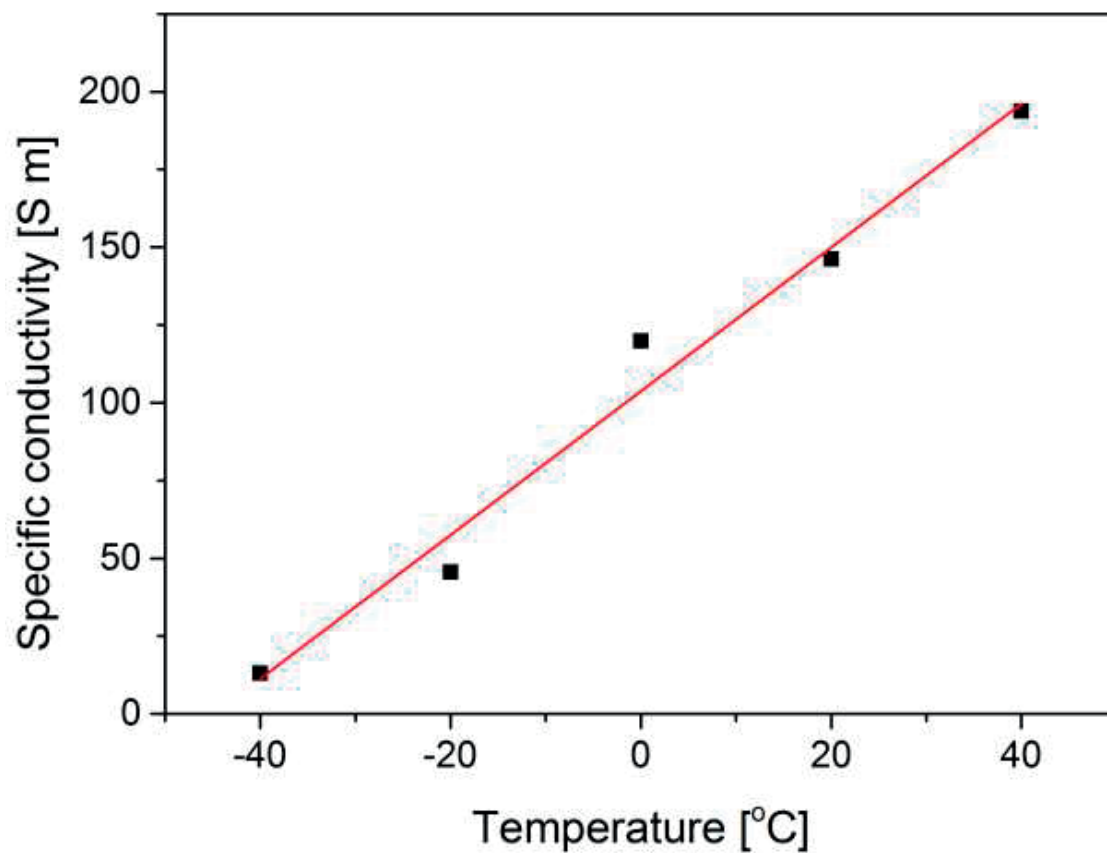
Supporting Figure 7. Time constants of current rise and decay (Supporting equation (1)) as a function of temperature.

Supporting Figure 8 present the simultaneous temperature and scan rate dependence on J-V characteristics of photodetector. With respect to the behavior under reverse bias conditions, it is found that decreasing the temperature by 20 K is equivalent to increasing the scan rate by approximately 3 times.



Supporting Figure 8. Scan rate- and temperature- dependent J-V characteristics of the detector under 1 mW cm^{-2} illumination. Scan rates are selected to visualize the similarity of J-V curves measured at an approx. 3 times lower rate when the temperature was decreased by 20 K.

Supporting Figure 9 presents the specific conductivity of Spiro-MeOTAD film sandwiched between FTO and gold electrodes.



Supporting Figure 9. Specific conductivity of Spiro-MeOTAD as a function of temperature. The thickness of the film was unknown.

Supporting Table 1 Experimental conditions and dark and photocurrent densities measured under -1 V potential for samples shown in **Figure 2**. Photocurrent measured under 100 mW cm⁻² white LED light. Scan rate: 200 mV s⁻¹.

Device type as in Figure 2	Blocking layer	Mesoporous scaffold	TiCl ₄ treatment	Spiro-MeOTAD	Perovskite deposition	Dark current density at -1 V potential [mA cm ⁻²]	Photocurrent density at -1 V potential [mA cm ⁻²]
1	porous TiO ₂	TiO ₂	no	yes	2step	0.105	98.95
1	porous TiO ₂	TiO ₂	no	yes	2step	0.116	74.74
2	porous TiO ₂	TiO ₂	yes	yes	2step	0.021	29.47
2	porous TiO ₂	TiO ₂	yes	yes	2step	0.032	24.21
2	porous TiO ₂	TiO ₂	yes	yes	2step	0.084	24.21
2	porous TiO ₂	TiO ₂	yes	yes	2step	0.011	24.21
2	porous TiO ₂	TiO ₂	yes	yes	2step	0.011	22.11
2	porous TiO ₂	TiO ₂	yes	yes	2step	0.011	18.95
3	no	TiO ₂	yes	yes	2step	0.147	161.05
3	no	TiO ₂	yes	yes	2step	0.116	145.26
3	no	TiO ₂	yes	yes	2step	0.137	136.84
3	no	TiO ₂	yes	yes	2step	0.179	130.53
3	no	TiO ₂	yes	yes	2step	0.084	109.47
3	no	TiO ₂	yes	yes	2step	0.126	109.47
3	no	TiO ₂	yes	yes	2step	0.053	96.84
3	no	TiO ₂	yes	yes	2step	0.053	94.74
4	no	TiO ₂	no	yes	2step	2.947	211.66
4	no	TiO ₂	no	yes	2step	0.811	202.17
4	no	TiO ₂	no	yes	2step	3.895	171.58
4	no	TiO ₂	no	yes	2step	8.000	169.47
4	no	TiO ₂	no	yes	2step	2.807	166.67
4	no	TiO ₂	no	yes	2step	2.211	160.00
4	no	TiO ₂	no	yes	2step	2.737	160.00
4	no	TiO ₂	no	yes	2step	3.509	157.89
4	no	TiO ₂	no	yes	2step	4.211	154.39
4	no	TiO ₂	no	yes	2step	2.456	152.63
4	no	TiO ₂	no	yes	2step	3.158	142.11
4	no	TiO ₂	no	yes	2step	4.035	140.35
4	no	TiO ₂	no	yes	2step	2.105	131.58
4	no	TiO ₂	no	yes	2step	2.281	129.82
4	no	TiO ₂	no	yes	2step	2.982	129.82
4	no	TiO ₂	no	yes	2step	1.246	121.05
4	no	TiO ₂	no	yes	2step	6.491	112.28
4	no	TiO ₂	no	yes	2step	5.789	108.77
4	no	TiO ₂	no	yes	2step	3.684	101.75
4	no	TiO ₂	no	yes	2step	0.491	96.49
4	no	TiO ₂	no	yes	2step	0.684	96.49
4	no	TiO ₂	no	yes	2step	0.579	94.74
4	no	TiO ₂	no	yes	2step	0.228	84.21
4	no	TiO ₂	no	yes	2step	0.316	84.21
4	no	TiO ₂	no	yes	2step	0.368	82.46
4	no	TiO ₂	no	yes	2step	0.807	80.70
4	no	TiO ₂	no	yes	2step	0.281	78.95
4	no	TiO ₂	no	yes	2step	0.281	77.19
4	no	TiO ₂	no	yes	2step	0.263	71.93
4	no	TiO ₂	no	yes	2step	0.912	64.91
5	no	TiO ₂	no	yes	1step	4.400	169.01
5	no	TiO ₂	no	yes	1step	3.080	164.96
5	no	TiO ₂	no	yes	1step	3.840	165.21
5	no	TiO ₂	no	yes	1step	5.544	119.47
5	no	TiO ₂	no	yes	1step	3.088	119.12
5	no	TiO ₂	no	yes	1step	3.702	114.56
5	no	TiO ₂	no	yes	1step	2.930	112.28
5	no	TiO ₂	no	yes	1step	2.509	107.72
5	no	TiO ₂	no	yes	1step	1.930	92.98
5	no	TiO ₂	no	yes	1step	2.105	91.23
5	no	TiO ₂	no	yes	1step	1.930	82.46
6	no	TiO ₂	no	no	1step	58.246	131.58
6	no	TiO ₂	no	no	1step	67.368	128.95
6	no	TiO ₂	no	no	1step	21.930	124.21
6	no	TiO ₂	no	no	1step	40.000	102.28
7	no	TiO ₂	no	no	2step	42.982	85.96
7	no	TiO ₂	no	no	2step	18.772	75.44
8	no	Al ₂ O ₃	no	yes	2step	1.684	131.12
8	no	Al ₂ O ₃	no	yes	2step	1.368	122.78
8	no	Al ₂ O ₃	no	yes	2step	1.895	122.02

8	no	Al ₂ O ₃	no	yes	2step	2.211	108.38
8	no	Al ₂ O ₃	no	yes	2step	1.895	106.11
8	no	Al ₂ O ₃	no	yes	2step	1.474	102.32
9	no	no	no	yes	2step	1.404	140.35
9	no	no	no	yes	2step	11.228	126.32
9	no	no	no	yes	2step	3.509	124.56
9	no	no	no	yes	2step	5.439	107.02
9	no	no	no	yes	2step	12.982	103.51
9	no	no	no	yes	2step	6.667	98.25
9	no	no	no	yes	2step	4.561	92.98
10	no	no	no	yes	1step	1.579	61.40
10	no	no	no	yes	1step	1.754	56.14
11	no	no	no	yes	evaporated	1.316	122.81
11	no	no	no	yes	evaporated	0.930	115.79

Chapter 9 Towards Consensus on How to Age Perovskite Solar Cells

THE CONTEXT

Having aged numerous devices, I realized that stability of perovskite solar cells can be rather sensitive to the way the experiment was conducted. Unfortunately, the way perovskite solar cells are measured by different groups is by no means standardized and the results are hardly comparable at the time this thesis is being submitted. I decided to systematically investigate the effect of different factors such as illumination, temperature, atmosphere and electric load on stability of state-of-the-art perovskite solar cells. Having identified the parameters that have to be precisely controlled, I comment on my perceived relevance of the ways PSCs are aged now. I also demonstrate how I implement stability measurements in our laboratory, as the first attempt to initiate discussion on how perovskite solar cells should be aged.¹³²

This chapter is based on a peer-reviewed, paper accepted for publication (November 2017) in *Nature Energy* entitled:

Systematic Investigation of the Impact of Operation Conditions on the Degradation Behaviour of Perovskite Solar Cells

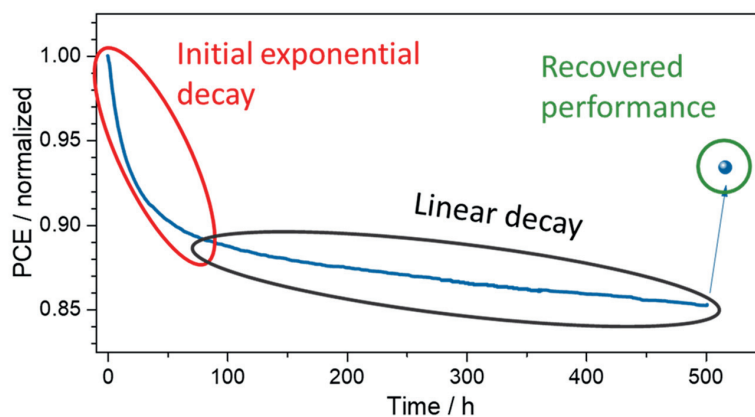
authored by:

Konrad Domanski, Essa Alharbi, Anders Hagfeldt, Michael Grätzel and Wolfgang Tress.

The version presented here is the accepted manuscript before the editorial changes.

My contribution:

I designed and led the study, performed all measurements presented in this work, analyzed the data, prepared the figures and wrote the manuscript. I also designed and built the stability setup, which is the centerpiece of this work. I consider this work to be a summary of my entire research into stability of perovskite solar cells and a synopsis of my experience gained alongside.





Systematic Investigation of the Impact of Operation Conditions on the Degradation Behaviour of Perovskite Solar Cells

Konrad Domanski*¹, Essa A. Alharbi¹, Anders Hagfeldt², Michael Grätzel¹, Wolfgang Tress*^{1,2}

¹Laboratory for Photonics and Interfaces, Institute of Chemical Sciences and Engineering, École Polytechnique Fédérale de Lausanne, CH-1015-Lausanne, Switzerland

²Laboratory of Photomolecular Science, Institute of Chemical Sciences and Engineering, École Polytechnique Fédérale de Lausanne, CH-1015-Lausanne, Switzerland

*Correspondance to: kn.domanski@gmail.com, wolfgang.tress@epfl.ch

Abstract

Perovskite solar cells have achieved power-conversion efficiency values approaching those of established photovoltaic technologies, making the reliable assessment of their operational stability the next essential step towards commercialization. Whereas studies increasingly often involve a form of stability characterization, they are conducted in non-standardized ways, which yields the data effectively incomparable. Furthermore, stability assessment of a novel material system with its own peculiarities might require an adjustment of common standards. Here, we investigate the effects of different environmental factors and electrical load on the ageing behaviour of perovskite solar cells. Based on this, we comment on our perceived relevance of different ways these are currently aged. We also demonstrate, how the results of the experiments can be distorted and how to avoid the common pitfalls. We hope this work will initiate the discussion on how to age perovskite solar cell and facilitate the development of consensus stability measurement protocols.

Introduction

The main parameters when talking about commercialization of an emerging photovoltaic (PV) technology are the performance measured in terms of a solar-to-electric power conversion efficiency (PCE), long-term stability (lifetime) and the production costs. These parameters paired with the operation conditions (e.g. location of installation) of the solar module define the costs per kWh of electricity provided. The recently emerged perovskite solar cells (PSCs) with efficiencies larger than 22%¹ show potential for low-cost production. For a novel material system in research maturing to a technology, scalability under technological, economical and regulatory restrictions needs to be demonstrated. This is currently under investigation for PSCs with promising results.²⁻⁴ On the other hand, a certain lifetime is required for a final product. Prerequisite for this is the demonstration of a certain stability of the components employed. As the employed perovskite materials are considered to be rather instable,⁵ research has been addressing the questions of stability and a shift from focussing on efficiency values towards stability can be observed. Performed stability tests range from leaving unencapsulated devices in the dark under uncontrolled ambient conditions and periodically measuring their PCE,⁶ to studies under controlled atmosphere, illumination, temperature and load.^{7,8} As these ambient conditions influence the ageing behaviour considerably, comparability of results is hardly given. Therefore, the term stability should be used with caution and only with a clear specification of the conditions and the criteria it refers to (e.g. thermal, ambient, operational stability). Otherwise, the credibility into the complete research area suffers – an issue that has been experienced by the PSC community regarding measuring power-conversion efficiencies,⁹ where the standard way of performing a current-voltage (J-V) sweep turned out to be unreliable due to a strong hysteresis in the J-V curve^{10,11} leading to erroneous efficiency reports.

For commercial PV panels, rigorous industrial standards exist to describe pass-fail qualification tests (IEC 61215), as outdoor testing under real operation conditions is not feasible due to the long times required (>20 years). All these protocols are designed for the product “PV panel”, which is exposed to accelerated stress tests targeting mainly design and material errors, which would lead to field failures (Supplementary **Table 1**). Thus, such tests (although required for any type of solar panel to be installed outdoors), are not the best choice to assess the stability of a novel material system and identify wear-out and failure mechanisms. On the other hand, to guarantee comparability and relevance of reported stability results, the perovskite research community should follow common protocols or even reach a consensus on how to report stability data similarly to the organic photovoltaics (OPV) community releasing specific testing protocols (ISOS, Supplementary **Table 2**).¹²

This study is an attempt to initiate the discussion on how to age PSCs, which should eventually lead to development and adoption of consensus stability measurement protocols for PSCs. It is not the purpose of this work to review degradation mechanisms but to demonstrate, which environmental conditions (atmosphere, humidity, temperature) and combinations thereof are crucial for the degradation of PSCs. Here, we distinguish extrinsic and intrinsic parameters. The former are harmful environmental factors (e.g. humidity or UV light) that can be blocked by use of encapsulation. The latter are crucial as they might exclude certain materials from being employed in a long-term stable device. Therefore, it is justified or sometimes even required to perform stability measurements under inert atmosphere to avoid a superposition with extrinsic factors. On the other hand, the extrinsic factors will determine the requirements (and costs) of the encapsulant e.g. regarding the moisture vapour transmission rate. Further important parameters to assess the operational stability are

illumination and load on the solar cell. Therefore, we investigate the differences in ageing behaviour with respect to these conditions and conclude that ageing under 1 sun illumination, preferably at maximum power point (MPP) and under both room and elevated temperatures is the most reliable way to show operational stability. We furthermore address perovskite-specific phenomena such as hysteresis and reversible losses by temperature and light-intensity cycling experiments. Our results, e.g. regarding the relevance of efficiency measurements by MPP tracking and recovery periods in the dark, give hints on what to consider when designing aging studies.

Effects of illumination and atmosphere on device degradation

We conducted the study using state-of-the-art devices (ref. ¹³) with FTO/compact TiO₂/mesoporous TiO₂/perovskite/Spiro-MeOTAD/Au architecture and Cs-containing “triple cation” perovskite; reaching efficiencies above 20% (**Supplementary note 1**). Only devices with initial PCE >17% were used for ageing experiments, and over 250 ageing curves were collected and analysed. All devices were used as fabricated and without any form of encapsulation.

Illumination is a critical intrinsic factor when considering ageing of PSCs. **Figure 1** shows the effect of UV light on stability. Devices aged at either unfiltered Xe lamp, rich in UV light or under a white, UV-free LED lamp (**Supplementary Figure 1**) seem to both display a two-regime degradation behaviour with the initial exponential loss followed by a linear one. Comparing these linear degradation slopes, it appears that the devices aged under Xe illumination on average suffer accelerated degradation. However, the difference does not appear to be statistically significant. The devices based on TiO₂ scaffolds have been speculated to be especially vulnerable to UV light¹⁴ and improved stability for alternative n-type materials has been reported.¹⁵ Having investigated “the extreme” case, we find it suitable to make a slightly generalizing observation that UV-light appears to be not catastrophic for degradation of PSCs under inert conditions. This is consistent with a UV degradation study performed under inert conditions, which showed slow degradation under UV light.¹⁶ However, there exist several reports of severe UV degradation when O₂ is present in the system¹⁷ - an observation that holds for illumination in general as discussed below (**Figure 2**).

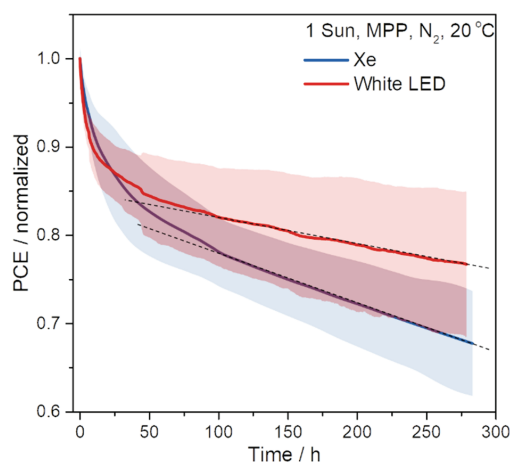


Figure 1 The effect of UV light on the stability of PSCs. Comparison of ageing under unfiltered Xe and UV-free white LED lamp. The values are normalized to the initial ones. 8 and 13 devices were measured under each condition respectively. The solid lines represent averaged behaviour of the devices, while the shaded area represents standard deviation. The broken lines are a guide to the eye.

In practice, UV protection layers can be employed for future perovskite solar panels without compromising their performance. This makes UV light an extrinsic degradation factor, which can be seen as analogous to O_2 and H_2O .¹⁸ Our results indicate that it may not always be crucial to use a solar simulator for ageing experiments and a white LED lamp is a practical solution. In order to avoid convoluting different degradation factors, we performed the remaining of the experiments described here under UV-free, white LED illumination.

Discussion has ensued on the effect of atmosphere in conjunction with illumination.^{19–21} In **Figure 2** we investigated the effect of O_2 , H_2O and light (again on unencapsulated devices). The devices experience relatively slow degradation when aged in inert, N_2 , atmosphere (**Figure 2 a**). However, the degradation is much accelerated if O_2 is present in the environment in atmospheric concentrations, consistent with previous reports.^{20,21} Further addition of small concentration of H_2O (at 5% relative humidity; RH) resulted in a very similar result. Conversely, when RH was increased to 100% the devices experienced a dramatically rapid degradation. This correlates with reported humidity induced bleaching of the perovskite.²²

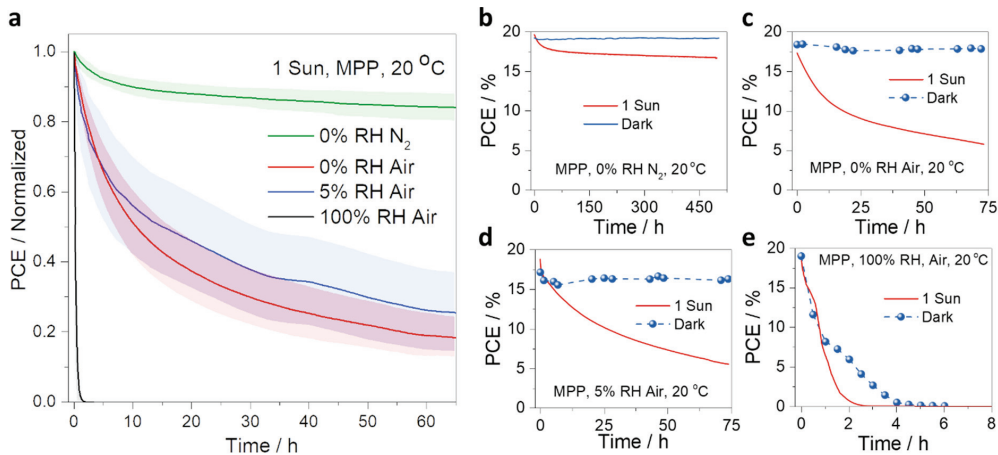


Figure 2 The effect of atmosphere and light on ageing. **a)** The effect of O_2 and H_2O on stability of illuminated PSCs. 8 devices were aged under 5% and 100% RH air, 6 under 0% RH air and 13 under N_2 . The values are normalized to the initial ones. The lines represent averaged behaviour of devices, while the shaded area represents standard deviation. Standard deviation for 100% RH curve is too small to be visible in the graph given the short degradation timescale. **b-e)** the effect of illumination under different atmospheres. The devices exposed to light continuously, were aged at MPP. The ones aged in the dark were measured only periodically and at each instance exposed to light for 1 min at MPP. Devices in **b-e)** were all fabricated in one batch. The illumination source was white LEDs. The flow rate of each gas was the same (around 0.5 l min^{-1}).

Figure 2 b-d) shows an additional effect of illumination on degradation. Storing the devices in dry conditions does not result in degradation regardless of presence of O_2 or a small quantity of H_2O . This points to the conclusion that O_2 is only harmful under illumination and a photo-oxidation is active in PSCs, where a mechanism including superoxide generation has been proposed.¹⁹ However, high levels of humidity in the environment very quickly degraded the devices regardless the presence of illumination and the perovskite turned to a yellow-white material in both cases (possibly PbI_2 , but hydrates have been observed as well²³). Whereas this degradation happens within several hours in our case, hydrophobic polymer layers^{18,24} and changes in perovskite synthesis route²⁵ can lead to a considerably higher resistivity against humidity.

In the past, some studies attempted to assess stability by leaving the devices in the dark and periodically measuring them.⁶ As we show here, the stability in the dark does not translate to operational stability, even under inert conditions (**Figure 2 b**) as also reported e.g. in ref. ²⁶ for encapsulated devices. We would like to stress that the assessment of operational stability of PSCs should be done under illumination to mimic the natural environment of solar cells, in particular as thermodynamic photoinstabilities of mixed halide perovskite compositions occurring even under inert atmosphere are under discussion.²⁷

Effects of temperature on device degradation

Temperature is known to have a critical effect on the stability of PSCs.²⁸ **Figure 3** shows the influence of temperature on ageing of PSCs. At 20 °C, the degradation is characterised by an initial exponential decay followed by a slow linear loss regime. The situation is similar for the device aged at -10 °C, but the dynamics of the initial component are slower and the subsequent linear loss - limited. Contrary to this, the degradation at 65 °C is very rapid and likely due to the well-known Au-diffusion problem²⁹, which can be circumvented by using alternative contact materials (e.g. PTTA as HTM⁷, carbon-based materials^{30,31} and metal oxide electrodes^{32,33}) showing that the perovskite itself embedded into a device can be stable at temperatures >100 °C.³⁴ **Supplementary Figure 2** shows a comparison of devices with Spiro-MeOTAD and PTAA aged at 65 °C. The PTAA-based device ages at a much lower degradation rate (although still faster than a Spiro-MeOTAD-based device at 20 °C). Since degradation is often accelerated at high temperatures, we measure operational stability at both 20 °C (to disentangle high-temperature effects) and, most importantly, at 65 °C (to demonstrate operational stability under realistic conditions).

The device in **Figure 3** cycled 80 times between -10 and 65 °C exhibits lower degradation rate than the device held continuously at 65 °C leading to the conclusion that cycling itself does not result in “temperature fatigue”. A closer inspection of the ageing curve (**Figure 3 b**) reveals that sustained degradation is only experienced when the device is held at 65 °C (dashed horizontal lines), while a transient behaviour is observed each time, the device is cooled to -10 °C. This transient at low temperatures is most likely due to a reversible slow response of PSC related to a temperature activated migration of ions^{35,36} upon changing the operation point (MPP voltage).

While the devices do not degrade at lower temperatures in the dark (**Supplementary Figure 3**), those exposed to 65 °C degraded at similar rate regardless of illumination. This isolates elevated temperature as a key degradation factor that is, as discussed, more due to the device stack than the perovskite itself. Such dark thermal stability test is a very useful tool to screen a large number of devices and to select most promising candidates for operational stability measurements. This can involve for example keeping devices inside a glovebox on a hotplate and measuring them periodically.

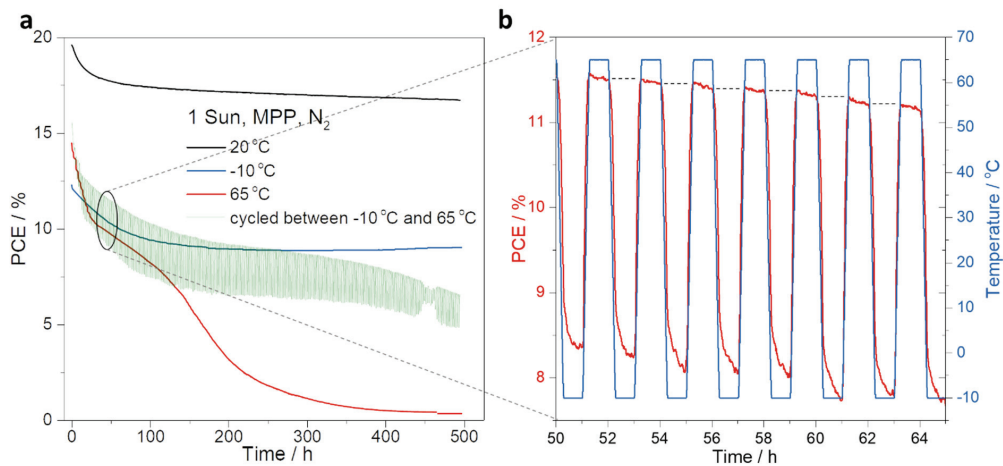


Figure 3 The effect of temperature on ageing. **a)** The effect of temperature and temperature cycling (80 cycles shown) on stability of illuminated PSCs. **b)** A close-up of the trace of the temperature-cycled device. The dashed line inside the figure is a guide to the eye. The temperature ramp for cycling was 5 K min^{-1} . The illumination source was white LEDs. Note the initial PCE of devices measured at either freezing or elevated temperatures is considerably lower than that measured at room temperature; all devices had initial performance $>18\%$.

Effects of electric load on device degradation

In **Figure 4**, we aged a number of devices at open circuit, short circuit and maximum power point (MPP) and we report PCE derived from periodic J-V scans (whereas the data shown so far was the MPP tracked PCE). We found that MPP tracking resulted in the least degradation of the devices, which is consistent with reports in the literature.³⁷ Ageing the devices at short circuit resulted in faster degradation (though after leaving the devices in the dark for 24 h, the “dark recovered” value was similar to that for MPP-aged devices). Degradation was the most severe at open circuit with limited subsequent recovery and it is a combined effect of FF and open circuit voltage (V_{oc}) loss. Possibly, photogenerated charge carriers that are not extracted are a source of degradation by leading to high concentrations of radicals in the PSCs, similar to what is observed for degradation under O_2 .^{20,21} Ageing at MPP simulates the native conditions of working solar cells and hence it is the most appropriate way to age PSCs; ageing at open or short circuit appear to provide a conservative estimation.

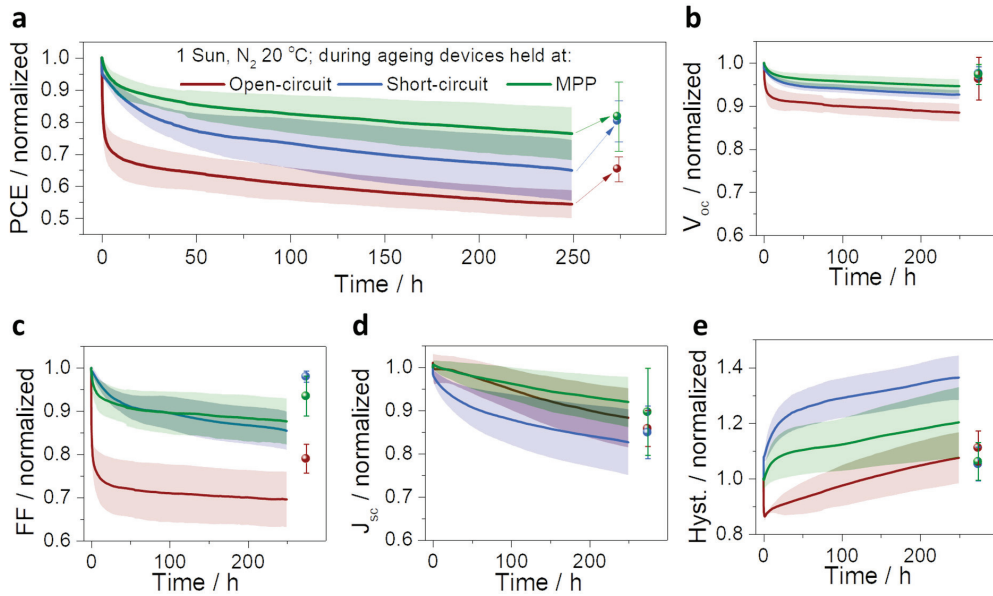


Figure 4 The effect of load on the device on its stability. The devices were held at MPP, open circuit or short circuit during ageing period and their J-V curves were measured periodically. 13, 8 and 5 identically prepared devices were aged at each condition respectively. Evolution of **a)** PCE, **b)** V_{oc} , **c)** J_{sc} , **d)** fill factor (FF) measured in the backward J-V scan (From V_{oc} to J_{sc}), as well as **e)** hysteresis (defined as ratio of efficiencies measured from backward and forward J-V scans). The values are normalized to the initial ones. The lines represent averaged behaviour of devices, while the shaded area represents standard deviation. After 250 h of ageing under illumination, the devices were allowed to recover in the dark for 24 h before being re-measured. Illumination source was white LEDs.

Design of stability measurement experiments

Valuable additional information can be obtained when periodically interrupting MPP tracking with a J-V measurement (including hysteresis; see **Figure 4**). For example, a loss of short circuit current (J_{sc}) may be an indication of reduced charge carrier extraction efficiency¹¹ or of bleaching³⁸, while loss of V_{oc} may signal increased charge carrier recombination.

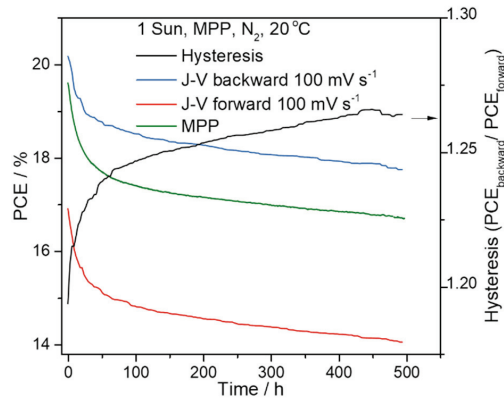


Figure 5 The dilemma of how to measure device PCE during ageing. Comparison of PCE extracted from backward and forward J-V scans and the MPP. Hysteresis is often found to increase during ageing increasing the difference between PCEs extracted in different ways. MPP performance is ultimately the "real" value.

Having employed this combined MPP and periodic J-V scans procedure, one obtains three different values of PCE: from MPP tracking as well as from backward (from V_{oc} to J_{sc}) and/or forward (J_{sc} to V_{oc}) periodic J-V scans. However, these three values are not equal due to hysteresis, which can additionally change as the device ages. The data in **Figure 5** shows an example, where the hysteresis monotonically increases during ageing. When conducting ageing experiments, one should ideally report PCE resulting from MPP tracking whenever possible. The MPP-tracked PCE is not necessarily an average of the two obtained from J-V scans (there is an additional J-V scan speed effect¹¹).

Reversible losses and dark recovery

Solar cells naturally undergo light cycling over day-night periods. Motivated by reports on partially reversible initial degradation^{37,39–41} we investigated the effect of light cycling (23 cycles performed) on stability in **Figure 6**. We found no detrimental effect due to light cycling – the behaviour is highly reproducible following each cycle.

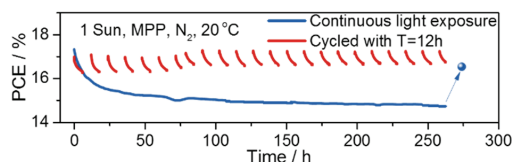


Figure 6 The effect of light cycling on ageing. One device was exposed to light continuously, while the other one was cycled with 6 h light, 6 h dark. Integrating over 135 h, (the cumulative time the cycled device was exposed to light) the cycled device produced 22.1 kWh m^{-2} , while the continuously-aged device yielded 20.6 kWh m^{-2} (despite being more efficient initially). Effectively, the cycled device worked on average at 96% of its initial efficiency, while the other one – at 88% (over the same period of 135 h). Illumination source was white LEDs.

Although degradation behaviour of PSCs depends on many factors, often devices behave in a qualitatively similar manner (*cf.* ref. ^{8,41,42} where different device architectures are studied). **Figure 7** shows a typical ageing trace as observed by us of a device aged under non-aggressive conditions (20 °C, N_2 , 1 Sun). Often devices show initially a fast, exponential decay phase (it is sometimes preceded by a short period of initial performance improvement). As shown in **Figure 6**, these losses are generally recoverable if a device is left in dark for an extended amount of time^{37,41} (similarly-looking “burn-in” exponential degradation phase has been observed in organic solar cells but the degradation is usually irreversible^{43,44}). However, this behaviour may not be universal for all PSC architectures and reports exist where this initial degradation component is not explicitly shown.^{33,45}

The exponential degradation regime is often followed by a more linear one, where performance decreases steadily. With a linear decay, it is possible to fit the slope and estimate device lifetime: e.g. T_{80} parameter. One has to remember to make any extrapolations disregarding the (potentially reversible) initial exponential losses. In the example in **Figure 7**, the linear slope is around $-0.0071\% \text{ h}^{-1}$. Hence it would take the device around 2800 h of operation under 1 Sun to linearly lose 20% of its PCE – the definition of T_{80} parameter.

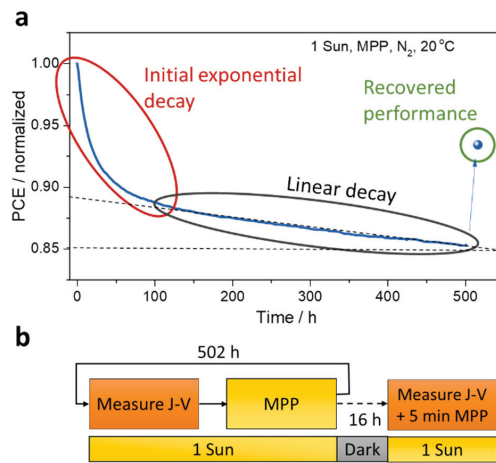


Figure 7 A typical result of keeping a device at MPP and N₂. **a)** The device shows an initial exponential loss region, followed by a slower linear region. A slope can be fitted to the linear region (broken line) to estimate device lifetime, T_{90} . The device can recover part of its initial performance after being kept in the dark – in this case for 16 hours. The device was aged under white LED lamp. **b)** a schematic of the ageing procedure combining MPP tracking and periodic J-V scans. One has to consider the balance between the time spent during J-V scans and that at MPP, as degradation may be different during J-V sweeps and at MPP. For this study, we performed 100 mV s^{-1} scans every 15 minutes, which results in devices spending 98% of the time at MPP. However, there is no “right” balance. More frequent J-V scans may sometimes be more suitable to resolve very fast degradation (e.g. rapid bleaching). On the other hand, frequent J-V scans are not required when the devices appear stable.

Researchers should decide the duration of the ageing experiments keeping in mind that initial, potentially reversible losses can occur in the initial phase of the measurements. The exact time should be decided based on whether a reasonable extrapolation can be made from the data already collected. We encourage the researchers to conduct the experiments until a clear linear regime has been reached, or alternatively, until the device has stopped working (e.g. **Figure 2 e**). We also would like to note that the dynamics of the exponential degradation regime, that we often observe, are sensitive to temperature (cf. **Figure 3**).

Because part of the losses incurred by aged PSCs are potentially reversible when the devices are left in the dark, we would like to invite the researchers to check and report on this behaviour. After completion of the ageing experiment under illumination, we usually allow our devices to recover in the dark for at least 10 h before re-measuring them again.

Towards consensus on how to age perovskite solar cells

Finally, we believe it is useful to gather statistics when investigating stability of PSCs. One can for example average many (normalized, if required) stability curves and plot the result along with standard deviation (cf. **Figure 1**, **2 a** and **Figure 4**). Additionally, one can compare the statistics of the performance before and after ageing following a recovery period.

Having identified the parameters that are mainly responsible for the degradation, one can exploit those in accelerated ageing studies. In our case, this could be the illumination intensity (cf. **Figure 2 b-d**), temperature (**Figure 3**) or humidity (**Figure 2 a**). For a quantitative comparison and predictive power of accelerated ageing, knowledge of a model for the underlying degradation mechanism is essential. For a temperature-activated process, it is common to assume an Arrhenius type behaviour and extract an acceleration factor.¹² If the absorbed photon flux and/or photogenerated charge

carriers trigger the degradation mechanisms, measurements under elevated light intensities can be performed to accelerate degradation. For PSCs, measurements under intensities up to 70 suns have been performed showing slow degradation at low efficiencies.⁴⁶ As ageing studies for the most stable PSCs have already been conducted for 500 to >1000 h,^{7,26,45,47,48} accelerated ageing studies are the next step towards an assessment of product-relevant operational stability.

To summarize, we discussed how illumination, temperature, atmosphere and load on the device can affect its stability. We drew a distinction between operational stability and thermal stability measured in the dark. We argued that the later can be a practical way to pre-screen a large number of devices prior to operational stability testing and in **Supplementary note 2**, we described the setup we built for stability measurements. In **Table 1** we summarize the conditions we use for ageing PSCs to best mimic the natural operational conditions of solar cells. Based on the results in this work and literature reports, we found that some of these can be potentially relaxed without compromising the experiments. This includes the light source, where white LEDs are a practical alternative to an AM 1.5G solar simulator. Furthermore, by substituting MPP tracking by easier-to-implement open or short-circuit load on the device, one would potentially arrive at a conservative stability estimate. Having said that, we invite the researchers to verify our observations for a variety of PSC architectures.

In contrast to this, we believe that it is important to measure stability of PSCs not only at room temperature but also at elevated temperatures (we used 65 °C). Similarly, for comparability of studies on stability of PSCs, it is important that the devices are protected from O₂ and H₂O i.e. inert environment is provided. This can be achieved either by controlling the atmosphere or by encapsulating the devices. However, by only encapsulating the devices and conducting the experiment under ambient conditions, one risks investigating the quality of encapsulation rather than that of device. On the other hand, continuous flushing with gas keeps the partial pressure of volatile decomposition products such as hydrogen iodide and methylamine⁴⁹ low and might promote a decomposition of (particularly CH₃NH₃PbI₃) perovskite, especially at elevated temperatures (this can be avoided for all-inorganic perovskites⁵⁰). Therefore, perhaps the safest way to investigate the stability of PSCs is to age encapsulated devices under inert atmosphere to minimize the undesired and uncontrolled effects of trace gases. A dedicated study would be needed to answer this question.

Table 1 Ageing conditions imitating natural environment of solar cells.

Illumination*	1 Sun solar simulator (possible to relax to white LEDs)
Load*	MPP (possible to relax to open/short-circuit)
Temperature	Room and elevated temperatures
Atmosphere	Inert environment

*based on results in this work and the literature, we think these conditions can be possibly relaxed for ageing PSCs without compromising the conclusions of the experiments

In an attempt to bring the researchers to a consensus on how to age PSCs, we demonstrate that the most reliable way to investigate PSC stability is under 1 sun illumination, preferably at MPP and both under room and elevated temperatures. Steps should be taken towards controlling the atmospheric environment of the experiment. We hope that our work will inspire the research community to repeat

the experiments presented here for a wide range of device architectures and perovskite compositions and that it will be helpful for eventually developing consensus protocols for ageing PSCs.

Methods

Device fabrication

Fluorine-doped tin oxide (FTO)-glass substrates (TCO glass, NSG 10, Nippon sheet glass, Japan) were etched from the edges by using Zn powder and 4 M HCl and then, cleaned by ultrasonication in Hellmanex (2%, deionized water), rinsed thoroughly with de-ionized water and ethanol, and then treated in oxygen plasma for 15 min. A 30 nm blocking layer (TiO_2) was deposited on the cleaned FTO by spray pyrolysis at 450 °C using a titanium diisopropoxide bis(acetylacetonate) solution (75% in 2-propanol, Sigma-Aldrich) diluted in anhydrous ethanol (1:9 volume ratio) as precursor and oxygen as a carrier gas. A 150-200 nm mesoporous TiO_2 layer was deposited by spin coating a diluted paste (1:6 wt. ratio) (Dyesol 30NRD: ethanol) (4000 rpm, acceleration 2000 rpm for 20 s) onto the substrate containing TiO_2 compact layer, and then sintered at 450 °C for 30 min in dry air.

Li doping of mesoporous TiO_2 , 150 μL of LiTFSI solution in acetonitrile (10mg/mL, freshly prepared in argon atmosphere) was spin coated (3000 rpm, acceleration 2000 rpm for 20 s) after a loading time of 10 s. Thereafter, Li treated substrates were sintered at 450 °C for 30 min. After cooling down to 150 °C the substrates were immediately transferred in a dry glove box (Humidity \leq 2%) for depositing the perovskite films.

The perovskite films were deposited using a single-step deposition method from the precursor solution containing FAI (1M), PbI_2 (1.1 M), MABr (0.2 M) and PbBr_2 (0.2 M) in anhydrous dimethylformamide/ dimethylsulphoxide (4:1 (volume ratio)). Thereafter, 5% of CsI (Acros 99.9%) (1.5 M DMSO) were added to achieve the desired composition: $\text{Cs}_5(\text{FA}_{83}\text{MA}_{17})_{95}\text{Pb}(\text{I}_{83}\text{Br}_{17})_3$.

The perovskite solution was spin coated in a two steps program at 1000 and 6000 rpm for 10 and 30 s respectively. During the second step, 150 μL of chlorobenzene was poured on the spinning substrate 10 s prior to the end of the program. Films with Cs-containing perovskite turned dark immediately after spin coating. The substrates were then annealed (at 100 °C) for 1 h in controlled atmospheric conditions with humidity <2%.

After the perovskite annealing, the substrates were cooled down for few minutes and a Spiro-MeOTAD (Merck) solution (70 mM in chlorobenzene) was spin coated at 4000 rpm for 20 s. Spiro-MeOTAD was doped with bis(trifluoromethylsulfonyl)imide lithium salt (Li-TFSI, Sigma-Aldrich), tris(2-(1H-pyrazol-1-yl)-4-tert-butylpyridine)- cobalt(III) tris(bis(trifluoromethylsulfonyl)imide) (FK209, Dynamo) and 4-tert-Butylpyridine (TBP, Sigma-Aldrich). The molar ratio of additives Spiro-MeOTAD was: 0.5, 0.05 and 3.3 for Li-TFSI, FK209 and TBP respectively.

Finally, 70-80 nm of Au top electrode was thermally evaporated under high vacuum. The active area of the device, as defined by the overlap of Au and FTO electrodes was 0.26 cm^2 .

The devices were used as-fabricated and without any form of encapsulation.

Device characterization

A Zeiss Merlin HR-SEM was used to characterize the morphology of as-fabricated devices. X-ray powder diffractions were recorded with an X'Pert MPD PRO (Panalytical) equipped with a ceramic

tube (Cu anode, $\lambda = 1.54060 \text{ \AA}$), a secondary graphite (002) monochromator and a RTMS X'Ceerator (Panalytical).

UV–vis measurements were performed with a Varian Cary 5.

Photoluminescence spectra were obtained with Florolog 322 (Horiba Jobin Yvon Ltd) with the range of wavelength from 500 nm to 850 nm by exciting at 460 nm.

Stability measurements

The stability setup used in this study is described in detail in **Supplementary note 2**.

Data availability

The data that support the plots within this paper and other findings of this study are available from the corresponding author upon reasonable request

Author contributions

WT and KD conceived the study, which was then supervised by WT. KD performed the stability measurements and analysed the data. The devices were prepared by EA. The stability measurement setup was designed and developed by KD, WT and AH. KD and WT wrote the first draft of the manuscript. MG and AH contributed to fruitful discussions and supervision of the project. All authors contributed to the writing of the manuscript.

Acknowledgements

We thank Benjamin Le Geyt, Supardi Sujito, Christophe Clement and Andre Fattet for their help in building the ageing setup used to collect the data presented here. We also thank Taisuke Matsui, Mozghan Yavari and Michael Saliba for providing devices used in a pilot study. KD thanks the SNF for funding within the framework of Umbrella project (grant agreement no. 407040-153952 and 407040-153990). EA acknowledges King Abdulaziz City for Science and Technology (KACST) for the fellowship, WT and MG for their financial support under a joint research project. WT thanks the Swiss National Science foundation for funding through an Ambizione fellowship.

Competing financial interests

The authors declare no competing financial interests

References

1. Correa-Baena, J.-P. *et al.* The rapid evolution of highly efficient perovskite solar cells. *Energy Environ. Sci.* **10**, 710–727 (2017).
2. Priyadarshi, A. *et al.* A large area (70 cm²) monolithic perovskite solar module with a high efficiency and stability. *Energy Environ. Sci.* **9**, 3687–3692 (2016).
3. Hu, Y. *et al.* Stable Large-Area (10 × 10 cm²) Printable Mesoscopic Perovskite Module Exceeding 10% Efficiency. *Sol. RRL* **1**, 1600019 (2017).
4. Agresti, A. *et al.* Graphene Interface Engineering for Perovskite Solar Modules: 12.6% Power Conversion Efficiency over 50 cm² Active Area. *ACS Energy Lett.* **2**, 279–287 (2017).
5. Conings, B. *et al.* Intrinsic Thermal Instability of Methylammonium Lead Trihalide Perovskite. *Adv. Energy Mater.* **5**, 1500477 (2015).
6. You, J. *et al.* Improved air stability of perovskite solar cells via solution-processed metal oxide transport layers. *Nat. Nanotechnol.* **11**, 75–81 (2016).
7. Saliba, M. *et al.* Incorporation of rubidium cations into perovskite solar cells improves photovoltaic performance. *Science* **354**, 206–209 (2016).
8. Anaraki, E. H. *et al.* Highly efficient and stable planar perovskite solar cells by solution-processed tin oxide. *Energy Environ. Sci.* **9**, 3128–3134 (2016).
9. Zimmermann, E. *et al.* Erroneous efficiency reports harm organic solar cell research. *Nat. Photonics* **8**, 669–672 (2014).
10. Snaith, H. J. *et al.* Anomalous Hysteresis in Perovskite Solar Cells. *J. Phys. Chem. Lett.* **5**, 1511–1515 (2014).
11. Tress, W. *et al.* Understanding the rate-dependent J–V hysteresis, slow time component, and aging in CH₃NH₃PbI₃ perovskite solar cells: the role of a compensated electric field. *Energy Environ. Sci.* **8**, 995–1004 (2015).
12. Reese, M. O. *et al.* Consensus stability testing protocols for organic photovoltaic materials and devices. *Sol. Energy Mater. Sol. Cells* **95**, 1253–1267 (2011).
13. Saliba, M. *et al.* Cesium-containing triple cation perovskite solar cells: improved stability, reproducibility and high efficiency. *Energy Environ. Sci.* **9**, 1989–1997 (2016).
14. Leijtens, T. *et al.* Overcoming ultraviolet light instability of sensitized TiO₂ with meso-structured organometal tri-halide perovskite solar cells. *Nat. Commun.* **4**, 3885 (2013).
15. Shin, S. S. *et al.* Colloidally prepared La-doped BaSnO₃ electrodes for efficient, photostable perovskite solar cells. *Science* **356**, 167–171 (2017).
16. Lee, S.-W. *et al.* UV Degradation and Recovery of Perovskite Solar Cells. *Sci. Rep.* **6**, 38150 (2016).
17. Li, W. *et al.* Enhanced UV-light stability of planar heterojunction perovskite solar cells with caesium bromide interface modification. *Energy Environ. Sci.* **9**, 490–498 (2016).
18. Bella, F. *et al.* Improving efficiency and stability of perovskite solar cells with photocurable fluoropolymers. *Science* **354**, 203–206 (2016).
19. Aristidou, N. *et al.* The Role of Oxygen in the Degradation of Methylammonium Lead Trihalide Perovskite Photoactive Layers. *Angew. Chem. Int. Ed.* **54**, 8208–8212 (2015).
20. Pearson, A. J. *et al.* Oxygen Degradation in Mesoporous Al₂O₃/CH₃NH₃PbI₃-xCl_x Perovskite Solar Cells: Kinetics and Mechanisms. *Adv. Energy Mater.* **6**, 1600014 (2016).
21. Bryant, D. *et al.* Light and oxygen induced degradation limits the operational stability of methylammonium lead triiodide perovskite solar cells. *Energy Environ. Sci.* **9**, 1655–1660 (2016).

22. Yang, J., Siempelkamp, B. D., Liu, D. & Kelly, T. L. Investigation of CH₃NH₃PbI₃ Degradation Rates and Mechanisms in Controlled Humidity Environments Using in Situ Techniques. *ACS Nano* **9**, 1955–1963 (2015).
23. Christians, J. A., Miranda Herrera, P. A. & Kamat, P. V. Transformation of the Excited State and Photovoltaic Efficiency of CH₃NH₃PbI₃ Perovskite upon Controlled Exposure to Humidified Air. *J. Am. Chem. Soc.* **137**, 1530–1538 (2015).
24. Hwang, I., Jeong, I., Lee, J., Ko, M. J. & Yong, K. Enhancing Stability of Perovskite Solar Cells to Moisture by the Facile Hydrophobic Passivation. *ACS Appl. Mater. Interfaces* **7**, 17330–17336 (2015).
25. Long, M. *et al.* Nonstoichiometric acid–base reaction as reliable synthetic route to highly stable CH₃NH₃PbI₃ perovskite film. *Nat. Commun.* **7**, 13503 (2016).
26. Chen, W. *et al.* Efficient and stable large-area perovskite solar cells with inorganic charge extraction layers. *Science* **350**, 944–948 (2015).
27. Brivio, F., Caetano, C. & Walsh, A. Thermodynamic Origin of Photoinstability in the CH₃NH₃Pb(1–xBrx)₃ Hybrid Halide Perovskite Alloy. *J. Phys. Chem. Lett.* **7**, 1083–1087 (2016).
28. Divitini, G. *et al.* In situ observation of heat-induced degradation of perovskite solar cells. *Nat. Energy* **1**, 15012 (2016).
29. Domanski, K. *et al.* Not All That Glitters Is Gold: Metal-Migration-Induced Degradation in Perovskite Solar Cells. *ACS Nano* **10**, 6306–6314 (2016).
30. Gholipour, S. *et al.* Highly Efficient and Stable Perovskite Solar Cells based on a Low-Cost Carbon Cloth. *Adv. Energy Mater.* **6**, 1601116 (2016).
31. Aitola, K. *et al.* High Temperature-Stable Perovskite Solar Cell Based on Low-Cost Carbon Nanotube Hole Contact. *Adv. Mater.* **29**, 1606398 (2017).
32. Bush, K. A. *et al.* Thermal and Environmental Stability of Semi-Transparent Perovskite Solar Cells for Tandems Enabled by a Solution-Processed Nanoparticle Buffer Layer and Sputtered ITO Electrode. *Adv. Mater.* **28**, 3937–3943 (2016).
33. Bush, K. A. *et al.* 23.6%-efficient monolithic perovskite/silicon tandem solar cells with improved stability. *Nat. Energy* **2**, 20179 (2017).
34. Zhao, X., Kim, H.-S., Seo, J.-Y. & Park, N.-G. Effect of Selective Contacts on the Thermal Stability of Perovskite Solar Cells. *ACS Appl. Mater. Interfaces* **9**, 7148–7153 (2017).
35. Eames, C. *et al.* Ionic transport in hybrid lead iodide perovskite solar cells. *Nat. Commun.* **6**, 7497 (2015).
36. Meloni, S. *et al.* Ionic polarization-induced current-voltage hysteresis in CH₃NH₃PbX₃ perovskite solar cells. *Nat. Commun.* **7**, 10334 (2016).
37. Nie, W. *et al.* Light-activated photocurrent degradation and self-healing in perovskite solar cells. *Nat. Commun.* **7**, 11574 (2016).
38. Huang, W., Manser, J. S., Kamat, P. V. & Ptasinska, S. Evolution of Chemical Composition, Morphology, and Photovoltaic Efficiency of CH₃NH₃PbI₃ Perovskite under Ambient Conditions. *Chem. Mater.* **28**, 303–311 (2016).
39. Bag, M. *et al.* Kinetics of Ion Transport in Perovskite Active Layers and Its Implications for Active Layer Stability. *J. Am. Chem. Soc.* **137**, 13130–13137 (2015).
40. Tress, W., Correa Baena, J. P., Saliba, M., Abate, A. & Graetzel, M. Inverted Current–Voltage Hysteresis in Mixed Perovskite Solar Cells: Polarization, Energy Barriers, and Defect Recombination. *Adv. Energy Mater.* **6**, 1600396 (2016).

41. Domanski, K. *et al.* Migration of cations induces reversible performance losses over day/night cycling in perovskite solar cells. *Energy Environ. Sci.* **10**, 604–613 (2017).
42. Abate, A. *et al.* Silolothiophene-linked triphenylamines as stable hole transporting materials for high efficiency perovskite solar cells. *Energy Environ. Sci.* **8**, 2946–2953 (2015).
43. Kong, J. *et al.* Long-term stable polymer solar cells with significantly reduced burn-in loss. *Nat. Commun.* **5**, 6688 (2014).
44. Peters, C. H. *et al.* The Mechanism of Burn-in Loss in a High Efficiency Polymer Solar Cell. *Adv. Mater.* **24**, 663–668 (2012).
45. Tan, H. *et al.* Efficient and stable solution-processed planar perovskite solar cells via contact passivation. *Science* **355**, 722–726 (2017).
46. Law, C. *et al.* Performance and Stability of Lead Perovskite/TiO₂, Polymer/PCBM, and Dye Sensitized Solar Cells at Light Intensities up to 70 Suns. *Adv. Mater.* **26**, 6268–6273 (2014).
47. Mei, A. *et al.* A hole-conductor-free, fully printable mesoscopic perovskite solar cell with high stability. *Science* **345**, 295–298 (2014).
48. Grancini, G. *et al.* One-Year stable perovskite solar cells by 2D/3D interface engineering. *Nat. Commun.* **8**, 15684 (2017).
49. Dualeh, A., Gao, P., Seok, S. I., Nazeeruddin, M. K. & Grätzel, M. Thermal Behavior of Methylammonium Lead-Trihalide Perovskite Photovoltaic Light Harvesters. *Chem. Mater.* **26**, 6160–6164 (2014).
50. Akbulatov, A. F. *et al.* Probing the Intrinsic Thermal and Photochemical Stability of Hybrid and Inorganic Lead Halide Perovskites. *J. Phys. Chem. Lett.* **8**, 1211–1218 (2017).

Supplementary Information

Supplementary tables

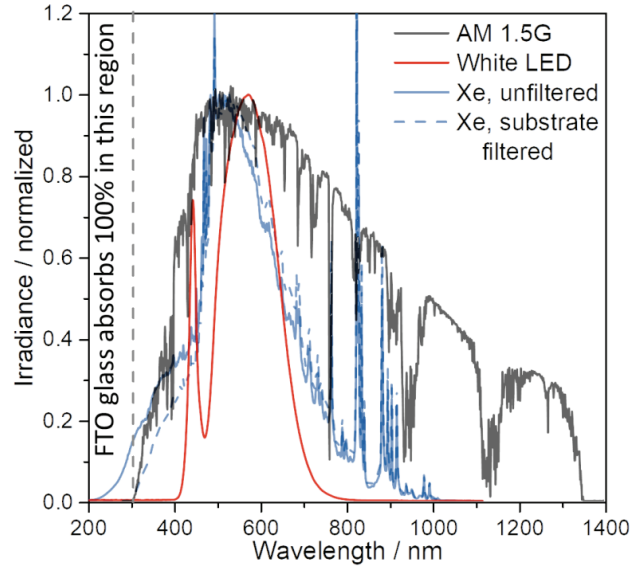
Supplementary Table 1 Common PV panel testing protocols for accelerated stress tests according to IEC 61215 standards.

Test	Details	Major addressed failures
<i>Thermal Cycling</i>	200 cycles, from -40 to 85 °C	Broken interconnects and cells, junction box adhesion, electrical bond failures
<i>Damp Heat</i>	1000 hours, 85 °C / 85% Relative Humidity	Corrosion, delamination, adhesion of encapsulant
<i>Humidity Freeze</i>	10 cycles, from -40 to 85 °C / 85% Relative Humidity	Delamination, junction box adhesion
<i>UV</i>	15 kWh m ⁻²	Colour change of encapsulant, delamination
<i>Further tests</i>	Hail, salt, static and dynamic mechanical load (wind, snow), hot spots	Corrosion, broken glass and interconnects, electrical bond failures, shunts in solar cells

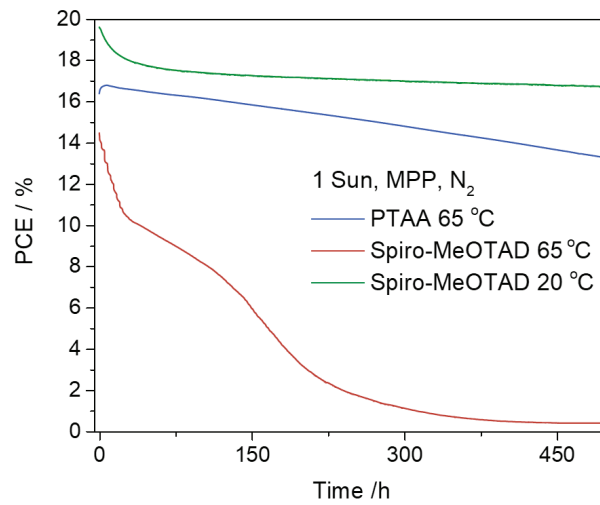
Supplementary Table 2 Examples of measurement guidelines for different stress conditions provided within the ISOS protocols by Reese et al.¹

Test ID	<i>ISOS-D-3 Damp heat</i>	<i>ISOS-L-3 Laboratory weathering</i>	<i>ISOS-T-3 Thermal cycling</i>	<i>ISOS-LT-3 Solar-thermal- humidity-freeze cycling</i>
Light source	None	Simulator	None	Simulator
Temperature	65/85 °C	65/85 °C	-40 to 85 °C	-25 to 65 °C
Relative humidity	85%	Near 50%	Near 55%	50% beyond 40 °C
Environment	Environmental chamber	Light, Temp. and Relative Humidity	Environmental chamber	Environmental chamber with light and freezing
Characterization light source	Solar simulator	Solar simulator	Solar simulator	Solar simulator
Load	Open circuit	MPP	Open circuit	MPP or open circuit

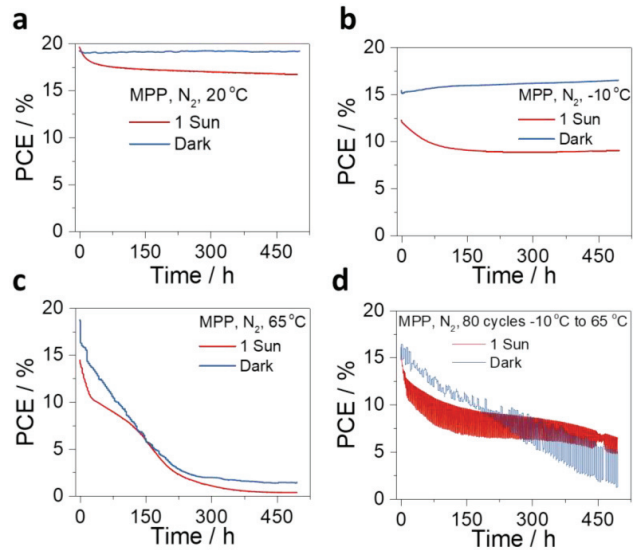
Supplementary figures



Supplementary Figure 1 Spectra of LED and Xe lamps used for ageing experiments



Supplementary Figure 2 Temperature-dependent stability of devices employing Spiro-MeOTAD and PTAA hole transporting layers. Both types of devices employ Au electrodes and are based on the same architecture. Illumination was white LEDs.

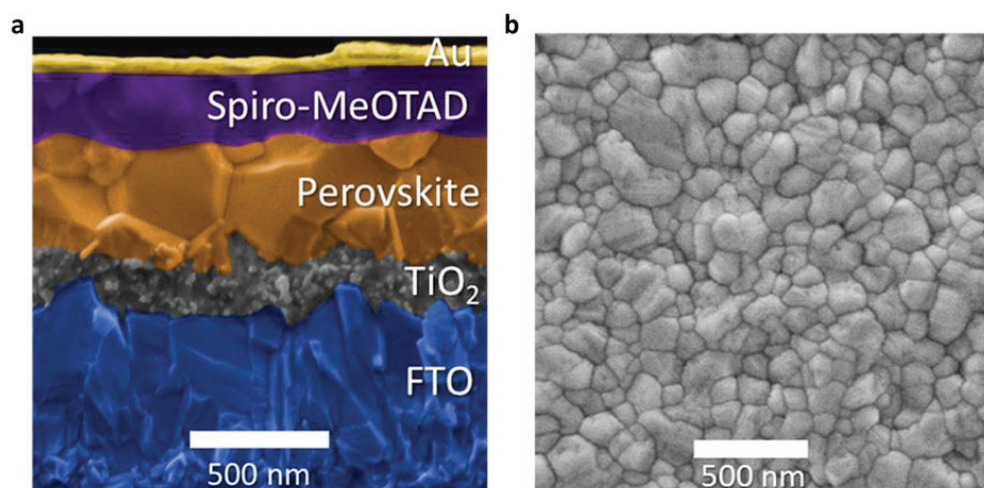


Supplementary Figure 3 The effect of illumination on devices aged a) 20, b) -10 and c) 65 °C. d) The effect of light on temperature-cycled device. The devices exposed to light continuously, were aged at MPP. The ones aged in the dark were exposed to light and measured for 1 min at MPP every 3 h. Illumination was white LEDs.

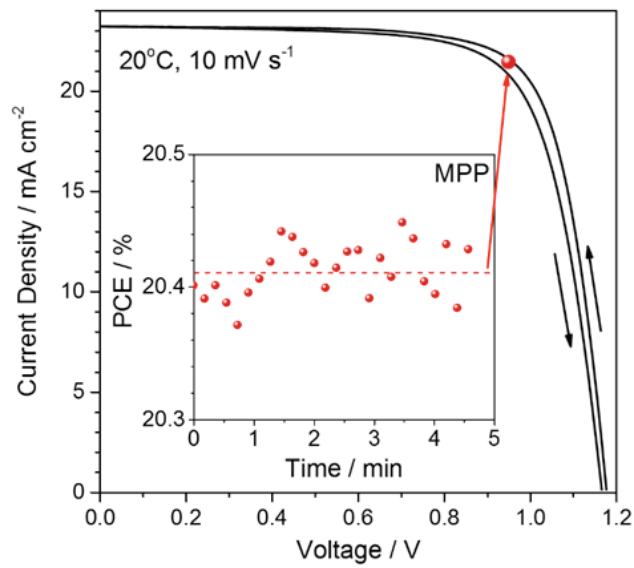
Supplementary note 1: Device architecture and characterization

PSCs were fabricated on fluorine-doped tin oxide (FTO) glass substrates and composed of a typical stack of compact TiO_2 / mesoporous TiO_2 /perovskite/Spiro-MeOTAD/Au. The active layer of the device consists of a perovskite-filled mesoporous TiO_2 scaffold and a solid perovskite layer sitting on top of it. The chemical composition of the perovskite precursor is a Cs-containing $\text{FA}_{0.83}\text{MA}_{0.17}\text{Pb}(\text{I}_{0.83}\text{Br}_{0.17})_3$ formulation, referred to as “triple cation” perovskite in this work. **Supplementary Figure 4 a** shows the cross-section SEM image of the device with a thin perovskite-infiltrated mesoporous TiO_2 layer (as electron selective layer, ESL) of ca. 200 nm and a 500 nm perovskite capping layer comprised of large crystals. (**Supplementary Figure 4 b**) A 200 nm layer of Spiro-MeOTAD (as hole transporting layer, HTL) sits atop the perovskite layer and finally a gold top electrode is deposited to contact the device.

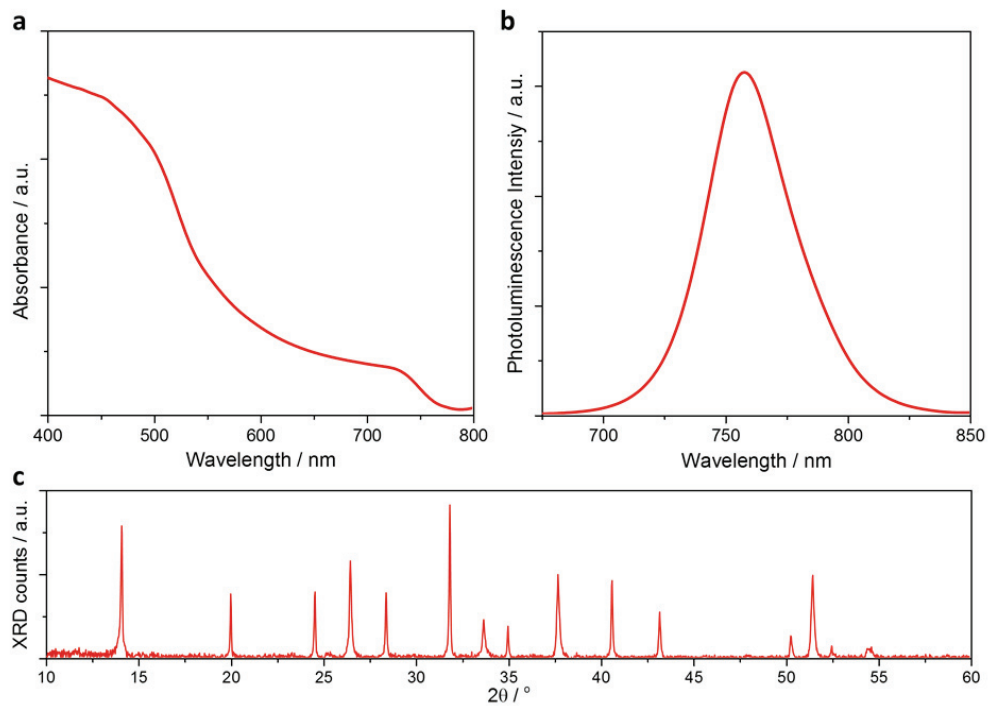
Supplementary Figure 5 shows a J-V curve measured at 10 mV s^{-1} of a typical high-performance device used in this study. The devices exhibit limited hysteresis and the efficiency extracted from the backward scan (20.6% in **Supplementary Figure 5**) is close to the stabilised power (20.4%).



Supplementary Figure 4 SEM images of the devices: a) cross-section and b) top view. Perovskite composition used was “triple cation” including Cs.



Supplementary Figure 5 Photovoltaic performance of the devices studied: J-V curve and the result of maximum power point tracking of one of the devices used in this study.



Supplementary Figure 6 Characterization of the devices studies. a) UV-visible spectroscopy absorption spectrum b) photoluminescence emission spectrum and c) XRD spectrum

Supplementary note 2: Our stability setup

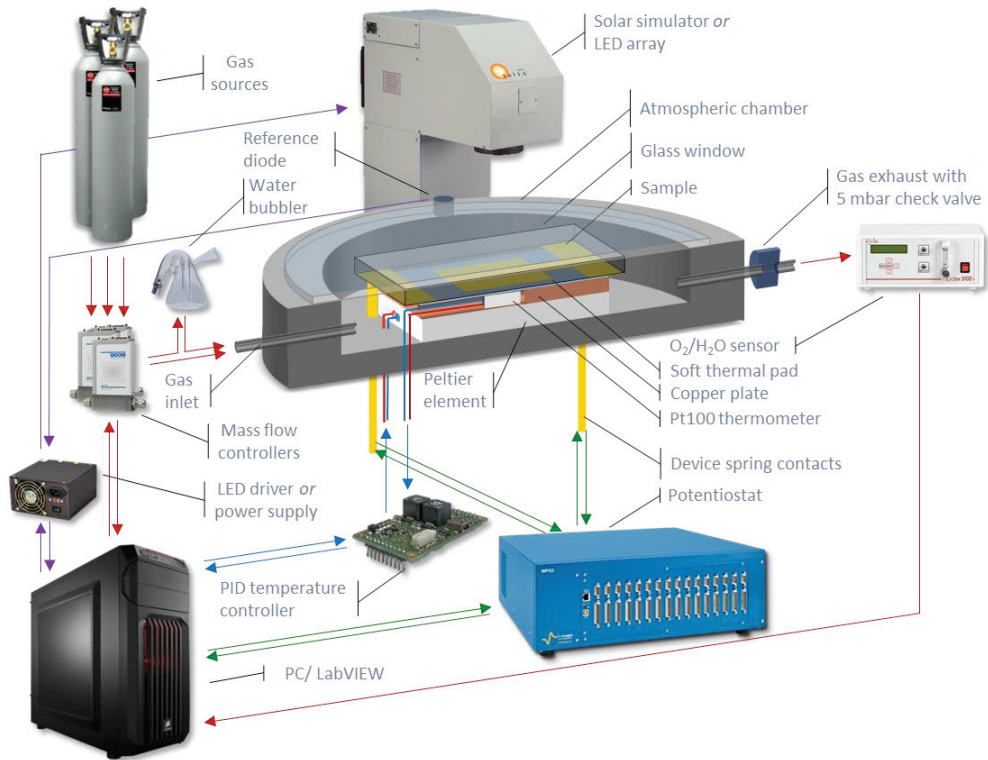
As an example, we describe here the stability setup built by us and used in this work. The central part of the stability setup is a custom-built airtight weathering chamber, which can host up to 4 samples (each having 2 pixels/devices). The devices can be masked (to 0.16 cm² in this study) and each device is connected to a separate channel of a potentiostat (Biologic MPG2; green arrows in **Supplementary Supplementary Figure 7**) and the temperature of each sample (blue arrows) can be independently regulated. Additionally, the illumination (purple arrows) and the atmosphere (red arrows) within the ageing chamber are controlled. The use of potentiostat allows for a broad range of electrical measurements such as MPP tracking, J-V as well as transient and EIS measurements to be done *in situ*.

The samples rest on spring legs and they are pressed against a copper plate lined with a soft thermally conductive rubber. The copper plate has a hole inside into which a Pt100 thermometer is inserted. Between the copper plate and the aluminium body of the weathering chamber sits a Peltier element – a small heat pump that can either cool or heat up the sample. Arctic Silver 5 paste is used to increase heat conductivity between the components. The Peltier element and Pt100 are connected to a computer-controlled PID controller (Meerstetter TEC-1091) to create a feedback loop. The setup allows for a temperature control from -15 °C – 180 °C.

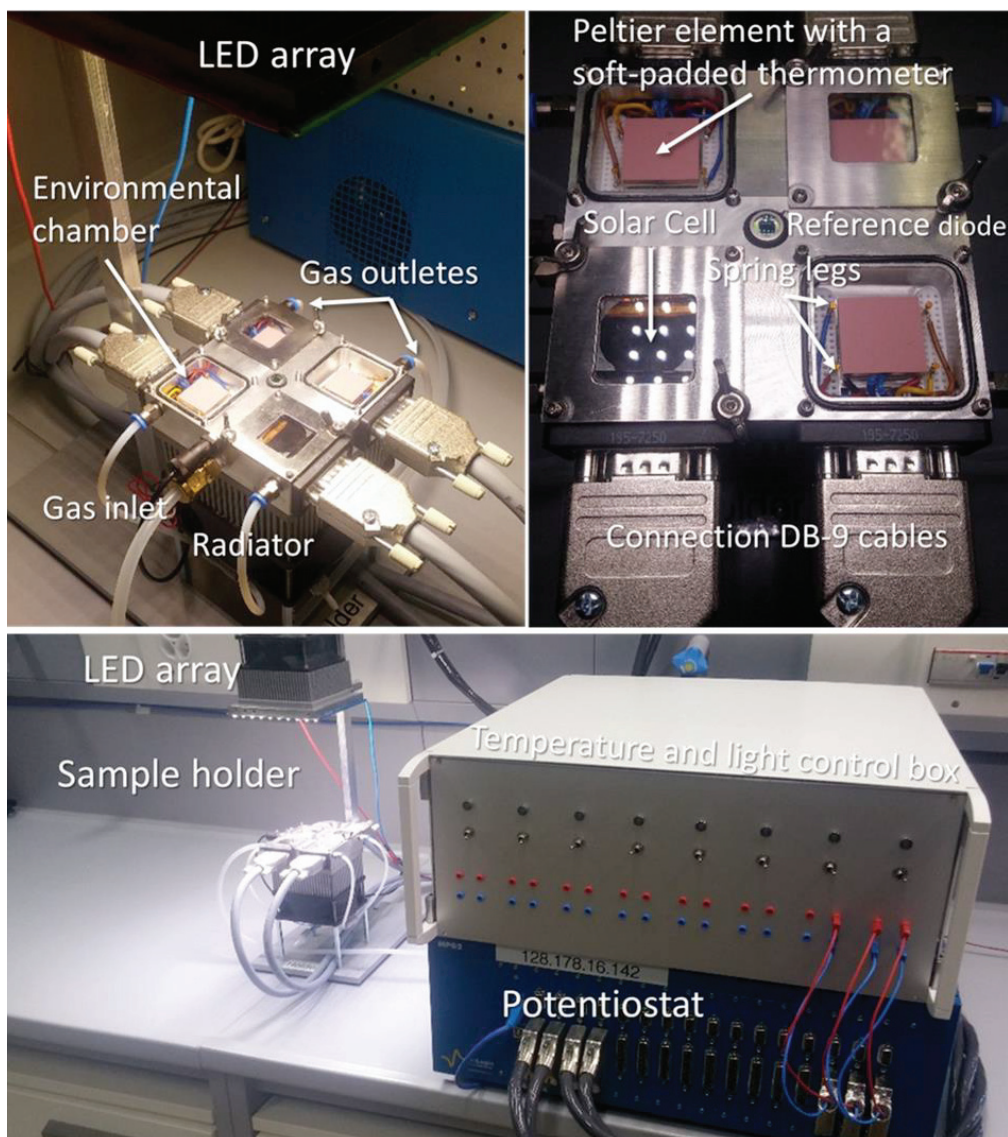
The weathering chamber is sealed with a soda-lime glass lid and all electrical connectors are airtight. A 5 mbar check valve is installed at the outlet of the chamber in order to maintain a small overpressure inside and prevent permeation of O₂ and H₂O into the environment (similar to how gloveboxes are designed). Mass flow controllers (Brooks Instruments GF40) are used to regulate flow of different gasses, which can optionally pass through a water bubbler on their way to the chamber. In this study we used around 0.5 l min⁻¹. The purity of the exhaust gas can be monitored with an O₂/H₂O sensor such as Rapidox 3100D and a feedback loop can be created in order to control the atmosphere (currently under development in our setup).

Illumination of the devices can be selected between a Xe solar simulator and an LED array. A reference diode is used to monitor the intensity of the light source (and in the case of the LED array, to create a feedback loop to precisely regulate the illumination from 0.00001 to equivalent of 3 Suns). When using a Xe lamp, it is important to monitor its intensity (which tends to oscillate and decrease over time – especially in the UV region) keeping in mind that a Si diode used for this purpose may itself degrade when exposed to UV light for extended period of time (a UV filter in front of the diode is a practical solution to the problem).

The setup is centrally-controlled through a LabVIEW interface allowing for automatic programming of experiments (temperature, illumination, atmosphere, electronic measurements). Up to 32 devices (16 samples) can be measured simultaneously in 4 separate weathering chambers. **Supplementary Figure 8** shows pictures of the main components of the setup.



Supplementary Figure 7 The schematics of the ageing setup used to perform all experiments presented in this work. The central weathering chamber is shown in cross-section. The differently coloured arrows show how different components of the setup interact with each other.



Supplementary Figure 8 A picture of the main parts of the stability measurement setup. Solar cells sit inside the environmental chamber, which is flushed with gas and illuminated from above. The solar cells are connected to the potentiostat. Light and temperature are controlled through a central control unit.

Supplementary references

1. Reese, M. O. *et al.* Consensus stability testing protocols for organic photovoltaic materials and devices. *Spec. Issue 3rd Int. Summit OPV Stab.* **95**, 1253–1267 (2011).

Conclusions

Achieved Results

PSCs have achieved power conversion efficiency values approaching these of established PV technologies. As was historically the case with other PV technologies, the focus of the PSC research community is at this point shifting towards making their devices not only efficient but also stable – the next essential step for the commercialization of the technology. In this thesis, I described how my efforts contributed towards improving stability of PSCs. Since its invention, PSCs have been speculated to be sensitive to environmental conditions such as atmosphere, temperature and illumination. In this thesis, I first described how I designed and built a dedicated solar cell stability setup that allows for keeping the devices under controlled atmosphere in airtight chambers. The user can illuminate the devices with white LED light or with a Xe lamp. The temperature of each sample can be controlled independently with use of Peltier elements and a range between approximately -15 °C to 180 °C can be achieved. Additionally, each of 32 devices is connected to a separate channel of a potentiostat, which allows for independent load control (MPP, open-/short-circuit, or any other voltage/current) as well as conducting experiments such as V_{oc}/J_{sc} tracking, transient measurements and measurements of rate-dependent J-V curves amongst others.

In the second part of this thesis, I focused on improving stability of PSCs. First, I described how “mixed” perovskites suffer from intrinsic photo instability. I showed, how tuning the perovskite composition and including Cs^+ into the mixture resulted in a breakthrough operational stability through means of entropic stabilisation and film morphology improvement. This was achieved with both TiO_2 -mesoporous scaffold based devices and planar devices based on SnO_2 ETLs. However, this way only room-temperature stability was achieved and I soon discovered that those same devices suffered from critical instability at elevated temperatures (>60 °C). Having employed time-of-flight secondary ion mass spectrometry, I found that Au can migrate from the electrode, across Spiro-MeOTAD and lodge itself deep in the perovskite layer. Again, I verified this for several different device architectures and perovskite compositions. I found this phenomenon to proceed both under illumination and load as well as in the dark. By series of control experiments, where Au electrode was replaced following ageing or ageing was done without an Au electrode on the device, I managed to pinpoint Au migration as the main cause of device degradation. The SEM analysis of Spiro-MeOTAD layer underneath Au electrode in high-temperature-aged devices revealed that HTL becomes porous. This points to the conclusion that HTL is the weak point of PSCs.

In an attempt to improve high-temperature stability of PSCs, I tried to reinforce Spiro-MeOTAD with Al_2O_3 nanoparticles. While the stability was improved this way, it was still unsatisfactory. Alternatively, I deposited a thin Cr layer between Au and Spiro-MeOTAD to act as a diffusion barrier. This approach turned out to effectively block Au migration, which I confirmed with elemental analysis of perovskite films constituting high temperature-aged devices. However, incorporation of the Cr diffusion barrier had an adverse effect on device efficiency due to the energetic mismatch of device components or increased series resistance. For this reason, I investigated the potential of PTAA as an alternative to Spiro-MeOTAD for high performance, high temperature-stable devices. Indeed, devices with PTAA HTL are critically more high temperature-stable than their Spiro-MeOTAD based counterparts. This is ascribed to the polymeric nature of PTAA as opposed to the small-molecule Spiro-MeOTAD. Additionally, unlike Spiro-MeOTAD, PTAA does not suffer from crystallisation at elevated temperatures. At the time

of this discovery, PTAA HTL was combined with state-of-the-art Rb-containing perovskite to demonstrate devices with both record efficiency and stability. As polymeric PTAA turned out to be effective for realisation of efficient and stable PSCs, I also investigated its additive-free derivatives to be employed as HTLs. This way, with my colleagues, we have shown that employing additive-free HTLs is a promising way to improve stability of PSCs.

While the stability of PSCs with polymeric HTLs is very promising, the organic HTMs and Au electrodes employed are rather expensive (both to purchase and, in case of Au, to vacuum-process) and of poor industrial applicability. Hence, I also investigated the potential of carbon electrodes, which do not require high temperature or vacuum processes for deposition. Removing Au from the system (the main culprit of high temperature degradation), resulted in much improved stability. Hence, the facile-to-process carbon electrodes hold a promise of inexpensive, stable and reasonably efficient PSCs.

In the final part of this thesis, the focus is on understanding degradation in the context of perovskites being novel materials showing new phenomena previously unknown to PV research community. This involves J-V-hysteresis and reversible losses when the devices are aged under illumination. I investigate these reversible losses to find the underlying mechanism. With the help of time-of-flight secondary ion mass spectrometry, I provided the first direct proof of halide defects being mobile in a complete device. It was found that electric field is enough to induce this behaviour. However, mobile halides only are not enough to explain the slow, reversible degradation in PSCs. Consequently, with the help of drift-diffusion simulations, an indirect proof of cation migration was also provided. Only combined halide and cation migration allows for reproducing the observed reversible degradation in PSCs in drift-diffusion simulations. This cation migration was found to be a very slow process occurring on the time-scale of hours and hence only seen when conducting long-term ageing of PSCs.

Working on ion migration in PSCs, I also discovered that mobile halide vacancies can accumulate at FTO/perovskite interfaces when ETL-free PSCs are biased in reverse direction. This in turn alters the energetic structure of the interface and allows for direct hole injection from FTO to perovskite. Under illumination, the conductivity of perovskite is increased (photoconductivity). As holes are considerably slower than electrons in perovskite, when the reverse-biased devices are illuminated, one observes photomultiplication effect (i.e. each absorbed photon results in collection of multiple electron-hole pairs). This allows the devices to work as photodetectors with very high internal gains. The responsivity of the devices (one of the main photodetector performance metric, which describes photodetector's ability to turn optical signals to electric ones) exceeded 200 A W^{-1} , which was at that time amongst the highest values achieved.

The early years of PSC research were plagued by inaccurate PCE reports due to the phenomenon of hysteresis and the lack of consensus on how to measure these devices. By the time this thesis was submitted, operational stability has emerged as the next main challenge to be addressed by the research community. It is important to avoid the missteps that haunted PCE measurements in the early days of the field and to reach a consensus on how to assess and report stability of PSCs. This is why, I conducted a systematic study on how different factors such as illumination, temperature, atmosphere and load on the device influence its stability. I concluded that the most reliable way to assess operational stability of PSCs is to conduct the experiments in inert atmosphere under illumination, MPP and at both room and elevated temperatures. I also proposed several protocols of varying sophistication

as well as data reporting practices as an effort to make published stability data more readily comparable. I hope that my work will trigger a discussion on how to age PSCs and that it will lead to eventual emergence and adoption of consensus protocols for measuring operational stability of these devices.

Future Work

Future work can be pursued in several directions. Firstly, the development of the ageing setup can be continued as outlined at the end of **Chapter 2** to include better atmospheric control, additional measurement capabilities and a secure power supply.

Secondly, more work is needed to bring the community into the consensus of how ageing of perovskite solar cells should be done in order to further the understanding of degradation processes and improve stability. This is a very important topic as the efficiency of the process of improving the stability of perovskite solar cells hinges on it. Work described in **Chapter 9** should be repeated (also by other research groups) for a broad range of device architectures with different contact materials and perovskite compositions. Indeed, the work described here is only the first of a kind and much more development is expected before a consensus PSC ageing protocols (analogous to ISOS-3 for OPV) can be developed.

Given the complex nature of the degradation of perovskite solar cells, one attractive research direction is to investigate stability and power output under real operating conditions – either by performing the experiments outdoor, or by simulating the conditions in the laboratory. This would give insights into realistic power outputs of PSCs working in the field.

Finally, all work described in this thesis was conducted using unencapsulated devices. The logics behind this is that creating inert conditions is a better strategy than encapsulating the devices, which poses the risk that one probes the quality of encapsulation rather than the device itself. However, I am suspecting that exposing the unencapsulated devices to gas flow can itself influence the devices and I reported such indications in work led by Juan-Pablo Correa-Baena.³⁸ Hence, an important research direction to further the work described in this thesis is to investigate the influence of inert gas flows on the stability of unencapsulated devices. Perhaps the correct way to age perovskite solar cells with respect to the atmospheric aspect, is to place encapsulated devices in inert atmosphere: this way the potential effect of gas flow is excluded and still the quality of encapsulation does not limit the device stability (as no O₂/H₂O is present in the environment anyways).

Quo Vadis? – The Outlook for Stability of Perovskite Solar Cells

Since I started the work on this thesis around 3 years ago, the stabilities of PSCs have experienced a dramatic improvement. While the lifetimes of PSCs were mostly measured in hours in 2014, by the end of 2017 they are already measured in years.¹⁰⁷ Hence, the next logical step will be to employ accelerated stability tests for PSCs. However, for a quantitative comparison and predictive power of accelerated ageing, knowledge of a model for the underlying degradation mechanism is essential. Hence, more work into understanding of degradation mechanisms in PSCs will be needed until accelerated protocols can be devised.

Despite the very promising developments, the stability of PSCs is still short of what would be required for commercial PV panels. PV products are often certified to degrade by less than 10-20 % on the timescale of 20-30 years. This certification requires the panel to withstand a series of aggressive accelerated stress tests involving high levels of humidity, high and low temperatures, large UV light doses, mechanical impact tests etc. (IEC standards).¹⁰⁵ However, these standardized certification tests are the result of many years of experience and analysis of common field failures (corrosion, delamination, broken cells and connecting elements, hot spots etc.) and vary slightly for different technologies. Hence, they cannot be readily applied to PSCs without furthering the understanding of common degradation pathways.

Once again, I would like to stress that the prerequisite for stable perovskite PV modules is the intrinsic stability of PSCs employed. However, in practice the sensitivity of PSCs to extrinsic factors such as UV light, moisture, oxygen and mechanical loads will impose the requirements on the quality of encapsulation to protect against these (it will also determine the price of encapsulation). Hence, eventually studies of encapsulated PSCs will become increasingly relevant and required.

Currently, the most promising directions for improving stability of PSCs focus on the weak point - HTLs. One strategy that has been very successful is to replace the organic HTLs with inorganic ones.^{93,108,109,133,134} Another promising route is to utilise metal electrode-free architectures based on e.g. carbon contacts.^{91,92,107} Whichever strategies are employed, one thing is certain though: the issue of stability of PSCs will receive increasing attention as the technology matures from laboratory towards commercial products and we will see many more scientists and companies join in *the quest for stability of perovskite solar cells*.

References

1. Solomon, S., Plattner, G.-K., Knutti, R. & Friedlingstein, P. Irreversible climate change due to carbon dioxide emissions. *Proc. Natl. Acad. Sci.* **106**, 1704–1709 (2009).
2. Hansen, J. *et al.* Target atmospheric CO₂: Where should humanity aim? *ArXiv Prepr. ArXiv08041126* (2008).
3. Intergovernmental Panel on Climate Change. *Climate change 2014: mitigation of climate change*. **3**, (Cambridge University Press, 2015).
4. World Energy Council, W. E. C. *World energy resources*. (2016).
5. Fridleifsson, I. B. *et al.* The possible role and contribution of geothermal energy to the mitigation of climate change. in **20**, 59–80 (Citeseer, 2008).
6. Mørk, G., Barstow, S., Kabuth, A. & Pontes, M. T. Assessing the global wave energy potential. in **20473**, (2010).
7. Philipps, S. & Warmuth, W. *Photovoltaics Report*. (Fraunhofer Institute for Solar Energy Systems, 2017).
8. Wirth, H. & Schneider, K. Recent Facts about Photovoltaics in Germany.
9. Woodhouse, M. *et al.* An economic analysis of photovoltaics versus traditional energy sources: Where are we now and where might we be in the near future? in 002481–002483 (IEEE, 2011).
10. Green, M. A. Commercial progress and challenges for photovoltaics. *Nat. Energy* **1**, 15015 (2016).
11. Dittrich, T., Awino, C., Prajontat, P., Rech, B. & Lux-Steiner, M. C. Temperature dependence of the band gap of CH₃NH₃PbI₃ stabilized with PMMA: A modulated surface photovoltage study. *J. Phys. Chem. C* **119**, 23968–23972 (2015).
12. Shockley, W. & Queisser, H. J. Detailed balance limit of efficiency of p-n junction solar cells. *J. Appl. Phys.* **32**, 510–519 (1961).
13. Ponseca, C. S. *et al.* Organometal Halide Perovskite Solar Cell Materials Rationalized: Ultrafast Charge Generation, High and Microsecond-Long Balanced Mobilities, and Slow Recombination. *J. Am. Chem. Soc.* (2014). doi:10.1021/ja412583t
14. Xing, G. *et al.* Long-range balanced electron-and hole-transport lengths in organic-inorganic CH₃NH₃PbI₃. *Science* **342**, 344–347 (2013).
15. Stranks, S. D. *et al.* Electron-Hole Diffusion Lengths Exceeding 1 Micrometer in an Organometal Trihalide Perovskite Absorber. *Science* **342**, 341–344 (2013).
16. Zhao, Y., Nardes, A. M. & Zhu, K. Solid-State Mesostuctured Perovskite CH₃NH₃PbI₃ Solar Cells: Charge Transport, Recombination, and Diffusion Length. *J. Phys. Chem. Lett.* **5**, 490–494 (2014).
17. Stoumpos, C. C., Malliakas, C. D. & Kanatzidis, M. G. Semiconducting Tin and Lead Iodide Perovskites with Organic Cations: Phase Transitions, High Mobilities, and Near-Infrared Photoluminescent Properties. *Inorg. Chem.* **52**, 9019–9038 (2013).
18. Kojima, A., Teshima, K., Shirai, Y. & Miyasaka, T. Organometal Halide Perovskites as Visible-Light Sensitizers for Photovoltaic Cells. *J. Am. Chem. Soc.* **131**, 6050–6051 (2009).

19. Kim, H.-S. *et al.* Lead iodide perovskite sensitized all-solid-state submicron thin film mesoscopic solar cell with efficiency exceeding 9%. *Sci. Rep.* **2**, (2012).
20. Burschka, J. *et al.* Sequential deposition as a route to high-performance perovskite-sensitized solar cells. *Nature* **499**, 316–319 (2013).
21. He, M., Zheng, D., Wang, M., Lin, C. & Lin, Z. High efficiency perovskite solar cells: from complex nanostructure to planar heterojunction. *J. Mater. Chem. A* (2013). doi:10.1039/C3TA14160H
22. Docampo, P., Ball, J. M., Darwich, M., Eperon, G. E. & Snaith, H. J. Efficient organometal trihalide perovskite planar-heterojunction solar cells on flexible polymer substrates. *Nat. Commun.* **4**, 2761 (2013).
23. Jeng, J.-Y. *et al.* CH₃NH₃PbI₃ Perovskite/Fullerene Planar-Heterojunction Hybrid Solar Cells. *Adv. Mater.* **25**, 3727–3732 (2013).
24. Lee, M. M., Teuscher, J., Miyasaka, T., Murakami, T. N. & Snaith, H. J. Efficient Hybrid Solar Cells Based on Meso-Superstructured Organometal Halide Perovskites. *Science* **338**, 643–647 (2012).
25. NREL. Best Research-Cell Efficiencies. (2017). Available at: http://www.nrel.gov/ncpv/images/efficiency_chart.jpg. (Accessed: 20th November 2017)
26. Domanski, K. *et al.* Not All That Glitters Is Gold: Metal-Migration-Induced Degradation in Perovskite Solar Cells. *ACS Nano* **10**, 6306–6314 (2016).
27. Anaraki, E. H. *et al.* Highly efficient and stable planar perovskite solar cells by solution-processed tin oxide. *Energy Environ. Sci.* **9**, 3128–3134 (2016).
28. Correa Baena, J. P. *et al.* Highly efficient planar perovskite solar cells through band alignment engineering. *Energy Environ. Sci.* **8**, 2928–2934 (2015).
29. Wu, C.-G. *et al.* High efficiency stable inverted perovskite solar cells without current hysteresis. *Energy Environ. Sci.* **8**, 2725–2733 (2015).
30. Chiang, C.-H., Tseng, Z.-L. & Wu, C.-G. Planar heterojunction perovskite/PC71BM solar cells with enhanced open-circuit voltage via a (2/1)-step spin-coating process. *J. Mater. Chem. A* **2**, 15897–15903 (2014).
31. Jeon, N. J. *et al.* Solvent engineering for high-performance inorganic–organic hybrid perovskite solar cells. *Nat. Mater.* (2014).
32. Li, X. *et al.* A vacuum flash–assisted solution process for high-efficiency large-area perovskite solar cells. *Science* aaf8060 (2016). doi:10.1126/science.aaf8060
33. Malinkiewicz, O. *et al.* Perovskite solar cells employing organic charge-transport layers. *Nat. Photonics* **8**, 128–132 (2014).
34. Liu, M., Johnston, M. B. & Snaith, H. J. Efficient planar heterojunction perovskite solar cells by vapour deposition. *Nature* **501**, 395–398 (2013).
35. Tress, W. *et al.* The role of the hole-transport layer in perovskite solar cells - reducing recombination and increasing absorption. *2014 IEEE 40th Photovolt. Spec. Conf. Pvsc* 1563–1566 (2014).
36. Bi, D., Yang, L., Boschloo, G., Hagfeldt, A. & Johansson, E. M. J. Effect of Different Hole Transport Materials on Recombination in CH₃NH₃PbI₃ Perovskite-Sensitized Mesoscopic Solar Cells. *J. Phys. Chem. Lett.* **4**, 1532–1536 (2013).

37. Adhikari, N. *et al.* Interfacial Study To Suppress Charge Carrier Recombination for High Efficiency Perovskite Solar Cells. *ACS Appl. Mater. Interfaces* **7**, 26445–26454 (2015).
38. Correa-Baena, J.-P. *et al.* Identifying and suppressing interfacial recombination to achieve high open-circuit voltage in perovskite solar cells. *Energy Environ. Sci.* (2017). doi:10.1039/C7EE00421D
39. Long, R., Liu, J. & Prezhd, O. V. Unravelling the Effects of Grain Boundary and Chemical Doping on Electron–Hole Recombination in CH₃NH₃PbI₃ Perovskite by Time-Domain Atomistic Simulation. *J. Am. Chem. Soc.* **138**, 3884–3890 (2016).
40. Tress, W. Perovskite Solar Cells on the Way to Their Radiative Efficiency Limit – Insights Into a Success Story of High Open-Circuit Voltage and Low Recombination. *Adv. Energy Mater.* (2017). doi:10.1002/aenm.201602358
41. Bi, D. *et al.* Efficient luminescent solar cells based on tailored mixed-cation perovskites. *Sci. Adv.* **2**, e1501170 (2016).
42. Saliba, M. *et al.* Incorporation of rubidium cations into perovskite solar cells improves photovoltaic performance. *Science* **354**, 206–209 (2016).
43. Snaith, H. J. *et al.* Anomalous Hysteresis in Perovskite Solar Cells. *J. Phys. Chem. Lett.* **5**, 1511–1515 (2014).
44. Dualeh, A. *et al.* Impedance Spectroscopic Analysis of Lead Iodide Perovskite-Sensitized Solid-State Solar Cells. *ACS Nano* (2013). doi:10.1021/nn404323g
45. Unger, E. *et al.* Hysteresis and transient behavior in current–voltage measurements of hybrid-perovskite absorber solar cells. *Energy Environ. Sci.* **7**, 3690–3698 (2014).
46. Tress, W. *et al.* Understanding the rate-dependent J–V hysteresis, slow time component, and aging in CH₃NH₃PbI₃ perovskite solar cells: the role of a compensated electric field. *Energy Environ. Sci.* (2015).
47. Shao, Y., Xiao, Z., Bi, C., Yuan, Y. & Huang, J. Origin and elimination of photocurrent hysteresis by fullerene passivation in CH₃NH₃PbI₃ planar heterojunction solar cells. *Nat. Commun.* **5**, 5784 (2014).
48. Frost, J. M., Butler, K. T. & Walsh, A. Molecular ferroelectric contributions to anomalous hysteresis in hybrid perovskite solar cells. *APL Mater.* **2**, 081506 (2014).
49. Chen, H.-W., Sakai, N., Ikegami, M. & Miyasaka, T. Emergence of Hysteresis and Transient Ferroelectric Response in Organo-Lead Halide Perovskite Solar Cells. *J. Phys. Chem. Lett.* (2014).
50. Liu, S. *et al.* Ferroelectric Domain Wall Induced Band-Gap Reduction and Charge Separation in Organometal Halide Perovskites. *J. Phys. Chem. Lett.* (2015). doi:10.1021/jz502666j
51. Kutes, Y. *et al.* Direct observation of ferroelectric domains in solution-processed CH₃NH₃PbI₃ Perovskite Thin Films. *J. Phys. Chem. Lett.* **5**, 3335–3339 (2014).
52. Hoke, E. T. *et al.* Reversible photo-induced trap formation in mixed-halide hybrid perovskites for photovoltaics. *Chem. Sci.* **6**, 613–617 (2015).
53. Meloni, S. *et al.* Ionic polarization-induced current-voltage hysteresis in CH₃NH₃PbX₃ perovskite solar cells. *Nat. Commun.* **7**, 10334 (2016).

54. Zhao, C. *et al.* Revealing Underlying Processes Involved in Light Soaking Effects and Hysteresis Phenomena in Perovskite Solar Cells. *Adv. Energy Mater.* (2015).
55. Azpiroz, J. M., Mosconi, E., Bisquert, J. & De Angelis, F. Defects Migration in Methylammonium Lead Iodide and their Role in Perovskite Solar Cells Operation. *Energy Environ. Sci.* (2015).
56. Albin, D. S., Dhere, R. G., Glynn, S. C., del Cueto, J. A. & Metzger, W. K. Degradation and capacitance: voltage hysteresis in CdTe devices. in **7412**, 74120-74120-12 (2009).
57. Monokroussos, C. *et al.* The Effects of Solar Cell Capacitance on Calibration Accuracy When using a Flash Simulator. in **2**, 2231-2234 (2006).
58. O'Regan, B. C. *et al.* Optoelectronic Studies of Methylammonium Lead Iodide Perovskite Solar Cells with Mesoporous TiO₂: Separation of Electronic and Chemical Charge Storage, Understanding Two Recombination Lifetimes, and the Evolution of Band Offsets during J-V Hysteresis. *J. Am. Chem. Soc.* **137**, 5087-5099 (2015).
59. Li, C. *et al.* Iodine Migration and its Effect on Hysteresis in Perovskite Solar Cells. *Adv. Mater.* **28**, 2446-2454 (2016).
60. Richardson, G. *et al.* Can slow-moving ions explain hysteresis in the current-voltage curves of perovskite solar cells? *Energy Environ. Sci.* **9**, 1476-1485 (2016).
61. Miller, D. W. *et al.* Defect states in perovskite solar cells associated with hysteresis and performance. *Appl. Phys. Lett.* **109**, 153902 (2016).
62. Tress, W. Metal Halide Perovskites as Mixed Electronic-Ionic Conductors: Challenges and Opportunities—From Hysteresis to Memristivity. *J. Phys. Chem. Lett.* 3106-3114 (2017). doi:10.1021/acs.jpcclett.7b00975
63. Jacobs, D. A. *et al.* Hysteresis phenomena in perovskite solar cells: the many and varied effects of ionic accumulation. *Phys. Chem. Chem. Phys.* **19**, 3094-3103 (2017).
64. Yin, W.-J., Shi, T. & Yan, Y. Unusual defect physics in CH₃NH₃PbI₃ perovskite solar cell absorber. *Appl. Phys. Lett.* **104**, 063903 (2014).
65. Kim, J., Lee, S.-H., Lee, J. H. & Hong, K.-H. The Role of Intrinsic Defects in Methylammonium Lead Iodide Perovskite. *J. Phys. Chem. Lett.* 1312-1317 (2014). doi:10.1021/jz500370k
66. Mizusaki, J., Arai, K. & Fueki, K. Ionic conduction of the perovskite-type halides. *Solid State Ion.* **11**, 203-211 (1983).
67. Ishigaki, T., Yamauchi, S., Kishio, K., Mizusaki, J. & Fueki, K. Diffusion of oxide ion vacancies in perovskite-type oxides. *J. Solid State Chem.* **73**, 179-187 (1988).
68. Xiao, Z. *et al.* Giant switchable photovoltaic effect in organometal trihalide perovskite devices. *Nat. Mater.* **14**, 193-198 (2015).
69. Yuan, Y. *et al.* Photovoltaic Switching Mechanism in Lateral Structure Hybrid Perovskite Solar Cells. *Adv. Energy Mater.* (2015).
70. Erdenebileg, E., Scholz, L. E., Hofacker, A., Koerner, C. & Leo, K. Very Small Inverted Hysteresis in Vacuum-Deposited Mixed Organic-Inorganic Hybrid Perovskite Solar Cells. *Energy Technol.* (2017). doi:10.1002/ente.201700002

71. Tress, W., Correa Baena, J. P., Saliba, M., Abate, A. & Graetzel, M. Inverted Current–Voltage Hysteresis in Mixed Perovskite Solar Cells: Polarization, Energy Barriers, and Defect Recombination. *Adv. Energy Mater.* **6**, 1600396 (2016).
72. Jena, A. K. *et al.* The Interface between FTO and the TiO₂ Compact Layer Can Be One of the Origins to Hysteresis in Planar Heterojunction Perovskite Solar Cells. *ACS Appl. Mater. Interfaces* **7**, 9817–9823 (2015).
73. Tubbs, M. R. The optical properties and chemical decomposition of halides with layer structures. II. defects, chemical decomposition, and photographic phenomena. *Phys. Status Solidi B* **67**, 11–49 (1975).
74. Zhang, Y. *et al.* Charge selective contacts, mobile ions and anomalous hysteresis in organic–inorganic perovskite solar cells. *Mater. Horiz.* **2**, 315–322 (2015).
75. Priyadarshi, A. *et al.* A large area (70 cm²) monolithic perovskite solar module with a high efficiency and stability. *Energy Environ. Sci.* **9**, 3687–3692 (2016).
76. Hu, Y. *et al.* Stable Large-Area (10 × 10 cm²) Printable Mesoscopic Perovskite Module Exceeding 10% Efficiency. *Sol. RRL* **1**, (2017).
77. Agresti, A. *et al.* Efficiency and Stability Enhancement in Perovskite Solar Cells by Inserting Lithium-Neutralized Graphene Oxide as Electron Transporting Layer. *Adv. Funct. Mater.* **26**, 2686–2694 (2016).
78. Niu, G. *et al.* Study on the stability of CH₃NH₃PbI₃ films and the effect of post-modification by aluminum oxide in all-solid-state hybrid solar cells. *J. Mater. Chem. A* **2**, 705–710 (2013).
79. Leijtens, T. *et al.* Overcoming ultraviolet light instability of sensitized TiO₂ with meso-superstructured organometal tri-halide perovskite solar cells. *Nat. Commun.* **4**, (2013).
80. Mei, A. *et al.* A hole-conductor–free, fully printable mesoscopic perovskite solar cell with high stability. *Science* **345**, 295–298 (2014).
81. Yang, J. & Kelly, T. L. Decomposition and Cell Failure Mechanisms in Lead Halide Perovskite Solar Cells. *Inorg. Chem.* **56**, 92–101 (2017).
82. Saliba, M. *et al.* Cesium-containing Triple Cation Perovskite Solar Cells: Improved Stability, Reproducibility and High Efficiency. *Energy Environ. Sci.* (2016). doi:10.1039/C5EE03874J
83. Nenon, D. P. *et al.* Structural and chemical evolution of methylammonium lead halide perovskites during thermal processing from solution. *Energy Environ. Sci.* **9**, 2072–2082 (2016).
84. Misra, R. K. *et al.* Temperature- and Component-Dependent Degradation of Perovskite Photovoltaic Materials under Concentrated Sunlight. *J. Phys. Chem. Lett.* **6**, 326–330 (2015).
85. Misra, R. K. *et al.* Effect of Halide Composition on the Photochemical Stability of Perovskite Photovoltaic Materials. *ChemSusChem* **9**, 2572–2577 (2016).
86. Beal, R. E. *et al.* Cesium Lead Halide Perovskites with Improved Stability for Tandem Solar Cells. *J. Phys. Chem. Lett.* **7**, 746–751 (2016).
87. Noh, J. H., Im, S. H., Heo, J. H., Mandal, T. N. & Seok, S. I. Chemical Management for Colorful, Efficient, and Stable Inorganic–Organic Hybrid Nanostructured Solar Cells. *Nano Lett.* **13**, 1764–1769 (2013).

88. Bryant, D. *et al.* Light and oxygen induced degradation limits the operational stability of methylammonium lead triiodide perovskite solar cells. *Energy Environ. Sci.* **9**, 1655–1660 (2016).
89. Kato, Y. *et al.* Silver iodide formation in methyl ammonium lead iodide perovskite solar cells with silver top electrodes. *Adv. Mater. Interfaces* **2**, 2196–7350 (2015).
90. Cacovich, S. *et al.* Gold and iodine diffusion in large area perovskite solar cells under illumination. *Nanoscale* **9**, 4700–4706 (2017).
91. Aitola, K. *et al.* Carbon nanotube-based hybrid hole-transporting material and selective contact for high efficiency perovskite solar cells. *Energy Environ. Sci.* **9**, 461–466 (2016).
92. Li, X. *et al.* Outdoor Performance and Stability under Elevated Temperatures and Long-Term Light Soaking of Triple-Layer Mesoporous Perovskite Photovoltaics. *Energy Technol.* **3**, 551–555 (2015).
93. Bush, K. A. *et al.* Thermal and Environmental Stability of Semi-Transparent Perovskite Solar Cells for Tandems Enabled by a Solution-Processed Nanoparticle Buffer Layer and Sputtered ITO Electrode. *Adv. Mater.* (2016). doi:10.1002/adma.201505279
94. Matsui, T. *et al.* Additive-Free Transparent Triarylamine-Based Polymeric Hole-Transport Materials for Stable Perovskite Solar Cells. *ChemSusChem* **9**, 2567–2571 (2016).
95. Niu, G., Guo, X. & Wang, L. Review of recent progress in chemical stability of perovskite solar cells. *J. Mater. Chem. A* **3**, 8970–8980 (2015).
96. Hwang, I., Jeong, I., Lee, J., Ko, M. J. & Yong, K. Enhancing Stability of Perovskite Solar Cells to Moisture by the Facile Hydrophobic Passivation. *ACS Appl. Mater. Interfaces* **7**, 17330–17336 (2015).
97. Smith, I. C., Hoke, E. T., Solis-Ibarra, D., McGehee, M. D. & Karunadasa, H. I. A Layered Hybrid Perovskite Solar-Cell Absorber with Enhanced Moisture Stability. *Angew. Chem.* **126**, 11414–11417 (2014).
98. Dong, X. *et al.* Improvement of the humidity stability of organic–inorganic perovskite solar cells using ultrathin Al₂O₃ layers prepared by atomic layer deposition. *J. Mater. Chem. A* **3**, 5360–5367 (2015).
99. Bella, F. *et al.* Improving efficiency and stability of perovskite solar cells with photocurable fluoropolymers. *Science* (2016). doi:10.1126/science.aah4046
100. Yang, J., Siempelkamp, B. D., Liu, D. & Kelly, T. L. Investigation of CH₃NH₃PbI₃ Degradation Rates and Mechanisms in Controlled Humidity Environments Using in Situ Techniques. *ACS Nano* **9**, 1955–1963 (2015).
101. Christians, J. A., Miranda Herrera, P. A. & Kamat, P. V. Transformation of the Excited State and Photovoltaic Efficiency of CH₃NH₃PbI₃ Perovskite upon Controlled Exposure to Humidified Air. *J. Am. Chem. Soc.* **137**, 1530–1538 (2015).
102. Li, W. *et al.* Enhanced UV-light stability of planar heterojunction perovskite solar cells with caesium bromide interface modification. *Energy Environ. Sci.* **9**, 490–498 (2016).
103. Ito, S., Tanaka, S., Manabe, K. & Nishino, H. Effects of Surface Blocking Layer of Sb₂S₃ on Nanocrystalline TiO₂ for CH₃NH₃PbI₃ Perovskite Solar Cells. *J. Phys. Chem. C* **118**, 16995–17000 (2014).

104. Pathak, S. K. *et al.* Towards Long-Term Photostability of Solid-State Dye Sensitized Solar Cells. *Adv. Energy Mater.* **4**, (2014).
105. International Electrotechnical Commission. IEC 61215 Terrestrial photovoltaic (PV) modules - Design qualification and type approval. (2016).
106. Reese, M. O. *et al.* Consensus stability testing protocols for organic photovoltaic materials and devices. *Spec. Issue 3rd Int. Summit OPV Stab.* **95**, 1253–1267 (2011).
107. Grancini, G. *et al.* One-Year stable perovskite solar cells by 2D/3D interface engineering. *Nat. Commun.* **8**, (2017).
108. Arora, N. *et al.* Perovskite solar cells with CuSCN hole extraction layers yield stabilized efficiencies greater than 20%. *Science* **358**, 768 (2017).
109. Bush, K. A. *et al.* 23.6%-efficient monolithic perovskite/silicon tandem solar cells with improved stability. *Nat. Energy* **2**, 17009 (2017).
110. Jeon, N. J. *et al.* Compositional engineering of perovskite materials for high-performance solar cells. *Nature* **517**, 476–480 (2015).
111. Yang, W. S. *et al.* High-performance photovoltaic perovskite layers fabricated through intramolecular exchange. *Science* **aaa9272** (2015).
112. You, J. *et al.* Improved air stability of perovskite solar cells via solution-processed metal oxide transport layers. *Nat Nano* **11**, 75–81 (2016).
113. Slotcavage, D. J., Karunadasa, H. I. & McGehee, M. D. Light-Induced Phase Segregation in Halide-Perovskite Absorbers. *ACS Energy Lett.* **1**, 1199–1205 (2016).
114. Rost, C. M. *et al.* Entropy-stabilized oxides. *Nat. Commun.* **6**, (2015).
115. Jones, N. G., Aveson, J. W., Bhowmik, A., Conduit, B. D. & Stone, H. J. On the entropic stabilization of an Al_{0.5}CrFeCoNiCu high entropy alloy. *Intermetallics* **54**, 148–153 (2014).
116. Bach, U. *et al.* Solid-state dye-sensitized mesoporous TiO₂ solar cells with high photon-to-electron conversion efficiencies. *Nature* **395**, 583–585 (1998).
117. Malinauskas, T. *et al.* Enhancing Thermal Stability and Lifetime of Solid-State Dye-Sensitized Solar Cells via Molecular Engineering of the Hole-Transporting Material Spiro-OMeTAD. *ACS Appl. Mater. Interfaces* **7**, 11107–11116 (2015).
118. Leijtens, T. *et al.* Hole Transport Materials with Low Glass Transition Temperatures and High Solubility for Application in Solid-State Dye-Sensitized Solar Cells. *ACS Nano* **6**, 1455–1462 (2012).
119. Barard, S. *et al.* Separate charge transport pathways determined by the time of flight method in bimodal polytriarylamine. *J. Appl. Phys.* **105**, 013701 (2009).
120. Yang, W. S. *et al.* High-performance photovoltaic perovskite layers fabricated through intramolecular exchange. *Science* **aaa9272** (2015).
121. Heo, J. H. *et al.* Efficient inorganic-organic hybrid heterojunction solar cells containing perovskite compound and polymeric hole conductors. *Nat. Photonics* **7**, 486–491 (2013).

122. Heo, J. H., Han, H. J., Kim, D., Ahn, T. K. & Im, S. H. Hysteresis-less inverted CH₃NH₃PbI₃ planar perovskite hybrid solar cells with 18.1% power conversion efficiency. *Energy Environ. Sci.* **8**, 1602–1608 (2015).
123. Li, W. *et al.* Montmorillonite as bifunctional buffer layer material for hybrid perovskite solar cells with protection from corrosion and retarding recombination. *J. Mater. Chem. A* **2**, 13587–13592 (2014).
124. Li, Z. *et al.* Extrinsic ion migration in perovskite solar cells. *Energy Environ. Sci.* (2017). doi:10.1039/C7EE00358G
125. Peters, C. H. *et al.* High efficiency polymer solar cells with long operating lifetimes. *Adv. Energy Mater.* **1**, 491–494 (2011).
126. Domanski, K. *et al.* Migration of cations induces reversible performance losses over day/night cycling in perovskite solar cells. *Energy Environ. Sci.* **10**, 604– (2017).
127. Dualeh, A., Gao, P., Seok, S. I., Nazeeruddin, M. K. & Grätzel, M. Thermal Behavior of Methylammonium Lead-Trihalide Perovskite Photovoltaic Light Harvesters. *Chem. Mater.* **26**, 6160–6164 (2014).
128. Akbulatov, A. F. *et al.* Probing the Intrinsic Thermal and Photochemical Stability of Hybrid and Inorganic Lead Halide Perovskites. *J. Phys. Chem. Lett.* **8**, 1211–1218 (2017).
129. Frost, J. M. & Walsh, A. What Is Moving in Hybrid Halide Perovskite Solar Cells? *Acc. Chem. Res.* **49**, 528–535 (2016).
130. Eames, C. *et al.* Ionic transport in hybrid lead iodide perovskite solar cells. *Nat. Commun.* **6**, (2015).
131. Domanski, K. *et al.* Working Principles of Perovskite Photodetectors: Analyzing the Interplay Between Photoconductivity and Voltage-Driven Energy-Level Alignment. *Adv. Funct. Mater.* **25**, 6936–6947 (2015).
132. Domanski, K., Alharbi, E., Hagfeldt, A., Gratzel, M. & Tress, W. Systematic Investigation of the Impact of Operation Conditions on the Degradation Behaviour of Perovskite Solar Cells. *Nat. Energy* (Accepted).
133. Hou, Y. *et al.* A generic interface to reduce the efficiency-stability-cost gap of perovskite solar cells. *Science* (2017). doi:10.1126/science.aao5561
134. Chen, W. *et al.* Efficient and stable large-area perovskite solar cells with inorganic charge extraction layers. *Science* **350**, 944–948 (2015).

Konrad Domanski

kn.domanski@gmail.com • +41 76 442 75 41 • Av. l'Eglise-Anglaise 14, 1006 Lausanne
[linkedin.com/in/konrad-domanski](https://www.linkedin.com/in/konrad-domanski) (references available online or on request)



Research and Development Scientist/Engineer with entrepreneurial mindset

Top-performing, ambitious leader and inquisitive scientist, who derives energy from solving complex problems. In my career, I seek to combine my technical background with entrepreneurial mindset to bridge the gap between research and innovation.

Strengths

Solar cell design & characterisation • Nanotechnology • Thin films • R&D • Problem solving • Project management

Core Experience

Sep 2014 - Feb 2018 **Doctoral Assistant at École Polytechnique Fédérale de Lausanne**

- Published 2 patents and 6 first-author papers in top journals including *Science*
- Improved solar cell measurement efficiency by 700% by building a dedicated setup
- Designed and built state-of-the-art stability measurement setup (€200' 000 budget)
- Improved workflow and maintained equipment as Laboratory Manager
- Presented my work at top international conferences (both orally and posters)
- Collaborated intensively with colleagues and led several projects simultaneously

Feb 2017 - Jun 2017 **CEO at Perosol** (within the framework of federal *CTI Business Concept* program, part-time)

- Assessed commercial potential of my PhD inventions while leading a four-member team
- Conducted market study, patent and regulation review; built proof-of-concept prototype

Dec 2013 - Mar 2014 **Technology Consultant at Archipelago Technology Group Ltd** (part-time)

- Devised a market entry strategy for a new nanoparticle product line
- Delivered a report and presented the findings to the client

Summer 2012 **Research Intern at École Polytechnique Fédérale de Lausanne**

- In cleanroom, optimised the photolithographic process for carbon nanocomposites
- Critically improved the dispersion of carbon nanotubes in composite thin films

Education

Sep 2014 - Feb 2018 **École Polytechnique Fédérale de Lausanne, Ph.D. Materials Science, dir.: Prof. M. Grätzel**

Thesis: *'The Quest for Stability of Perovskite Solar Cells'*

- Won Dimitris N. Chorafas Foundation Prize for exceptional research achievements

Oct 2013 - Jul 2014 **University of Cambridge, M.Phil. Micro & Nanotechnology Enterprise, dir.: Prof N. Greenham**

Thesis: *'In-situ Studies of Degradation Processes in Solution-Processed Photovoltaics'*

- Graduated top of the class with *Distinction* and GPA 3.96/4.00
- Won the prestigious *Gates Cambridge Scholarship* (<1% success rate)

Oct 2010 - Jun 2013 **Imperial College London, B.Eng. Materials Science and Engineering**

Thesis: *'Design and Commercialization of a Desert-Compatible Wind Turbine'*

- Graduated top of the class with *High 1st-Class Degree* and GPA 4.00/4.00

Konrad Domanski • kn.domanski@gmail.com • +41 76 442 75 41**Additional Experience**

- Dec 2016 - Present **Senior Project Manager at Innovation Forum Lausanne** (part-time)
- Organized IMAGINE IF! Lausanne 2017 startup accelerator for science ventures
 - Supervised a team of three, collaborated with range of academic and industrial partners
 - Won "EPFL Innovation Night" business idea and pitching competition
- Jun 2009 - Present **Mountain Guide** (freelance, non-profit)
- Organized and guided several-day hiking trips of up to 25 people
 - Responsible for logistics, safety, planning and budgeting
- Sep 2012 - Jul 2014 **Private Tutor in Maths** (high school level, part-time)
- Explained mathematical concepts in a concise, simple and individually-tailored way
- Summer 2011 **Research Intern at Imperial College London**
- Found an effective method for synthesis of silver nanoparticles of given specifications
- Summers 2009-2011 **Head Gardener at Eur-Ogród – Landscaping and Garden Designing**
- Supervised a team of three, planned work schedule and logistics

Languages

English:	Full proficiency
French:	Good command, B2 level
German	Basic communication skills, A1 level
Polish:	Native

Technical Skills

IT Skills:	Solidworks (CAD), Origin, LaTeX, MS Office
Research Skills:	Prototyping, Data analysis, Technology transfer, Experimental design, Project management, Complex problem solving, Strong presentation and redaction skills, Good collaboration ability
Laboratory Skills:	Thin film deposition, Solar cell design and characterisation, UV-vis, IR spectroscopy, Mass spectrometry, XRD, Electron microscopy, AFM, Profilometry, Cleanroom experience

Interests

Mountaineering:	Climbed several challenging mountains incl. Mont Blanc (4810 m) and Illiniza Norte (5126 m) Organised and guided ambitious, multi-day mountain expeditions (2007 - Present)
Cycling:	Organised long bike tours in different countries (2014 - Present)
Music:	Leader, vocalist and guitarist of a music band (2009 - 2010)
Geopolitics:	Avid reader and subscriber of <i>The Economist</i> , <i>BBC</i> and <i>Politico</i>

Personal Information

Date of birth:	18.03.1991
Status:	Married
Nationality:	Polish (Swiss work Permit B)
Driving:	Driving licence category B
Military:	No military obligations

Konrad Domanski • kn.domanski@gmail.com • +41 76 442 75 41**Main Publications**

1. **Domanski K**, Alharbi E, Hagfeldt A, Grätzel M, Tress W. Systematic investigation of the impact of operation conditions on the degradation behaviour of perovskite solar cells. *Nature Energy*. Accepted.
2. Aitola K, **Domanski K**, Correa-Baena J-P, Sveinbjornsson K, Saliba M, Abate A, et al. High Temperature-Stable Perovskite Solar Cells Based on Low-Cost Carbon Nanotube Hole Contact. *Adv Mater*. 2017.
3. **Domanski K**, Roose B, Matsui T, Saliba M, Turren-Cruz S-H, Correa-Baena J-P, et al. Migration of Cations Induces Reversible Performance Losses over Day/Night Cycling in Perovskite Solar Cells. *Energy Environ. Sci*. 2017.
4. Saliba M, Matsui T, **Domanski K**, Seo J-Y, Ummadisingu A, Zakeeruddin SM, et al. Incorporation of Rubidium Cations into Perovskite Solar Cells Improves Photovoltaic Performance. *Science*. 2016.
5. **Domanski K**, Correa-Baena J-P, Mine N, Nazeeruddin MK, Abate A, Saliba M, et al. Not All That Glitters Is Gold: Metal-Migration-Induced Degradation in Perovskite Solar Cells. *ACS Nano*. 2016.
6. Saliba M, Matsui T, Seo J-Y, **Domanski K**, Correa-Baena J-P, Nazeeruddin MK, et al. Cesium-Containing Triple Cation Perovskite Solar Cells: Improved Stability, Reproducibility and High Efficiency. *Energy Environ. Sci*. 2016.
7. **Domanski K**, Tress W, Moehl T, Saliba M, Nazeeruddin MK, Grätzel M. Working Principles of Perovskite Photodetectors: Analyzing the Interplay between Photoconductivity and Voltage-Driven Energy-Level Alignment. *Adv Funct Mater*. 2015.

Full list of publications available at [Google Scholar](#)**Patents (published)**

1. Saliba M, Matsui T, **Domanski K**, Seo J, Zakeeruddin SM, Tress W, Grätzel M. Mixed Cation Perovskite Solid State Solar Cell and Fabrication Thereof. *EPO application number 16180656.7*.
2. Moehl T, Nazeeruddin M, Grätzel M, Im J-H, Park N-G, **Domanski K**. Perovskite Devices, Especially Photodetectors, and Their Fabrication, Operation, and Devices Using Them. *WO 2016038501, A2 20160317*.

Conference contributions

1. **Domanski K**. Stability of Perovskite Solar Cells. *Global Young Scientist Summit*. Poster. 2018
2. **Domanski K**. Towards Consensus on Ageing Perovskite Solar Cells. *Next Generation of Solar Energy Conf*. Oral. 2017
3. **Domanski K**. Towards Experimental Standards for Ageing Perovskite Solar Cells. *10th International Summit on Stability of Organic and Perovskite Solar Cells*. Oral. 2017
4. **Domanski K**. The Quest for Stability of Perovskite Solar Cells. *Hybrid and Organic Photovoltaics Conf*. Oral. 2017
5. **Domanski K**. Not All That Glitters Is Gold: Metal-Migration-Induced Degradation in Perovskite Solar Cells. *Hybrid and Organic Photovoltaics Conf*. Poster. 2016
6. **Domanski K**. Perovskite Photodetector. *Perovskite Solar Cells and Optoelectronics Conf*. Poster. 2015
7. **Domanski K**. Working Principles of Perovskite Photodetectors. *Hybrid and Organic Photovoltaics Conf*. Oral. 2015

